THE UNIVERSITY of ADELAIDE

Interface Design and Electrolyte Engineering for Highly Reversible Metal-Based Batteries

Yanyan Wang

School of Chemical Engineering

Faculty of Sciences, Engineering and Technology

A thesis submitted for the degree of Doctor of Philosophy

The University of Adelaide

April 2023

Contents

Abstract

Battery technologies have been revolutionizing industries and our daily lives. As energy storage and conversion systems, batteries are playing the role of transitioning the source of energy from fossil fuel dependence to renewable-fuel dominance. Battery-powered electric vehicles are replacing petrol vehicles, which has been intensifying the need for batteries with high energy density. Lithium metal batteries (LMBs) are regarded as such a potential candidate, which could achieve an energy density of up to 500 Wh kg^{-1}. The main drawbacks for LMBs are severe corrosion of Li metal during air exposure, dendrite growth induced short-circuit risk, excessive side reaction between Li metal and electrolyte, and poor battery life. Large-scale energy storage is essential for renewable energy such as solar and wind to balance electricity supply and demand. Zinc ion batteries (ZIBs), featured with safety, low cost and environment-friendliness, are promising in this field. However, real applications of ZIBs are hindered by unwanted dendrite growth, Zn corrosion, cathode material degradation, insufficient temperature adaptability and electrochemical stability window (ESW).

This Thesis aims to optimize the battery performance of LMBs and ZIBs, especially anode reversibility and cathode stability, via electrode/electrolyte interface modification and electrolyte design.

In this Thesis, a systematic literature review is provided in Chapter 2 covering the most advanced strategies of artificial protection layer design for LMBs, in the category of mono-component inorganic layers, reactive inorganic layers, hybrid inorganic layers, polymer-like inorganic layers, polymer layers, and inorganic-organic composite layers. Chapter 2 also includes a review of the ZIBs electrolyte design, with the aspects of optimizing the compatibility between cathode materials and electrolytes, inhibiting anode corrosion and dendrite growth, extending electrochemical stability windows, enabling wearable applications, and enhancing temperature tolerance.

Chapter 3 focuses on designing a protection layer on the Li metal surface. A silane coupling agent is used as the adhesion promoter to address the adhesion issue between the SEI layer and Li metal anode, and as a protection layer to avoid the Li metal from corrosion by air. This design provides a promising pathway for the development of Li metal electrodes that will be stable both in electrolytes and in the air.

Chapter 4 proposes a hybrid electrolyte (HE) with dimethylacetamide (DMAC), trimethyl phosphate (TMP) and H_2O as the solvent for ZIBs. We show that the strong polar DMAC and TMP molecules have a significant impact on H_2O to strengthen the O−H bonds and suppress activity. We evidence that the hybrid electrolyte obviates anode corrosion, extends operation temperature, guides the (002) plane preferred orientation during Zn plating, and is compatible with the high-voltage cathode.

Chapter 5 investigates the different electrochemical performances of sodium vanadate in the hybrid electrolyte and the aqueous electrolyte. It is observed that the structural stability of the $NaV_3O_8 \cdot 1.5H_2O$ cathode is significantly improved during continuous charging/discharging if fewer water molecules are included in the Zn^{2+} solvation structure. This is the reason accounting for the longer lifespan of $Zn||NaV_3O_8 \cdot 1.5H_2O$ cell obtained in the HE compared to that in aqueous electrolyte.

Declaration

I certify that this work contains no material which has been accepted for the award of any other degree or diploma in my name, in any university or other tertiary institution and, to the best of my knowledge and belief, contains no material previously published or written by another person, except where due reference has been made in the text. In addition, I certify that no part of this work will, in the future, be used in a submission in my name, for any other degree or diploma in any university or other tertiary institution without the prior approval of the University of Adelaide and where applicable, any partner institution responsible for the joint award of this degree.

The author acknowledges that copyright of published works contained within the thesis resides with the copyright holder(s) of those works.

I give permission for the digital version of my thesis to be made available on the web, via the University's digital research repository, the Library Search and also through web search engines, unless permission has been granted by the University to restrict access for a period of time.

Signed: … … Date: 05/07/2023

Acknowledgments

First and foremost, I would like to express my deepest gratitude to my supervisor, Prof. Zaiping Guo, for her great support and guidance throughout my research journey. Prof. Guo has extensive knowledge and expertise in the field of batteries, which is helpful in shaping my research. Her patience, encouragement, and enthusiasm have been invaluable to me, and I am genuinely grateful for the opportunity to work with such a dedicated and inspiring mentor. Prof. Guo always provides insightful feedback and constructive criticism, helping me to develop my critical thinking.

I would also like to thank Prof. Yan-Bing He, Prof. Baohua Li and Dr. Jianfeng Mao for their invaluable guidance during my study. Their continuous support has given me the strength to overcome the challenges and obstacles that arise during the research. I am deeply grateful to my team members, including Dr. Wei Kong Pang, Dr. Sailin Liu, Dr. Gemeng Liang, Dr. Jinshuo Zou, Dr. Shilin Zhang, Dr. Cheng Wang, Dr. Fuhua Yang, Dr. Xiaohui Zeng, Ms. Yameng Fan, Ms. Ruizhi Zhang, Ms. Fangli Zhang, Ms. Wei Zheng, Mr. Liang Sun, Mr. Yanqiu Lv, Mr. Guanjie Li, Mr. Mingnan Li, Mr. Jingxi Li, Mr. Caoyu Wang, and others. I would like to thank all the members of Guo LAB. Their kind help and support have made my study and life in Australia wonderful.

I would like to acknowledge the University of Adelaide for providing me with a supportive environment to carry out my research.

Finally, I would like to express my gratitude to my parents, my sister, and my boyfriend, Zhijie Wang. Without their tremendous understanding and encouragement over the past few years, it would be impossible for me to complete my studies.

Chapter 1 Introduction

1.1 Project Significance

The development of battery technologies is essential for numerous modern technologies, such as portable devices, electric vehicles, and renewable energy systems. Researchers, therefore, have higher expectations for battery technologies, such as higher energy density, higher safety, lower cost, better durability, and more friendly environmental impact.

LMBs are featured with considerably higher energy density, up to 500 Wh kg^{-1}, compared with Li-ion batteries, 150~260 Wh kg^{-1}, because Li metal, with a specific capacity as high as 3860 mAh g^{-1}, is used as the anode to supersede for traditional graphite anode. However, new challenges raise when Li metal serves as the anode. Because of high activity of Li metal with air, severe atmospheric corrosion may occur during battery assembly unless strict inert atmosphere protection is applied, which may result in increased production costs. Dendrite growth and continuous side reactions between Li metal anode and electrolyte are also crucial factors accounting for the failure of LMBs. To address the above issues, interface chemistry analysis and protection layer design are of great significance for optimizing the performance of LMBs.

Another challenge for energy storage technologies is the limited resource of lithium, which calls for searching for suitable alternatives, especially one that can be used in the large-scale energy storage area. ZIBs stand out from the alternative options as the most promising stationary energy storage systems to cope with renewable energies, due to their safety, low cost, environment-friendliness and impressive electrochemical performance. Before real applications, significant drawbacks, including unwanted dendrite growth, Zn corrosion, cathode material degradation, insufficient temperature adaptability and electrochemical stability window (ESW), need to be properly addressed. The electrolyte is an essential component, which determines the temperature properties, ESW, and ionic conductivity of ZIBs. Moreover, it has significant impacts on the interface properties of the Zn anode and the Zn^{2+} ion storage mechanisms of cathode materials. Optimizing the electrolyte would be an effective way to improve the battery performance of ZIBs.

1.2 Research Objectives

The main goal of Thesis is to optimize the battery performance of LMBs and ZIBs, in particular the anode reversibility and cathode stability, via electrode/electrolyte interface modifications

and electrolyte design. To achieve this, we use a combination of electrochemistry, interface chemistry characterization, in-situ structural observations, theoretical calculations, and material characterization techniques. To be specific, the objective is to:

- Design an artificial protection layer on the surface of Li metal. The function of this layer is to increase the air tolerance of the Li metal anode and to mitigate side reactions between the electrolyte and the Li metal.
- Formula promising electrolytes that are highly stable with Zn anode, compatible with the high-voltage cathode, and have excellent temperature adaptability and sufficient stable electrochemical window.
- Compare the electrochemical performance of $NaV_3O_8 \cdot 1.5H_2O$ cathode in aqueous electrolytes and hybrid electrolytes, observe the structural evolution of $NaV_3O_8 \cdot 1.5H_2O$ cathode during charging/discharging, and reveal the underlying mechanisms of the performance difference.

1.3 Thesis Outline

This Thesis presents the results of research conducted during my PhD candidature. The chapters in this Thesis are presented as follows:

- **Chapter 1** provides background to the thesis and outlines the project scope and key contributions to the field of energy storage and conversion.
- **Chapter 2** is a literature review covering the recent development of Li metal batteries and ZIBs, especially reviewing the interface modification strategies and advantaged electrolyte design principles.
- **Chapter 3** explores the surface modification of Li metal derived from the self-assembly of the silane coupling agent and characterizes the mechanisms of this layer in increasing air stability and reinforcing the solid electrolyte interphase (SEI) layer of Li metal anode.
- **Chapter 4** proposes a high-quality hybrid electrolyte for ZIBs and determines its functions in inducing dendrite-free Zn deposition, confining water activity, extending the temperature range of battery operation and stabilizing $Zn_3(Fe(CN)_6)_2$ cathode.
- **Chapter 5** investigates how the solvation structure of electrolytes affects the structure and the electrochemical performance of the $NaV_3O_8 \cdot 1.5H_2O$ cathode in ZIBs.
- **Chapter 6** presents the key findings and conclusions and provides outlooks for future work on the design of electrolytes and functional interfaces toward LMBs and ZIBs.

Chapter 2 Literature Review

Metal anodes, such as Li and Zn, distinguish themselves from anodes based on ion insertion or alloying reactions by employing a plating/stripping mechanism to store or release charge carriers, resulting in superior energy density. During the charging process, Li^+ or Zn^{2+} ions are reduced and deposited at the anode/electrolyte interface, while metallic Li or Zn is oxidized and dissolves into the electrolyte upon discharging. However, the utilization of Li and Zn metal anodes presents notable challenges associated with electrolyte activity and interface properties, including volumetric expansion, dendrite formation, and side reactions with electrolytes, all of which contribute to the deterioration of cycle performance and raise safety concerns. The plating behavior of Li^+ or Zn^{2+} ions is profoundly influenced by ion diffusion in the electrolyte, particularly in the proximity of the anode/electrolyte interface, as well as the distribution of the electric field. Once the Li^+ or Zn^{2+} ions become depleted at the interface, dendritic growth can initiate, potentially leading to short-circuiting of the batteries. Concurrently, side reactions between the anode and electrolyte often lead to the formation of by-products or SEI layers, which significantly impede ionic transport during plating processes. Research efforts on Li and Zn metal anodes commonly focus on key parameters such as Coulombic efficiency, morphologies of deposited metal, side reaction products, and the stability of the anode/electrolyte interface.

Given that these challenges primarily originate from the electrode/electrolyte interface and electrolyte itself, optimizing the electrochemical performance of Li and Zn metal anodes necessitates effective strategies in interfacial engineering and electrolyte design. Interfacial engineering entails the introduction of functional components onto the surface of the metal anode. Artificial solid electrolyte interface (ASEI) layers have emerged as a promising approach to passivate the metal anode and mitigate side reactions with the electrolyte. For both Li and Zn metal anodes, the primary requirement for ASEI layers is to enable the transport of Li^+ or Zn^{2+} ions while impeding electron conduction. Moreover, these layers must exhibit sufficient stability and robustness to endure the repetitive plating/stripping processes. Low interfacial resistance is a crucial consideration during the design phase, as polarization effects can significantly impact charge transfer efficiency. Mechanical integrity, flexibility, and adhesion are also vital factors, as they govern the long-term durability of ASEI layers. Alternatively, protective layers can be generated through electrolyte engineering. The incorporation of specific additives or selection of appropriate electrolyte salts can facilitate the formation of desirable SEI layers. The concentration and composition of the electrolyte

solvents can also be adjusted to modulate the properties of the SEI layers. Furthermore, electrolyte design should prioritize enhanced compatibility with Li and Zn metal anodes by considering the solvation structure, which dictates the thermodynamic stability of the electrolytes.

In conclusion, the main strategies and underlying principles for optimizing the performance of Li and Zn metal anodes exhibit substantial similarities. This chapter provides a comprehensive literature review on the recent advancements in Li metal batteries and Zn-ion batteries (ZIBs), with particular emphasis on interface modification strategies and advantageous electrolyte design principles

2.1 Recent advances in interfacial engineering towards practical lithium metal electrodes

This part is under preparation and has not been submitted. It includes recent literature covering the most advanced strategies of artificial protection layer design for LMBs. In this review, the contents are classified according to the chemical composition and structure, which are mono-component inorganic layers, multi-component inorganic layers, inorganic layers with polymeric network, organic polymer layers, and inorganic-organic composite layers. This topic is relevant to my research as presented in Chapter 3.

Statement of Authorship

Title of Paper	Recent advances in developing artificial solid electrolyte interphase towards practical lithium metal electrodes
Publication Status	☐ Published ☐ Accepted for Publication ☐ Submitted for Publication ☑ Unpublished and Unsubmitted work written in manuscript style
Publication Details	Yanyan Wang, Zaiping Guo. Recent advances in developing artificial solid electrolyte interphase towards practical lithium metal electrodes.

Principal Author

Name of Principal Author (Candidate)	Yanyan Wang
Contribution to the Paper	Collected the related information, devised the idea and structure with supervisor, wrote and edited the manuscript.
Overall percentage (%)	70%
Certification:	This paper reports on original research I conducted during the period of my Higher Degree by Research candidature and is not subject to any obligations or contractual agreements with a third party that would constrain its inclusion in this thesis. I am the primary author of this paper.
Signature	Date 15/03/2023

Co-Author Contributions

By signing the Statement of Authorship, each author certifies that:

i. the candidate's stated contribution to the publication is accurate (as detailed above);

ii. permission is granted for the candidate in include the publication in the thesis; and

iii. the sum of all co-author contributions is equal to 100% less the candidate's stated contribution.

Name of Co-Author	Zaiping Guo
Contribution to the Paper	Supervision of the work, discussion of the whole manuscript, revision and conceptualization.
Signature	Date 15/03/2023

2.1.1 Introduction

Battery electric vehicles (BEVs) play an essential role in eliminating the use of fossil fuels and building a carbon-neutral world. However, the development of the BEV market has been hindered by so-called "range anxiety"[1, 2]. This is because traditional graphite-based lithium-ion batteries (LIBs), which are the main power sources of current BEVs, have almost reached the theoretical limit in energy density (~250 W h kg^{-1})[2, 3]. The best strategy to break this bottleneck is to improve the output voltage and specific capacity of batteries. Compared with a traditional graphite anode, metallic Li has an ultra-high specific capacity of 3860 mA h g^{-1} (**Figure 2.1a**), which is 9 times higher than that of graphite[4, 5]. In addition, Li metal anode has the lowest electrochemical potential of −3.04 V vs. the standard hydrogen electrode (SHE) among the alkali metals. When matched with high-voltage cathodes, such as $Li_{1-x}Mn_{2-y}M_yO_4$, the Li metal batteries (LMBs) can deliver a working potential of approaching 5 V[4, 6]. Therefore, LMBs can achieve a boosted energy density of 500 Wh kg^{-1}, and it has been regarded as the most promising candidate for power sources for future BEVs[7].

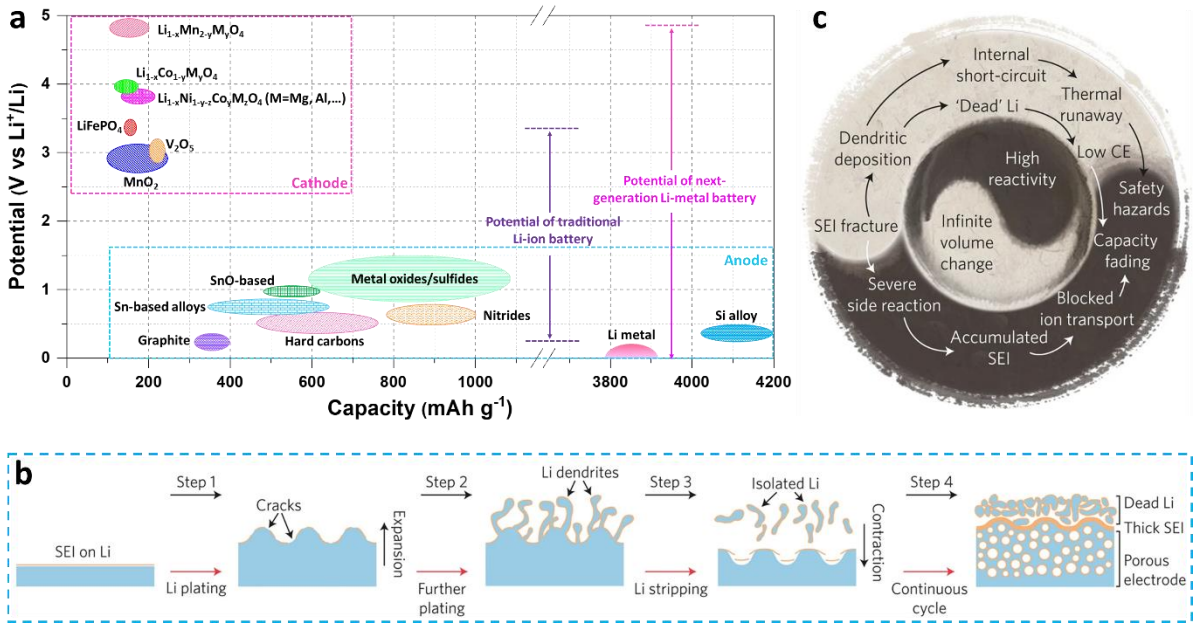

Figure 2.1 Opportunities and challenges of Li metal anode. (a) Voltage versus capacity for anode and cathode materials of Li-ion batteries and Li-metal batteries. Reproduced with permission. Copyright 2021, Royal Society of Chemistry[4]. (b) Schematic showing the Li stripping/plating process. (c) Correlations among the different challenges in the Li metal anode, originating from high reactivity and infinite relative volume change. Reproduced with permission. Copyright 2017, Springer Nature[11].

Nevertheless, Li metal anode is thermodynamically unstable against electrolytes. It will react with all electrolytes to form a solid-electrolyte interphase (SEI)[8]. The SEI layer is electrically isolated but ionically conductive, and thus it can block e-tunneling but allow the diffusion of Li^+. Unfortunately, the natural SEI is brittle and fragile, which can be easily destroyed by the morphology and volume change of Li metal anode[9]. Moreover, Li^+ is prone to deposit on the negatively charged prominent points of the substrates, inducing a dendritic morphology. In the following non-uniform stripping from the routes of the dendrite, the Li metal may lose electrical contact with substrate and become electrically "dead" Li[10]. The SEI layer is broken up and repaired during the continuous plating/stripping cycles. As a consequence, the electrode becomes porous, and finally, a "dead" Li layer is accumulated (Figure 2.1b)[11]. Worse still, the Li dendrite could pierce separators and incur an internal short-circuit. These challenges lead to electrochemical performance decay and even safety hazards in working batteries, and fundamentally hinder the practical applications of LMBs (**Figure 2.1c**)[11].

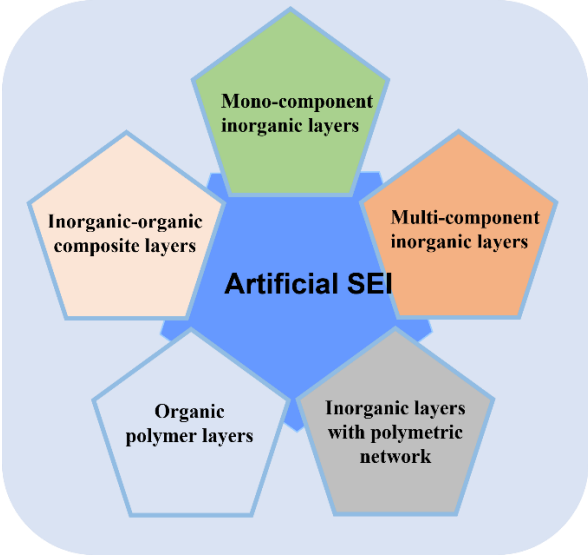

Figure 2.2 Illustration of the categories of ASEI discussed in this chapter.

An ideal SEI layer should be electrically insulative but ionically conductive, and therefore prevent further reaction between Li metal and electrolytes[8, 12]. However, the natural SEI layer formed in the traditional carbonate and ether electrolytes is organic-rich, which is fragile and can be easily destroyed by the interfacial strains [9, 13]. Constructing artificial SEI (ASEI) layers is a widely used and effective strategy to address these challenges[14, 15]. According to the chemical composition and structure, the reported ASEI can be classified into five categories, i.e., mono-component inorganic layers, multi-component inorganic layers, inorganic layers

with polymetric network, organic polymer layers, and inorganic-organic composite layers, as illustrated in **Figure 2.2**.

2.1.2 Mono-component inorganic layers

In the early research stage of ASEI, researchers mainly focused on mono-component inorganic layers, because they can be feasibly modified on Li metal anode *via in-situ* or *ex-situ* methods. Generally, these ASEI layers are characterized by higher Young's modulus than that of Li dendrite, and are expected to suppress the formation and growth of Li dendrite[15, 16]. Newman et al.[17] proved that a Young's module at least 6 GPa is required to stop the growth of Li dendrite. Based on this criterion, a thin Li_3PO_4 layer with a thickness of 200 nm was prepared by *in-situ* chemical reaction on Li metal[18], in which the Young's module is measured to be as high as ~11 GPa and the suppressing effect on Li dendrite was achieved. The passivation layer composed with high hardness Al_2O_3[19] was also verified to be useful in protecting the Li metal from electrolyte erosion and dendrite formation.

Besides the requirement for high Young's modulus, high ionic conductivity of Li^+ is also a crucial factor to be considered when design ASEI layers. Alloys such as Li_xSb[20] have high superior ionic conductivity and have been applied as ASEI layer for Li metal anode. Li_3N[21], Li_3P[22], Li_2S[23], and Li_2Se[24], featured with ionic conductivity higher than ~10^{-5} S cm^{-1}, also attract intensive interests. The most common fabrication methods for these ASEI layers are treating the Li metal foil with N_2 gas or vapor elemental P/S/Se, and wet chemistry treatments. Cui et al. developed a pinhole free α-Li_3N ASEI layer, in which the grain boundaries are strongly interconnected to improve the mechanical strength of the layer[25]. This group also proposed a Li_2S coated Li anode[26], which extends the lifespan of LMBs even under the working condition of low negative/positive electrode capacity (n/p) ratios. Lithium halides, mainly including LiF, LiCl, and LiBr, are another category worth investigating. These components exhibit both high Young's modules and high interfacial energy, promoting Li deposition in a parallel rather than vertical direction[20, 27]. Although the ionic conductivity is relatively low (~10^{-9} S cm^{-1}), lithium halides, especially LiF, can facilitate Li^+ transportation through the grain boundaries.

2.1.3 Multi-component inorganic layers

In general, the advantages and disadvantages of the mono-component inorganic layer are quite distinct, and their functions are relatively limited. To maximize the superiority and overcome

the shortcomings of these inorganic components, researchers pay more attention to the compositions and structure of ASEI layers.

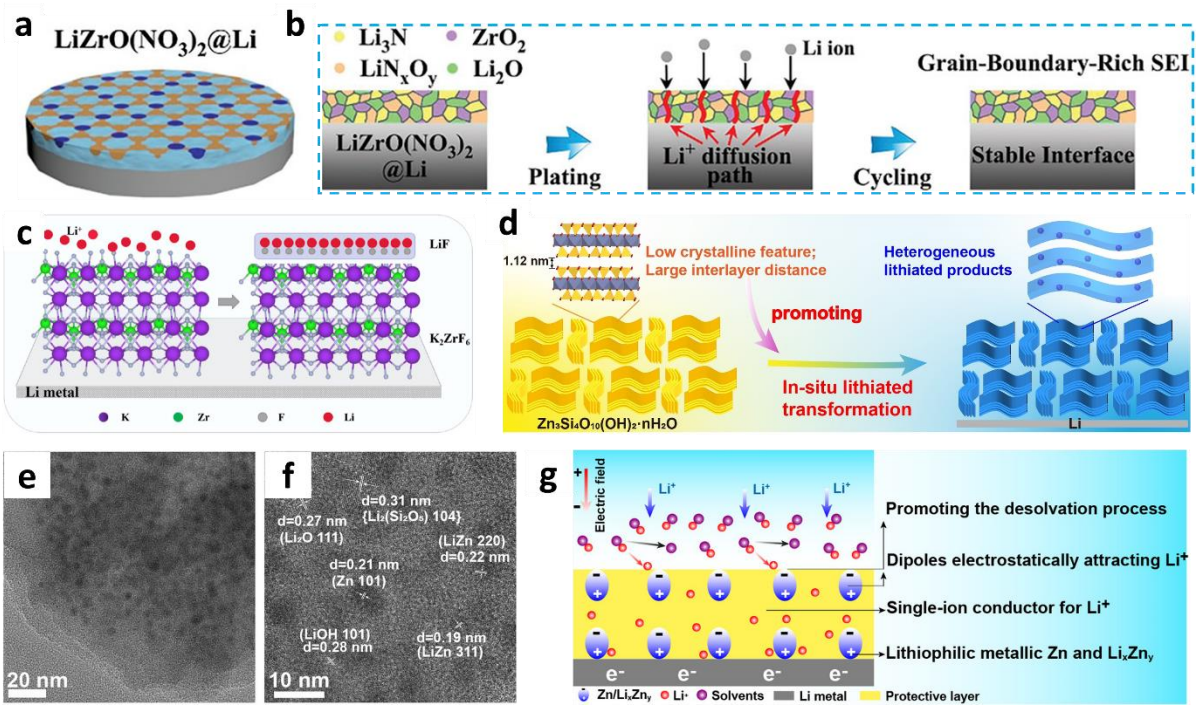

Figure 2.3 Reactive inorganic ASEI layers. (a) Illustration for the $LiZrO(NO_3)_2$ layer coated on Li, (b) Working mechanism of the $LiZrO(NO_3)_2$ layer[28]. Reproduced with permission. Copyright 2022, Wiley-VCH. (c) Collaborative assembly process of the LiF-enriched hetero-structured SEI[31]. Reproduced with permission. Copyright 2022, American Chemical Society. (d) Schematic illustration of the reaction process for zinc silicates and Li metal. (e) and (f) HRTEM images of cycled zinc silicate. (g) Schematic illustration of the mechanism of Li^+ transference and deposition process in the modified Li. Reproduced with permission. Copyright 2023, Wiley-VCH.[32]

Xiong et al. proposed a $LiZrO(NO_3)_2$ ASEI layer synthesized *via* a spontaneous reaction between Li metal and $ZrO(NO_3)_2$ solution[28] (**Figure 2.3a**). The $LiZrO(NO_3)_2$ could form a dense and uniform inorganic SEI layer composed of ZrO_2, Li_2O, Li_3N, and LiN_xO_y on Li surface with a grain-boundary-rich structure (**Figure 2.3b**). This structure ensures fast diffusion of Li^+, while high mechanical strength grains, ZrO_2 and Li_3N, can inhibit dendrite growth. With this functional layer, the symmetric cell can run for more than 500 h even at ultrahigh current density of 10 mA cm^{-2} and high plating capacity of 10 mAh cm^{-2}. A similar strategy is adopted by inducing the precursors on the surface of the Li metal. These precursors can react with Li^+

to generate useful SEI components that regulate Li^+ uniform deposition, conduct Li^+, and suppress Li dendrite formation. Metal sulfides[29] and nitrides[30], were reported to react with Li^+ and form Li_2S or Li_3N on Li surface. Yi et al. modified a K_2ZrF_6 layer on Li metal, which can react with Li^+ to form F-enrich (LiF) layer on the outer surface[31] (**Figure 2.3c**). The residual K_2ZrF_6 and the formed LiF construct a heterostructure that cooperatively enables fast conduction of Li^+ and inhibits the formation of Li dendrites. Qu et al. constructed a dense multi-functional ASEI layer *via* an *in-situ* reaction between zinc silicate ($Zn_3Si_4O_{10}(OH)_2 \cdot nH_2O$) nanosheets and Li. The lithiophilic phase, Zn metal and Li_xZn_y alloy, and single-ion conductor phase, Li_xSiO_y, Li_2O and LiOH, are reasonably distributed in this layer[32] (**Figure 2.3d-f**). In thus a design, the lithiophilic phase works as the nucleation sites to reduce nucleation barrier and facilitate the charge transfer during the deposition of Li^+, while the single-ion conductor phase could increase the Li^+ conductivity and reduce the concentration gradient (**Figure 2.3g**). MXene[33] is also reported to generate a fluorinated SEI layer because of the reaction between its terminal fluorine groups and Li^+, which will contribute to the deposition behaviour of Li^+ and stabilize the Li metal surface.

Researchers also concern the microstructure optimization of ASEI layers and therefore investigate a series of hybrid inorganic layers combining functionalized inorganic materials with three-dimensional (3D) structure. Lithium halides and nitrides[34] are the widely adopted components to build 3D inorganic hybrids, because these chemicals have positive interaction with Li^+. The inert Cr metal is an ideal framework because of its high mechanical strength and the inability to form an alloy with metallic Li. A hybrid ASEI layer is constructed by Wu et al. using LiF as the ionic conductor phase and the *in-situ* formed nano-Gr as the reinforcement phase (**Figure 2.4a**)[35]. The Cr/LiF layer facilitates the Li deposition even at high current densities and large area capacities in the plating/stripping process, and it also prevents the side reactions between the electrolyte and the Li metal, as evidenced by the significantly reduced corrosion current of the Cr/LiF coated Li. It has been reported that a combination of Li_2C_2 and LiF can be realized by treating the Li metal with CF_4 plasma. This hybrid layer shows the advantages of LiF with high interfacial energy and mechanical strength, and the merit of Li_2C_2 with low Li^+ diffusion barrier (**Figure 2.4b**), achieving a ultralong lifespan of 6500 h in the symmetric cell test at a current density of 2 mA cm^{-2} and a capacity of 1 mAh cm^{-2}.[36] Similar hybrid ASEI layers including sulfide/LiF[37], Li_2Se/LiCl[38], Ag/LiF[39], and Li_3Sb/LiF[40] also achieve impressive effects in improving the electrochemical performance of LMBs. Zhang et al. realized that flexibility of the ASEI layer should be taken into account and therefore adopted

flexible carbon nanotubes as the scaffold for the Li_3N@c/s-CNT layer. One side of this layer is dense enough to isolate the Li metal from electrolytes while the other side leaves sufficient space to accommodate deposited Li (**Figure 2.4c**)[41]. Graphene-like carbon nitride (g-C_3N_4) nanosheets are featured with abundant N species, which interact with Li^+ to form Li−N bonds and homogenize the Li^+ flux. When combined with MXene, the hybrid ASEI layer therefore has enough space to cope with the shape change of Li metal anode during plating/stripping processes (**Figure 2.4e-f**)[42]. Inspired by the intercalation behavior of Li-ion batteries, Gong et al. designed an insulator/metal/insulator sandwiched structure using graphene as the electron conductive phase and g-C_3N_4 as the 3D ASEI layer. During plating, Li^+ is deposited into the van der Waals gap of the graphene/g-C_3N_4 interface, resulting in uniform Li deposition and effective electrolyte isolation (**Figure 2.4g**)[43].

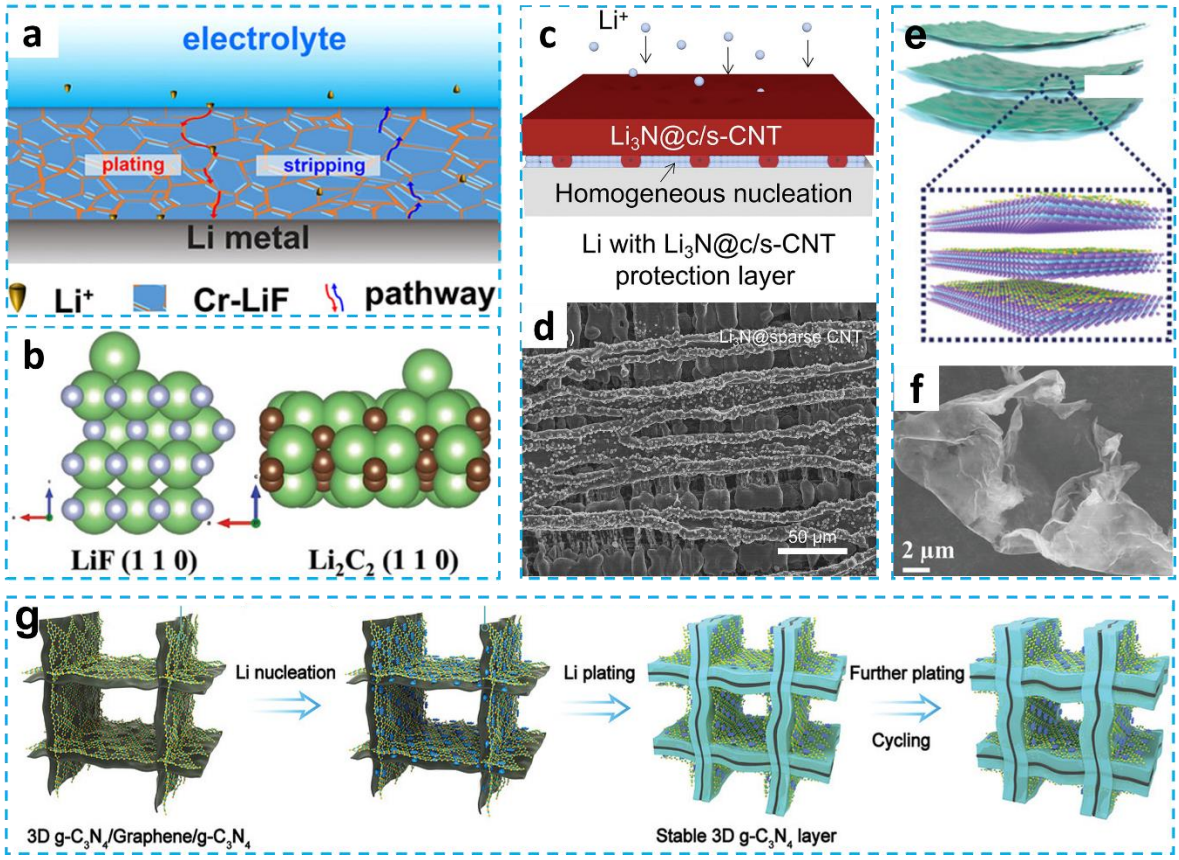

Figure 2.4 Hybrid inorganic ASEI layers with 3D structure. (a) Schematic diagram of for the working mechanism of Cr-LiF layer. Reproduced with permission. Copyright 2021, American Chemical Society.[35] (b) Depiction of the crystal lattice plane and Li^+ diffusion energy barriers for LiF (110) and Li_2C_2 (110). Reproduced with permission. Copyright 2022, the authors[36] (c) Schematic diagram of for the working mechanism and (d) SEM image of the Li_3N@c/s-CNT. Reproduced with permission. Copyright 2022, Elsevier[41] (e) Schematic illustration and (f)

SEM image of the $Ti_3C_2T_x$/g-C_3N_4 hybrid layer. Reproduced with permission. Copyright 2022, the authors. [42] (g) Schematic illustration for Li deposition on the 3D g-C_3N_4/G/g-C_3N_4 electrode. Reproduced with permission. Copyright 2021, Wiley-VCH. [43]

2.1.4 Inorganic layers with polymeric network

One of the shortcomings of the inorganic ASEI is fragile, which could be destroyed by the strains caused by the volume expansion/shrink of Li anode. Increasing the toughness of the inorganic ASEI layer can be realized by building polymer-like networks.

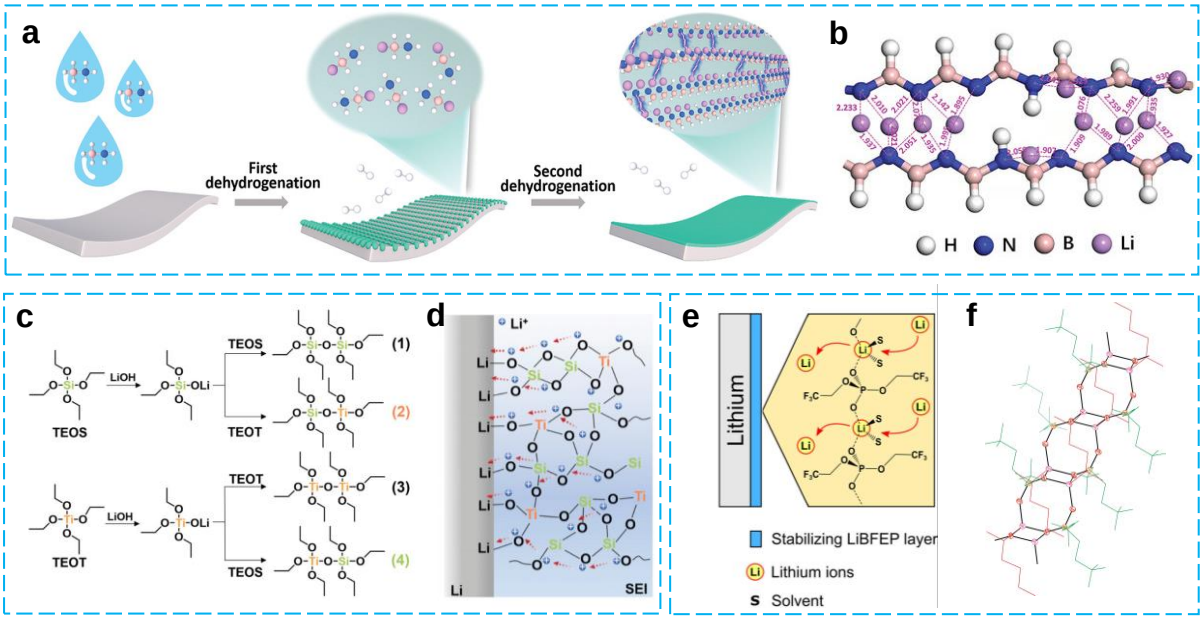

Figure 2.5 Polymer-like inorganic ASEI layers. (a) Schematic illustration of the preparation for the $[LiNBH]_n$ layer. (b) Relaxed atomic configurations of two adjacent $[LiNBH]_n$ chains and the bond lengths between Li and N atoms (the unit of the values is Å). Reproduced with permission. Copyright 2020, Wiley-VCH.[44] (c-d) Schematic illustration of the role of TEOS/TEOT additives in forming a polymer-like SEI. Reproduced with permission. Copyright 2021, Wiley-VCH.[45] (e) Schematic illustration of the working mechanism of HBFEP on Li surface. (f) Molecular structure of the coordination polymer $(LiBFEP)_2 \cdot DME$, where O is in red, P in orange, and Li in purple. Reproduced with permission. Copyright 2022, Wiley-VCH.[46]

Our group fabricated a $[LiNBH]_n$ layer on the Li metal anode *via* a two-step dehydrogenation reaction between Li metal and ammonia borane (NH_3BH_3) (**Figure 2.5a**)[44]. In this layer, the $[LiNBH]_n$ chains are crosslinked with the intermolecular Li−N bonds to form a 3D polymer-

like structure (**Figure 2.5b**), effectively reinforcing mechanical flexibility. The $[LiNBH]_n$ could tolerate the interfacial change and keep effective for more than 700 h even under the current density of 3 mA cm^{-2}. This structure can also be constructed by using silicate/titanate-based coupling reagents. Lai et al. introduced tetraethyl orthosilicate (TEOS) and tetraethyl orthotitanate (TEOT) into the electrolyte to form a polytitanosiloxane (PTS) networks *via* spontaneous condensation reaction. The Si−O−Si linkages facilitate the Li^+ diffusion by reducing the diffusion energy barriers, while the Si−O−Ti linkages strengthen the PTS skeleton and help to mitigate the strains derived from volume changes (**Figure 2.5c-d**)[45]. The phosphoric-acid derivate, bis-(1,1,1-trifluoroethyl)-phosphoric acid $[(CF_3CH_2O)_2PO(OH)]$ (HBFEP), is reported to react with Li to generate LiBFEP and further form an inorganic coordination polymer when contacting with electrolytes(**Figure 2.5e**)[46]. It is revealed that the polymeric structure is constructed with two $[BFEP]^-$ chains linked with Li_2O_2 units, in which dimethoxyethane (DME) molecules are coordinated to the Li atoms via oxygen atoms (**Figure 2.5f**). Such a structure exhibits self-healing or self-adaptive properties, resulting in improved electrochemical performance of Li anode.

2.1.5 Organic polymer layers

The most noteworthy characteristics of the polymer ASEI layer is the excellent flexibility, allowing this layer to bend, stretch, and twist. The flexibility of polymer is derived from the freedom of rotation around the covalent bonds and is affected by the intermolecular force strength among chains. Targeting at the application in Li metal anode, researchers have been introducing lithiophilic functional (polar) groups into the polymer chains to have positive interaction with Li^+ ions. Sun et al. developed a thin "polyurea" layer on the surface of Li metal using molecular-layer deposition method[47]. The polyurea contains abundant −NH groups, which have intensive interactions with the F atoms of Li salt by forming N−H−F bonds and therefore induce the formation of LiF. Moreover, the −NH groups also contribute to the uniform distribution of Li^+ flux and dendrite-free Li plating. Silk fibroin, a natural polymer containing plenty of peptide bonds and amino groups, is regarded as a ready-made functional layer for the Li metal anode. Upon direct contact, a Li_3N-rich SEI with fast Li^+ diffusion ability and high Young's modulus is generated on the surface of Li metal anode[48]. Besides, poly-dioxolane (PDOL)[49], poly(propylene carbonate) (PPC)[50], polymer of intrinsic microporosity[51] were also developed to stabilize Li metal anode.

In addition to polymers with a single structure/component, the design of novel polymers with functional structures makes it possible to effectively manipulate the surface properties of Li

metal anode. Wang et al. synthesized a dual functional polymer layer, poly((N-2,2-dimethyl-1,3-dioxolane-4-methyl)-5-norbornene-exo-2,3-dicarboximide), in which cyclic ether groups ensure good affinity with Li and the polycyclic main chain could exhibit high modulus. Such a design helps to isolate electrolyte and accommodate deposited Li under the polymeric skin[52]. Pan et al. designed a self-healing ASEI layer with trifluorophenyl-modified poly(ethylene imine) (PEI-3F) (**Figure 2.6a**)[53]. In this layer, the trifluorophenyl moieties serve as the active site to attract Li^+ and regulate Li^+ flux while the imine bonds contribute to the flexibility, elasticity, and self-healing capability (**Figure 2.6b**). A bicomponent polymer, polyvinylidenefluoride/polyacrylonitrile (PVDF/PAN), is introduced as the ASEI layer for Li metal (**Figure 2.6c**)[54]. The porous structure derived from phase separation process works as fast Li^+ diffusion channels to regulate the distribution of Li^+ flux (**Figure 2.6d**) and the functional groups, C≡N and C−F, could interact with Li^+ to promote uniform Li plating (**Figure 2.6e**). To guarantee a high ionic conductivity and Li^+ ion transference number, zwitterionic polymer, which have both cationic and anionic in the molecule, are designed using a reversible addition-fragmentation chain transfer polymerization and spin-coating approach.[55] The obtained novel polymer hybrid, 3-((2-(methacryloyloxy) ethyl) (dimethyl) ammonio)-1-propanesulfonate (PDMAPS)/2-methacryloyloxyethyl phosphorylcholine (PMPC), has functions in promoting Li salt dissociation and homogenizing Li^+ flux (**Figure 2.6f**). The ionic conductivity of the proposed ASEI layer is measured to be as high as 0.75×10^{-4} S cm^{-1}, and the Li^+ ion transference number is up to 0.81. Park et al. developed a block copolymer consisting of two portions of chemicals with specific functions, in which the styrene portion (PS) determines the mechanical strength, and the butadiene portions (PB) decides the deformability and adhesive ability (**Figure 2.6g**). A good balance in mechanical and elastic properties can be achieved when the weight ratio of PS/PB reaches 4:6, and the structural integrity of the ASEI layer is well maintained during Li plating/stripping[56]. A similar design principle was adopted by rationally integrating poly(oligo(ethylene glycol) methyl ether methacrylate)-grafted (*x*PCMS), hypercrosslinked poly(4-chloromethylstyrene) nanospheres (PEGMA), and lithiated Nafion, in which the *x*PCMS functions as rigid skeletons to enhance the mechanical strength, the flexible PEGMA helps to homogenize the three-component layer, and the lithiated Nafion facilitates Li^+ diffusion and increases the Li^+ transference number[57]. With this ASEI layer, impressive lifespan of Li metal anode, 1 year, was achieved even at an ultrahigh current density of 10 mA cm^{-2}.

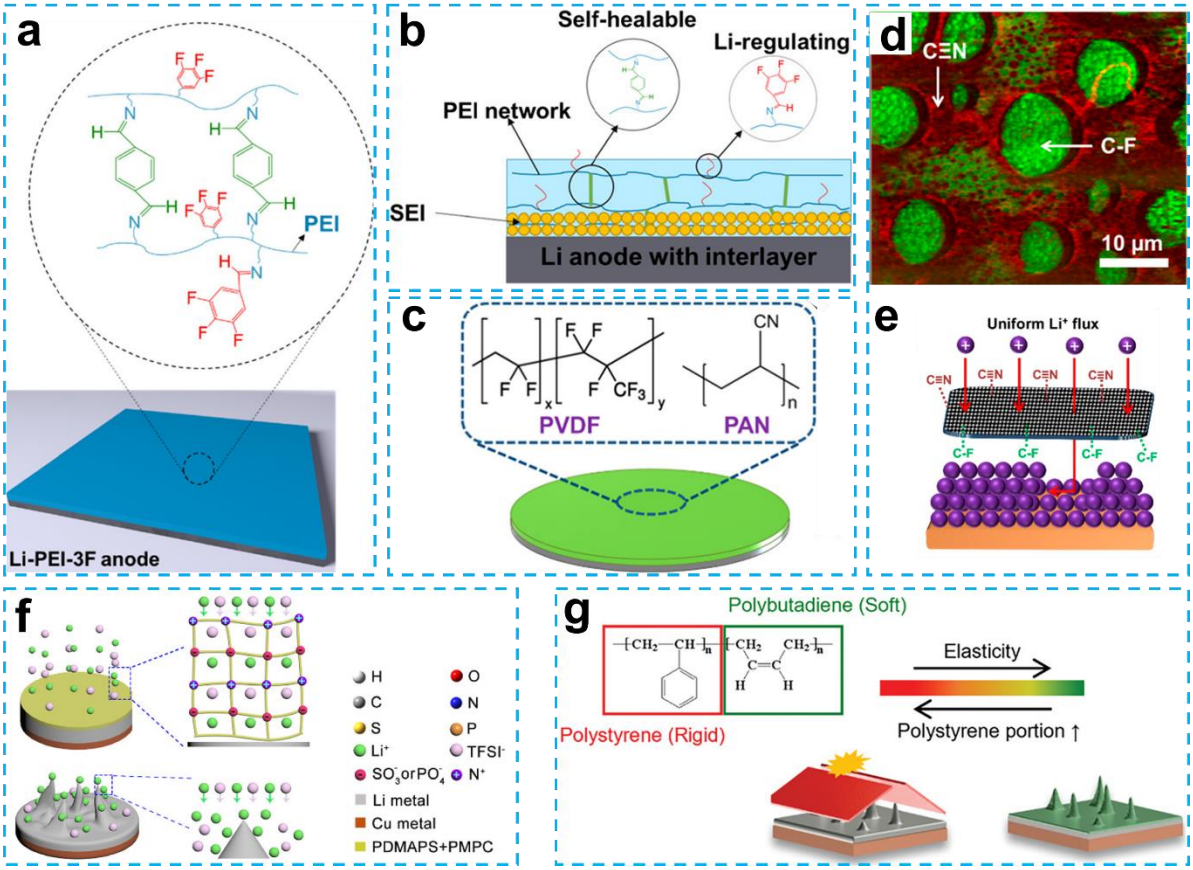

Figure 2.6 Organic polymer ASEI layers. (a) Schematic illustration of the PEI ASEI coated on Li surface and (b) its working mechanism. Reproduced with permission. Copyright 2021, American Chemical Society.[53] (c) Schematic illustration of structure of PVDF-PAN protective layer on Li foil. (d) SEM image of the PVDF-PAN blending layer. (e) Schematic illustration of the C≡N and C−F groups in stabilizing Li metal anode. Reproduced with permission. Copyright 2022, American Chemical Society.[54] (f) Schematic illustration of the Li deposition behaviors on a substrate with and without the (PDMAPS+PMPC) coating. Reproduced with permission. Copyright 2021, American Chemical Society.[55] (g) Chemical structure of SBS-BCP polymer and schematics showing the Li deposition morphologies underneath the polymer layer as a function of PB/PS ratio. Reproduced with permission. Copyright 2021, Wiley-VCH.[56]

2.1.6 Inorganic-organic composite layers

In general, inorganic ASEI layers have high ionic conductivity and high Young's modulus but low toughness, while organic layers have high elasticity and high flexibility but low ionic conductivity. Inorganic-organic composite ASEI layers have been proposed to overcome the

shortcomings and maintain the advantages of both individual components. To date, significant progress has been made on this front. The conventional organic parts were mono-component polymers, such as poly(tetramethylene ether glycol) (PTMEG)[58], poly(vinylidene fluoride) (PVDF)[59], poly(tetrahydrofuran) (PTMG)[60], poly(1H,1H,2H,2H-perfluorodecylmethacrylate) (PFDMA)[61], polydopamine (PDA)[62], polyacrylonitrile (PAN)[63] etc. The inorganic components are generally Li_xSn, SiO_2, Li_3N, and lithium halides, etc. The Li_xSn/PTMEG hybrid layer[58] exhibits fast Li^+ transport ability because of the abundant Li vacancies in the Li/Sn alloy and excellent affinity to Li metal because of the plentiful C−O bonds. The 3D $ZnCl_2$/PVDF networking exhibits an additional advantage, superlithiophilia, originating from the Zn−F bonds because of the intensive interaction between $ZnCl_2$ and PVDF[59]. The composite of mesoporous TiO_2 and F-rich PFDMA has excellent mechanical strength and the abundant mesoporous channels in TiO_2 facilitate rapid transport of Li^+ ions. Fan et al. developed a molybdenum (MoO_3) anchored polysulfone composite ASEI to improve the Li deposition kinetics.[63] The composite ASEI can reduce the Li^+ transport resistance, lower the overpotential for Li plating, and guide Li uniform deposition. A SiO_2/PDA composite with high-dielectric property is fabricated to homogenize the electric field at the Li electrode/electrolyte interface[62]. It is revealed that SiO_2 improves the dielectric permittivity and therefore prevents current variation during Li plating/stripping, and the elastic PDA is lithiophilic/hydrophilic, which can stabilize Li metal and suppress dendrite growth.

In addition to the above-mentioned conventional organic parts, novel organic parts with hybrid structures have been designed in recent years. Among them, the poly(vinylidene fluoride-hexafluoropropylene) (PVDF-HFP) gel was representative because it provided more functional groups than individual PVDF or HFP. It can be used as a matrix to load or anchor inorganic particles. Liu et al. introduced Li_xSn_y alloy into the PVDF-HFP matrix *via* dropping SnF_2/PVDF-HFP solutions on Li surface[64]. The SnF_2 is reduced by Li metal and forms Li-Sn alloy and LiF (**Figure 2.7a**). The Li_xSn_y alloy serves as fast ion conductor to promote dendrite-free Li deposition while the flexible PVDF-HFP matrix helps to improve the interfacial compatibility and overcome the fragile nature of Li_xSn_y alloy. A sandwiched rGO-SiO_2-rGO with additional PVDF-HFP top layer is also designed out of similar consideration(**Figure 2.7b**)[65]. On the one hand, the lithiophilic SiO_2 acts as nucleation sites for Li deposition, and on the other hand, these particles are beneficial to maintain a floatable storage space for Li. The insulated PVDF-HFP top layer guarantees that the Li deposition occurs in the SiO_2-filled rGO space. He et al. *in-situ* photopolymerized the pentaerythritol tetraacrylate (PETEA) and

poly(ethylene glycol)diacrylate (PEGDA) in a PVDF-HFP matrix incorporated with GO[66]. This ASEI layer is compatible with carbonate electrolyte and achieves satisfactory ionic conductivity. Another example of hybrid ASEI layer is constructing a LiCl layer at the bottom of PVDF-HFP *via in-situ* dehalogenation[67]. The LiCl layer exhibits reduced Li+ diffusion barriers (0.09 eV) and high mechanical strength (6.5 GPa), which is beneficial to suppressing dendrite growth, and the upper PVDF-HDF layer is used to isolate the Li metal from electrolyte.

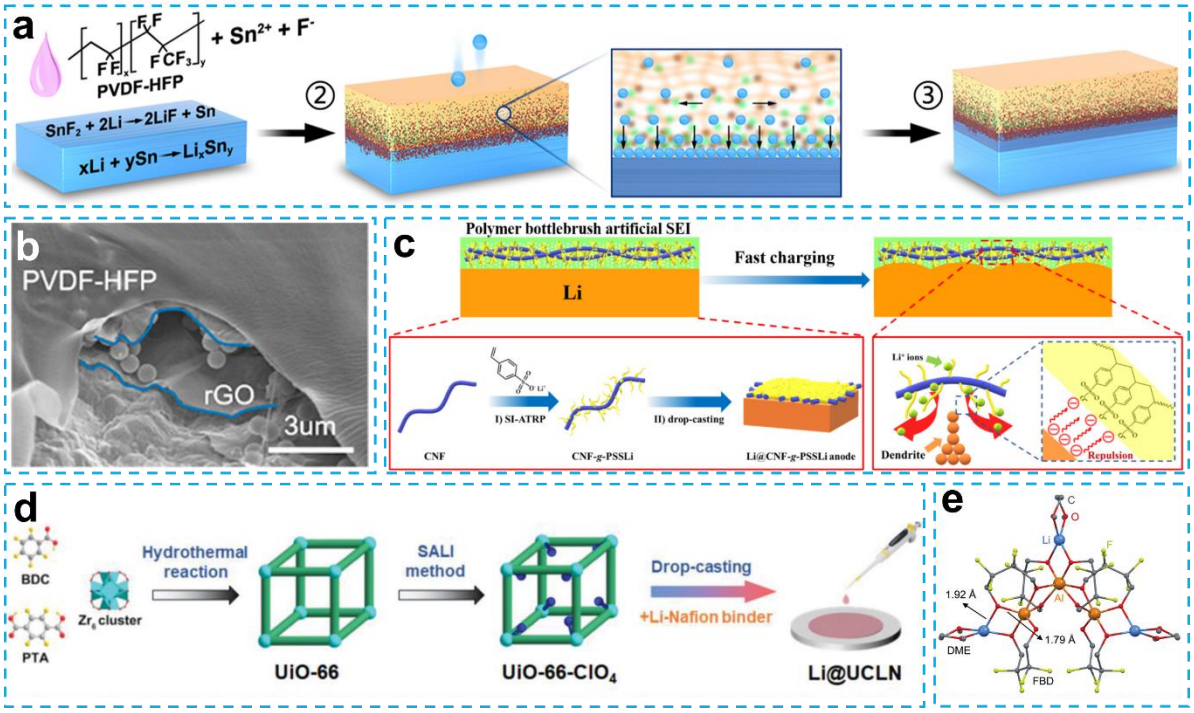

Figure 2.7 Inorganic-organic composite layer. (a) Schematic diagrams of the working principle of Li_xSn/PVDF-HFP protective layers in regulating Li deposition. Reproduced with permission. Copyright 2022, Elsevier.[64] (b) SEM image of the rGO-SiO2/PVDF-HFP composite. Reproduced with permission. Copyright 2021, American Chemical Society.[65] (c) Schematic illustrations of the evolution of polymer bottlebrush ASEI layer, the synthesis route of CNF-g-PSSLi and Li@CNF-g-PSSLi anode (bottom left), and the electrostatic repulsion between the negatively charged $-SO_3^-$ groups of side chains and the negatively charged tip surface of Li dendrite (bottom right). Reproduced with permission. Copyright 202, Elsevier.[68] (d) Schematic illustrations for the bionic design and rational synthesis of UiO-66-ClO_4 and the UCLN ASEI layer. Reproduced with permission. Copyright 2021, Wiley-VCH.[69] (e) Refined crystal structure of the LiAl-FBD composite. Reproduced with permission. Copyright 2022, Wiley-VCH.[70]

In addition to PVDF-HFP based polymers, novel polymer components can bring additional functions. Wu et al. synthesized a polymer brush with a single-ion conductor character by grafting poly(lithium pstyrenesulfonate) (PSSLi) from cellulose nanofibril (CNF) via surface-initiated atom transfer radical polymerization (**Figure 2.7c**)[68]. The role of the CNF is to maintain the mechanical strength and the functions of PSSLi are to coordinate with Li^+ and facilitate Li^+ transport with the $-SO_3^-$ functional groups. The proposed ASEI layer exhibits a high elastic modulus of 5.3 GPa, comfortable interfacial contacts, and fast Li^+ diffusion. A combination of ClO_4^--anchored metal-organic framework (UiO-66-ClO_4) and flexible lithiated Nafion is proposed as ASEI layer to meet the requirements of fast Li^+ transport and good structural stability (**Figure 2.7d**)[69]. The highly electronegative and lithiophilic ClO_4^- groups provide the single-ion conducting pathway for Li^+ and the flexible lithiated Nafion ensures the interfacial integral stability of this protective layer during battery operation. Bao et al. designed a brand-new ASEI component, LiAl cooperated with 2,2,3,3-tetrafluoro-1,4-butanediol (LiAl-FBD), in which anion clusters are contrasted by bridging the FBD_2^- ligands to the Al^{3+} ions and the Li^+ ions are weakly bound (**Figure 2.7e**)[70]. Benefiting from this structure, the Li^+ ion conductivity reaches 9.4×10^{-6} S cm^{-1} and the fluorinated anions make the ASEI layer phobic to electrolyte. The LiAl-FBD protected Li metal works well to pair the NCM811 cathode, even under harsh testing conditions. Yun et al. prepared a 3D ASEI hybrid layer with poly(sulfur-random-1,3-diisopropenylbenzene) (poly(S-r-DIB)) and carbon black[71]. Sulfur copolymer reacts with Li^+ ions to form Li_2S, and the DIB molecules are involved in the formation of organic SEI compounds with the electrolyte. This layer protects the Li metal anode during the long-term cycling and achieves an increased Coulombic efficiency.

2.1.7 Summary

ASEI layers are an interfacial modification strategy that aims to mimic and go beyond the properties of the natural SEI layer. In this review, we have compared five categories of ASEI layers based on the basic requirements including high Li-ion conductivity, stability, and good mechanical properties. Fast and uniform transport of Li^+ ion ability is the first principle in designing the ASEI layers, because this factor directly determines the morphology of deposited Li. Some inorganic components, such as Li_3N, Li_3P, Li_2S, Li_2Se, LiN_xO_y, and Li_xSiO_y, have a natural sort of advantage in Li^+ ion diffusion and electronic insulation, and therefore, they are usually used as the crucial components in the design of ASEI layers. However, these chemicals are usually fragile and are likely to be damaged by the interfacial strains originating from the volume changes during Li plating/ stripping. Since the lack of effective chemical bonds, the

inorganic ASEI may fall off the surface of the Li metal anode in the first few cycles. Adhesion between the inorganic ASEI and the Li metal is an overlooked issue. Polymeric ASEI layers show tremendous potential because of their designable functions, especially in terms of mechanical properties and lithiophilic groups. Adjustable strength and elasticity can be achieved in polymeric ASEI layers by selecting specific sections and adjusting the ration. Lithiophilic groups, such as −NH, C≡N, C−F, $-SO_3^-$, and ClO_4^-, can be inserted into the polymer chains via specific synthesis methods, which makes it possible for the ASEI layers to interact with Li^+ effectively and guide dendrite-free deposition. One more merit of the polymeric ASEI layer is its affinity to electrolytes because of similar functional groups, which is important in reducing interfacial resistance. Inorganic-organic hybrid ASEI layers can combine the benefits of inorganic and organic materials and have a large possibility to design targeted functions. For hybrid ASEI layers, the key point lies in further reducing the thickness and achieving a rational distribution of different compositions.

2.1.8 Reference

1. Liu Y, *et al*. Challenges and opportunities towards fast-charging battery materials. *Nature Energy* **4**, 540-550 (2019).
2. Albertus P, *et al*. Status and challenges in enabling the lithium metal electrode for high-energy and low-cost rechargeable batteries. *Nature Energy* **3**, 16-21 (2018).
3. Zhang Y, *et al.* Towards better Li metal anodes: Challenges and strategies. *Materials Today* **33**, 56-74 (2020).
4. Wang Z, *et al*. Constructing nitrided interfaces for stabilizing Li metal electrodes in liquid electrolytes. *Chemical Science* **12**, 8945-8966 (2021).
5. Liu B, *et al*. Advancing Lithium Metal Batteries. *Joule* **2**, 833-845 (2018).
6. Liu W, *et al.* Nickel-Rich Layered Lithium Transition-Metal Oxide for High-Energy Lithium-Ion Batteries. *Angewandte Chemie International Edition* **54**, 4440-4457 (2015).
7. Liu J, *et al.* Pathways for practical high-energy long-cycling lithium metal batteries. *Nature Energy* **4**, 180-186 (2019).
8. Suo L, *et al.* Fluorine-donating electrolytes enable highly reversible 5-V-class Li metal batteries. *Proceedings of the National Academy of Sciences* **115**, 1156-1161 (2018).
9. Xu W, *et al.* Lithium metal anodes for rechargeable batteries. *Energy & Environmental Science* **7**, 513-537 (2014).
10. Cheng X-B, *et al*. Toward Safe Lithium Metal Anode in Rechargeable Batteries: A Review. *Chemical Reviews* **117**, 10403-10473 (2017).
11. Lin D, *et al*. Reviving the lithium metal anode for high-energy batteries. *Nature Nanotechnology* **12**, 194-206 (2017).
12. Peled E, *et al*. Review—SEI: Past, Present and Future. *Journal of The Electrochemical Society* **164**, A1703 (2017).
13. Yu X, *et al*. Electrode–electrolyte interfaces in lithium-based batteries. *Energy & Environmental Science* **11**, 527-543 (2018).

14. Meyerson ML, *et al*. Recent Developments in Dendrite-Free Lithium-Metal Deposition through Tailoring of Micro- and Nanoscale Artificial Coatings. *ACS Nano* **15**, 29-46 (2021).

15. Jiang C, *et al*. Materials chemistry among the artificial solid electrolyte interphases of metallic lithium anodes. *Materials Chemistry Frontiers* **5**, 5194-5210 (2021).

16. Kang D, *et al*. Artificial Solid-Electrolyte Interphase for Lithium Metal Batteries. *Batteries & Supercaps* **4**, 445-455 (2021).

17. Monroe C, *et al*. Dendrite Growth in Lithium/Polymer Systems : A Propagation Model for Liquid Electrolytes under Galvanostatic Conditions. *Journal of The Electrochemical Society* **150**, A1377 (2003).

18. Li N-W, *et al*. An Artificial Solid Electrolyte Interphase Layer for Stable Lithium Metal Anodes. *Advanced Materials* **28**, 1853-1858 (2016).

19. Kozen AC, *et al.* Next-Generation Lithium Metal Anode Engineering via Atomic Layer Deposition. *ACS Nano* **9**, 5884-5892 (2015).

20. Liu W, *et al*. Review of Emerging Concepts in SEI Analysis and Artificial SEI Membranes for Lithium, Sodium, and Potassium Metal Battery Anodes. *Advanced Energy Materials* **10**, 2002297 (2020).

21. Park K, *et al*. Dendrite-Suppressed Lithium Plating from a Liquid Electrolyte via Wetting of Li3N. *Advanced Energy Materials* **7**, 1700732 (2017).

22. Wu N, *et al.* In Situ Formation of Li3P Layer Enables Fast Li+ Conduction across Li/Solid Polymer Electrolyte Interface. *Advanced Functional Materials* **30**, 2000831 (2020).

23. Di J, *et al.* Dendrites-Free Lithium Metal Anode Enabled by Synergistic Surface Structural Engineering. *Advanced Functional Materials* **32**, 2200474 (2022).

24. Ma Y, *et al.* Insulative Ion-Conducting Lithium Selenide as the Artificial Solid–Electrolyte Interface Enabling Heavy-Duty Lithium Metal Operations. *Nano Letters* **21**, 7354-7362 (2021).

25. Li Y, *et al.* Robust Pinhole-free Li3N Solid Electrolyte Grown from Molten Lithium. *ACS Central Science* **4**, 97-104 (2018).

26. Chen H, *et al.* Uniform High Ionic Conducting Lithium Sulfide Protection Layer for Stable Lithium Metal Anode. *Advanced Energy Materials* **9**, 1900858 (2019).

27. Fan X, *et al.* Non-flammable electrolyte enables Li-metal batteries with aggressive cathode chemistries. *Nature Nanotechnology* **13**, 715-722 (2018). Lu Y, *et al*. Stable lithium electrodeposition in liquid and nanoporous solid electrolytes. *Nature Materials* **13**, 961-969 (2014). Liu P, *et al.* LiBr–LiF-Rich Solid–Electrolyte Interface Layer on Lithiophilic 3D Framework for Enhanced Lithium Metal Anode. *Small Structures* **3**, 2200010 (2022).

28. Chen C *et al*. Grain-Boundary-Rich Artificial SEI Layer for High-Rate Lithium Metal Anodes. *Advanced Functional Materials* **32**, 2107249 (2022).

29. Yang Z, *et al.* Ultrasmooth and Dense Lithium Deposition Toward High-Performance Lithium-Metal Batteries. *Advanced Materials* **n/a**, 2210130 (2023).

30. Ding D, *et al*. Flexible Mg3N2 layer regulates lithium plating-striping for stable and high capacity lithium metal anodes. *Nano Research* **15**, 8128-8135 (2022).

31. Zhang Y, *et al.* Collaborative Assembly of a Fluorine-Enriched Heterostructured Solid Electrolyte Interphase for Ultralong-Life Lithium Metal Batteries. *ACS Applied Materials & Interfaces* **14**, 43917-43925 (2022).

32. Liu H-J, *et al.* In-Situ Constructing A Heterogeneous Layer on Lithium Metal Anodes for Dendrite-Free Lithium Deposition and High Li-ion Flux. *Angewandte Chemie International Edition* **62**, e202217458 (2023).

33. Ha S, *et al*. Lithiophilic MXene-Guided Lithium Metal Nucleation and Growth Behavior. *Advanced Functional Materials* **31**, 2101261 (2021). Yao W, *et al.* V2CTx MXene Artificial Solid Electrolyte Interphases toward Dendrite-Free Lithium Metal Anodes. *ACS Sustainable Chemistry & Engineering* **9**, 9961-9969 (2021).

34. Wang S, *et al.* Artificial Alloy/Li3N Double-Layer Enabling Stable High-Capacity Lithium Metal Anodes. *ACS Applied Energy Materials* **4**, 13132-13139 (2021).

35. Du P, *et al*. Harnessing Stiffness and Anticorrosion of Chromium in an Artificial SEI to Achieve a Longevous Lithium-Metal Anode. *ACS Applied Energy Materials* **4**, 5043-5049 (2021).

36. Cao S, *et al.* CF4 Plasma-Generated LiF-Li2C2 Artificial Layers for Dendrite-Free Lithium-Metal Anodes. *Advanced Science* **9**, 2201147 (2022).

37. Yang J, *et al.* Simultaneously in-situ fabrication of lithium fluoride and sulfide enriched artificial solid electrolyte interface facilitates high stable lithium metal anode. *Chemical Engineering Journal* **433**, 133193 (2022).

38. Lee D, *et al.* Stable artificial solid electrolyte interphase with lithium selenide and lithium chloride for dendrite-free lithium metal anodes. *Journal of Power Sources* **506**, 230158 (2021).

39. Cheng Z, *et al*. Long-Lifespan Lithium Metal Batteries Enabled by a Hybrid Artificial Solid Electrolyte Interface Layer. *ACS Applied Materials & Interfaces* **15**, 10585-10592 (2023).

40. Hu A, *et al.* An artificial hybrid interphase for an ultrahigh-rate and practical lithium metal anode. *Energy & Environmental Science* **14**, 4115-4124 (2021).

41. Liu H, *et al.* A flexible artificial solid-electrolyte interlayer supported by compactness-tailored carbon nanotube network for dendrite-free lithium metal anode. *Journal of Energy Chemistry* **69**, 421-427 (2022).

42. Zhao F, *et al.* Constructing Artificial SEI Layer on Lithiophilic MXene Surface for High-Performance Lithium Metal Anodes. *Advanced Science* **9**, 2103930 (2022).

43. Zhai P, *et al.* 3D Artificial Solid-Electrolyte Interphase for Lithium Metal Anodes Enabled by Insulator–Metal–Insulator Layered Heterostructures. *Advanced Materials* **33**, 2006247 (2021).

44. Wang Z, *et al.* Building Artificial Solid-Electrolyte Interphase with Uniform Intermolecular Ionic Bonds toward Dendrite-Free Lithium Metal Anodes. *Advanced Functional Materials* **30**, 2002414 (2020).

45. Zhong Y, *et al.* Ion-Conductive Polytitanosiloxane Networks Enable a Robust Solid-Electrolyte Interface for Long-Cycling Lithium Metal Anodes. *Advanced Functional Materials* **32**, 2110347 (2022).

46. Beichel W, *et al.* An Artificial SEI Layer Based on an Inorganic Coordination Polymer with Self-Healing Ability for Long-Lived Rechargeable Lithium-Metal Batteries. *Batteries & Supercaps* **5**, e202100347 (2022).

47. Sun Y, *et al.* A Novel Organic "Polyurea" Thin Film for Ultralong-Life Lithium-Metal Anodes via Molecular-Layer Deposition. *Advanced Materials* **31**, 1806541 (2019).

48. Li X, *et al.* Elevated Lithium Ion Regulation by a “Natural Silk” Modified Separator for High-Performance Lithium Metal Anode. *Advanced Functional Materials* **31**, 2100537 (2021).

49. Chen T, *et al.* Synthetic poly-dioxolane as universal solid electrolyte interphase for stable lithium metal anodes. *Journal of Energy Chemistry* **62**, 172-178 (2021).

50. Yu Q, *et al.* Sacrificial Poly(propylene carbonate) Membrane for Dispersing Nanoparticles and Preparing Artificial Solid Electrolyte Interphase on Li Metal Anode. *ACS Applied Materials & Interfaces* **12**, 27087-27094 (2020).

51. Yang Q, *et al.* PIM-1 as an artificial solid electrolyte interphase for stable lithium metal anode in high-performance batteries. *Journal of Energy Chemistry* **42**, 83-90 (2020).

52. Gao Y, *et al*. Interfacial Chemistry Regulation via a Skin-Grafting Strategy Enables High-Performance Lithium-Metal Batteries. *Journal of the American Chemical Society* **139**, 15288-15291 (2017).

53. Cui X, *et al*. Stabilizing Lithium Metal Anodes by a Self-Healable and Li-Regulating Interlayer. *ACS Applied Materials & Interfaces* **13**, 44983-44990 (2021).

54. Wang D, *et al.* Phase-Separation-Induced Porous Lithiophilic Polymer Coating for High-Efficiency Lithium Metal Batteries. *Nano Letters* **21**, 4757-4764 (2021).

55. Jin T, *et al.* Polymer Zwitterion-Based Artificial Interphase Layers for Stable Lithium Metal Anodes. *ACS Applied Materials & Interfaces* **13**, 57489-57496 (2021).

56. Song G, *et al.* Breathable Artificial Interphase for Dendrite-Free and Chemo-Resistive Lithium Metal Anode. *Small* **18**, 2105724 (2022).

57. Li S, *et al.* A robust all-organic protective layer towards ultrahigh-rate and large-capacity Li metal anodes. *Nature Nanotechnology* **17**, 613-621 (2022).

58. Jiang Z, *et al.* Facile Generation of Polymer–Alloy Hybrid Layers for Dendrite-Free Lithium-Metal Anodes with Improved Moisture Stability. *Angewandte Chemie International Edition* **58**, 11374-11378 (2019).

59. Hu Y, *et al.* Suppressing Local Dendrite Hotspots via Current Density Redistribution Using a Superlithiophilic Membrane for Stable Lithium Metal Anode. *Advanced Science* **n/a**, 2206995 (2023).

60. Ma W, *et al.* Regulated lithium deposition behavior by chlorinated hybrid solid-electrolyte-interphase for stable lithium metal anode. *Chemical Engineering Journal* **442**, 136297 (2022).

61. Guan M, *et al.* Stabilization of Lithium Metal Interfaces by Constructing Composite Artificial Solid Electrolyte Interface with Mesoporous TiO2 and Perfluoropolymers. *Small* **18**, 2202981 (2022).

62. Sun X, *et al.* Regulating Li-ion flux with a high-dielectric hybrid artificial SEI for stable Li metal anodes. *Nanoscale* **14**, 5033-5043 (2022).

63. Dong C, *et al.* A robust interface enabled by electrospun membrane with optimal resistance in lithium metal batteries. *Journal of Energy Chemistry* **55**, 1-9 (2021).

64. Zhao F, *et al*. Seamlessly integrated alloy-polymer interphase for high-rate and long-life lithium metal anodes. *Materials Today Energy* **26**, 100988 (2022).

65. Cai Q, *et al.* Gradient Structure Design of a Floatable Host for Preferential Lithium Deposition. *Nano Letters* **21**, 10252-10259 (2021).

66. Li S, *et al.* A multifunctional artificial protective layer for producing an ultra-stable lithium metal anode in a commercial carbonate electrolyte. *Journal of Materials Chemistry A* **9**, 7667-7674 (2021).

67. Zhang K, *et al.* Chlorinated dual-protective layers as interfacial stabilizer for dendrite-free lithium metal anode. *Energy Storage Materials* **41**, 485-494 (2021).

68. Zeng J, *et al.* A polymer brush-based robust and flexible single-ion conducting artificial SEI film for fast charging lithium metal batteries. *Energy Storage Materials* **41**, 697-702 (2021).

69. Jiang G, *et al.* Robust Artificial Solid-Electrolyte Interfaces with Biomimetic Ionic Channels for Dendrite-Free Li Metal Anodes. *Advanced Energy Materials* **11**, 2003496 (2021).

70. Yu Z, *et al.* A Solution-Processable High-Modulus Crystalline Artificial Solid Electrolyte Interphase for Practical Lithium Metal Batteries. *Advanced Energy Materials* **12**, 2201025 (2022).

71. Ha S, *et al.* 3D-structured organic-inorganic hybrid solid-electrolyte-interface layers for Lithium metal anode. *Energy Storage Materials* **37**, 567-575 (2021).

2.2 Electrolyte engineering enables high performance zinc ion batteries

This part is published in the journal *Small* 2022, 18, 2107033. In this review, we overview advanced electrolyte strategies for optimizing the compatibility between cathode materials and electrolytes, inhibiting anode corrosion and dendrite growth, extending electrochemical stability windows, enabling wearable applications, and enhancing temperature tolerance. The underlying scientific mechanisms, electrolyte design principles and recent progress are presented to provide better understanding and inspiration to readers. In addition, a comprehensive perspective on electrolyte design and engineering for ZIBs is included. This topic is relevant to my research as presented in Chapter 4, Chapter 5, Chapter 6.

Statement of Authorship

Title of Paper	Electrolyte engineering enables high performance zinc ion batteries
Publication Status	☑ Published ☐ Accepted for Publication ☐ Submitted for Publication ☐ Unpublished and Unsubmitted w ork w ritten in manuscript style
Publication Details	Yanyan Wang, Zhijie Wang, Fuhua Yang, Sailin Liu, Shilin Zhang, Jianfeng Mao, Zaiping Guo. Electrolyte Engineering Enables High Performance Zinc-Ion Batteries. Small 2022, 18, 2107033

Principal Author

Name of Principal Author (Candidate)	Yanyan Wang
Contribution to the Paper	Collected the related information, devised the idea and structure with supervisor, wrote and revised the manuscript.
Overall percentage (%)	50%
Certification:	This paper reports on original research I conducted during the period of my Higher Degree by Research candidature and is not subject to any obligations or contractual agreements with a third party that would constrain its inclusion in this thesis. I am the primary author of this paper.
Signature	Date: 10 / Mar. / 2023

Co-Author Contributions

By signing the Statement of Authorship, each author certifies that:

i. the candidate's stated contribution to the publication is accurate (as detailed above);

ii. permission is granted for the candidate in include the publication in the thesis; and

iii. the sum of all co-author contributions is equal to 100% less the candidate's stated contribution.

Name of Co-Author	Zhijie Wang
Contribution to the Paper	Gathered the information, discussed the framework, wrote and edited the manuscript.
Signature	Date: 10/Mar./2023

Name of Co-Author	Fuhua Yang
Contribution to the Paper	Gathered the information, discussed the framework, wrote and edited the manuscript.
Signature	Date: 10.03.2023

Name of Co-Author	Sailin Liu
Contribution to the Paper	Wrote a part of the manuscript.
Signature	Date 10/03/2023

Name of Co-Author	Shilin Zhang
Contribution to the Paper	Discussion and revision of the manuscript.
Signature	Date 10/03/2023

Name of Co-Author	Jianfeng Mao
Contribution to the Paper	Discussion and revision of the manuscript.
Signature	Date 10/03/2023

Name of Co-Author	Zaiping Guo
Contribution to the Paper	Supervision of the work, discussion of the whole manuscript, revision and conceptualization.
Signature	Date 10/03/2023

2.2.1 Introduction

Energy storage and conversation technology has revolutionized the world and human's life styles *via* paving the way for multi-functional applications such as portable devices, electronic products, and electronic vehicles.[1, 2] Nowadays, the rising concern about environmental protection and targets for carbon neutrality further intensify the demand for suitable energy storage systems.[3] Moreover, the increasing scale of alternative energy sources, such as solar and wind power, also calls for reliable battery technologies to integrate the generated electricity into electric grids.[4, 5, 6] Lithium (Li)-based batteries have achieved great commercial success due to their relatively high output voltage, high energy density and long lifespan.[7, 8, 9, 10, 11, 12, 13] However, their flammable nature, limited Li resources and ever-increasing price make them unsuitable for use in large-scale energy storage,[14, 15, 16] leading to the development of resourceful sodium ion batteries,[17, 18, 19, 20] potassium ion batteries,[21, 22, 23] and ZIBs.[24, 25] ZIBs stand out from the alternative options as the most promising stationary energy storage systems to cope with renewable energies, due to their safety, low cost, environment-friendliness and impressive electrochemical performance. Their valuable merits also make them representative of green batteries and widely considered as candidate for various applications.

Metallic Zn is the most ideal choice for a ZIBs anode. Unlike metallic Li, sodium (Na) and potassium (K), metallic Zn shows excellent tolerance to atmosphere and the majority of solvents, which is a solid foundation for battery safety.[26] Its theoretical capacity reaches 820 mAh g^{-1}, higher than that of intercalation-type anode materials, and its reduction potential is −0.76 V *vs* Standard Hydrogen Electrode (SHE). Moreover, its abundance is evaluated to be 300 times that of Li. Thanks to the high chemical stability of metallic Zn, both aqueous and nonaqueous electrolytes can be applied in ZIBs.[27, 28, 29] Among these options, researchers think highly of aqueous electrolytes due to their intrinsic safety and fast kinetics. Although metallic Zn is relatively inert to aqueous electrolyte, unwanted side reactions still cannot be entirely avoided.[26] In early 1900s, Zn-based primary batteries, such as Zn/Ni, Zn/Ag, Zn/air batteries, were proposed using alkaline electrolyte, like KOH solution, in which Zn anode is greatly corroded and the dendrite growth is quite severe. The situation is effectively relieved in mild electrolyte, like $ZnSO_4$ solution. In late 1900s, researchers replaced alkaline electrolytes with mild electrolytes, making it possible to construct rechargeable ZIBs based on reversible Zn plating/stripping processes.[30] Xu et al. proposed a rechargeable zinc ion chemistry composed of an α-MnO_2 cathode, a zinc anode, and a mild aqueous electrolyte, in which Zn^{2+} ions can be reversibly intercalated into the host of α-MnO_2, as illustrated in **Figure 2.8a**.[31] To date, the

mild electrolytes, based on $ZnSO_4$, $Zn(CF_3SO_3)_2$ and $Zn(N(CF_3SO_2)_2)_2$ solution , are widely applied in ZIBs because of their stability and good compatibility with electrodes. Nevertheless, dendrite growth, similar to other metal anodes,[32, 33, 34, 35] has not been eliminated and remains a pressing problem for real application of ZIBs, which may lead to the formation of inactive powdery Zn particles, poor Coulombic efficiency (CE) and even short-circuiting of batteries if dendrites penetrate separators.[36] For cathode materials, manganese-based compounds, vanadium-based compounds, organic materials and Prussian blue analogues all exhibit the ability to store Zn^{2+}.[37] The divalent Zn^{2+} is expected to provide high energy density since two-electron transfer occurs during insertion/extraction of a single ion at the cathode. However, the divalent cation induces much higher electrostatic attraction with the host materials, leading to difficult solid-state diffusion.[38] The inherent disadvantages of cathode materials can further increase the difficulties in reversible Zn^{2+} storage. Vanadium-based materials are challenged by their intrinsic dissolution character, which causes severe capacity loss during storage or a slow discharge process.[39] Manganese-based cathodes suffer from irreversible phase changes, structural collapse, the Jahn-Teller effect inducing Mn^{2+} dissolution and low electric conductivity, resulting in fast capacity fading and unsatisfying cyclability.[40]

Electrolyte is an essential component of ZIBs, serving as transport medium to transfer charge carriers between cathode and anode. It has multifaceted impacts on the performance of batteries, such as electrolyte/electrode interfacial properties, charge carrier movements, temperature tolerance and mechanical properties. The liquid aqueous electrolytes are characterized for their high ionic conductivity (range from 1~10 S cm^{-1}) and low viscosity,[41, 42] which enable excellent rate performance of ZIBs. The ionic conductivity is affected by viscosity, concentration, solvation structure and temperature. The movement of charged carriers associates with the fluidity of solvents. The ionic conductivity of an electrolyte decreases as the viscosity increases, and that is the reason why aqueous electrolytes have much higher ionic conductivity than the non-aqueous electrolytes. Restricted to the solid/quasi solid-state, the ionic conductivity of polymer hydrogels is much lower than the liquid electrolytes, and that is the main obstacle for their applications. The transference number of Zn^{2+} is defined as the fraction of total electrical current carried by Zn^{2+}, reflecting the electrical mobility of Zn^{2+}. In liquid electrolytes, Zn^{2+} is solvated by more solvent molecules than the anion, and therefore its migration ability is lower than the anion. Low transfer number of Zn^{2+} would induce high concentration polarization and arise dendrite growth when Zn^{2+} is depleted. It can be increased by restricting the migration of anions and reducing the solvation degree of Zn^{2+}. Attention

should also be paid to the electrochemical stability window (ESW) of electrolyte, which determines the working voltage range of cathode materials. Restricted by activity of water, the ESW of dilute aqueous electrolytes can reach to around 2.0 V due to the existence of overpotential and the effect of salts.[43] Strategies for reducing water activity, such as increasing salt concentration and adding functional additives with inhibiting effects, should be taken if an ESW higher than 2.0 V is required.[43] Another important issue is the unsatisfactory operation-temperature window of aqueous ZIBs, resulting from the low boiling point and high freezing point of water, plus aggravated side reactions at high temperature. Nonaqueous electrolytes have superiority for both wide ESWs and good temperature tolerance, but the balance between performance and safety needs to be carefully evaluated. In some applications, such as wearable devices, the requirements for good mechanical properties, prevention of liquid leakage and flexibility lead to polymer electrolytes being favourably viewed. In ZIBs, the challenges lie in overcoming the low ionic conductivity, insufficient mechanical strength and poor interfacial properties.[44] To increase the feasibility of ZIBs for various applications, researchers have developed a variety of functional electrolyte formulas. In this review, we provide a deep understanding of fundamental mechanisms, overview detailed synthesis and construction methods and evaluate materials engineering design effects on the resultant battery performance. Lastly, we also outline unsolved challenges and proposed some potential solutions.

2.2.2 Enhancing compatibility between cathodes and electrolyte

Vanadium-based materials

Over the past decade, vanadium-based materials have attracting growing interest as the electrode materials for the ZIBs, owing to the various oxidation states (+5, +4, +3, +2) of vanadium and their distinctive redox processes.[45] To date, many vanadium-based cathode materials, including vanadium oxides and metal vanadates have been studied, showing superior capacity and rate capability in ZIBs.[4, 46, 47] Vanadium-based materials, especially vanadium pentoxides (V_2O_5), possess large interlayer distances or large-tunnel frameworks, presenting good possibilities to accommodate numerous Zn^{2+} ions for high-energy-density storage. In addition to vanadium oxides, metal vanadate materials with different metal ions have also been widely investigated. The presence of alkaline or divalent ions (eg. Li^+, Na^+, K^+ and Zn^{2+}) can act as "pillars" to enhance the structure stability of the materials and favor fast Zn^{2+} diffusion. Although, most of these materials can achieve excellent capacities at large rates, they are facing the challenge of significant capacity decay at small current densities (<0.1 A g^{-1}) and disputable reaction mechanisms caused by multi-ion intercalations. The main reason behind the

degradation of vanadium-based materials is their intrinsic dissolution property in water-based electrolytes, resulting in structural or phase transformation, which has been a big obstacle for their application. Besides these effects, the underlying reaction mechanism of Zn^{2+} ions with vanadium-based materials is controversial, as protons usually contribute most capacity to the overall performance during the fast-charging process, and the vanadium cathodes undergo phase or structure evolution. Therefore, the true charge carriers in the vanadium-based cathodes along with their by-products needed to be pin-pointed by future research.[48]

Although it is tempting to thoroughly inhibit the side reactions of vanadium-based materials with electrolytes, it is worth the effort to probe the underlying mechanisms and adopt appropriate methods to buffer the adverse reaction processes. To boost the performance of vanadate-based materials for water-based ZIBs, various electrolyte strategies have been put forward: (i) adjusting electrolyte composition through increasing salt concentration or adding organic solvent;[49, 50] (ii) utilizing the electrode/electrolyte reaction for reversible intercalation or conversion reactions.[51]

Following these strategies, advanced techniques, such as operando pH and *in-situ* XRD measurements are necessary for shedding light on the failure mechanisms and transformation processes in vanadium-based materials in water-based solutions. As shown in **Figure 2.8b**. Liu et al. highlighted the importance of a pH technique for probing the real interfacial reactions.[52] A novel pH detection was set up to uncover the separate intercalation roles of Zn^{2+} and H^+ in δ-V_2O_5, where the two ions follow an exchange intercalation/deintercalation mechanism in 3 M $Zn(CF_3SO_3)_2$ aqueous electrolyte. Since the H^+ comes from the electrolyte, the intercalation/deintercalation causes pH changes, monitoring the electrolyte's pH is an indirect tool to discriminate clearly between the H^+ and Zn^{2+} intercalation processes.

Electrolyte concentrations are reported to have significant effects on the performance of vanadium-based cathode materials. The early report by Liang's group on V_2O_5 has preliminarily evaluated aqueous electrolytes with different concentrations and salts affecting the performance of V_2O_5 cathodes, highlighting the better result of $ZnSO_4$ salt than $ZnCl_2$, $Zn(CH_3COO)_2$, and $Zn(NO_3)_2$.[53] Adjusting the electrolyte composition by adding organic co-solvent into the aqueous solution is also reported to reduce side reactions of V_2O_5 and enhance stability. Zhang et al. reported a hybrid aqueous/organic electrolyte ($Zn(ClO_4)_2$/EC+EMC+10%H_2O,[50] where EC is ethylene carbonate and EMC is ethyl methyl carbonate) that enabled long cycling performance of free-standing V_2O_5/carbon nanotube (CNT) film electrode. This is a successful example of the hybrid strategy for inhibiting cathode

dissolution. The resultant electrolyte adopted 90% of EC and EMC (1:1 v/v) solvents and 10% of H_2O, which may sacrifice the safety of the electrolyte, and results in slow Zn^{2+} ion intercalation/de-intercalation kinetics. In addition, the high proportion of highly flammable EMC solvent in the electrolyte sacrifices the intrinsic safety of the aqueous electrolyte. Therefore, others safe organic solvents, were also studied as hybrid solvent components for solving the cathode issue in water-based electrolyte. It is reported by Liu et al. that triethyl phosphate (TEP) is a promising co-solvent,[24] as it not only has a fire-retardant property, but also possesses a much higher donor number (DN = 26 kcal mol^{-1}), favouring a stronger coordination capability with Zn^{2+} and H_2O. Compared with EC (DN = 16.4 kcal mol^{-1}) and EMC (DN = 6.5 kcal mol^{-1}), the higher DN of TEP will need less water to achieve a good side reaction depressing effect. This is because the TEP can form a strong bonding with H_2O and can better regulate the electrolyte behaviour with the electrode interface, as illustrated in **Figure 2.8c**.

Other than vanadium oxides and metal vanadates, layered $VOPO_4$ has received a lot of attention due to its high working potential and high oxygen redox (over 2.2 V).[54] Benefiting from the 21 M LiTFSI/1 m $Zn(CF_3SO_3)_2$ electrolyte, $VOPO_4$ material showed highly reversible oxygen redox chemistry in addition to the traditional vanadium redox process, which is promising for high-voltage operation, as seen in **Figure 2.8d**. However, this material is extremely unstable in water-based solution, limiting its potential for aqueous ZIBs. Reports have made about controlling the content of water in electrolyte to utilize the advantages of this material. It is reported by Wang et al. that restricting the water ratio to 1% in 0.1 M $Zn(CF_3SO_3)_2$-AN can boost the intercalation kinetics of Zn^{2+} in $VOPO_4$.[55]

Progress has also been made through utilizing the spontaneous reactions of vanadium oxide with electrolyte to obtain new stable metal vanadate phases. As reported by Huang et al. V_2O_5 formula units can transfer into $Zn_3V_2O_7(OH)_2$ H_2O ("ZVO") as a new intercalation material by soaking the material in 3 M of $Zn(CF_3SO_3)_2$electrolyte for 10 days, as shown in **Figure 2.8e** and **f**.[56] This work also provided insights into the pH influence on the transformation of V_2O_5 by giving a H-log [V^{5+}] diagram (as seen **Figure 2.8g**), where different pH ranges favor different valence species. Following this work, related works on the *in-situ* or phase transformation of vanadium-based materials, such as interlayer-expanded $VS_2{\cdot}NH_3$,[56] dual-cation pre-intercalated-VO_2[57] and $Zn_xV_2O_5{\cdot}nH_2O$,[58] were also investigated.

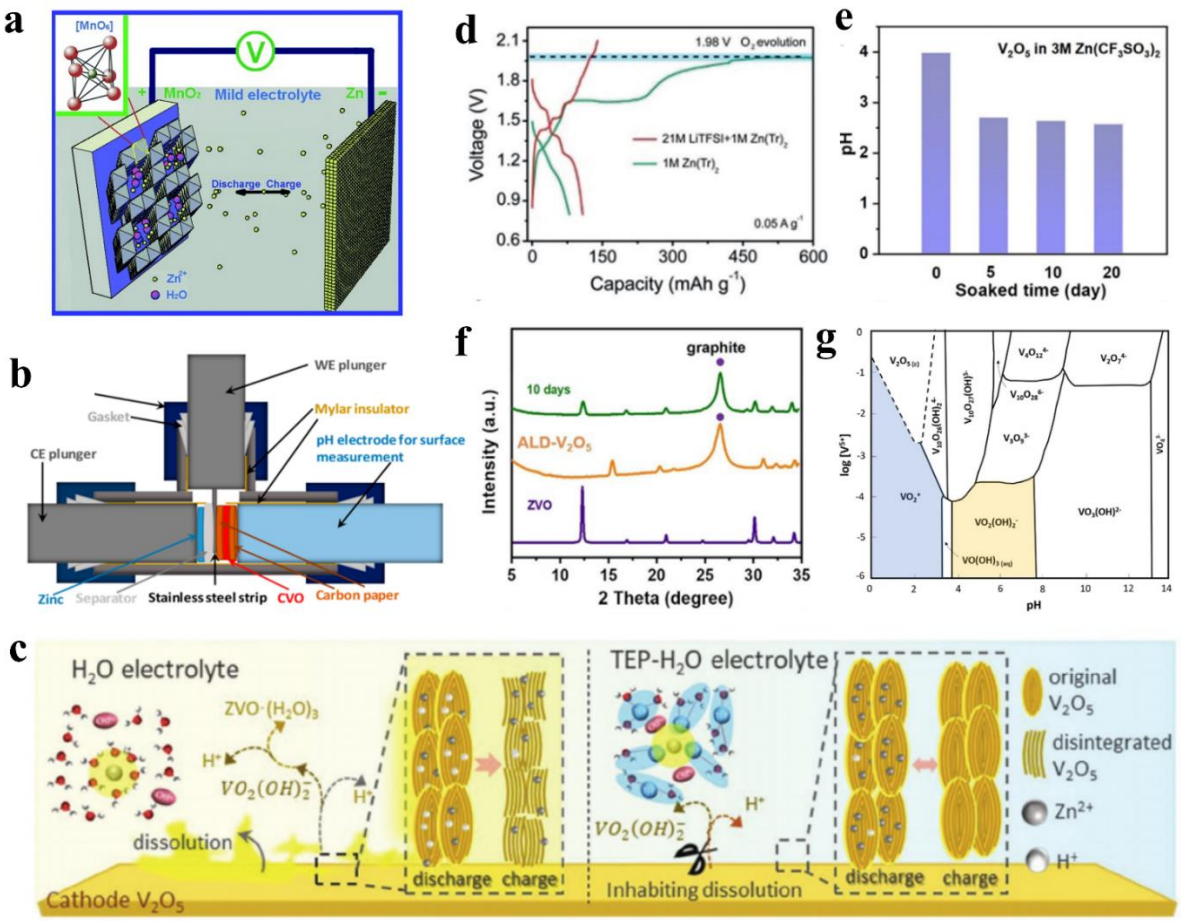

Figure 2.8. (**a**) Schematics of the chemistry of the zinc ion battery;[31] Reproduced with permission. Copyright 2012, Wiley-VCH. (**b**) The configuration for operando pH measurement in a battery;[52] Reproduced with permission. Copyright 2020, American Chemical Society. (**c**) Schematic illustration of the effects of hybrid TEP-H_2O electrolytes on V_2O_5 electrode during the electrochemical reactions;[24] Reproduced with permission. Copyright 2021, John Wiley and Sons. (**d**) First charge/discharge curves of $VOPO_4$-Zn full batteries with two different electrolytes;[54] Reproduced with permission. Copyright 2021, John Wiley and Sons. (**e**) The pH changes of V_2O_5 with soaking time in 3M $Zn(CF_3SO_3)_2$ aqueous electrolyte; (**f**) XRD pattern of the soaked material compared to the standard ZVO phase; (g) Log[V^{5+}] *vs* pH phase diagram showing V valence changes in response to pH.[56] Reproduced with permission. Copyright 2022, Elsevier.

To sum up, although vanadium-based materials have the merit of high-capacity, it is still challenging to employ vanadium-based materials as cathodes in ZIBs due to their inherent dissolution property in water. To address the above issue, strategies of electrolyte modification

are one of the most effective ways to improve the compatibility of cathode with electrolyte. The other strategy of letting the material transform into another more stable and workable state is also useful but is not suitable for large-scale application. Therefore, it is worth the effort to improve the stability of vanadium-based cathodes through exploring low-cost and effective electrolyte combinations. Meanwhile, to assist the study of different strategies, a comprehensive understanding of vanadium-based material reaction mechanisms in water-based electrolytes is required. Since protons and Zn^{2+} co-exist during the electrochemical charging/discharging process, it is necessary to figure out the roles of protons in the electrolyte via advanced interfacial analysis techniques.

Manganese-based materials

Manganese oxide (MnO_2) materials had a resurgence in attention as rechargeable ZIBs became a hot research topic. MnO_2 is characterized by various crystal structures, such as α-MnO_2, β-MnO_2, γ-MnO_2, λ-MnO_2, R-MnO_2, δ-MnO_2, and ε-MnO_2.[59] In microcosm, they are all composed of MnO_6 octahedral subunits, which can form tunnels, chains and layered configurations by choosing different bonding orientations. Besides MnO_2, researchers also developed $Na_2Mn_3O_7$, $ZnMn_2O_4$, $MgMn_2O_4$,Ca_2MnO_4 and other manganese-based materials as cathode materials for ZIBs.[40] Generally, the working principles of manganese-based materials can be concluded as a reversible Zn^{2+} intercalation mechanism,[60] a H^+/Zn^{2+}co-insertion mechanism,[61] a chemical conversion reaction mechanism,[62] and Mn^{2+} electrochemical deposition/dissolution.[63] When serving as cathode in aqueous ZIBs, manganese-based materials are facing scientific challenges through the dissolution of manganese in the form of Mn^{2+} ions. This mainly occurs during discharge processes, where Mn^{3+} ions are generated due to the electrochemical reduction of Mn^{4+} in cathode materials. Unstable Mn^{3+} is susceptible to undergoing a disproportionation reaction and forms Mn^{4+} and Mn^{2+} based on the following reactions.[64]

$$Mn^{4+}\,(s) + e^{-} \rightarrow Mn^{3+}\,(s) \qquad (1)$$

$$2Mn^{3+}\,(s) \rightarrow Mn^{4+}\,(s) + Mn^{2+}\,(aq) \qquad (2)$$

Continuously dissolved Mn^{2+} ions can account for nearly 1/3 of the total amount of manganese in a cathode, leaving abundant manganese vacancy sites in the electrode.[65] Even worse, the original structure of the host materials will be destroyed, resulting in significant capacity fading. These undesirable issues can be effectively relieved by skilled electrolyte chemistry.

It has been reported that pre-adding Mn^{2+} into an electrolyte is a useful strategy to control the equilibrium between the dissolution and recombination of active materials, and therefore improve the electrochemical performance of manganese-based materials.[66] The addition of $MnSO_4$ in 2M $ZnSO_4$ electrolyte notably increased the specific capacity and cyclability of Zn/δ-MnO_2 cells, and the improvement is attributed to the function of $MnSO_4$ in facilitating the charge process, suppressing the dissolution of manganese and inhibiting the formation of basic zinc sulphates ($ZnSO_4{\cdot}3Zn(OH)_2{\cdot}nH_2O$).[67] Using 3 M $Zn(CF_3SO_3)_2$ as electrolyte with 0.1 M $Mn(CF_3SO_3)_2$ as additive can boost the electrochemical performance of Zn/MnO_2 cells, with a reaction mechanism as illustrated in **Figure 2.9a**. Besides the functions of compensating the loss manganese of cathode material, increasing ionic conductivity and improving initial Coulombic efficiency, the pre-added Mn^{2+} also contributes to the formation of a porous MnO_x film on the electrode, which can promote charge transfer and protect the cathode.[68] Although the positive role of Mn^{2+} additive has been widely recognized, researchers have made differing claims about the underlying mechanisms. Some researchers disagree that manganese dissolution is suppressed by Mn^{2+} additive, instead ascribing the improvement to the electrodeposition process of Mn^{2+}, which counteracts the capacity loss caused by phase transition from layered to spinel structure.[69] They point out that the continuously increased capacity and extended lifespan of Zn/MnO_2 cells is highly related to the concentration of Mn^{2+} additive. The more Mn^{2+} additive added, the more MnO_2 can be electrodeposited onto the cathode, and thus higher capacity can be achieved. Once the Mn^{2+} from additive is exhausted due to the generation of inactive phase, then capacity fading is inevitable. This opinion is supported by the analysis of Zn/$ZnMn_2O_4$ cells, in which an electrochemical deposition/dissolution of manganese occurs simultaneously when a $ZnMn_2O_4$ cathode undergoes charge/discharge processes. Besides these aforementioned effects, insoluble MnO_x that is deposited on the surface of a $ZnMn_2O_4$ cathode could also serve as host material for Zn^{2+} insertion/extraction, further increasing the capacity of the cell.[70] Another useful approach to solve the manganese dissolution issue is to form an interfacial layer on the cathode. When 2 M $ZnSO_4$ and 0.1 M $MnSO_4$ is used as electrolyte to couple with Ca_2MnO_4 cathodes, the sulphate from the electrolyte combines with calcium ions extracted from the cathode and generates a high-quality $CaSO_4{\cdot}2H_2O$ film on the surface of cathode, as illustrated in **Figure 2.9b**. This layered SEI film is verified to significantly supress the dissolution of manganese and promote cyclability of the battery.[71]

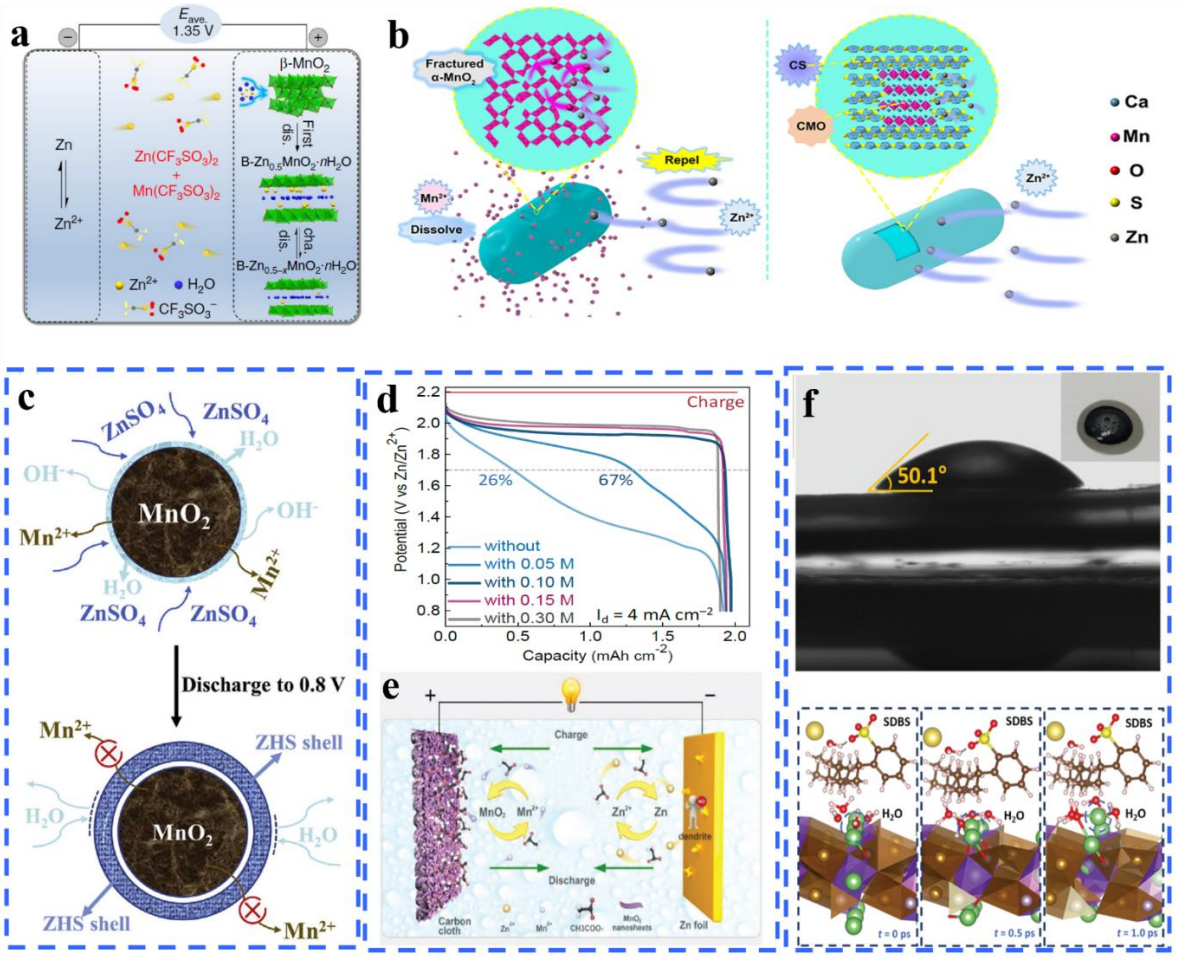

Figure 2.9. (**a**) The working principle of a Zn/MnO_2 cell using $CF_3SO_3^-$ based electrolyte;[68] Reproduced with permission. Copyright 2017, Springer Nature. (**b**) Schematic of interface layer formed *in-situ* on a Ca_2MnO_4 cathode;[71] Reproduced with permission. Copyright 2019, American Chemical Society. (**c**) The role of $Zn_4SO_4(OH)_6{\cdot}4H_2O$ in the Zn/MnO_2 discharge process;[76] Reproduced with permission. Copyright 2020, Elsevier. (**d**) Discharge curves of a Zn/MnO_2 battery using electrolytes with different amounts of H_2SO_4;[72] Reproduced with permission. Copyright 2020, John Wiley and Sons. (**e**) Schematic illustration of a Zn/MnO_2 energy storage system in acetate-based electrolyte;[74] Reproduced with permission. Copyright 2020, John Wiley and Sons. (**f**) The function of SDBS in Li-ion migration.[77] Reproduced with permission. Copyright 2019, John Wiley and Sons.

Considering the instability of Mn^{3+} and solubility of Mn^{2+}, some researchers regard the Mn^{4+}/Mn^{2+}redox mechanism may be a better choice for constructing Zn/MnO_2 batteries. Soluble Mn^{2+} from a suitable electrolyte is electrochemically deposited onto the cathode in the form of solid MnO_2 during charging and it undergoes a reverse reaction during discharging,

achieving a highly reversible energy storage system. Compared with the one-electron reaction based on the Mn^{4+}/Mn^{3+} redox couple, this two-electron redox reaction boosts the theoretical capacity of cathode material to a high 616 mAh g^{-1}.[63] Besides these good features, the discharge voltage during MnO_2 dissolution process can even reach a higher value than that of the insertion mechanism. However, this theoretical state is hard to achieve because $Zn_4SO_4(OH)_6{\cdot}4H_2O$ (ZHS) generated during the first discharge process covers the surface of MnO_2 and impedes its further dissolution (**Figure 2.9c**). The situation is mitigated in acidic solution. By adding H_2SO_4 into 1M $ZnSO_4$ and 1M $MnSO_4$ electrolyte in an electrolytic Zn/MnO_2 system, the capacity contribution of the high-voltage region, corresponding to the reaction of $Mn^{2+} + 2H_2O \leftrightarrow MnO_2 + 4H^+ + 2e^-$ (E=1.228 V *vs* SHE), increases with the increasing concentration of H_2SO_4 and reaches 100% at 0.1 M, realizing a stable output voltage of 1.95 V (**Figure 2.9d**).[72] Although acidic electrolyte favours the reaction of MnO_2, it brings the risk of hydrogen evolution and corrosion of a Zn anode. To meet the different pH value requirements for anodes and cathodes, hybrid electrolytes have been proposed and realized by separating an acidic catholyte and alkaline anolyte with a selective separator.[73] In such a design, the Mn^{4+}/Mn^{2+} redox mechanism dominates the cathode reaction and high capacity and discharge voltage can be obtained. Alternatively, a more compatible solution environment for both MnO_2 and Zn anode can be created by using acetate-based electrolyte, 1 M $Zn(CH_3COO)_2$ with 0.4 M $Mn(CH_3COO)_2$.[74] This near-neutral electrolyte is anode-friendly and the acetate ions play an important role in facilitating the dissolution process of MnO_2 via modifying its surface properties (**Figure 2.9e**). Similar functions can be achieved by a I^-/I_3^- mediator strategy, in which I^- reduces solid MnO_2 into Mn^{2+} and its product, I_3^-, can subsequently get electrons from electrode to reduce into I^-.[75] With I^-/I_3^- serving as an electron shuttle, the dissolution process of MnO_2 is promoted and its capacity is completely delivered.[75]

Based on above discussion, we agree that manganese-based materials are the most promising cathode candidates for Zn-based batteries, not only because of their environment-friendliness and low cost but also because of their controllable reaction mechanisms. For the conventional insertion reaction, the effects of pre-adding Mn^{2+} into electrolyte is quite prominent in enhancing the capacity and cyclability of batteries. However, its full functions are still in dispute and need further investigation. Compared with the sluggish cation insertion reaction, the deposition/dissolution reaction of MnO_2/Mn^{2+} can fully exhibit the merits of Zn/MnO_2 batteries, in terms of theoretical capacity, output voltage, rate performance and reversibility. Nonetheless, it is worth noting that the theoretical capacity calculation based on MnO_2 is not

reasonable when it comes to practical application. In fact, the capacity is stored in the electrolyte so its weight and volume should be taken into consideration when labelling the energy density. In addition, some proposed battery systems would not use regular assembly methods, such as coin cells or pouch cells, and therefore, the devices design and optimisation should be taken seriously to minimize the mass and volume of inactive materials.

Other materials

Prussian blue analogues (PBAs) usually refer to low-cost transition-metal hexacyanoferrate metal-organic frameworks (MOFs),[78] which have three-dimensional (3D) pathways permitting the insertion/extraction of Zn^{2+}. It has been verified that $Zn_3[Fe(CN)_6]_2$ can serve as an intercalation host material and exhibits an discharge voltage of 1.7 V.[79] $KCuFe(CN)_6$ is reported to deliver a capacity of 60 mAh g^{-1} in a 20 mM $ZnSO_4$ electrolyte.[80] Despite the impressive voltage, extremely low capacity and poor cyclability make PBAs less competitive. To further boost the capacity, a two-species redox reaction of Co^{2+}/Co^{3+} and Fe^{2+}/Fe^{3+} is induced by $CoFe(CN)_6$. It is realized by extracting K^+ *in-situ* from $KCoFe(CN)_6$ in 4 M $Zn(CF_3SO_3)_2$ electrolyte during the first discharge process. Due to the overwhelming superiority in concentration, Zn^{2+} rather than K^+ is inserted into the host material in the following cycles, contributing a capacity as high as 173 mAh g^{-1}.[81] Xu et al. reported a manganese metal-organic framework, Mn(BTC), in which BTC is 1,3,5-benzenetricarboxylic acid, serving as the cathode material for ZIBs[82]. The Mn(BTC) exhibits a Zn^{2+}-storage capacity of 112 mAh g^{-1} and an outstanding cycling stability of 900 cycles. Similar MOFs, such as Mn(BDC), Fe(BDC), Co(BDC), and V(BDC) (in which BDC is 1,4-dicarboxybenzene), also show the capability to storage Zn^{2+} ions in their frameworks, but the electrochemical performance is not as good as that of Mn(BTC). Some other oxides, such as TiO_2, Fe_3O_4, Co_3O_4 and MoO_3 were also reported to be used as cathode materials.[83] Zhi's group fabricated a Co(III) rich-Co_3O_4 cathode material, where the ratio of Co^{3+}/Co^{2+} is 1.696, and applied mild electrolyte (2 M $ZnSO_4$ with 0.2 M $CoSO_4$) to replace alkaline electrolyte, realizing both improved voltage (2.2 V) and capacity (158 mAh g^{-1}).[84] Strategic electrolyte choices are also made for optimizing interfacial properties. Sodium dodecyl benzene sulfonate (SDBS), a low-cost additive, is added into a hybrid Zn/$LiFePO_4$ battery, promoting its rate capability to 5C for 500 cycles.[77] The wettability of electrolytes for $LiFePO_4$ electrodes has been greatly enhanced (**Figure 2.9f**). The advantages are attributed to the reduced wetting free energy, where SDBS is adsorbed on $LiFePO_4$ (010) crystal faces and serves as medium to facilitate water absorption and Li^+ migration.

Layered transition-metal disulfides, such as VS_2 and MoS_2, are investigated as the host materials for the Zn^{2+} insertion/extraction, due to their graphene-like structure.[85] The weak van der Waals forces between layers facilitate the diffusion of Zn^{2+}, however, these materials usually exhibit low redox potentials. Organic cathode materials, represented by quinones and polyaniline, are emerging recently, exhibiting advantages in flexibility, considerable capacity, eco-friendliness and lightweight. At present, the research towards these materials still focus on their energy storage mechanism, design of molecular structure and material modification.[86] How electrolytes affect the performance of organic cathode has rarely been reported, so these contents are not involved in this review.

2.2.3 Protection of Zn anode and the development of dendrite-free Zn anode

Technically, H_2 evolution potential (−0.41 V *vs* SHE) is higher than zinc reduction potential of −0.76 V *vs* SHE, which means H_2 evolution is thermodynamically preferred in aqueous electrolyte. Thanks to the high H_2 evolution overpotential of Zn metal, H_2 evolution becomes a slow process, thus making Zn metal a possible anode choice. As H_2 evolution progress, the local pH value within a cell fluctuates due to the increase of OH^- concentration. This can trigger the formation of $Zn(OH)_2$ and ZnO by-products on the Zn metal surface. It is believed that electrolyte salt also takes part in parasitic side reactions to form Zn-based basic salts. Another major issue for zinc metal anodes is dendrite growth. Zn^{2+} tends to distribute and deposit unevenly on Zn metal anodes. The notorious dendrites not only compromise battery performance but also present safety issues.

Solvation structure manipulation

In the aqueous ZIBs electrolyte, one zinc ion is typically coordinates with six water molecules to form $Zn(H_2O)_6^{2+}$, which is deemed detrimental to Zn metal anodes. The strong coordination between Zn^{2+} and water molecules means the Zn^{2+} needs to overcome a high energy barrier to desolvate and deposit on a Zn metal surface, which leads to a high overpotential.[87] Apart from this, the interaction between Zn^{2+} and O atoms in the solvating water molecules weakens the H-O bonds. As a result, the solvated water molecules are more likely to decompose.[88]

Using highly concentrated electrolyte can prevent the formation of $Zn(H_2O)_6^{2+}$, as the high population of the salt anions would force them into the inner solvation shell of Zn^{2+} to replace the water molecules [89, 90, 91, 92, 93, 94]. The solvation shell in concentrated electrolyte facilitates fast and even zinc deposition. The elimination of solvated water molecules and the scarcity of free water effectively avoids water decomposition-related hydrogen evolution and other

parasitic side reactions.[95] Therefore, high CE and excellent cycling stability are achieved. However, the use of large amounts of salt in the electrolyte certainly compromises the cost advantages of aqueous electrolyte. Also, ionic conductivity of concentrated electrolyte is even lower than the dilute electrolyte, due to the high viscosity.

To avoid the use of large quantities of expensive salt, relatively low-cost organic solvents such as dimethyl sulfoxide (DMSO),[96, 97] ethylene glycol (EG),[98, 99] TEP,[24, 100] dimethyl carbonate (DMC),[101] 1,2-dimethoxyethane (DME)[102] and glycerol,[103] were applied to reorganize the solvation structure of zinc ion electrolyte. Compared to the concentrated electrolyte, electrolyte containing organic solvent is cheaper, but in most of cases, the organic component is either toxic or flammable. In a previous report, the addition of TEP in electrolyte was found be able to suppress hydrogen evolution and parasitic side reactions, and achieve enhanced electrochemical performance of zinc metal anodes (**Figure 2.10a-d**),[100] but the mechanism behind the positive effect remained unexplained. Wang et al. first ascribed the organic solvent DMSO's influence over the zinc metal anode performance due to solvation structure manipulation, as DMSO has higher DN of 29.8 than that of water (18), which promotes a region of the inner solvation shell being occupied by DMSO molecules (**Figure 2.10e-i**).[96] Soon after that, "antisolvents" were introduced into electrolytes. When methanol as an antisolvent, was added into 2M $ZnSO_4$ electrolyte, the interaction between water and methanol was stronger than between Zn^{2+} and water, which means that methanol molecule is able to enter the inner sheath of Zn^{2+} and replace the position of water.[104] Coordination between Zn^{2+} and other organic molecules has also been detected in solvation shells after the use of various cosolvents.[101, 103, 104]

Low-cost and eco-friendly solid additives are considered a better choice for solvation structure manipulation than organic solvents. A series of small Lewis base molecules, including triethylamine hydrochloride (TEHC), diethylamine hydrochloride (DEHC), ethylamine hydrochloride (EHC), and ammonium chloride (NH_4Cl) have been reported to regulate Zn^{2+} solvation structure.[105] Similarly, glucose was found to replace water molecules in the inner solvation shell.[106] The introduction of Mg^{2+} ion into electrolytes also promotes interaction with water molecules and impairs water inclusion in Zn^{2+} solvation sheath.[107] Very recently, a water-free solvation structure was achieved by after adding chloride salt with a bulky cation. The elimination of solvated water molecules results in an average Zn plating/stripping CE of 99.9%.[88]

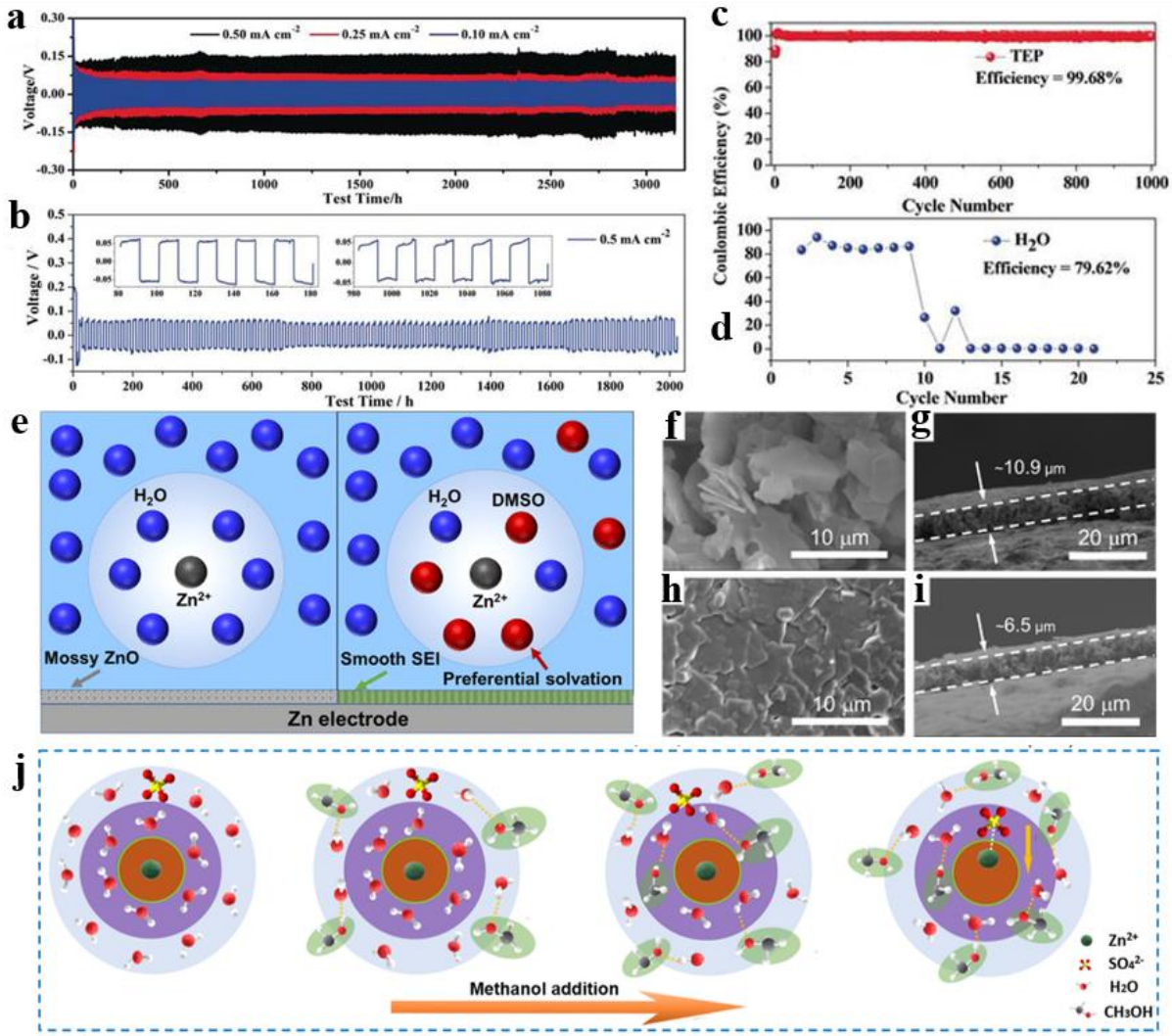

Figure 2.10 (**a**) Galvanostatic cycling of Zn/Zn cells at 0.1 $mAcm^{-2}$ (blue), 0.25 $mAcm^{-2}$ (red) and 0.5 $mAcm^{-2}$ (black) in a 0.5M $Zn(CF_3SO_3)_2$-TEP electrolyte. (**b**) Cycling stability of a Zn/Zn cell with 10 h deposition followed by 10 h stripping, Cycling performance of a Zn/SS cell in TEP (**c**) and an aqueous electrolyte (**d**).[100] Reproduced with permission. Copyright 2019, John Wiley and Sons. (**e**) Scheme of Zn^{2+} solvation structure and zinc surface passivation in H_2O (left) and H_2O-DMSO (right) solvents. SEM images of Zn electrodes in Zn/Zn symmetrical cells after 50 plating/stripping cycles at 0.5 mA cm^{-2} and 0.5 mAh cm^{-2} in $ZnCl_2$-H_2O (**f**) and (**g**), and $ZnCl_2$-H_2O-DMSO electrolytes (**h**) and (**i**). Reproduced with permission.[96] Copyright 2020, American Chemical Society. (**j**) Schematic of changes in the Zn^{2+} solvent sheath, together with methanol addition.[104] Reproduced with permission. Copyright 2021, John Wiley and Sons.

Eutectic electrolyte is another strategy to manipulate the solvation structure. The scarcity of water molecules make it impossible for the zinc ion to form an complete $Zn(H_2O)_6^{2+}$ solvation structure. Cui et al. reported a eutectic electrolyte composed of hydrated salt ($Zn(ClO_4)_2 \cdot 6H_2O$) and a neutral ligand.[108] The Lewis basic SN participate inner zinc ion solvation structure to form $[Zn(OH_2)_x(SN)_y]^{2+}$ cations, resulting in enhanced Coulombic efficiency and prolong cycling performance. It is widely believed that less solvation by water molecules favours enhanced electrochemical performance. However, most of the additives employed only eliminated part of the solvated water from the inner solvation shell and the mechanism behind the solvation structure influence on zinc metal anode performance remains a bit vague.

Electrolyte and Zn metal electrode interface engineering

The construction of artificial solid electrolyte interface (SEI) layers is considered to be an effective strategy to protect Zn anode, with the advantage of blocking direct contact between Zn metal and liquid electrolytes. However, artificial SEI layers are fragile and would crack during cycling, exposing fresh Zn metal to electrolytes. *In-situ* SEI layers could make up the shortage because of their self-repairable advantages.

In most cases, decomposable component is needed to construct an SEI layer. A zinc fluoride (F)-rich organic/inorganic hybrid SEI derived from FSI^- anions was obtained in an acetamide-$Zn(TFSI)_2$ eutectic electrolyte (**Figure 2.11a-b**).[109] It is still challenging to construct SEI *in-situ* with an aqueous electrolyte, since most of the chemicals are quite stable in the narrow working voltage window of aqueous electrolyte. Wang's group conducted pioneering research work in *in-situ* SEI formation by introducing decomposable additives, including $SnCl_2$,[110] $Zn(NO_3)_2$ (**Figure 2.11c-d**),[111] phosphonium-based cations,[112] alkylammonium salt[113] and tris(2,2,2-trifluoroethyl)-phosphate (TFEP),[110] to form SEI layers together with other electrolyte components. The as-prepared SEI layers not only possess high ionic conductivity to allow the transportation of Zn^{2+} between electrode and electrolyte, but also protect the zinc metal surface from electrolyte to prevent further corrosion. $NaPF_6$,[114] $Zn(ClO_4)_2$,[115] and LiCl[116] were also used by other researchers to achieve protected layers for zinc metal anodes. Very recently, our group added $Zn(H_2PO_4)_2$(**Figure 2.11e**)[117] and dopamine[118] into the electrolyte as SEI precursors for hopeite and polydopamine SEI, respectively. The constructed SEI layers shown strong adhesion to the surface of the Zn metal, remarkable hydrophilicity and high Zn^{2+} conductivity.

SEI layers can also be created by the adsorption of additive molecules. Some additives, such as ethylene diamine tetraacetic acid tetrasodium salt (Na_4EDTA)[119], polyacrylamide (PAM),[120] polyethylene oxide (PEO),[121] MXene,[122] and polyethylene glycol (PEG),[123] possess functional groups that have strong interaction with Zn^{2+}. By adsorbing on the surface of Zn anode, these functional groups play an important role in regulating the Zn^{2+} flux and therefore facilitating smooth Zn deposition. In addition, the adsorpted molecules also build a protection layer to shield the anode from the attack from electrolytes, mitigating the H_2 evolution.

An ideal SEI should possess high ionic conductivity to facilitate Zn^{2+} transportation, strong mechanical strength to withstand volume change and prevent dendrite growth, and also a "self-healing" ability to maintain integration during cycling. *In-situ* SEI normally outperforms an artificial counterpart because of its self-healing ability, but it should be noted that it is easier to optimize artificial SEI component to obtain high ionic conductivity and enhanced mechanical properties.

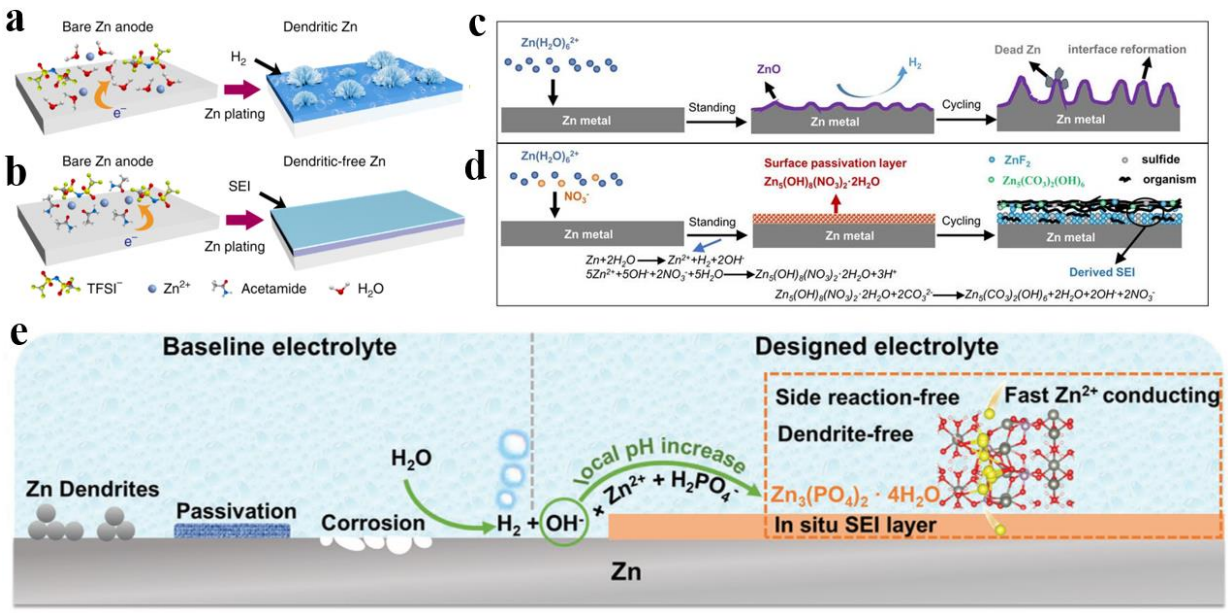

Figure 2.11 (**a**) Zn dendrite growth along with H_2 evolution observed in 1M $Zn(TFSI)_2$ and (**b**) SEI-regulated uniform Zn deposition in $Zn(TFSI)_2$-based eutectic solvent.[109] Copyright 2019, Springer Nature. (**c**) Zn dendrite growth in aqueous electrolytes; (**d**) ZnF_2-$Zn_5(CO_3)_2(OH)_6$-organic SEI formation mechanism.[111] Reproduced with permission. Copyright 2021, John Wiley and Sons. (**e**) Schematic illustration of Zn surface evolution and the SEI formation mechanism.[117] Reproduced with permission. Copyright 2021, John Wiley and Sons.

Zn deposition behaviour regulation

Similar to other metal anodes, Zn metal anode also suffers from the dendrite formation. During initial cycles, some protuberant tips develop due to uneven Zn^{2+} deposition. These protuberant tips have higher local electric field which attract more Zn^{2+} and evolve into Zn dendrites. Introducing metal ions with more negative deposition potential than Zn^{2+} into electrolytes is expected to suppress the so called "tip effect". For example, Mg^{2+} (**Figure 2.12a**) [107] and Na^{+}[124] as additives preferentially adsorb on the protuberant tips due to the higher electric fields. The occupied sites prevent further deposition of Zn^{2+} and drive Zn^{2+} to other nearby regions.[125] Beside metal cation, tetrabutylammonium (TBA^{+}) cation (**Figure 2.12b**)[126] as well as highly-polarized Et_2O molecules (**Figure 2.12c-e**) [127] also have the ability to regulate Zn^{2+} deposition under the same mechanism. Pb^{2+} and Sn^{2+} ion also play a role in nucleation and growth of zinc metal.[128] Both of the metal ions would reduce to metal because of their higher standard potential than Zn^{2+}. Detailed investigation revealed that, in the case of Pb, nucleation behaviour was significantly changed from initial stages of deposition, while, micro-steps evolution was gradually mitigated by Sn addition. Qin et al. reported that graphene oxide (GO) can promote an even electric fields near the electrode/electrolyte interface.[129] Organic solvents, including cetyltrimethylammonium bromide (CTAB), sodium dodecyl sulfate (SDS), polyethylene-glycol (PEG-8000), thiourea (TU) and branched polyethyleneimine (BPEI) have been proved to have an influence on the Zn crystal growth.[130, 131] The presence of BPEI helped reduce the Zn crystal size and achieve relatively smooth Zn deposition.

Some effort also devoted in electrolyte salt optimization. Salt has direct influence on some of the electrolyte properties, such as pH value, ionic conductivity, stable working voltage window, as well as reversibility of Zn anode. Different salts, including $ZnSO_4$, $ZnCl_2$, $Zn(ClO_4)_2$, $ZnNO_3$, ZnF_2, $Zn(CH3COO)_2$, $Zn(TFSI)_2$ and $Zn(CF_3SO_3)_2$, have been employed as salt for electrolyte in the ZIBs.[28] It is found that some salts ($ZnCl_2$, $Zn(ClO_4)_2$, $ZnNO_3$) with strong oxidizing ability are not desired choice for uniform zinc deposition. The use of these salts are tend to form loose, rough and insulated by-product on the zinc anode surface, which would worsen dendrite growth.[31, 132] Recently, $Zn(CF_3SO_3)_2$ and $Zn(TFSI)_2$ are investigated and show remarkable electrochemical performance.[42, 133] The $CF_3SO_3^{-}$ and $TFSI^{-}$ anions have the ability to alleviate the solvation effect and reduce the solvated water molecules around the zinc ion, as a result, facilitate the migration of zinc ion. A dendrite-free zinc deposition on Ti foil was observed when used 3 M $Zn(CF_3SO_3)_2$.

Under the above-mentioned zinc deposition regulation mechanism, uniform Zn deposition is much easier to achieve at low current density. It is still challenging to obtain satisfactory

electrochemical performance at high current density, as most of additives would lose their function to regulate the Zn deposition. Efforts needed to develop strategies to prevent dendrite growth at high current density in order to meet practical application.

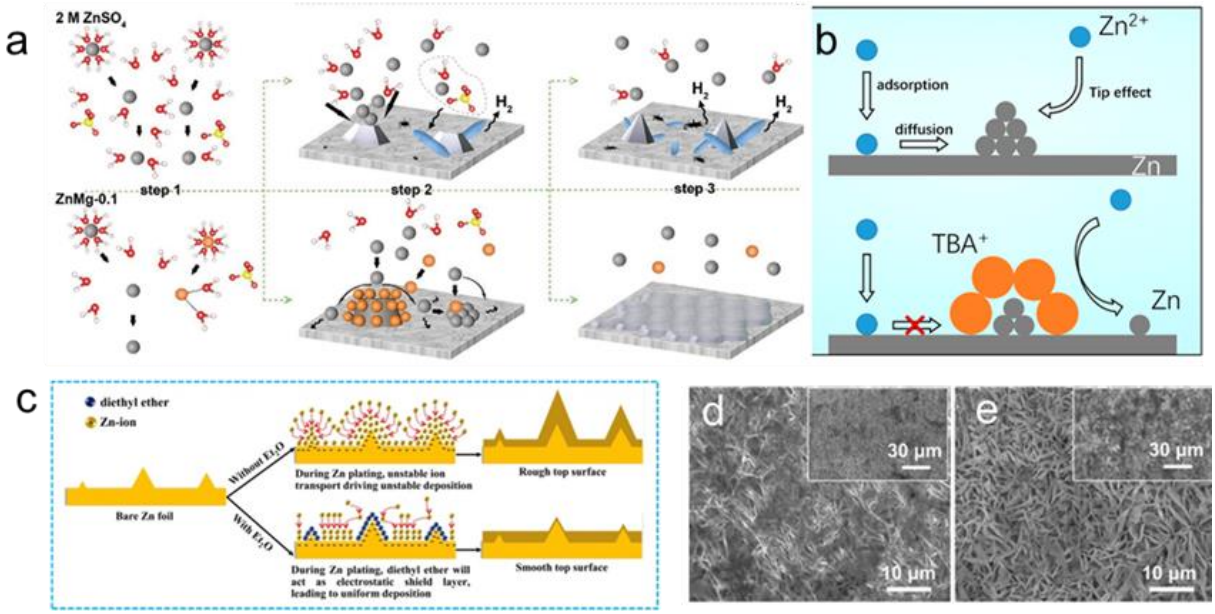

Figure 2.12 (**a**) Schematics of Zn deposition process in the 2 M $ZnSO_4$ (top row) and ZnMg-0.1 (bottom row) electrolyte. Reproduced with permission.[107] Copyright 2021, John Wiley and Sons. (**b**) Schematics of the Zn^{2+} ion diffusion and reduction processes on electrodes in 2 M ZnSO4 electrolyte (upper part) and 2 M $ZnSO_4$ electrolyte with 0.05 mM TBA_2SO_4 (lower part). Reproduced with permission. Copyright 2020, American Chemical Society. (**c**) Schematics of morphological evolution of Zn anodes in mild aqueous electrolyte with and without Et_2O additive during Zn stripping/plating cycling. Planar SEM images of Zn anode surface after 125 plating/stripping cycles obtained from Zn/Zn symmetrical cells with (**d**) and without (**e**) Et_2O additive.[125] Reproduced with permission. Copyright 2019, Elsevier.

2.2.4 Widening electrochemical stability window

Although many advantages are highlighted in aqueous electrolytes, their relatively narrow electrochemical stability window (ESW) confines the application of high-voltage cathode materials, greatly limiting the energy density of ZIBs. The ESW of electrolyte is codetermined by solvents and solutes, and the concentration of solutes also has great influence on the stability of solvents. Dahn found the stability of water can be modified by high salt concentrations.[134] In 2015, Wang's group reported a 'water in salt' electrolyte, more than 20 M LiTFSI dissolved in water, dramatically expanding the ESW to an upper value of ~ 3.0 V.[135] This group later

applied this design in ZIBs by using 1 M $Zn(TFSI)_2$ and 20 M LiTFSI in their electrolytes.[87] The extremely high concentration ensures that the water molecules are severely confined in Li^+ solvation clusters, therefore weakening the interaction between water and Zn^{2+} and further eliminated the hydrolysis effects. This electrolyte formula is stable enough to support the high-voltage cathode, $Co_{0.247}V_2O_5{\cdot}0.944H_2O$, in which a voltage of 1.7 V is obtained.[136] A similar electrolyte, 21 M LiTFSI and 0.5 M $ZnSO_4$, was used in a $Zn/LiMn_{0.8}Fe_{0.2}PO_4$ cell, allowing a high cut-off voltage of 2.35 V (**Figure 2.13a**).[137] Considering the high cost of organic salts, low cost inorganic salt-dominant electrolytes have been proposed, such as 30 M $ZnCl_2$ aqueous electrolyte.[138]

Another example is acetate-based concentrated electrolyte, composed of 1 M zinc acetate and 31 M potassium acetate.[138] The ultra-high concentration of salts successfully minimises water-splitting reactions and widens the ESW to 3.4 V (**Figure 2.13b**). This mild alkaline electrolyte brings a different mechanism of energy storage to the cathodes of Zn/MnO_2 cells, in which OH^- ions serve as charge carriers. The concentrated and 'water in salt' electrolytes confine the activity of water, but it is at the cost of reducing ionic conductivity. Expanding the ESW of dilute electrolytes is of realistic significance. Unlike confining free water with great amount of salts, adding antisolvent can induce strong interactions with water and therefore suppress water-induced H_2 generation and enhance electrolytes stability.[104] Surfactant additives, such as sodium dodecyl sulfate, can prevent water from splitting by building a dense hydrophobic barrier layer on electrode, which means more energy will be consumed when water molecules pass this layer.[139] Therefore, the evolution of hydrogen or oxygen should occur at a higher overpotential, and the ESW of electrolyte spans between −1.15 V and 1.4 V *vs* SHE.[139] Li et al. put forward a bi-cation electrolyte, composed of 1 M $Al(CF_3SO_3)_3$ and 1 M $Zn(CF_3SO_3)_2$, to increase the output voltage of Zn/MnO_2 cells and simultaneously expand the ESW of their electrolyte. They discovered a new phase formation during the first charge process in a bi-cation electrolyte, where the host material reacts with Al^{3+} from electrolyte and generates layered $Al_xMnO_2{\cdot}nH_2O$, leading to a higher discharge plateau at around 1.7 V. The presence of Al^{3+} also enhances the stability of its coordinated water molecules and supresses the hydrogen as well as oxygen evolution, widening the ESW to 1.9 V (**Figure 2.13c**).[140]

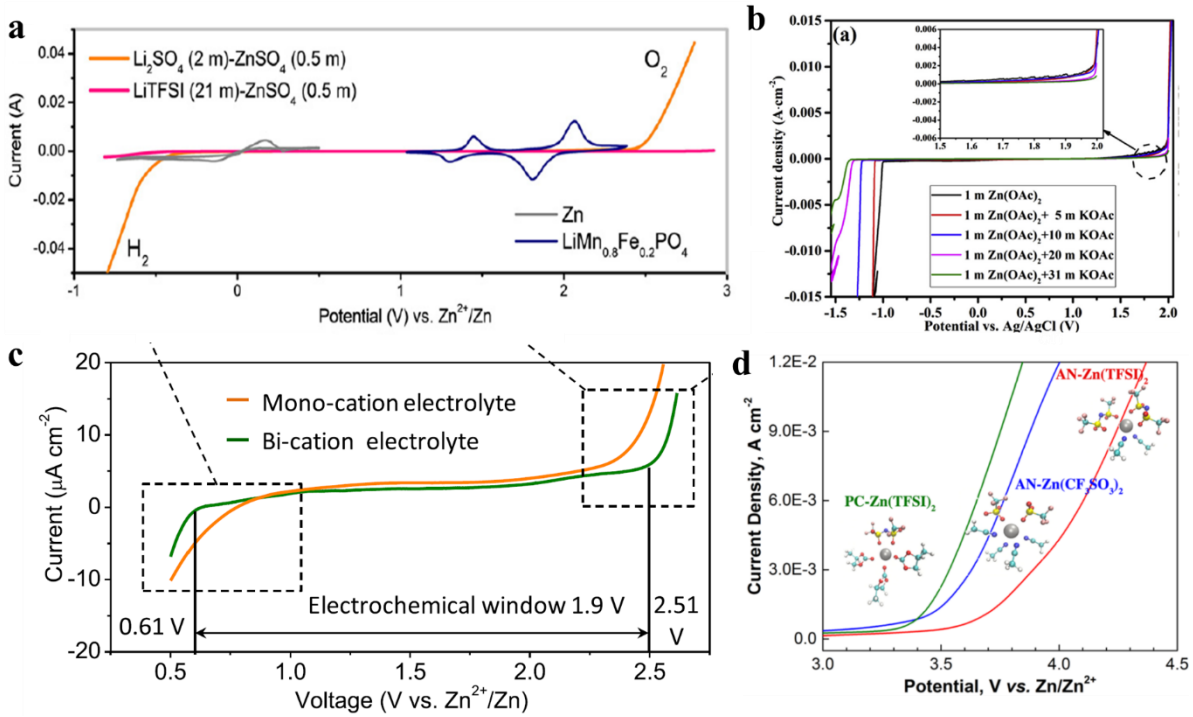

Figure 2.13. (**a**) CV curves of Zn and $LiMn_{0.8}Fe_{0.2}PO_4$ in electrolyte containing LiTFSI (21 M) and $ZnSO_4$ (0.5 M); the ESW of the LiTFSI-$ZnSO_4$ electrolyte and Li_2SO_4-$ZnSO_4$ electrolyte;[137] Reproduced with permission. Copyright 2016, Elsevier. (**b**) ESW of acetate-based concentrated electrolytes;[138] Reproduced with permission. Copyright 2019, John Wiley and Sons. (**c**) The ESW of bication and mono-cation electrolytes.;[140] Reproduced with permission. Copyright 2020, American Chemical Society.(**d**) LSV curves of 0.5 M AN-$Zn(TFSI)_2$, AN-$Zn(CF_3SO_3)_2$, and PC-$Zn(TFSI)_2$ electrolytes.[141] Reproduced with permission. Copyright 2016, American Chemical Society.

Unlike aqueous electrolytes limited by the proton/hydroxyl electrolytic decomposition, the nonaqueous electrolytes are able to bear a wide operating window of more than 3V. Burrell et al. analysed the oxidation behaviours of various salts and organic chemicals, and found that acetonitrile shows an outstandingly better stability than propylene carbonate, N,N-dimethylformamide or diglyme. The electrolyte, 0.5 M $Zn(TFSI)_2$ dissolved in acetonitrile, shows a wide ESW up to 3.7 V *vs* Zn/Zn^{2+} (**Figure 2.13d**).[141] Inspired by the result, a nonaqueous electrolyte, 0.3 M solution of $Zn(CF_3SO_3)_2$ in acetonitrile, was applied to a $Zn/ZnAl_xCo_{2-x}O_4$ battery, ensuring a high-voltage output of around 1.7 V.[142] N,N-dimethylformamide also proved to be feasible as solvent in a Zn/phenanthrenequinone

macrocyclic trimer (PQ-MCT) battery,[143] whose anodic stability extends to about 2.5 V *vs* Zn/Zn^{2+}.

To develop a wide ESW electrolyte for ZIBs, some strategies, including increasing salt concentration, adding functional additives/solvents and using nonaqueous solvents, have been put forward and achieved some improvements. However, it should be noted that the value of ZIBs is determined by low cost, high safety, environmental-friendliness and excellent kinetic properties. Taking this into consideration, it is hard to say this issue has been addressed successfully. The concentrated and 'water in salt' electrolytes are too expensive to be applied in real applications. Besides, their high viscosity and reduced ionic conductivity also damage the performance of batteries at high current densities. The use of nonaqueous solvents, generally harmful and flammable organic chemicals, sacrifice the safety and environment-friendliness principles. What is more, these materials also induce compatibility issues between nonaqueous electrolytes and cathode materials, such as low capacity and slow rate capability. Nazar et al. noticed that the interfacial charge transfer in nonaqueous electrolyte is very sluggish because high desolvation energy is required for Zn^{2+} to escape its solvation shell.[144] Adding additives into dilute electrolytes could suppress water decomposition, but any improvements are limited, failing to support high-voltage cathode materials.

2.2.5 Extending operating temperature adaptability

For ZIBs that operate in grid-scale energy storage systems, there are huge challenges resulting from weather changes, load and temperature fluctuations. The traditional aqueous electrolytes cannot work at sub-zero temperature due to the high freezing point of water and their low ionic conductivity at low temperatures. On the other hand, the side reactions between the electrodes and the electrolyte become more serious at high temperatures, leading to rapid battery performance decay as well as gas-generation issues. Therefore, extending the operating temperature adaptability of electrolytes is of great importance for the practical application of ZIBs.

The high freezing point of water comes from the unique intermolecular H-O···H hydrogen bonds (HBs).[145, 146, 147] When water transform into ice below 0 ℃, there is 0.52 extra HB per H_2O molecule.[95] By introducing HB acceptors into aqueous electrolytes, the freezing point of the electrolytes can be reduced.[148, 149, 150] The mechanism utilizes the competition between the intermolecular HBs of water to water and the strong electrostatic interactions of these HB acceptors to water. The HBs between H_2O molecules can thus be weakened, and the electrolyte

solvation structure can thus be modulated. Aqueous electrolytes with HB acceptors exhibit low freezing points, enhanced ionic conductivity, and reduced viscosity at low temperature, therefore improved battery performance at sub-zero temperatures. The Zn^{2+} and anions in salt-concentrated electrolytes can be simply used as HB acceptors to break some HBs between H_2O molecules. The strong dipole-dipole force between Zn^{2+} and O atoms of water leads to solvation structural rearrangement in the electrolytes, and thus promotes the binding of O atoms with Zn^{2+} rather than with H atoms of water. For example, Chen et al. studied the relationship between the concentration of $ZnCl_2$ and the freezing point (solid-liquid transition temperature, T_t) of aqueous electrolyte, and found that T_t reduced with the increase in $ZnCl_2$ concentration and reached lowest level of −114 ℃ at 7.5 M.[95] The 7.5 M $ZnCl_2$ electrolyte exhibited a high ionic conductivity of 1.79 mS cm^{-1} at −60 ℃, and remained liquid even at −70 ℃ (**Figure 2.14a**).[95] The ZIBs using the 7.5 M $ZnCl_2$ electrolyte delivered an impressive lifespan of 2000 cycles with a capacity retention of ~100% at 0.2 A g^{-1} (**Figure 2.14b**). A 1.15 Ah pouch cell with stacked multilayers can power light emitting diodes (**Figure 2.14c**) and can retain a high capacity of 0.50 Ah at –70 °C.[95] Furthermore, it was pointed out that F atoms of salt anions had higher electronegativity compared with N and O, and can easily form HBs with the O atoms of water (O-H···F), which can significantly influence the original HB network of water and render an ultralow freezing point for the electrolyte.[148] 4 M $Zn(BF_4)_2$ aqueous solution was used as an electrolyte, and achieved a freezing point of −122 ℃ and a high ionic conductivity of 1.47 mS cm^{-1} at −70 ℃.[148] It was proved that each BF_4^- anion can form weak HBs with up to three H_2O molecules, and thus disrupt their ordinary HB network.[148]

In addition to the application in aqueous electrolytes, concentrated salts are also useful HB acceptors in hydrogel electrolytes. One related approach is to introduce cooperatively hydrated cations. In previous work conducted by Zhu et al., 2 M $ZnSO_4$ and 4 M LiCl were dissolved in a PAM based hydrogel.[151] It was found that the cooperative cation hydration significantly dissociated the HBs between water molecules (**Figure 2.14d**). The designed electrolyte delivered satisfactory electrochemical performance at −20 ℃ when tested in Zn/$LiFePO_4$ hybrid cells. Due to the highly solubility of $ZnCl_2$ salt, $ZnCl_2$ is the most commonly-used salt in the high concentration anti-freezing hydrogel electrolytes. Wang et al. obtained a hydrogel electrolyte at low temperature of −40 ℃ by simply increasing the $ZnCl_2$ concentration to 4 M in a xanthan gum polymer gel.[152] Zhou et al. further reduced the salt concentration (2 M $ZnSO_4$ and 0.1 M $MnSO_4$) and developed a GG/SA/EG hydrogel electrolyte.[153] In the resultant hydrogel, the EG formed stable molecular clusters with H_2O molecules that compete with

water-water HBs , which decreases the vapor pressure of water and reduced the electrolyte freezing point. The cross-linked GG-SA network gave a flexible mechanical characteristic (**Figure 2.14e**).[153]

Besides, organic solvents, such as DMSO,[154, 155] Et_2O, EG,[98, 156] and oligomer poly(ethylene glycol) dimethyl ether (PEGDME),[157] can be also used as additives to regulate aqueous electrolyte solvation structure and widen the operating temperature range of ZIBs. In this regard, Wu et al. added 20% DMSO into aqueous electrolyte, which participated in the solvation of Zn^{2+} and broke HBs between water molecules (**Figure 2.14f-g**), thus enabling a stable cycling in Zn/MnO_2 battery at –20 °C.[155] PEGDME was introduced into aqueous as a competitive solvent,[157] and it indicated that PEGDME could re-construct HBs with water and take part in the solvation of Zn^{2+}. Therefore, both HBs of water and the water/Zn^{2+} interactions have been weakened, and the ionic conductivity at low temperature has been improved, which could help to suppress Zn dendrite growth. Benefiting the re-constructed solvation structure, the side reaction between the electrolyte and electrodes has also been alleviated even at high temperature (65 ℃) (**Figure 2.14h**).[157] Similarly, adding organic components into hydrogel electrolytes is an effective approach to decrease their freezing point. In this regards, 'vicinal' is used to describe the structure of a compound in which the two groups are bonded to neighbouring carbons. Meanwhile, an alcohol "ol" group can compete with water molecules for hydrogen bonds, thus, preventing the formation of intermolecular HBs between water molecules.[158, 159] As a result, an aqueous electrolyte in polymer gel networks with added "ol" groups can maintain liquid state even at subzero temperatures. One of the most-used vicinal alcohols is EG, known for its environmental friendliness. To obtain anti-freeze hydrogel electrolyte while maintaining flexibility, Zhi et al. reported a novel EG-based waterborne anionic polyurethane acrylate (EG-waPUA)/PAM electrolyte.[160] The strong HBs with water in the EG-WAPUA and PAM matrix can inhibit water-water interactions and hence inhibit ice crystallization. The obtained EG-waPUA/PAM hydrogel electrolyte shows a high ionic conductivity at −20 ℃. Other researchers also applied EG in different hydrogel electrolytes, including PAM/GO/EG[161] and guar gum (GG)/sodium alginate (SA)/EG electrolytes,[162] wherein similar results were also observed.

Relacing water with organic solvents in electrolytes is also other strategy to extend the temperature adaptability of ZIBs. For instance, a DMF-based electrolyte remained liquid and worked well even at –70 °C. Because of its enhanced stability with electrodes, it was shown to support battery functioning even at 150 °C (**Figure 2.14i**).[143] Apart from liquid electrolytes

with full organic solvents, full polymer electrolytes are also promising. For example, Zhi et al. developed a solid polymer electrolyte based on poly(vinylidene fluoride-co-hexafluoropropylene) filled by the poly(methyl acrylate) grafted MXenes (denoted as PVHF/MXene-g-PMA).[163] In the electrolyte, there were abundant F-H HBs between PVHF and PMA, and homogeneous dispersion of MXenes was achieved from the intriguing interaction between the highly grafted PMA and PVHF matrix. The electrolyte functioned well across a temperature range of −35 ℃ to +100 ℃.

In brief, various HB accepters, including Zn salts, anions, and organic solvents, have been introduced into aqueous and hydrogel electrolytes to reduce the electrolyte freezing point and enable sub-zero temperature ZIBs. Despite these advances, the capacities and rate performances of ZIBs at low temperature are still unsatisfactory, as summarized in **Table 2.1**. To improve this, the electrolyte recipes and SEI structures should be further optimized and the ionic conductivity at low temperature should be enhanced. In addition, to achieve high energy density, the area capacity of cathodes and the electrolyte amounts should be further controlled in low temperature tests, because these aspects are not mentioned in most of the published results. Besides the aforementioned considerations, the cycling stability and gas-generation issues in aqueous or aqueous-based electrolytes at high temperature have not been fully explored and should be carefully considered in future studies. Furthermore, polymer electrolytes for ZIBs have mostly been focused on low-temperature (anti-freezing) performance. Test batteries have normally been tested at −35 ^{o}C or higher temperatures, and low current densities (see **Table 2.1**), suggesting the mass transfer kinetics in these electrolytes is still poor. Similar to the studies involving liquid electrolytes, the studies about high temperature performance are fairly sparse. In addition, to guarantee appropriate volumetric energy density, the thickness of polymer electrolytes should be quantified and adequately controlled.

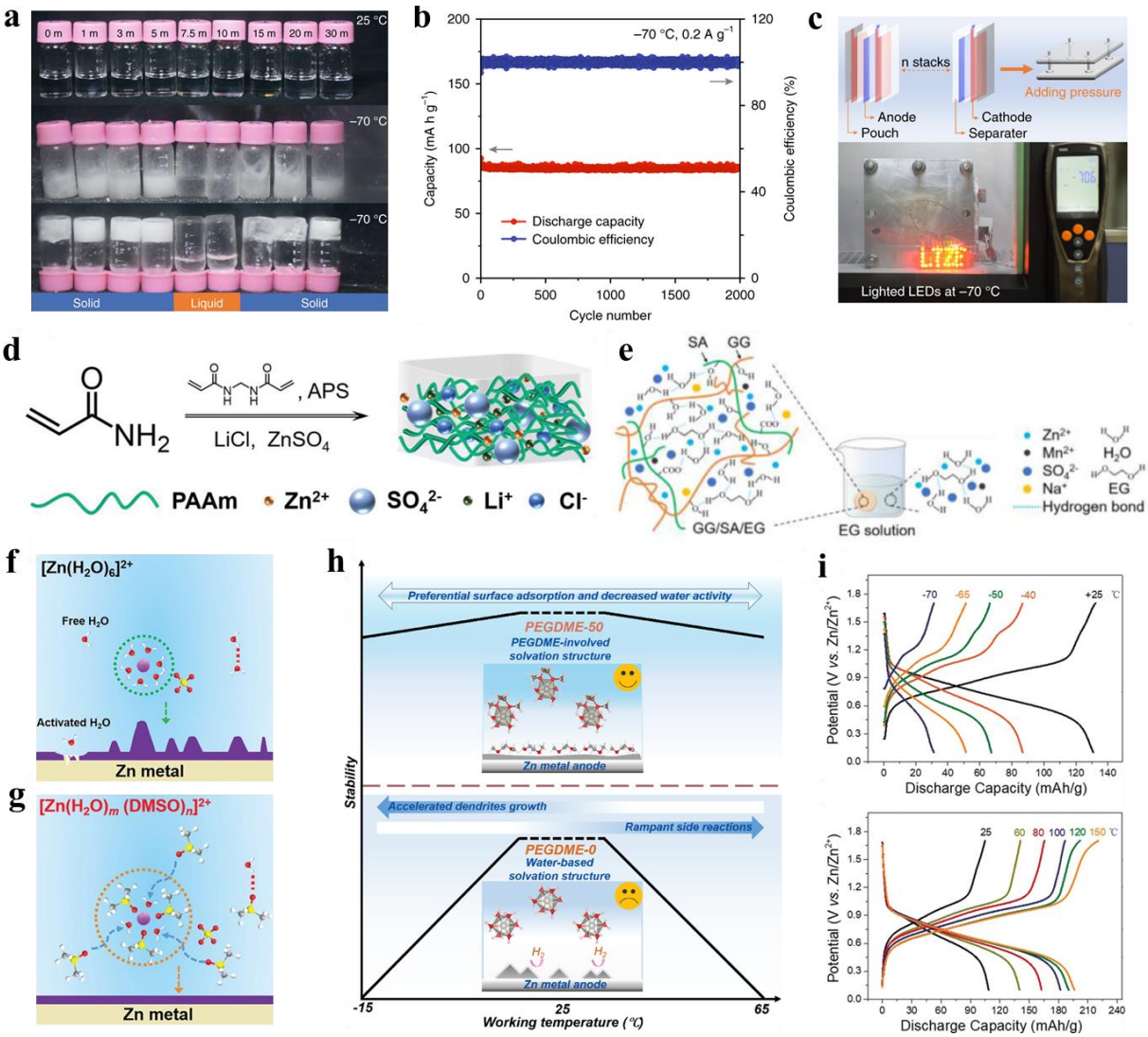

Figure 2.14. Extending the operating temperature adaptability of liquid electrolytes. (**a**) Optical photographs of the electrolytes with different $ZnCl_2$ concentrations at 25 and −70 °C, (**b**) Cycling performance of polyaniline batteries at –70 °C and 0.2 A g^{-1}, and (**c**) Schematic of assembled pouch cell used to light LEDs by two series-wound cells at –70 °C.[95] Reproduced with permission. Copyright 2020, Springer Nature. Schematic illustration of synthesis of the PAM based hydrogel (**d**),[151] (Reproduced with permission, Copyright 2020, John Wiley and Sons), and the structure of GG/SA/EG hydrogel electrolytes (**e**).[153] Reproduced with permission. Copyright 2020, Elsevier. Conceptual diagrams of Zn^{2+} solvation structure evolution in aqueous electrolyte (**f**) and DMSO hybrid electrolytes (**g**).[155] Reproduced with permission. Copyright 2021, John Wiley and Sons. (**h**) Illustration of thermal instability of Zn metal anodes in PEGDME-0 (without PEGDME) and highly improved stability in PEGDME-50 (50% PEGDME).[157] Reproduced with permission. Copyright 2021, Elsevier. (**i**)

Temperature-dependent investigation of a Zn/phenanthrenequinone macrocyclic trimer rechargeable battery.[143] Reproduced with permission. Copyright 2020, John Wiley and Sons.

Table 2.1. Summary of electrolyte engineering towards wide-temperature range ZIBs.

Electrolyte	Electrolyte components	Anode/Cathode	Low temperature	Cycles/capacity retention	High temperature	Cycles/capacity retention	Ref.
Liquid	4 M $Zn(BF_4)_2$ aqueous solution	Zn/Tetrachlorobenzoquinone/Zn	−30 ℃	1000/94% at 1 C	/	/	148
	7.5 M $ZnCl_2$ aqueous solution	Zn/Polyaniline	−70 ℃	2000/~100% at 0.2 A g^{-1}	/	/	95
	2 M $ZnSO_4$ + 0.2 M $MnSO_4$ aqueous solution + 1% Et_2O and 30% EG	Zn/MnO_2	−10 ℃	500/~77% at 3 A g^{-1}	25 ℃	500/88.3% at 3 A g^{-1}	156
	2 M $ZnSO_4$/H_2O-DMSO	Zn/MnO_2	−20 ℃	300/~63% at 1 C	RT	3000/~100% at 10 C	155
	1 M $Zn(CF_3SO_3)_2$ aqueous solution + PEGDME competitive solvent	Zn/V_2O_5	−15 ℃	450/~50% at 0.1 A g^{-1}	50 ℃	200/32% at 0.1 A g^{-1}	157

	0.5 M ZnTFMS in DMF	Zn/Phenanthrenequinone macrocyclic trimer	−70 ℃	/	150 ℃	/	143
Hydrogel/ polymer	3 M $Zn(CF_3SO_3)_2$ PAM hydrogel	Zn/$Mg_{0.1}V_2O_5·H_2O$/	−30 ℃	100/~110% at 0.2 A g^{-1}	60 ℃	100/~100% at 0.2 A g^{-1}	164
	PAM hydrogel with 2 M $ZnSO_4$ and 4 M LiCl solution	Zn/$LiFePO_4$	−20 ℃	500/~95% at 0.2 A g^{-1}	/	/	151
	Polyzwitterionic hydrogel electrolyte with 2 M $ZnSO_4$	Zn/MnO_2	−20 ℃	/	RT	600/~95% at 1.5 A g^{-1}	165
	5.5 M $ZnCl_2$ + PAAM hydrogel	Zn/MnO_2	/	/	50 ℃	100/~10% at 12 mA cm^{-2}	166
	PVA/glycerol gel with 2 M $ZnSO_4$ and 0.2 M $MnSO_4$	Zn/MnO_2	−35 ℃	2000/~95% at 1 A g^{-1}	25 ℃	2000/95% at 1 A g^{-1}	167
	PAM/GO/EG gel	Zn/MnO_2	−20 ℃	1000/~62.5% at 1 A g^{-1}	20 ℃	1000/~80.6% at 1 A g^{-1}	161

	EG-waPUA/PAM gel electrolyte	Zn/MnO_2	−20 ℃	600/~64% at 0.2 A g^{-1}	20 ℃	600/~80% at 0.2 A g^{-1}	160
	4 M $ZnCl_2$ + xanthan gum	Zn/$NH_4V_3O_8$·1·9 H_2O	−20 ℃	1500/~72% at 1 A g^{-1}	/	/	168
	12 M $ZnCl_2$ + xanthan gum electrolyte	Zn/$NH_4V_3O_8$·1.9 H_2O	−20 ℃	450/~128% at 0.5 A g^{-1}	20 ℃	800/~74% at 1.5 A g^{-1}	152
	PEG/bacterial cellulose electrolyte	Zn/$LiFePO_4$	−20 ℃	300/~100% at 85m A g^{-1}	/	/	169
	PVHF/MXene-g-PMA	Zn/Manganese hexacyanoferrate	−35 ℃	/	100 ℃	/	163

2.2.6 Summary

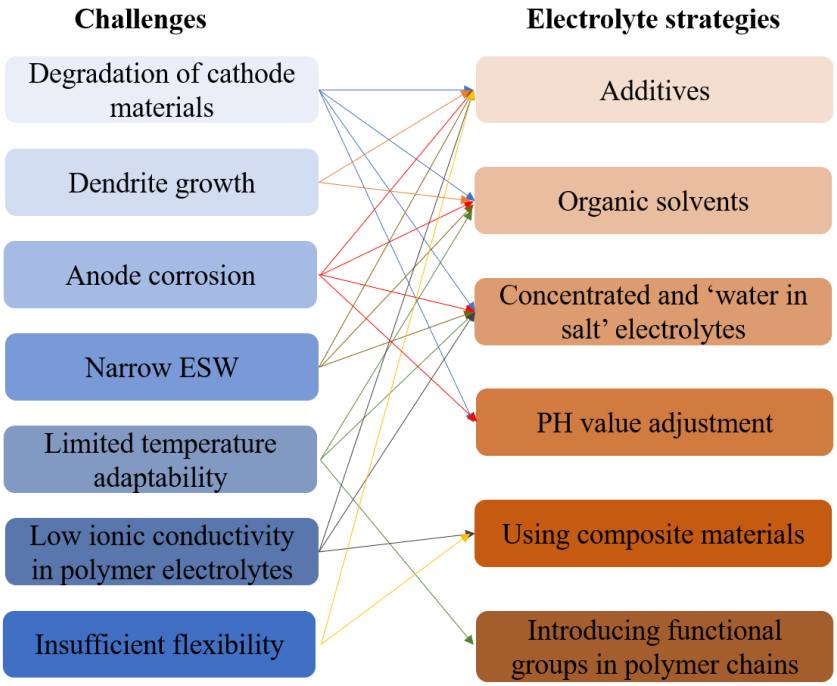

Figure 2.15 The challenges and associated strategies for electrolytes of ZIBs.

We have discussed the main challenges that ZIBs are facing and the corresponding solutions in terms of electrolytes, which is summarized in **Figure 2.15** ZIBs are the most alternatives for lithium ion batteries for grid-scale energy storage, therefore, good temperature adaptability and excellent electrochemical stability are the essential consideration in designing electrolytes for ZIBs. Organic, aqueous-organic hybrid or concentrated electrolytes have been reported so far to meet the requirements. Their temperature adaptability is based on eliminating or breaking HBs, while their functions in enhancing reversibility of Zn anode relies on solvation structure manipulation. Organic components are aprotic and their side reactions with Zn metal are minimal, while concentrated electrolytes could supress the activity of water but significantly increase the viscosity and the cost of electrolyte.

ZIBs are also proposed as the candidate power for portable devices, in which the energy density of ZIBs becomes incredibly important. To cope with high-voltage cathode materials, electrolyte strategies such as adding additives, using organic solvents and high concentrated electrolytes should be taken to mitigate O_2/H_2 evolution reactions and therefore ensure a sufficient ESW. Additives work by adsorbing on the surface of electrode to increase the overpotential of O_2/H_2 evolution, however, their effect on preventing water splitting are far

from enough, especially considering that a high cut-off voltage at around 2.4 V is required. Benefiting from the aprotic nature of non-aqueous electrolytes and the low water activity in ‘water in salt’ electrolytes, organic or “water in salt” electrolyte could be used for high-voltage cathodes. However, the high cost of ‘water in salt’ electrolytes make it almost impossible for ZIBs to replace lithium ion batteries. Non-aqueous electrolytes suffer from high desolvation penalty and high charge-transfer impedance, which restrain the cathode materials from delivering their full capacity. Reducing the cost of concentrated electrolytes and increasing the compatibility between organic solvent and cathode materials are the remaining challenges for further research.

2.2.7 Reference

1. Armand M, *et al*. Building better batteries. *Nature* **451**, 652-657 (2008).
2. Yoshino A. The Birth of the Lithium-Ion Battery. *Angewandte Chemie International Edition* **51**, 5798-5800 (2012).
3. Arbabzadeh M, *et al*. The role of energy storage in deep decarbonization of electricity production. *Nature Communications* **10**, 3413 (2019).
4. Zeng X, *et al*. Recent progress and perspectives on aqueous Zn-based rechargeable batteries with mild aqueous electrolytes. *Energy Storage Materials* **20**, 410-437 (2019).
5. Gielen D, *et al*. The role of renewable energy in the global energy transformation. *Energy Strategy Reviews* **24**, 38-50 (2019).
6. Zhao J, *et al*. Hybrid and Aqueous Li+–Ni Metal Batteries. *CCS Chemistry* **3**, 2498-2508 (2021).
7. Wang Z, *et al*. Construction of a Unique Two-Dimensional Hierarchical Carbon Architecture for Superior Lithium-Ion Storage. *ACS Applied Materials & Interfaces* **8**, 33399-33404 (2016).
8. Huang C, *et al*. Achieving high initial coulombic efficiency and low voltage dropping in Li-rich Mn-based cathode materials by Metal-Organic frameworks-derived coating. *Journal of Power Sources* **499**, 229967 (2021).
9. Li Q, *et al*. Progress in electrolytes for rechargeable Li-based batteries and beyond. *Green Energy & Environment* **1**, 18-42 (2016).
10. Palacín MR. Recent advances in rechargeable battery materials: a chemist's perspective. *Chemical Society Reviews* **38**, 2565-2575 (2009).
11. Yang T, *et al*. A General Strategy for Antimony-Based Alloy Nanocomposite Embedded in Swiss-Cheese-Like Nitrogen-Doped Porous Carbon for Energy Storage. *Advanced Functional Materials* **31**, 2009433 (2021).
12. Yu X, *et al*. A dual-carbon-anchoring strategy to fabricate flexible LiMn2O4 cathode for advanced lithium-ion batteries with high areal capacity. *Nano Energy* **67**, 104256 (2020).

13. Deng J, *et al.* Co–B Nanoflakes as Multifunctional Bridges in ZnCo2O4 Micro-/Nanospheres for Superior Lithium Storage with Boosted Kinetics and Stability. *Advanced Energy Materials* **9**, 1803612 (2019).

14. Swain B. Cost effective recovery of lithium from lithium ion battery by reverse osmosis and precipitation: a perspective. *Journal of Chemical Technology & Biotechnology* **93**, 311-319 (2018).

15. Jo C-H, *et al*. Efficient recycling of valuable resources from discarded lithium-ion batteries. *Journal of Power Sources* **426**, 259-265 (2019).

16. Pinegar H, *et al*. Recycling of End-of-Life Lithium Ion Batteries, Part I: Commercial Processes. *Journal of Sustainable Metallurgy* **5**, 402-416 (2019).

17. Zhang W, *et al.* Architecting Amorphous Vanadium Oxide/MXene Nanohybrid via Tunable Anodic Oxidation for High-Performance Sodium-Ion Batteries. *Advanced Energy Materials* **11**, 2100757 (2021).

18. Yang F, *et al*. Phosphorus-Based Materials as the Anode for Sodium-Ion Batteries. *Small Methods* **1**, 1700216 (2017).

19. Yang F, *et al.* Ultrathin Few-Layer GeP Nanosheets via Lithiation-Assisted Chemical Exfoliation and Their Application in Sodium Storage. *Advanced Energy Materials* **10**, 1903826 (2020).

20. Lei Y-J, *et al.* Tailoring MXene-Based Materials for Sodium-Ion Storage: Synthesis, Mechanisms, and Applications. *Electrochemical Energy Reviews* **3**, 766-792 (2020).

21. Liu S, *et al.* An Intrinsically Non-flammable Electrolyte for High-Performance Potassium Batteries. *Angewandte Chemie International Edition* **59**, 3638-3644 (2020).

22. Zhang Q, *et al.* Structural Insight into Layer Gliding and Lattice Distortion in Layered Manganese Oxide Electrodes for Potassium-Ion Batteries. *Advanced Energy Materials* **9**, 1900568 (2019).

23. Zhang Q, *et al*. Cathode Materials for Potassium-Ion Batteries: Current Status and Perspective. *Electrochemical Energy Reviews* **1**, 625-658 (2018).

24. Liu S, *et al.* Tuning the Electrolyte Solvation Structure to Suppress Cathode Dissolution, Water Reactivity, and Zn Dendrite Growth in Zinc-Ion Batteries. *Advanced Functional Materials* **31**, 2104281 (2021).

25. Guo Z, *et al.* Horizontally Arranged Zinc Platelet Electrodeposits Modulated by Fluorinated Covalent Organic Framework Film for High-Rate and Durable Aqueous Zinc Ion Batteries. (2021).

26. Hao J, *et al*. Deeply understanding the Zn anode behaviour and corresponding improvement strategies in different aqueous Zn-based batteries. *Energy & Environmental Science* **13**, 3917-3949 (2020).

27. Zhang T, *et al.* Fundamentals and perspectives in developing zinc-ion battery electrolytes: a comprehensive review. *Energy & Environmental Science* **13**, 4625-4665 (2020).

28. Huang S, *et al*. Recent Progress in the Electrolytes of Aqueous Zinc-Ion Batteries. *Chemistry – A European Journal* **25**, 14480-14494 (2019).

29. Liu C, *et al*. Electrolyte Strategies toward Better Zinc-Ion Batteries. *ACS Energy Letters* **6**, 1015-1033 (2021).

30. Yamamoto T, *et al*. Rechargeable Zn|ZnSO4|MnO2-type cells. *Inorganica Chimica Acta* **117**, L27-L28 (1986).

31. Xu C, *et al*. Energetic Zinc Ion Chemistry: The Rechargeable Zinc Ion Battery. *Angewandte Chemie International Edition* **51**, 933-935 (2012).

32. Wang Y, *et al.* Spherical Li Deposited inside 3D Cu Skeleton as Anode with Ultrastable Performance. *ACS Applied Materials & Interfaces* **10**, 20244-20249 (2018).

33. Wang Z, *et al.* Building Artificial Solid-Electrolyte Interphase with Uniform Intermolecular Ionic Bonds toward Dendrite-Free Lithium Metal Anodes. *Advanced Functional Materials* **30**, 2002414 (2020).

34. Wang Y, *et al.* Lithium Metal Electrode with Increased Air Stability and Robust Solid Electrolyte Interphase Realized by Silane Coupling Agent Modification. *Advanced Materials* **33**, 2008133 (2021).

35. Wang Z, *et al*. Constructing nitrided interfaces for stabilizing Li metal electrodes in liquid electrolytes. *Chemical Science* **12**, 8945-8966 (2021).

36. Yuan L, *et al.* Regulation methods for the Zn/electrolyte interphase and the effectiveness evaluation in aqueous Zn-ion batteries. *Energy & Environmental Science*, (2021).

37. Fang G, *et al*. Recent Advances in Aqueous Zinc-Ion Batteries. *ACS Energy Letters* **3**, 2480-2501 (2018).

38. Blanc LE, *et al*. Scientific Challenges for the Implementation of Zn-Ion Batteries. *Joule* **4**, 771-799 (2020).

39. Ming J, *et al*. Zinc-ion batteries: Materials, mechanisms, and applications. *Materials Science and Engineering: R: Reports* **135**, 58-84 (2019).

40. Xiong T, *et al*. Defect Engineering in Manganese-Based Oxides for Aqueous Rechargeable Zinc-Ion Batteries: A Review. *Advanced Energy Materials* **10**, 2001769 (2020).

41. Bešter-Rogač M. Electrical Conductivity of Concentrated Aqueous Solutions of Divalent Metal Sulfates. *Journal of Chemical & Engineering Data* **53**, 1355-1359 (2008).

42. Zhang N, *et al.* Cation-Deficient Spinel ZnMn2O4 Cathode in Zn(CF3SO3)2 Electrolyte for Rechargeable Aqueous Zn-Ion Battery. *Journal of the American Chemical Society* **138**, 12894-12901 (2016).

43. Zhang H, *et al*. Challenges and Strategies for High-Energy Aqueous Electrolyte Rechargeable Batteries. *Angewandte Chemie International Edition* **60**, 598-616 (2021).

44. Wu K, *et al.* Recent Advances in Polymer Electrolytes for Zinc Ion Batteries: Mechanisms, Properties, and Perspectives. *Advanced Energy Materials* **10**, 1903977 (2020).

45. Liu Y, *et al*. Review of vanadium-based electrode materials for rechargeable aqueous zinc ion batteries. *Journal of Energy Chemistry* **56**, 223-237 (2021).

46. Tang B, *et al.* Structural Modification of V2O5 as High-Performance Aqueous Zinc-Ion Battery Cathode. *Journal of The Electrochemical Society* **166**, A480-A486 (2019).

47. Zuo S, *et al*. Cathodes for Aqueous Zn-Ion Batteries: Materials, Mechanisms, and Kinetics. *Chemistry – A European Journal* **27**, 830-860 (2021).

48. Park MJ, *et al*. Multivalent-Ion versus Proton Insertion into Battery Electrodes. *ACS Energy Letters* **5**, 2367-2375 (2020).

49. Huang J-Q, *et al*. Hybrid Aqueous/Organic Electrolytes Enable the High-Performance Zn-Ion Batteries. *Research* **2019**, 2635310 (2019).

50. Senguttuvan P, *et al.* A High Power Rechargeable Nonaqueous Multivalent Zn/V 2 O 5 Battery. *Advanced Energy Materials* **6**, 1600826 (2016).

51. Lu Y, *et al*. A High Performing Zn-Ion Battery Cathode Enabled by In Situ Transformation of V2O5 Atomic Layers. *Angewandte Chemie International Edition* **59**, 17004-17011 (2020).

52. Liu X, *et al*. Operando pH Measurements Decipher H+/Zn2+ Intercalation Chemistry in High-Performance Aqueous Zn/δ-V2O5 Batteries. *ACS Energy Letters* **5**, 2979-2986 (2020).

53. Zhou J, *et al*. Investigation of V2O5 as a low-cost rechargeable aqueous zinc ion battery cathode. *Chemical Communications* **54**, 4457-4460 (2018).

54. Wan F, *et al.* Reversible Oxygen Redox Chemistry in Aqueous Zinc-Ion Batteries. *Angewandte Chemie International Edition* **58**, 7062-7067 (2019).

55. Wang F, *et al.* How Water Accelerates Bivalent Ion Diffusion at the Electrolyte/Electrode Interface. *Angewandte Chemie International Edition* **57**, 11978-11981 (2018).

56. Yang M, *et al.* Boosting the zinc ion storage capacity and cycling stability of interlayer-expanded vanadium disulfide through in-situ electrochemical oxidation strategy. *Journal of Colloid and Interface Science* **607**, 68-75 (2022).

57. Zhao X, *et al*. Dual-cation preintercalated and amorphous carbon confined vanadium oxides as a superior cathode for aqueous zinc-ion batteries. *Carbon* **186**, 160-170 (2022).

58. Hu K, *et al.* Metallic vanadium trioxide intercalated with phase transformation for advanced aqueous zinc-ion batteries. *Journal of Energy Chemistry* **61**, 594-601 (2021).

59. Zhang W, *et al.* Application of Manganese-Based Materials in Aqueous Rechargeable Zinc-Ion Batteries. *Frontiers in Energy Research* **8**, (2020).

60. Lee B, *et al*. Elucidating the intercalation mechanism of zinc ions into α-MnO2 for rechargeable zinc batteries. *Chemical Communications* **51**, 9265-9268 (2015).

61. Sun W, *et al.* Zn/MnO2 Battery Chemistry With H+ and Zn2+ Coinsertion. *Journal of the American Chemical Society* **139**, 9775-9778 (2017).

62. Pan H, *et al.* Reversible aqueous zinc/manganese oxide energy storage from conversion reactions. *Nature Energy* **1**, 16039 (2016).

63. Li M, *et al.* A Novel Dendrite-Free Mn2+/Zn2+ Hybrid Battery with 2.3 V Voltage Window and 11000-Cycle Lifespan. *Advanced Energy Materials* **9**, 1901469 (2019).

64. Lee B, *et al.* Critical Role of pH Evolution of Electrolyte in the Reaction Mechanism for Rechargeable Zinc Batteries. *ChemSusChem* **9**, 2948-2956 (2016).

65. Lee B, *et al*. Electrochemically-induced reversible transition from the tunneled to layered polymorphs of manganese dioxide. *Scientific Reports* **4**, 6066 (2014).

66. Guo S, *et al.* Fundamentals and perspectives of electrolyte additives for aqueous zinc-ion batteries. *Energy Storage Materials* **34**, 545-562 (2021).

67. Kim SH, *et al*. Degradation mechanism of layered MnO2 cathodes in Zn/ZnSO4/MnO2 rechargeable cells. *Journal of Power Sources* **72**, 150-158 (1998).

68. Zhang N, *et al.* Rechargeable aqueous zinc-manganese dioxide batteries with high energy and power densities. *Nature Communications* **8**, 405 (2017).

69. Qiu C, *et al.* The function of Mn2+ additive in aqueous electrolyte for Zn/δ-MnO2 battery. *Electrochimica Acta* **351**, 136445 (2020).

70. Soundharrajan V, *et al.* The dominant role of Mn2+ additive on the electrochemical reaction in ZnMn2O4 cathode for aqueous zinc-ion batteries. *Energy Storage Materials* **28**, 407-417 (2020).

71. Guo S, *et al*. Cathode Interfacial Layer Formation via in Situ Electrochemically Charging in Aqueous Zinc-Ion Battery. *ACS Nano* **13**, 13456-13464 (2019).

72. Chao D, *et al.* An Electrolytic Zn–MnO2 Battery for High-Voltage and Scalable Energy Storage. *Angewandte Chemie International Edition* **58**, 7823-7828 (2019).

73. Zhong C, *et al.* Decoupling electrolytes towards stable and high-energy rechargeable aqueous zinc–manganese dioxide batteries. *Nature Energy* **5**, 440-449 (2020).

74. Zeng X, *et al.* Toward a Reversible Mn4+/Mn2+ Redox Reaction and Dendrite-Free Zn Anode in Near-Neutral Aqueous Zn/MnO2 Batteries via Salt Anion Chemistry. *Advanced Energy Materials* **10**, 1904163 (2020).

75. Lei J, *et al*. Towards high-areal-capacity aqueous zinc–manganese batteries: promoting MnO2 dissolution by redox mediators. *Energy & Environmental Science* **14**, 4418-4426 (2021).

76. Guo X, *et al*. Zn/MnO2 battery chemistry with dissolution-deposition mechanism. *Materials Today Energy* **16**, 100396 (2020).

77. Hao J, *et al.* Toward High-Performance Hybrid Zn-Based Batteries via Deeply Understanding Their Mechanism and Using Electrolyte Additive. *Advanced Functional Materials* **29**, 1903605 (2019).

78. Peng J, *et al.* Defect-free-induced Na+ disordering in electrode materials. *Energy & Environmental Science* **14**, 3130-3140 (2021).

79. Zhang L, *et al*. Towards High-Voltage Aqueous Metal-Ion Batteries Beyond 1.5 V: The Zinc/Zinc Hexacyanoferrate System. *Advanced Energy Materials* **5**, 1400930 (2015).

80. Trócoli R, *et al*. An Aqueous Zinc-Ion Battery Based on Copper Hexacyanoferrate. *ChemSusChem* **8**, 481-485 (2015).

81. Ma L, *et al.* Achieving High-Voltage and High-Capacity Aqueous Rechargeable Zinc Ion Battery by Incorporating Two-Species Redox Reaction. *Advanced Energy Materials* **9**, 1902446 (2019).

82. Pu X, *et al.* High-Performance Aqueous Zinc-Ion Batteries Realized by MOF Materials. *Nano-Micro Letters* **12**, 152 (2020).

83. Zhou Y, *et al.* Oxide-based cathode materials for rechargeable zinc ion batteries: Progresses and challenges. *Journal of Energy Chemistry* **57**, 516-542 (2021).

84. Ma L, *et al.* Initiating a mild aqueous electrolyte Co3O4/Zn battery with 2.2 V-high voltage and 5000-cycle lifespan by a Co(iii) rich-electrode. *Energy & Environmental Science* **11**, 2521-2530 (2018).

85. He P, *et al.* Layered VS2 Nanosheet-Based Aqueous Zn Ion Battery Cathode. *Advanced Energy Materials* **7**, 1601920 (2017).

86. Xu S, *et al*. Recent progress in organic electrodes for zinc-ion batteries. *Journal of Semiconductors* **41**, 091704 (2020).

87. Wang F, *et al.* Highly reversible zinc metal anode for aqueous batteries. *Nature Materials* **17**, 543-549 (2018).

88. Zhang Q, *et al.* Designing Anion-Type Water-Free Zn2+ Solvation Structure for Robust Zn Metal Anode. *Angewandte Chemie International Edition* **60**, 23357-23364 (2021).

89. Li H, *et al*. Ultrahigh-Capacity and Fire-Resistant LiFePO4-Based Composite Cathodes for Advanced Lithium-Ion Batteries. *Advanced Energy Materials* **9**, 1802930 (2019).

90. Liu K, *et al.* Lithium Metal Anodes with an Adaptive "Solid-Liquid" Interfacial Protective Layer. *Journal of the American Chemical Society* **139**, 4815-4820 (2017).

91. Bian Y, *et al.* Using an AlCl3/Urea Ionic Liquid Analog Electrolyte for Improving the Lifetime of Aluminum-Sulfur Batteries. *ChemElectroChem* **5**, 3607-3611 (2018).

92. Chang W-C, *et al*. Solution Synthesis of Iodine-Doped Red Phosphorus Nanoparticles for Lithium-Ion Battery Anodes. *Nano Letters* **17**, 1240-1247 (2017).

93. Lu W, *et al*. Inhibition of Zinc Dendrite Growth in Zinc-Based Batteries. *ChemSusChem* **11**, 3996-4006 (2018).

94. Patil N, *et al*. An Ultrahigh Performance Zinc-Organic Battery using Poly(catechol) Cathode in Zn(TFSI)2-Based Concentrated Aqueous Electrolytes. *Advanced Energy Materials* **11**, 2100939 (2021).

95. Zhang Q, *et al.* Modulating electrolyte structure for ultralow temperature aqueous zinc batteries. *Nature Communications* **11**, 4463 (2020).

96. Cao L, *et al.* Solvation Structure Design for Aqueous Zn Metal Batteries. *Journal of the American Chemical Society* **142**, 21404-21409 (2020).

97. Kao-ian W, *et al.* Highly stable rechargeable zinc-ion battery using dimethyl sulfoxide electrolyte. *Materials Today Energy* **21**, 100738 (2021).

98. Chang N, *et al.* An aqueous hybrid electrolyte for low-temperature zinc-based energy storage devices. *Energy & Environmental Science* **13**, 3527-3535 (2020).

99. Qin R, *et al.* Tuning Zn2+ coordination environment to suppress dendrite formation for high-performance Zn-ion batteries. *Nano Energy* **80**, 105478 (2021).

100. Naveed A, *et al*. Highly Reversible and Rechargeable Safe Zn Batteries Based on a Triethyl Phosphate Electrolyte. *Angewandte Chemie International Edition* **58**, 2760-2764 (2019).

101. Dong Y, *et al.* Non-concentrated aqueous electrolytes with organic solvent additives for stable zinc batteries. *Chemical Science* **12**, 5843-5852 (2021).

102. Cui J, *et al.* Improved electrochemical reversibility of Zn plating/stripping: a promising approach to suppress water-induced issues through the formation of H-bonding. *Materials Today Energy* **18**, 100563 (2020).

103. Zhang Y, *et al.* An in-depth insight of a highly reversible and dendrite-free Zn metal anode in an hybrid electrolyte. *Journal of Materials Chemistry A* **9**, 4253-4261 (2021).

104. Hao J, *et al.* Boosting Zinc Electrode Reversibility in Aqueous Electrolytes by Using Low-Cost Antisolvents. *Angewandte Chemie International Edition* **60**, 7366-7375 (2021).

105. Qian L, *et al.* Cations Coordination-Regulated Reversibility Enhancement for Aqueous Zn-Ion Battery. *Advanced Functional Materials* **31**, 2105736 (2021).

106. Sun P, *et al.* Simultaneous Regulation on Solvation Shell and Electrode Interface for Dendrite-Free Zn Ion Batteries Achieved by a Low-Cost Glucose Additive. *Angewandte Chemie International Edition* **60**, 18247-18255 (2021).

107. Wang P, *et al.* Mechanistic Insights of Mg2+-Electrolyte Additive for High-Energy and Long-Life Zinc-Ion Hybrid Capacitors. *Advanced Energy Materials* **11**, 2101158 (2021).

108. Yang W, *et al.* Hydrated Eutectic Electrolytes with Ligand-Oriented Solvation Shells for Long-Cycling Zinc-Organic Batteries. *Joule* **4**, 1557-1574 (2020).

109. Qiu H, *et al.* Zinc anode-compatible in-situ solid electrolyte interphase via cation solvation modulation. *Nature Communications* **10**, 5374 (2019).

110. Cao L, *et al.* Highly Reversible Aqueous Zinc Batteries enabled by Zincophilic–Zincophobic Interfacial Layers and Interrupted Hydrogen-Bond Electrolytes. *Angewandte Chemie International Edition* **60**, 18845-18851 (2021).

111. Li D, *et al*. Design of a Solid Electrolyte Interphase for Aqueous Zn Batteries. *Angewandte Chemie International Edition* **60**, 13035-13041 (2021).

112. Ma L, *et al.* Functionalized Phosphonium Cations Enable Zinc Metal Reversibility in Aqueous Electrolytes. *Angewandte Chemie International Edition* **60**, 12438-12445 (2021).

113. Cao L, *et al.* Fluorinated interphase enables reversible aqueous zinc battery chemistries. *Nature Nanotechnology* **16**, 902-910 (2021).

114. Chu Y, *et al*. In situ built interphase with high interface energy and fast kinetics for high performance Zn metal anodes. *Energy & Environmental Science* **14**, 3609-3620 (2021).

115. Wang L, *et al.* A Zn(ClO4)2 Electrolyte Enabling Long-Life Zinc Metal Electrodes for Rechargeable Aqueous Zinc Batteries. *ACS Applied Materials & Interfaces* **11**, 42000-42005 (2019).

116. Guo X, *et al.* Alleviation of Dendrite Formation on Zinc Anodes via Electrolyte Additives. *ACS Energy Letters* **6**, 395-403 (2021).

117. Zeng X, *et al.* Electrolyte Design for In Situ Construction of Highly Zn2+-Conductive Solid Electrolyte Interphase to Enable High-Performance Aqueous Zn-Ion Batteries under Practical Conditions. *Advanced Materials* **33**, 2007416 (2021).

118. Zeng X, *et al.* Bio-inspired design of an in situ multifunctional polymeric solid–electrolyte interphase for Zn metal anode cycling at 30 mA cm−2 and 30 mA h cm−2. *Energy & Environmental Science*, (2021).

119. Zhang S-J, *et al.* Dual-Function Electrolyte Additive for Highly Reversible Zn Anode. *Advanced Energy Materials* **11**, 2102010 (2021).

120. Zhang Q, *et al.* The Three-Dimensional Dendrite-Free Zinc Anode on a Copper Mesh with a Zinc-Oriented Polyacrylamide Electrolyte Additive. *Angewandte Chemie International Edition* **58**, 15841-15847 (2019).

121. Jin Y, *et al.* Stabilizing Zinc Anode Reactions by Polyethylene Oxide Polymer in Mild Aqueous Electrolytes. *Advanced Functional Materials* **30**, 2003932 (2020).

122. Sun C, *et al*. Interface Engineering via Ti3C2Tx MXene Electrolyte Additive toward Dendrite-Free Zinc Deposition. *Nano-Micro Letters* **13**, 89 (2021).

123. Banik SJ, *et al*. Suppressing Dendrite Growth during Zinc Electrodeposition by PEG-200 Additive. *Journal of The Electrochemical Society* **160**, D519-D523 (2013).

124. Xu Y, *et al.* A rechargeable aqueous zinc/sodium manganese oxides battery with robust performance enabled by Na2SO4 electrolyte additive. *Energy Storage Materials* **38**, 299-308 (2021).

125. Li T, *et al*. Fluorinated Solid-Electrolyte Interphase in High-Voltage Lithium Metal Batteries. *Joule* **3**, 2647-2661 (2019).

126. Bayaguud A, *et al*. Cationic Surfactant-Type Electrolyte Additive Enables Three-Dimensional Dendrite-Free Zinc Anode for Stable Zinc-Ion Batteries. *ACS Energy Letters* **5**, 3012-3020 (2020).

127. Xu W, *et al.* Diethyl ether as self-healing electrolyte additive enabled long-life rechargeable aqueous zinc ion batteries. *Nano Energy* **62**, 275-281 (2019).

128. Otani T, *et al*. Effect of lead and tin additives on surface morphology evolution of electrodeposited zinc. *Electrochimica Acta* **242**, 364-372 (2017).

129. Abdulla J, *et al.* Elimination of Zinc Dendrites by Graphene Oxide Electrolyte Additive for Zinc-Ion Batteries. *ACS Applied Energy Materials* **4**, 4602-4609 (2021).

130. Sun KEK, *et al.* Suppression of Dendrite Formation and Corrosion on Zinc Anode of Secondary Aqueous Batteries. *ACS Applied Materials & Interfaces* **9**, 9681-9687 (2017).

131. Bani Hashemi A, *et al*. The effect of polyethyleneimine as an electrolyte additive on zinc electrodeposition mechanism in aqueous zinc-ion batteries. *Electrochimica Acta* **258**, 703-708 (2017).

132. Chae MS, *et al*. Organic electrolyte-based rechargeable zinc-ion batteries using potassium nickel hexacyanoferrate as a cathode material. *Journal of Power Sources* **337**, 204-211 (2017).

133. Peng Z, *et al.* Novel layered iron vanadate cathode for high-capacity aqueous rechargeable zinc batteries. *Chemical Communications* **54**, 4041-4044 (2018).

134. Li W, *et al.* Rechargeable Lithium Batteries with Aqueous Electrolytes. *Science* **264**, 1115-1118 (1994).

135. Suo L, *et al.* "Water-in-salt" electrolyte enables high-voltage aqueous lithium-ion chemistries. *Science* **350**, 938-943 (2015).

136. Ma L, *et al.* Achieving Both High Voltage and High Capacity in Aqueous Zinc-Ion Battery for Record High Energy Density. *Advanced Functional Materials* **29**, 1906142 (2019).

137. Zhao J, *et al.* High-voltage Zn/LiMn0.8Fe0.2PO4 aqueous rechargeable battery by virtue of "water-in-salt" electrolyte. *Electrochemistry Communications* **69**, 6-10 (2016).

138. Zhang L, *et al.* ZnCl2 “Water-in-Salt” Electrolyte Transforms the Performance of Vanadium Oxide as a Zn Battery Cathode. *Advanced Functional Materials* **29**, 1902653 (2019).

139. Hou Z, *et al*. Surfactant widens the electrochemical window of an aqueous electrolyte for better rechargeable aqueous sodium/zinc battery. *Journal of Materials Chemistry A* **5**, 730-738 (2017).

140. Li N, *et al.* Bi-Cation Electrolyte for a 1.7 V Aqueous Zn Ion Battery. *ACS Applied Materials & Interfaces* **12**, 13790-13796 (2020).

141. Han S-D, *et al.* Origin of Electrochemical, Structural, and Transport Properties in Nonaqueous Zinc Electrolytes. *ACS Applied Materials & Interfaces* **8**, 3021-3031 (2016).

142. Pan C, *et al*. ZnAlxCo2–xO4 Spinels as Cathode Materials for Non-Aqueous Zn Batteries with an Open Circuit Voltage of ≤2 V. *Chemistry of Materials* **29**, 9351-9359 (2017).

143. Wang N, *et al.* Zinc–Organic Battery with a Wide Operation-Temperature Window from −70 to 150 °C. *Angewandte Chemie International Edition* **59**, 14577-14583 (2020).

144. Kundu D, *et al*. Aqueous vs. nonaqueous Zn-ion batteries: consequences of the desolvation penalty at the interface. *Energy & Environmental Science* **11**, 881-892 (2018).

145. Matsumoto M, *et al*. Molecular dynamics simulation of the ice nucleation and growth process leading to water freezing. *Nature* **416**, 409-413 (2002).

146. Yannacone SF, *et al*. Quantitative assessment of intramolecular hydrogen bonds in neutral histidine. *Theoretical Chemistry Accounts* **139**, 125 (2020).

147. Salazar-Cano J-R, *et al*. Hydrogen bonds in methane–water clusters. *Physical Chemistry Chemical Physics* **18**, 23508-23515 (2016).

148. Sun T, *et al.* An ultralow-temperature aqueous zinc-ion battery. *Journal of Materials Chemistry A* **9**, 7042-7047 (2021).

149. Sun T, *et al*. Synergistic Effect of Cation and Anion for Low-Temperature Aqueous Zinc-Ion Battery. *Nano-Micro Letters* **13**, 204 (2021).

150. Nian Q, *et al.* Designing Electrolyte Structure to Suppress Hydrogen Evolution Reaction in Aqueous Batteries. *ACS Energy Letters* **6**, 2174-2180 (2021).

151. Zhu M, *et al.* Antifreezing Hydrogel with High Zinc Reversibility for Flexible and Durable Aqueous Batteries by Cooperative Hydrated Cations. *Advanced Functional Materials* **30**, 1907218 (2020).

152. Chen Y, *et al*. Quasi-Solid-State Zinc Ion Rechargeable Batteries for Subzero Temperature Applications. *ACS Applied Energy Materials* **3**, 9058-9065 (2020).

153. Wang J, *et al.* Flexible and anti-freezing zinc-ion batteries using a guar-gum/sodium-alginate/ethylene-glycol hydrogel electrolyte. *Energy Storage Materials* **41**, 599-605 (2021).

154. Nian Q, *et al.* Aqueous Batteries Operated at −50 °C. *Angewandte Chemie International Edition* **58**, 16994-16999 (2019).

155. Feng D, *et al*. Immunizing Aqueous Zn Batteries against Dendrite Formation and Side Reactions at Various Temperatures via Electrolyte Additives. *Small* **17**, 2103195 (2021).

156. Wang A, *et al*. Developing improved electrolytes for aqueous zinc-ion batteries to achieve excellent cyclability and antifreezing ability. *Journal of Colloid and Interface Science* **586**, 362-370 (2021).

157. Hou Z, *et al*. Realizing wide-temperature Zn metal anodes through concurrent interface stability regulation and solvation structure modulation. *Energy Storage Materials* **42**, 517-525 (2021).

158. Stehle S, *et al*. Hydrogen Bond Networks in Binary Mixtures of Water and Organic Solvents. *The Journal of Physical Chemistry B* **123**, 4425-4433 (2019).

159. Nagy PI. Competing Intramolecular vs. Intermolecular Hydrogen Bonds in Solution. *International Journal of Molecular Sciences* **15**, (2014).

160. Mo F, *et al.* A flexible rechargeable aqueous zinc manganese-dioxide battery working at −20 °C. *Energy & Environmental Science* **12**, 706-715 (2019).

161. Quan Y, *et al*. High-Performance Anti-freezing Flexible Zn-MnO2 Battery Based on Polyacrylamide/Graphene Oxide/Ethylene Glycol Gel Electrolyte. *Frontiers in Chemistry* **8**, (2020).

162. Zhang X, *et al.* Remarkable capacitive performance in novel tungsten bronze ceramics. *Dalton Transactions* **50**, 124-130 (2021).

163. Chen Z, *et al.* Grafted MXene/polymer electrolyte for high performance solid zinc batteries with enhanced shelf life at low/high temperatures. *Energy & Environmental Science* **14**, 3492-3501 (2021).

164. Deng W, *et al.* High-Capacity Layered Magnesium Vanadate with Concentrated Gel Electrolyte toward High-Performance and Wide-Temperature Zinc-Ion Battery. *ACS Nano* **14**, 15776-15785 (2020).

165. Leng K, *et al.* A Safe Polyzwitterionic Hydrogel Electrolyte for Long-Life Quasi-Solid State Zinc Metal Batteries. *Advanced Functional Materials* **30**, 2001317 (2020).

166. Yang P, *et al.* Thermal Self-Protection of Zinc-Ion Batteries Enabled by Smart Hygroscopic Hydrogel Electrolytes. *Advanced Energy Materials* **10**, 2002898 (2020).

167. Chen M, *et al.* Anti-freezing flexible aqueous Zn–MnO2 batteries working at −35 °C enabled by a borax-crosslinked polyvinyl alcohol/glycerol gel electrolyte. *Journal of Materials Chemistry A* **8**, 6828-6841 (2020).

168. Wang Y, *et al*. A flexible zinc-ion battery based on the optimized concentrated hydrogel electrolyte for enhanced performance at subzero temperature. *Electrochimica Acta* **395**, 139178 (2021).

169. Yan C, *et al*. Hygroscopic Double-Layer Gel Polymer Electrolyte toward High-Performance Low-Temperature Zinc Hybrid Batteries. *Batteries & Supercaps* **4**, 1627-1635 (2021).

Chapter 3 Lithium metal electrode with increased air stability and robust solid electrolyte interphase realized by silane coupling agent modification

This chapter includes work published in the journal *Adv. Mater*. 2021, 33, 2008133. It proposes to use a silane coupling agent as an adhesion promoter to address the adhesion problem between the SEI layer and the Li metal anode, and as a protection layer to avoid the Li metal from air corrosion. This design provides a promising pathway for the development of Li metal electrodes that will be stable both in electrolytes and in air.

Statement of Authorship

Title of Paper	Lithium Metal Electrode with Increased Air Stability and Robust Solid Electrolyte Interphase Realized by Silane Coupling Agent Modification.
Publication Status	☑ Published ☐ Accepted for Publication ☐ Submitted for Publication ☐ Unpublished and Unsubmitted w ork w ritten in manuscript style
Publication Details	Yanyan Wang, Zhijie Wang, Liang Zhao, Qining Fan, Xiaohui Zeng, Sailin Liu, Wei Kong Pang, Yan-Bing He, Zaiping Guo. Lithium Metal Electrode with Increased Air Stability and Robust Solid Electrolyte Interphase Realized by Silane Coupling Agent Modification. Adv. Mater. 2021, 33, 2008133.

Principal Author

Name of Principal Author (Candidate)	Yanyan Wang
Contribution to the Paper	Devised the idea, performed experiments, analyzed and interpreted data, wrote and revised the manuscript.
Overall percentage (%)	70%
Certification:	This paper reports on original research I conducted during the period of my Higher Degree by Research candidature and is not subject to any obligations or contractual agreements with a third party that would constrain its inclusion in this thesis. I am the primary author of this paper.
Signature	Date: 10 / Mar. /2023

Co-Author Contributions

By signing the Statement of Authorship, each author certifies that:

i. the candidate's stated contribution to the publication is accurate (as detailed above);

ii. permission is granted for the candidate in include the publication in the thesis; and

iii. the sum of all co-author contributions is equal to 100% less the candidate's stated contribution.

Name of Co-Author	Zhijie Wang
Contribution to the Paper	Guided to design of the whole experiment, helped with data analysis, and revised the manuscript.
Signature	Date: 08/ Mar. /2023

Name of Co-Author	Liang Zhao
Contribution to the Paper	Assisted in performing characterization on samples with the atomic force microscope.
Signature	Date: 10/03/2023

Name of Co-Author	Qining Fan		
Contribution to the Paper	Assisted in sulfur electrode fabrication.		
Signature		Date	2023-Mar-14

Name of Co-Author	Xiaohui Zeng		
Contribution to the Paper	Discussed the TOF-SIMS data.		
Signature		Date	14/03/2023

Name of Co-Author	Sailin Liu		
Contribution to the Paper	Discussed and revised the manuscript.		
Signature		Date	10/03/2023

Name of Co-Author	Wei Kong Pang		
Contribution to the Paper	Helped to conduct fourier transform infrared (FTIR) spectroscopy on Samples.		
Signature		Date	15 Mar 2023

Name of Co-Author	Yan-Bing He		
Contribution to the Paper	Supervised development of work, helped in data interpretation and manuscript evaluation.		
Signature		Date	16 Mar 2023

Name of Co-Author	Zaiping Guo		
Contribution to the Paper	Supervised development of work, discussed the whole design, revised and conceptualized the manuscript.		
Signature		Date	10/03/2023

3.1 Introduction and significance

Li metal is widely regarded as an ideal anode material for next-generation batteries because of its ultra-high theoretical specific capacity (3860 mAh g^{-1}) and low redox potential (−3.04 V vs. standard hydrogen electrode).[1, 2, 3, 4] The commercial promotion of Li metal based batteries are greatly hindered, however, by Li metal's intrinsic shortcomings.[5] Li metal is themodynamically unstable with non-aqueous solvent and therefore, continuous chemical reactions occur until the Li metal surface is passivated by a solid electrolyte interphase (SEI) layer. This layer is mechanically unstable under the large interfacial fluctuations during Li plating/stripping processes, and it cracks and reforms continuously, consuming both the Li anode and the electrolyte.[6] What is worse, Li dendrites, the main hidden danger of Li metal based batteries, are prone to grow from cracks in the SEI layer.[7] It has been observed by *operando* scanning transmission electron microscopy that the SEI layer is damaged during interfacial fluctuations and finally exfoliated, leaving an exposed electrode surface in the electrolyte.[8] The SEI layer exfoliation can be attributed to poor chemical adhesion between the SEI layer and the Li substrate. Obviously, a stable and robust SEI layer is the decisive factor for safe, dendrite-free, and long-lifespan Li metal based batteries. To optimize the SEI layer, researchers developed functional additives,[9,10] novel solvents,[11,12] and high concentration electrolytes[13] to adjust its composition and structure *in situ*. Reinforcement of the SEI layer was also realized by *ex-situ* coated protective layers, such as Nafion,[14] hexagonal boron nitride (h-BN), [15,16] LiF,[17] and Li_3PO_4.[18] Although various strategies have been proposed, these research efforts have been mainly focused on the properties of the SEI layer itself, while attention has hardly been paid to the bonding between the SEI layer and the Li metal substrate.

Besides the serious challenges in the electrochemistry, how to increase the air stability of Li metal and thereby simplify operation conditions is another significant challenge. Li metal is immediately corroded by oxygen, carbon dioxide, and moisture when exposed to air, forming electronically insulating products such as Li_2O, Li_2CO_3 and LiOH,[19] which will greatly degrade the electrochemical activity of the Li metal electrode. To increase the air tolerance of Li metal, various methods have been proposed to fabricate isolation layers. Polymers or composite materials, such as poly(tetramethylene ether glycol) (PTMEG)-Li/Sn,[20] wax-poly(ethylene oxide) (PEO),[21] polyvinylidene fluoride (PVDF)-hexafluoropropylene (HFP),[22] paraffin wax,[23] poly(methyl methacrylate) (PMMA),[24] polyphosphoric ester (PPE)-Li_3PO_4,[25] and $(Li_2O)_m(Al_2O_3)_n$-LiF[26] were coated on Li metal via solution methods, and the derived modified layers were usually on the micron-meter scale, sacrificing both actual volumetric and

gravimetric energy densities of Li metal electrodes. Nanoscale modification layers, such as h-BN,[27] ZrO_2,[28] and Al,[29] are usually fabricated by chemical vapor deposition, atomic-layer deposition, or magnetron sputtering, which are costly and unsuitable for large-scale industrial processes.

To solve these challenges, herein, we design a facile but feasible way to realize both SEI layer reinforcement and enhanced air stability via modifying the Li metal with 3-methacryloxypropyltrimethoxysilane (MPS), an inexpensive silane coupling agent. By immersing commercial Li foil in an MPS containing solution, MPS molecules are grafted spontaneously to the surface of the Li foil and assembled into a thin and dense layer, denoted as the MPS layer. This layer firmly adheres to the Li metal surface by forming covalent bonds (Li-O-Si), and it connects with the SEI layer by chemical bonds and physical intertwining effects. In this way, the Li metal and the SEI layer, two dissimilar materials can be well connected. With reinforced adhesion, the MPS modified Li metal foil (MPS-Li) exhibits excellent electrochemical performance. MPS-Li||MPS-Li symmetric cells shows excellent cycling stability for 1400 hours at a current density of 1 mA cm^{-2} and 600 hours at 3 mA cm^{-2} with a fixed capacity of 3 mAh cm^{-2}. Even with high cathode mass loading and limited electrolyte, an MPS-Li||$LiFePO_4$ full cell delivers a specific capacity of 122 mAh g^{-1} after 300 cycles at 1 C and an MPS-Li||S cell maintains a specific capacity of 652 mAh g^{-1} after 300 cycles at 0.2 C. Meanwhile, the dense MPS layer is able to prevent the Li metal from being corroded by air. The MPS-Li still maintains up to 88.1% of its theoretical capacity after exposure to air for 2 hours, and batteries with air-exposed MPS-Li foil as anode shows comparable electrochemical performance.

3.2 Experiments

Chemicals

3-methacryloxypropyltrimethoxysilane (MPS, 98%), anhydrous tetrahydrofuran (THF, 99.9%), Lithium nitrate ($LiNO_3$, >99%), bis(trifluoromethane)sulfonimide lithium salt (LiTFSI, 99.95%), 1,3-dioxolane (DOL, 99.8%), 1,2-dimethoxyethane (DME, 99.5%), ethylene carbonate (EC, 99%), diethyl carbonate (DEC, 99%), sulfur powder, carbon nanotube (CNT), polyvinylpyrrolidone (PVP), N-methyl-2-pyrrolidone (NMP), and polyvinylidene difluoride (PVDF) were purchased from Sigma-Aldrich. Li foil was purchased from China Energy Lithium Co., Ltd. and stored in an argon filled glove box with oxygen and moisture concentrations below 0.1 ppm. Lithium hexafluorophosphate ($LiPF_6$, 99.99%) was purchased

from Duoduo Chem Co., Ltd. MPS, THF, and DOL were used without any further purification. $LiNO_3$ was dried at 60 °C. and LiTFSI was vacuum-dried at 110 °C in a glove box. DME was dried with a molecular sieve for over 2 days. $LiFePO_4$ powder was purchased from Shenzhen Dynanonic Co., Ltd. CMK-3 was purchased from Nanjing XFNANO Materials Tech Co., Ltd..

MPS-Li fabrication

5% MPS/THF solution was prepared by thoroughly mixing MPS and THF in a volume ratio of 1:19. Li foil was totally immersed in 5% MPS/THF solution for 30 minutes. Upon removal from the solution, excess liquid was removed by dripping, and then followed by a heating process at 100 °C for 1 hour. The as-obtained sample was denoted as MPS-Li.

Characterization

The XRD measurements on pristine Li were conducted on GBC MMA diffractometer with Cu Kα radiation. To prevent oxidation, the Li metal foil was well sealed with a Kapton tape. The surface morphology of fresh and cycled MPS-Li/Li foils was observed with a JEOL JSM-7500FA field emission scanning electron microscope. XPS spectra were collected on a Thermo Scientific Nexsa X-Ray Photoelectron Spectrometer System. The depth profiles was obtained by etching the MPS-Li with a Ar^+ ion gun with energy of 3000 eV and a raster size of 2.00 mm. AFM characterization was conducted on a Bruker Dimension Icon instrument in an argon-filled glove box. The Time-of-Flight Secondary Ion Mass Spectrometer analysis was conducted on an ION-TOF TOF-SIM^5, and data for both the positive and negative polarities were collected with Bi_3^+ at 30 keV as the ion source. To identify the components of the SEI layer, 1 mAh of Li^+ was plated on MPS-Li and then stripped before TOF-SIMS analysis. Fourier-transform infrared spectra were obtained with a PerkinElmer Frontiers instrument with an attenuated total reflectance (ATR) attachment. EIS tests were conducted on VMP3 instruments. To obtain the cycled MPS-Li and Li anodes for SEM and XPS analysis, MPS-Li||MPS-Li and Li|| Li cells were cycled at a current density of 1 mA cm^{-2} with an areal capacity of 3 mAh cm^{-2} for 100 cycles.

Electrochemical Testing

To prepare LFP electrode, a slurry containing 80 wt% LFP, 10 wt% Super P, and 10 wt% PVDF in NMP solvent was casted on aluminium foil. The areal mass loading of LFP cathode was around 12 mg cm^{-2}. For S cathode, S powders and CMK-3 were well mixed in a weight ratio of 3:7 and heated at 155 °C for 12 hours to obtain CMK-3@S composite. A slurry containing 80 wt% CMK-3@S, 10 wt% CNT, and 10 wt% PVP in NMP solvent was well

mixed and loaded on carbon cloth. Afterward, the S electrode was vacuum dried at 55 °C for 12 h. The active material in the as obtained S electrode was around 3.6 mg cm^{-2}. CR2032-type coin cells were adopted for testing all electrochemical performances. 1 M LiTFSI in DOL/DME (1:1 by volume) with 2% $LiNO_3$ was used as ether electrolyte and 1 M $LiPF_6$ in EC/DEC (1:1 by volume) was used as carbonate ester electrolyte. The amount of electrolyte was controlled at 50 µl for the symmetric cells. The E/C ratio was limited to 3 µl mg^{-1} for Li||LFP and MPS-Li||LFP cells, and 15 µl mg^{-1} for Li||S and MPS-Li||S cells. Before galvanostatic long-term cycling, the Li||LFP and MPS-Li||LFP cells were activated at 0.1 C for 5 cycles, while the Li||S and MPS-Li||S cells were activated at 0.1 C for 2 cycles.

3.3 Reaction mechanism investigation

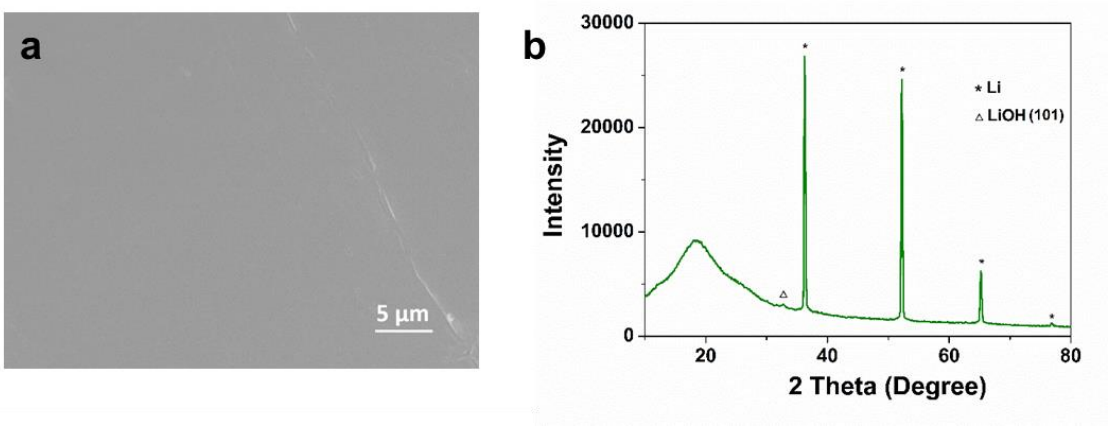

Figure 3.1 (a) Top-view SEM image of pristine Li metal foil; (b) XRD partten of fresh pristine Li metal foil.

MPS contains alkoxy groups (-OCH_3) and organic reactive group (-$COOC(CH_3)=CH_2$) on the two ends of the molecule, and it therefore shows good adhesion on metal surfaces and excellent compatibility in organics. The presence of LiOH is an essential prerequisite for the hydrolysis reaction of alkoxy groups, and it is found on the surface of pristine Li foil, as proved by its X-ray diffraction (XRD) pattern (**Figure 3.1**).

To graft MPS molecules onto the metal surface, commercial Li foil is immersed in 5% (vol%) MPS/tetrahydrofuran solution for 30 minutes, and the reaction between LiOH and the MPS molecule, which is displayed as Equation 1, occurs spontaneously. A heating process at 100 °C for 1 hour is then applied to promote the solidification of MPS layer. The thus-derived Li foil is denoted as MPS-Li.

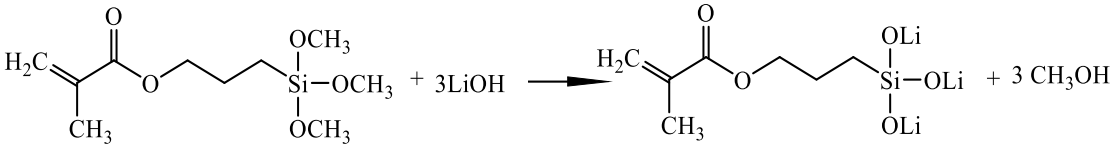

(1)

The surface morphology of MPS-Li foil was observed by scanning electron microscopy (SEM) and atomic force microscopy (AFM). As shown in Figure 1a, the surface of MPS-Li is as smooth as that of pristine Li (**Figure 3.2a**), and the AFM image (**Figure 3.2b**) further confirms that the modified layer covers the Li metal uniformly without obvious aggregates.

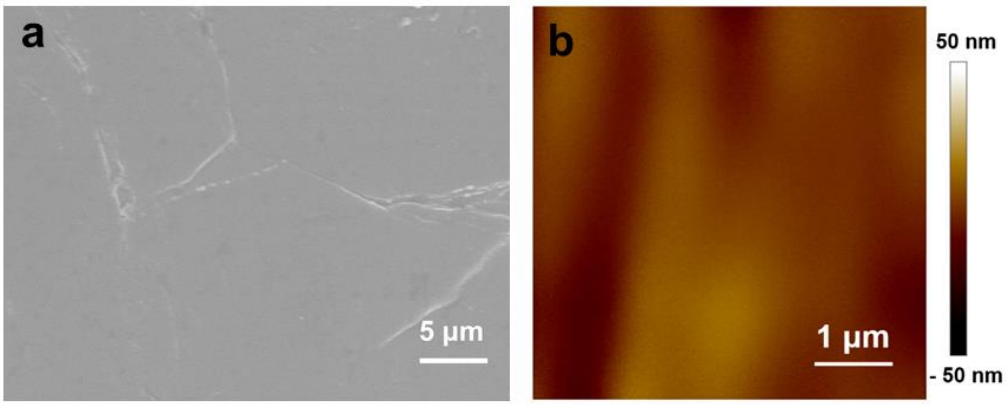

Figure 3.2 (a) Top-view SEM image of MPS-Li. (b) AFM morphology of MPS-Li.

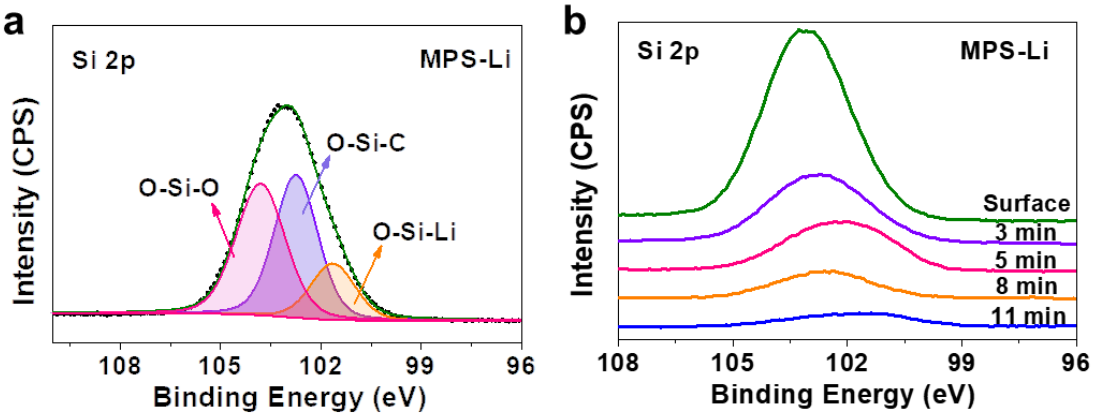

Figure 3.3 (a) XPS spectrum of Si 2p of MPS-Li; (b) XPS depth profiles of Si 2p for MPS-Li.

The Fourier transform infrared (FTIR) spectrum of MPS-Li (**Figure 3.4**) shows strong absorption bands of Si-O stretching vibrations at 1193 cm^{-1} and 1089 cm^{-1}, a C=O stretching vibrations band at 1728 cm^{-1}, and a Si-C stretching vibrations band at 819 cm^{-1}.

The X-ray photoelectron spectroscopy (XPS) spectrum in **Figure 3.3a** exhibits a strong peak for Si 2p, indicating that MPS molecules have been grafted onto the surface of the Li foil. The detailed peak interpretation is as follows: the peak at 103.8 eV is attributed to O-Si-O,[30] the one at 102.6 eV is attributed to O-Si-C, while the one at 101.6 eV is assigned to Li-O-Si.[31] XPS depth profiling of Si 2p was further conducted to investigate the thickness of the modified layer on MPS-Li. According to **Figure 3.3b**, the peak intensity of Si 2p decreases greatly after etching by Ar^+ ion beam for 3 minutes, and the signal disappears after etching for 11 minutes, indicating that the modified layer has a multimolecular structure and its thickness is around 320 nm.

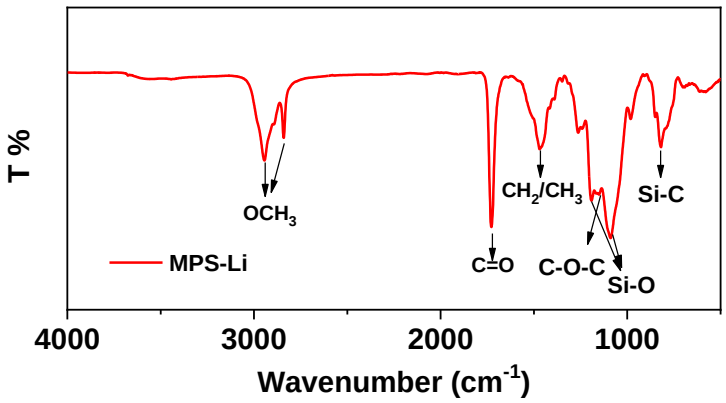

Figure 3.4 FTIR spectrum of MPS-Li.

To further investigate the bonds between the MPS layer and the Li metal substrate, time-of-flight secondary ion mass spectrometry (TOF-SIMS) was adopted to investigate the chemical components on fresh MPS-Li. As displayed in **Figure 3.5**, ion fragments of $Li\text{-}O\text{-}Si^+$, $CH_2CH_2CH_2\text{-}O^+$, $(LiO)_2Si^+$, and $(LiO)_3Si^+$ are detected at the mass-to-charge ratio (m/z)= 51, 74, and 97, respectively, from positive spectra of MPS-Li, illustrating that chemical bonds form between the MPS molecule and the Li metal substrate via Li-O-Si bonds. The organic part of MPS is also detected at m/z = 58 and m/z = 85 from its negative spectra, which are assigned to $COO\text{-}CH_2^-$ and $COO\text{-}C(CH_3)=CH_2^-$. A weak peak belonging to the $O\text{-}Si\text{-}O\text{-}Si\text{-}O^-$ is found from the negative spectra of MPS-Li at m/z = 104, indicating that a slight condensation among siloxanes occurred during heating the modified Li metal foil at 100 °C.

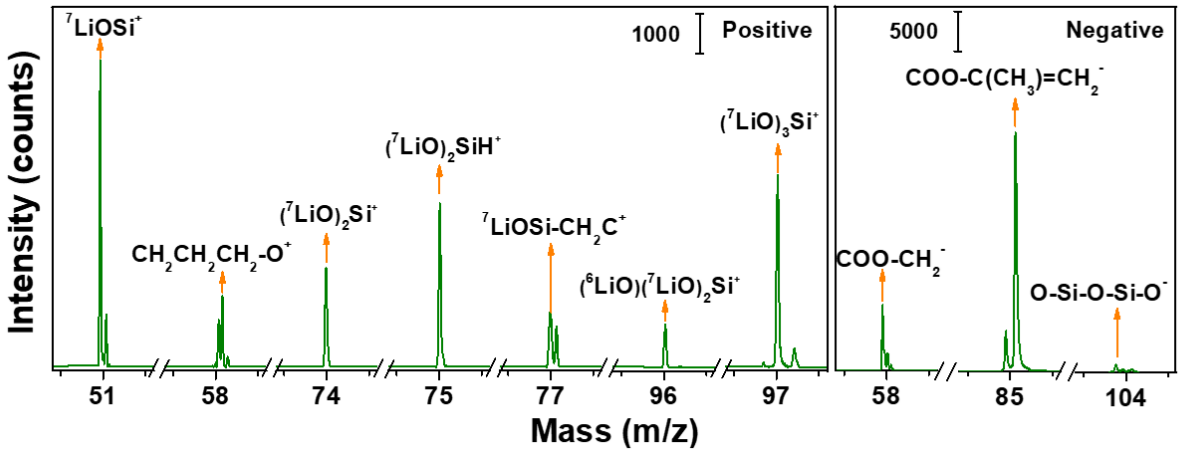

Figure 3.5 Selected TOF-SIMS ion spectra of fresh MPS-Li.

Based on the above comprehensive analysis, the structure of the MPS layer can be clearly determined, as shown in **Figure 3.6**. The MPS layer clearly adheres to Li metal substrate by forming firm Li-O-Si bonds instead of by weak adsorption. The condensation of siloxanes leads to a multimolecular structure with cross-linked O-Si-O-Si-O bonds. This cross-linked structure allows organic species to interpenetrate into the siloxane networks and thereby form electrostatic forces. The physical effect based on interpenetration and intertwining is a significant part of bonding mechanism and has been successfully applied to improve the adhesion of composite materials.[32]

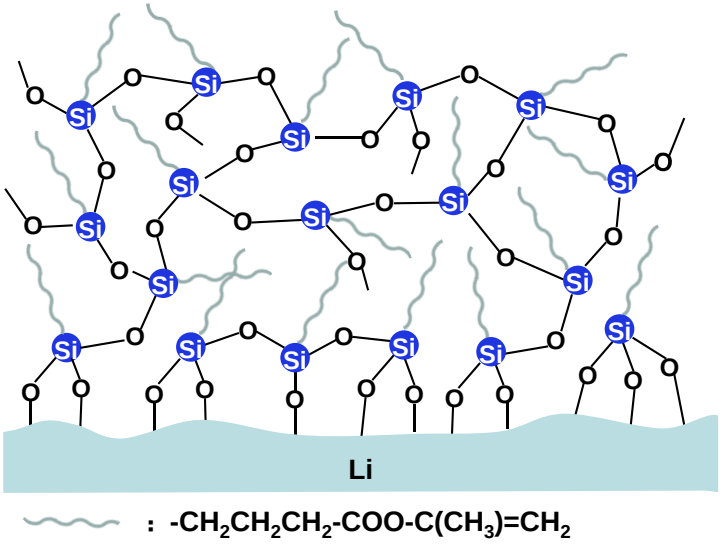

Figure 3.6 Schematic illustration of the structure of MPS-Li.

3.4 The effect of MPS layer during battery operation

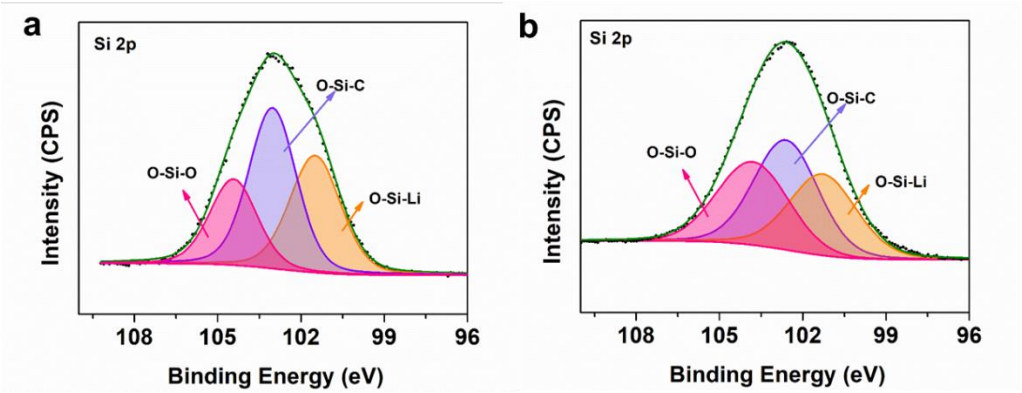

Figure 3.7 XPS spectrum of Si 2p for MPS-Li foils after immersion in two electrolytes respectively for 10 days: (a) ether based electrolyte; (b) carbonate ester based electrolyte.

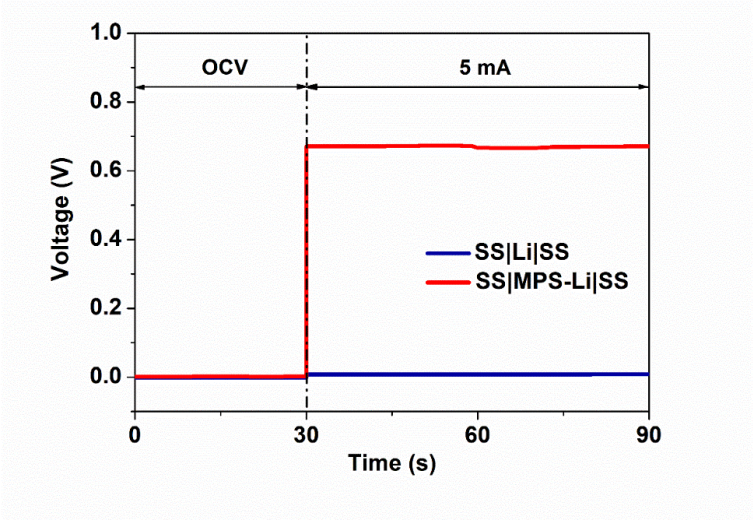

Figure 3.8 The comparison of the current response of Li and MPS-Li. During the direct current-voltage measurement, the Li and MPS-Li were sandwiched between two stainless steel (SS) blocking electrodes and subjected to a direct current of 5 mA.

To test the stability of the MPS layer in non-aqueous electrolyte, two MPS-Li foils were immersed in an ether based electrolyte, which was 1 M lithium bis(trifluoromethanesulfonyl)imide (LiTFSI) in 1,3-dioxolane (DOL)/1,2-dimethoxyethane (DME) (1:1 by volume) with 2wt% $LiNO_3$; and in an carbonate ester based electrolyte, which was 1 M $LiPF_6$ in ethylene carbonate (EC)/diethyl carbonate (DEC) (1:1 by volume), for 10 days respectively. After through cleaning, the XPS characterizations were conducted on the

MPS-Li foils and a strong peak of Si 2p was detected from their corresponding XPS spectrum (**Figure 3.7**), indicating that the MPS layer is stable and insoluble in both kinds of electrolytes. The electronic insulation property of MPS layer is verified by using direct current-voltage measurement (**Figure 3.8**), revealing that this passivation layer can block electron transport and thereby ensure that Li^+ is deposited beneath the MPS layer instead of on the top surface.

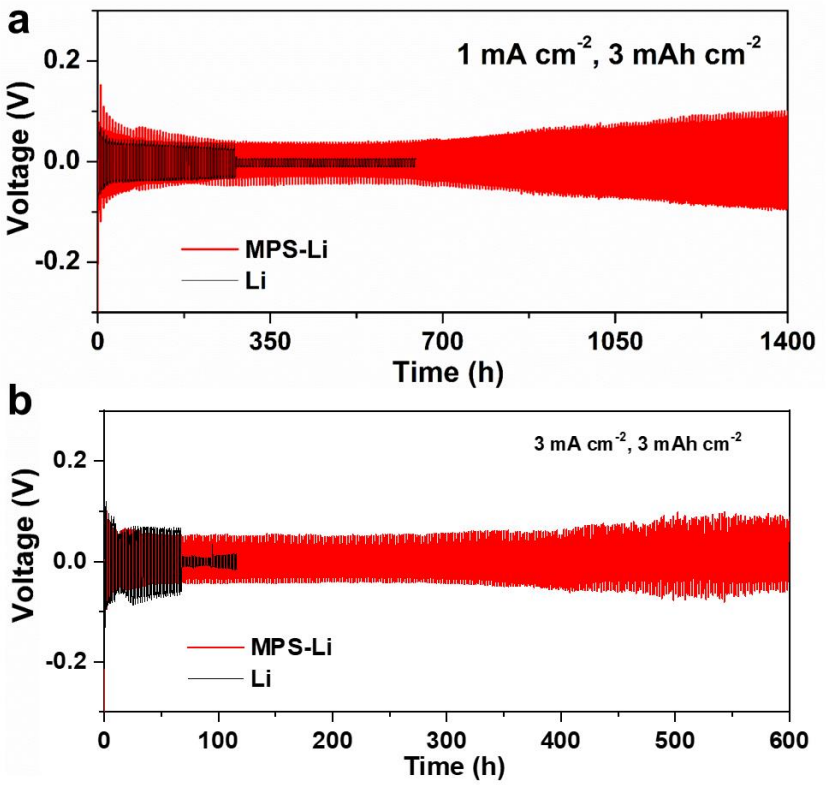

Figure 3.9 The effects of the MPS layer towards suppressing Li dendrite growth. (a-b) Voltage profiles of Li||Li and MPS-Li||MPS-Li symmetric cells tested at different current densities.

The growth of Li dendrites is the main cause of battery failure. The weak SEI layer tends to crack under volume changes, and these defects would stimulate the growth of Li dendrites. To find out if the Li dendrites are effectively suppressed by reinforcing the SEI layer, MPS-Li||MPS-Li symmetric cells were tested. Voltage profiles from galvanostatic charge-discharge cycling of MPS-Li||MPS-Li and Li||Li cells with a fixed areal capacity of 3 mA h cm^{-2} are shown in **Figure 3.9**. 1 M LiTFSI in DOL/DME (1:1 by volume) with 2wt% $LiNO_3$ was used as electrolyte. When the cells works at a current density of 1 mA cm^{-2}, although the polarization of the MPS-Li||MPS-Li cell is slightly high in the initial Li plating, it declines rapidly from 750 mV to 80 mV and remains at around 60 mV during the subsequent cycling (**Figure 3.10**).

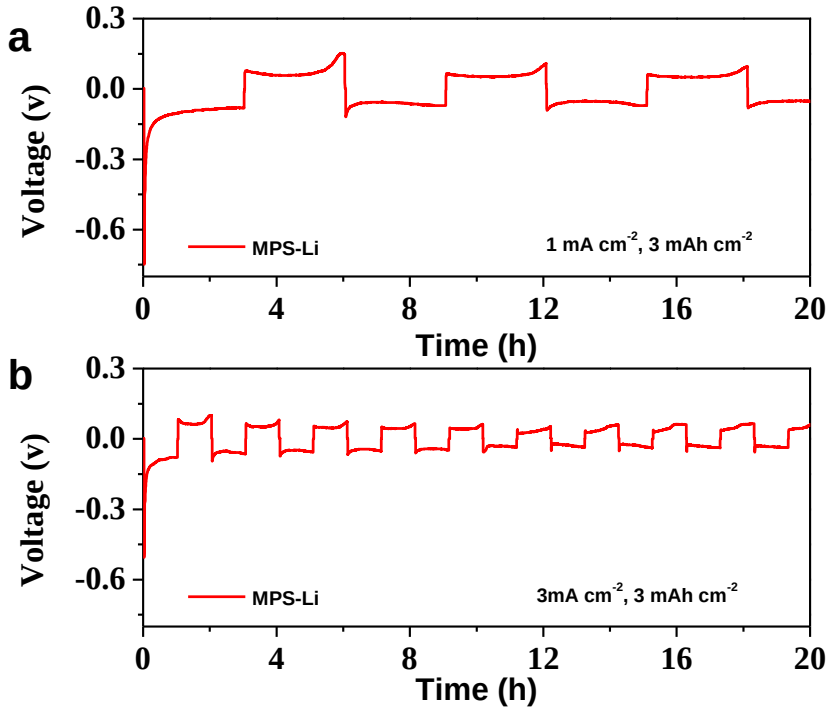

Figure 3.10 Voltage profiles for the first 20 hours of the MPS-Li||MPS-Li cells.

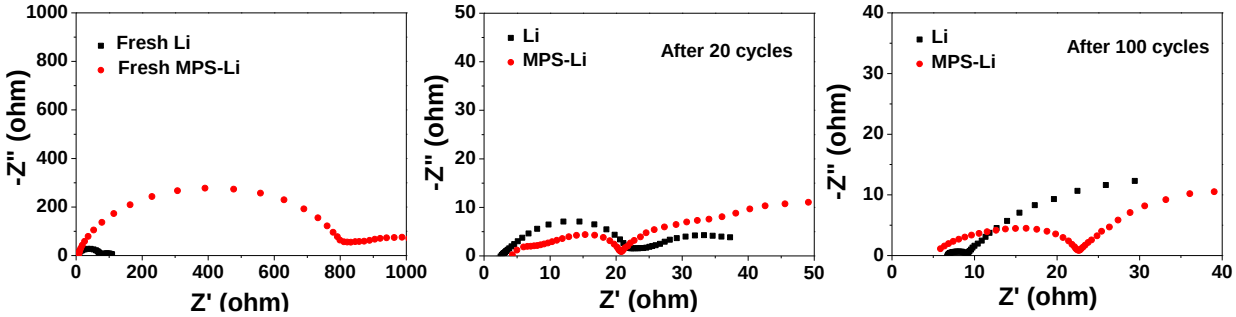

Figure 3.11 EIS curves of Li||Li and MPS-Li||MPS-Li symmetric cells during different cycling stages. The symmetric cells were cycled at a current density of 1 mA cm^{-2} with a fixed areal capacity of 3 mAh cm^{-2}.

After working for 1400 hours, the MPS-Li||MPS-Li cell exhibits a slightly increased voltage oscillation to around 100 mV. The Li||Li cell, in contrast, shows relatively lower plating/stripping polarization at the beginning, but it has an obvious plunge after 280 h, revealing that the continuously growing dendrites has eventually touched the counter electrode and causes a micro-short circuit. Electrochemical impedance spectroscopy (EIS) tests were futher applied to investigate the interfacial changes during different cycling stages. As shown

in **Figure 3.11**, the fresh MPS-Li||MPS-Li cell has a high charge transfer resistance but it falls back to the same level as for the Li||Li cell because of the activation process for the modified layer that takes place during the first few cycles. These changes are well consistent with the variation in the voltage profiles of MPS-Li||MPS-Li cell.

When the working current density is increased to 3 mA cm^{-2}, the MPS-Li||MPS-Li cell is able to work stablely for 600 hours, while Li||Li cell fails due to the micro-short circuit caused by dendrites after 70 hours. Based on the performance comparison, it is obvious that pristine Li is prone to generate Li dendrites during repeated plating/stripping processes, and the dendrite growth rate accelerates at high working current density. To further investigate the depletion of Li metal during cycling, the thin Li metal anode with a thickness around 100 μm was adopted in the symmetric cells and tested at a current density of 3 mA cm^{-2} with a plating/stripping capacity of 3 mAh cm^{-2}. As shown in **Figure 3.12**, the voltage polarization of the Li (100 μm)||Li (600 μm) cell soars up to 2 V after cycling for 80 hours, indicating that the thin Li foil has been depleted. The MPS-Li (100 μm)||MPS-Li (600 μm) cell, in contrast, has a longer lifespan of 180 hours. This advantage can be attributed to the robust SEI layer of MPS-Li, which suffers from less damages during volume change, so that there is less Li consumption during SEI layer repairs.

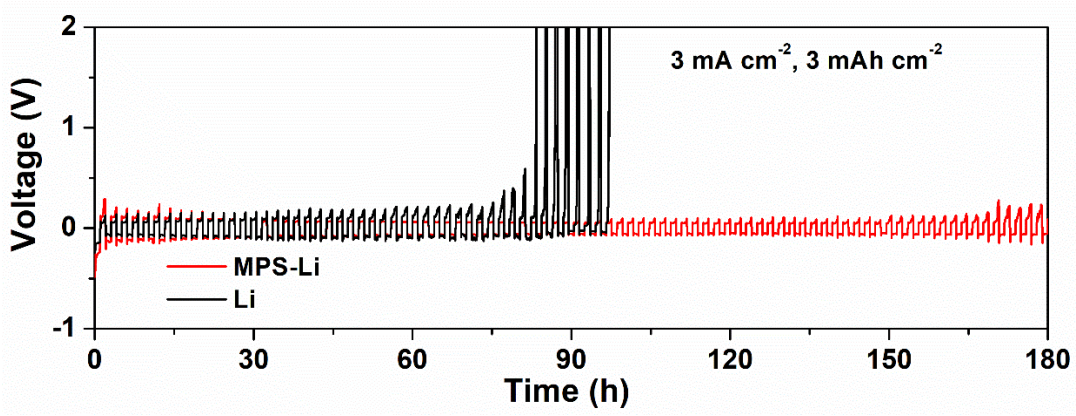

Figure 3.12 Voltage profiles of symmetric cells. The Li||Li and MPS-Li||MPS-Li cells were assembled with a thin foil around 100 μm thick on the one side and a thick foil around 600 μm thick on the other side.

To observe the morphology of cycled MPS-Li and Li foils, the symmetric cells, which worked at a current density of 1 mA cm^{-2} with a constant plating/stripping capacity of 3 mAh cm^{-2} for 100 cycles, were disassembled. According to the SEM images in **Figure 3.13**, the cycled Li

anode has a rough surface, and its magnified image shows a large amount of irregular branched Li. Most of these fragmented Li particles are electrochemically inactive, since they are covered with an SEI layer and dissociated from the Li metal matrix. The irregular morphology of cycled Li particles in Li metal anode can be ascribed to the brittle SEI layer. It has been reported that Li^+ tends to deposit in the cracks in the SEI layer and grow into dendrites.[33] The cycled MPS-Li anode, by contrast, has a smooth surface, and its large grains closely grow into a relatively dense structure (**Figure 3.13c**). No obvious dendritic Li particles are found in its enlarged image (**Figure 3.13d**). Obviously, the MPS modified layer plays a positive role in preventing the formation of Li dendrites and "dead" Li. The brittle SEI layer of pristine Li metal results in uneven Li^+ flux which in turn leads to the dendritic Li growth. The cell will fail when dendrites reach the counter electrode. In contrast, the strengthened interlayer of MPS-Li anode promotes uniform deposition of Li and therefore extends the lifespan of Li metal batteries.

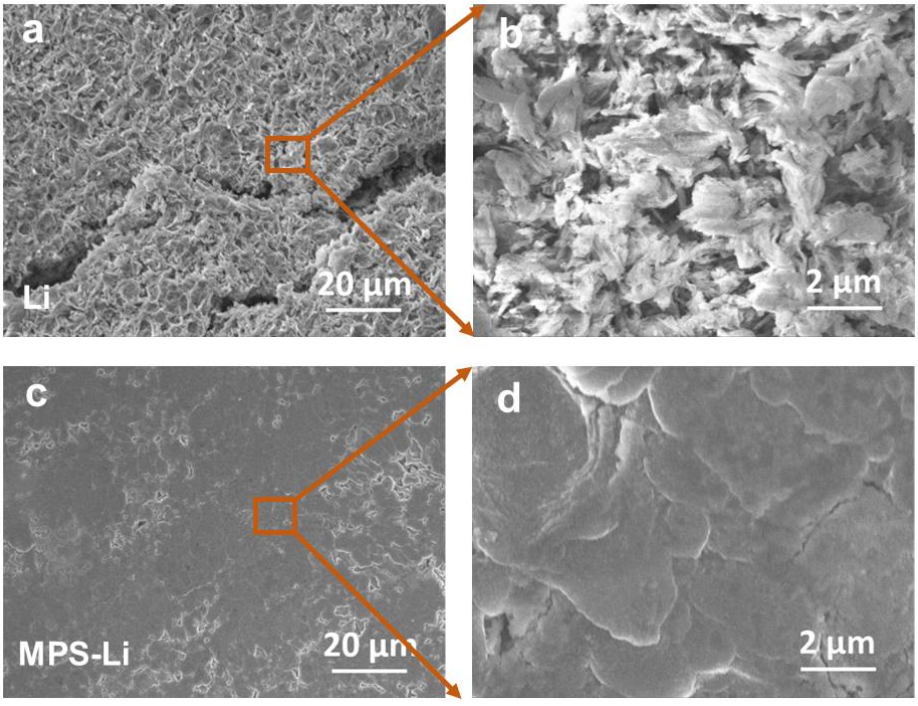

Figure 3.13 Top-view SEM images of Li (a-b) and MPS-Li (c-d) electrodes after 100 cycles at a current density of 1 mA cm^{-2} with a capacity of 3 mAh cm^{-2}.

3.5 Surface chemistry analysis of Li and MPS-Li

To investigate the components of SEI layer, XPS analysis was applied on cycled Li and MPS-Li anodes. As shown in **Figure 3.14**, peaks at 684.9 eV,[34] 686.5 eV,[35] and 688.4 eV[36] in the F

1s specturm belong to Li-F, C-F, and C-F_3 respectively, while peaks at 397 eV,[37] 398.2 eV, 399.3 eV,[31] and 404 eV in N 1s are assigned to LiN_xO_y, Li_3N, N-S, and $LiNO_2$, respectively. Based on a relative peak intensity comparation, it is obvious that cycled Li anode has much more by-products of electrolyte decomposition than the cycled MPS-Li anode, revealing that the MPS modified layer is effective in alleviating the side reactions between the active Li metal and the electrolyte.

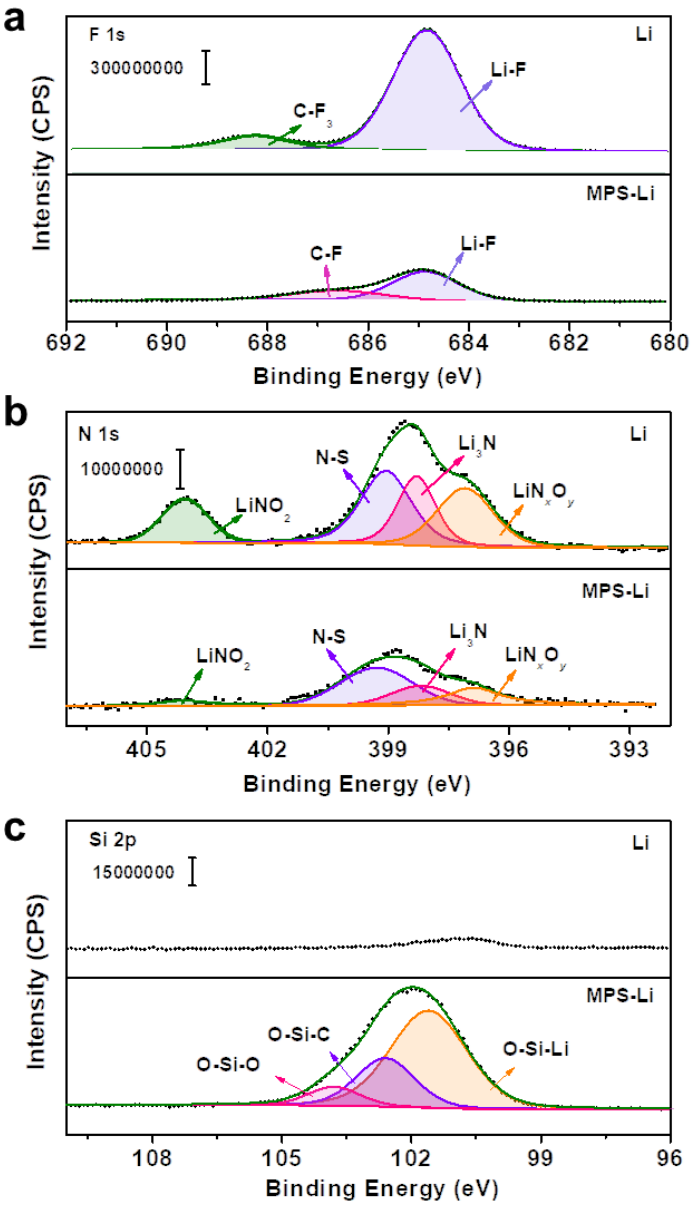

Figure 3.14 The surface chemicals of cycled MPS-Li and Li. High-resolution XPS spectra of Li and MPS-Li anodes after 100 cycles.

Moreover, a strong Si 2p peak is detected from the MPS-Li anode even after 100 cycles, and the components of split peaks remain the same as for the fresh MPS-Li foil, indicating that the MPS modified layer is quite stable. Interestingly, the amount of Li-Si-O, which is proved to be effective in facilitating Li^+ transportation through the interphase,[31] increases after cycling, verifying the activation process of the modified layer.

TOF-SIMS characterization was further used to indentify the component changes. As displayed in **Figure 3.15**, the relevant peaks of Li-O-Si bonds are all found in the TOF-SIMS ion spectrum of cycled MPS-Li anode, illustrating that the bonds between the MPS layer and the Li substrate are well retained. Nevertheless, the organic reactive part of the MPS layer, COO-$C(CH_3)=CH_2^-$, is found to be greatly depleted in **Figure 3.16a** compared with that of fresh MPS-Li, which means that it takes part in reactions during the formation process of the SEI layer. Meanwhile, its possible derivatives, CO-$CH(CH_3)$-CH_2-CH_2-Li_2^+ and COO-$CF(CH_3)$-CH_2-Li^+, appear at m/z = 96/97 and m/z = 110/111 in **Figure 3.16b**, respectively. We suppose that the carbon-carbon double bonds of COO-$C(CH_3)=CH_2$ may be opened up and bonded with the SEI components. Besides the fragment ions of the MPS layer, some new peaks are found on cycled MPS-Li. These peaks can be assigned to LiOH (m/z = 31), Li_2O (m/z = 36/37), Li_3N (m/z = 66/67), Li_2CO_3 (m/z = 80/81) and CH_3CH_2-O-COO-Li (m/z = 102/103). A small amount of decomposition products of Li salt are also found in **Figure 3.17**. The NO_2^- at m/z = 46 belongs to $LiNO_2$, while N-S=O^- and N-SO_2^- are assigned to the decomposition products of LiTFSI. These new species all belong to typical SEI components.

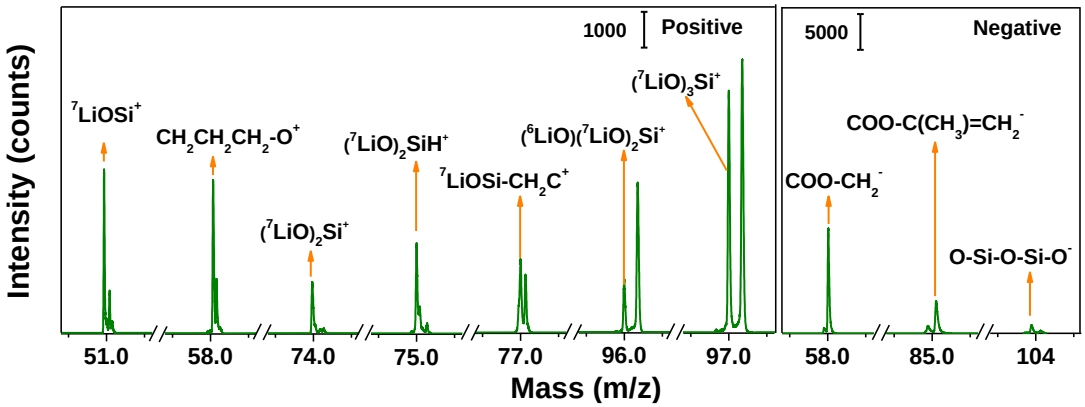

Figure 3.15 Selected TOF-SIMS ion spectrum of cycled MPS-Li foil.

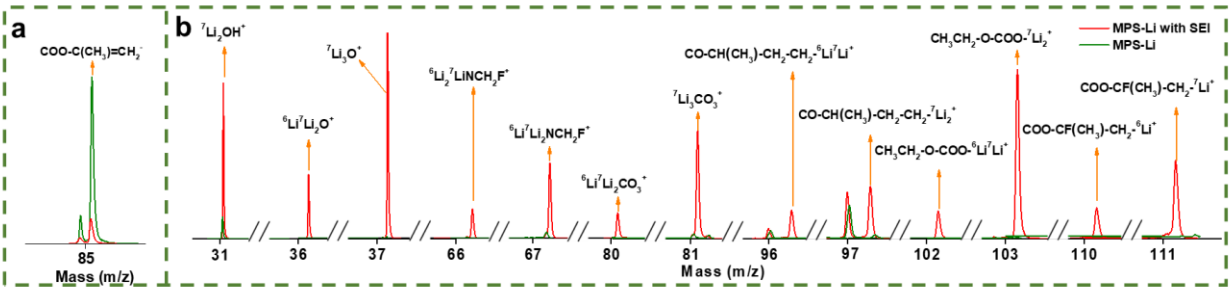

Figure 3.16 Comparison of TOF-SIMS ion spectra of fresh MPS-Li (green line) and cycled MPS-Li (red line): (a) the weakened peak; (b) the newly emerged peaks. Full TOF-SIMS spectra of cycled MPS-Li are presented in Figures 3.17-18 and the precise values of the peaks are listed in **Table 3.1**. Since only electrically charged fragments can be received by the detector, some of the detected components are non-stoichiometric and have one more Li^+ than the stoichiometric ratio.

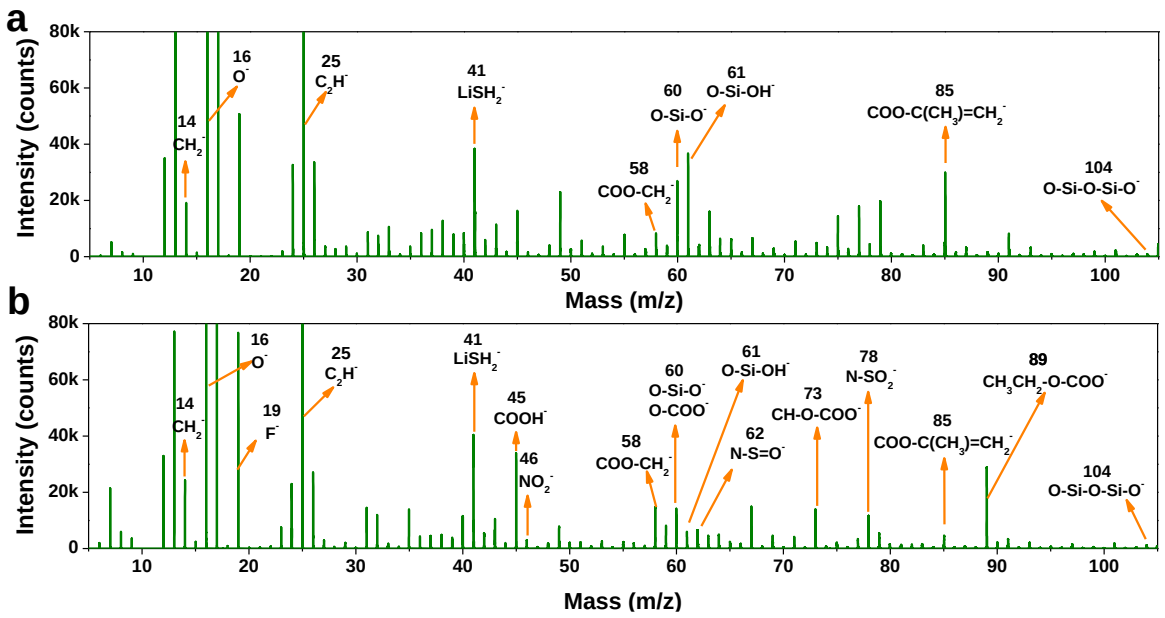

Figure 3.17 The full negative TOF-SIMS spectrum of (a) fresh MPS-Li and (b) cycled MPS-Li.

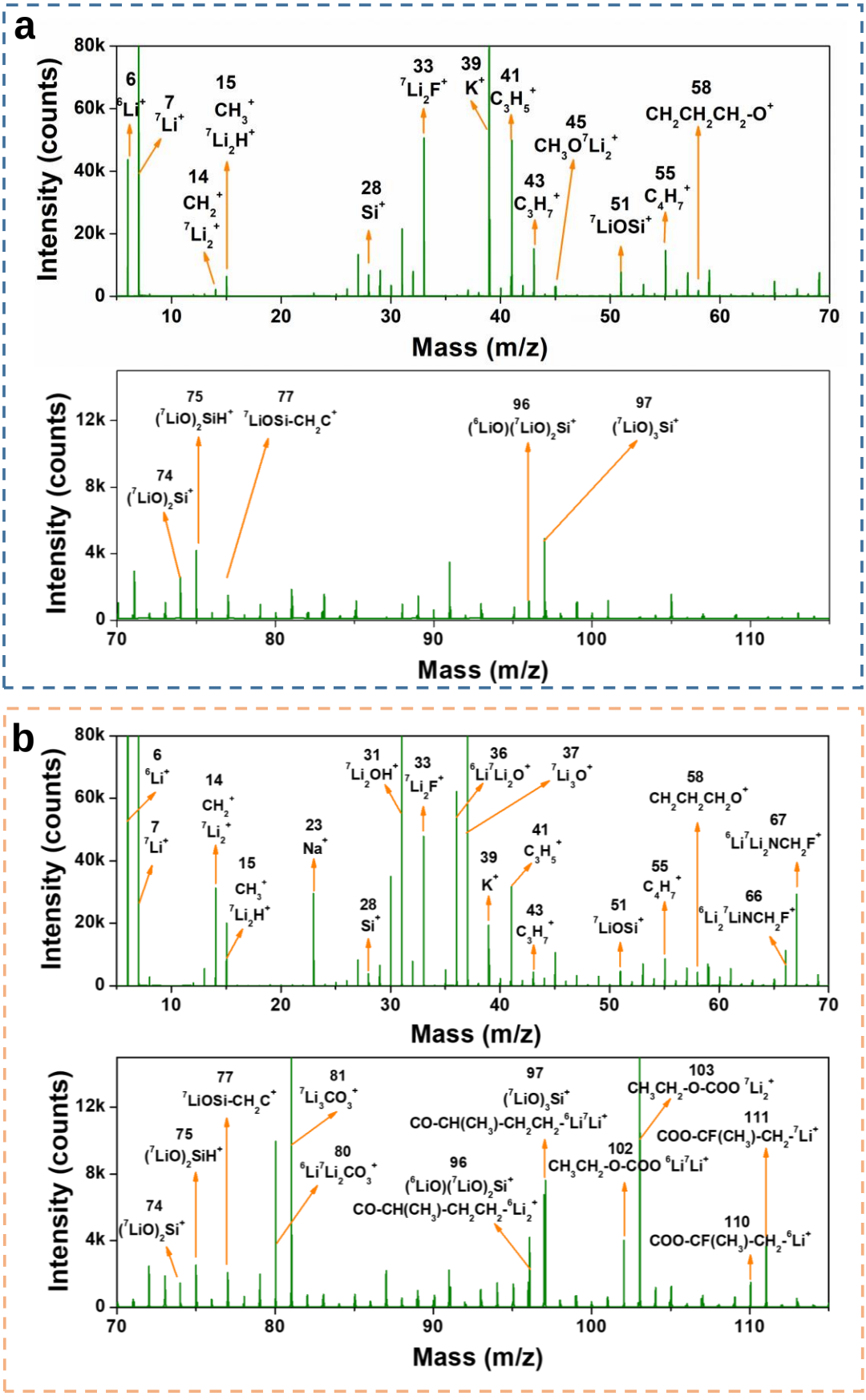

Figure 3.18 The full positive TOF-SIMS spectra of (a) fresh MPS-Li and (b) cycled MPS-Li.

Table 3.1. The theoretical and tested masses of the fragment ions of MPS-Li and MPS-Li with SEI.

Polarity	Fragment Ions	Theoretical Mass	Tested Value	
			MPS-Li	MPS-Li with SEI
Positive	$^{6}Li^{+}$	6.0151	6.0147	6.0153
	$^{7}Li^{+}$	7.0160	7.0159	7.0162
	CH_2^{+}	14.0157	14.0144	14.0147
	$^{7}Li_2^{+}$	14.0320	14.0307	14.0317
	CH_3^{+}	15.0235	15.0227	15.0232
	$^{7}Li_2H^{+}$	15.0398	15.0391	15.0396
	Si^{+}	27.9769	27.9752	27.9740
	$^{7}Li_2OH^{+}$	31.0347	31.0338	31.0341
	$^{7}Li_2F^{+}$	33.0304	33.0299	33.0296
	$^{6}Li\ ^{7}Li_2\ O$	36.0420		36.0420
	$^{7}Li_3\ O$	37.0429		37.0423
	K^{+}	38.9637	38.9643	38.9630
	$C_3H_5^{+}$	41.0391	41.0392	41.0384
	$C_3H_7^{+}$	43.0548	43.0547	43.0542
	$^{7}LiOSi^{+}$	50.9878	50.9875	50.9865
	$C_4H_7^{+}$	55.0548	55.0550	55.0540
	$CH_2CH_2CH_2O^{+}$	58.0419	58.0414	58.0412
	$^{6}Li_2\ ^{7}LiN\text{-}CH_2F^{+}$	66.0634		66.0637
	$^{6}Li\ ^{7}Li_2N\text{-}CH_2F^{+}$	67.0643		67.0648
	$(^{7}LiO)_2Si^{+}$	73.9988	73.9988	73.9974
	$(^{7}LiO)_2SiH^{+}$	75.0066	75.0059	75.0048
	$^{7}LiOSi\text{-}C_2H_2^{+}$	77.0035	77.0026	77.0034
	$^{6}Li^{7}Li_2CO_3$	80.0319		80.0313
	$^{7}Li_3CO_3$	81.0328		81.0315
	$(^{6}LiO)(^{7}LiO)_2Si^{+}$	96.0088	96.0086	96.0079
	$CO\text{-}CH(CH_3)\text{-}CH_2\text{-}CH_2\text{-}{}^{6}Li_2^{+}$	96.0878		96.0880
	$(^{7}LiO)_3Si^{+}$	97.0097	97.0091	97.0083

Polarity	Fragment Ions	Theoretical Mass	Tested Value	
			MPS-Li	MPS-Li with SEI
Positive	CH_3CH_2-O-COO-^{6}Li $^{7}Li^{+}$	102.0550		102.0542
	CH_3CH_2-O-COO-$^{7}Li_2^{+}$	103.0559		103.0554
	COO-CF(CH_3)-CH_2-$^{6}Li^{+}$	110.0425		110.0426
	COO-CF(CH_3)-CH_2-$^{7}Li^{+}$	111.0434		111.0439
Negative	CH_2^{-}	14.0157	14.0163	14.0159
	O^{-}	15.9949	15.9956	15.9952
	F^{-}	18.9984	18.9987	18.9991
	C_2H^{-}	25.0078	25.0087	25.0077
	$LiSH_2^{-}$	41.0037	41.0037	41.0034
	$COOH^{-}$	44.9977		44.9972
	NO_2^{-}	45.9929		45.9927
	COO-CH_2^{-}	58.0055	58.0053	58.0051
	O-Si-O^{-}	59.9668	59.9673	59.9664
	O-COO^{-}	59.9847		59.9847
	O-Si-OH^{-}	60.9746	60.9750	60.9739
	N-S=O^{-}	61.9701		61.9693
	CH-O-COO^{-}	72.9926		72.9930
	N-SO_2^{-}	77.9650		77.9643
	CH_2=C(CH_3)-COO^{-}	85.0290	85.0295	85.0285
	CH_3CH_2-O-COO^{-}	89.0239		89.0239
	O-Si-O-Si-O^{-}	103.9386	103.9392	103.9383

3.6 The electrochemical performance of MPS-Li anode

To evaluate the electrochemcial advantages of MPS-Li anode, a full cell with $LiFePO_4$ (LFP) as cathode material was tested at 1 C (1 C = 170 mA g^{-1}). The mass loading of the cathode was as high as 12 mg cm^{-2}, and the ether electrolyte, which was 1 M LiTFSI in DOL/DME (1:1 by volume) with 2% $LiNO_3$, was limited to only 3 µl mg^{-1}. The Li||LFP and MPS-Li||LFP cells show a very close initial specific capacity at around 140 mAh g^{-1}, but the Li||LFP cell falls behind after 40 cycles (**Figure 3.20a**). The MPS-Li||LFP cell delivers a capacity of 122 mAh g^{-1} after 300 cycles, as shown in **Figure 3.20c**, which is much higher than that of the Li||LFP cell (105 mAh g^{-1}). The full cells were disassambled after 20 cycles and the morphology of the cycled Li anodes are presented in **Figure 3.22a-b.** There are some obvious cracks on the Li foil of the Li||LFP cell, whereas the MPS-Li of the MPS-Li||LFP cell has a relatively sound surface.

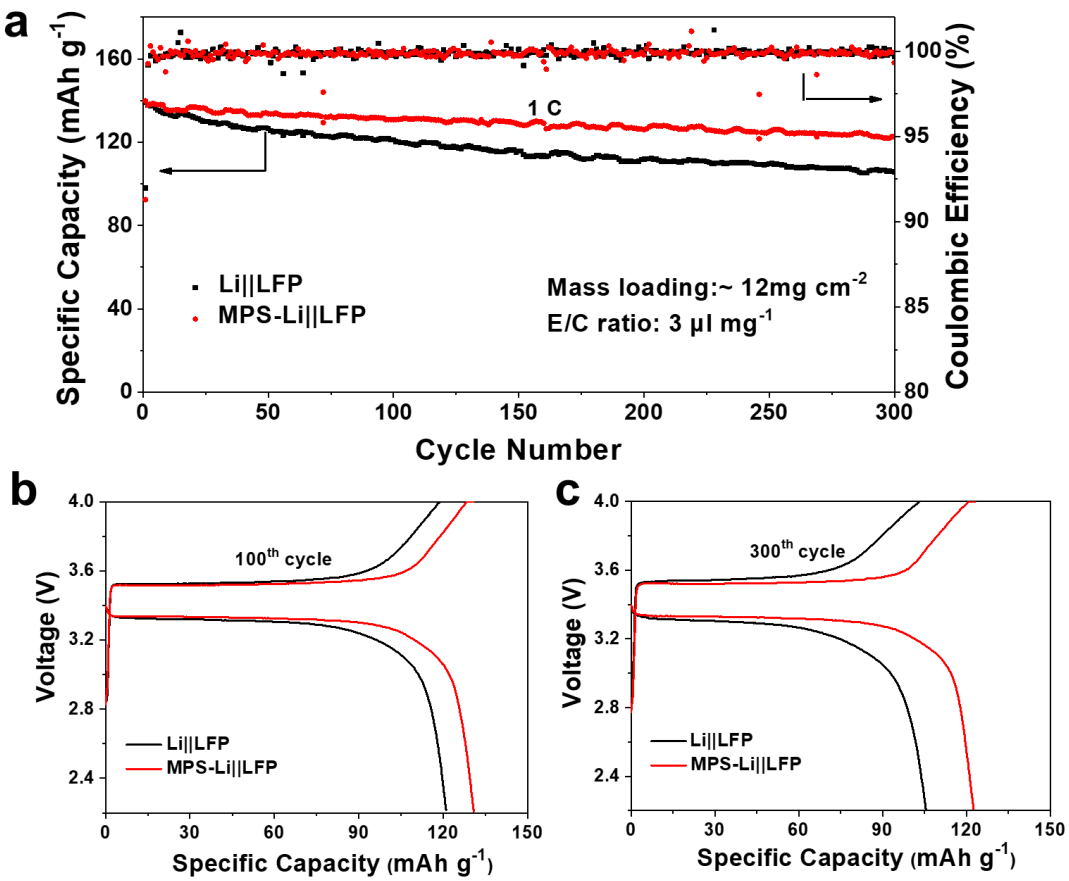

Figure 3.20 (a) Cycling stability of Li||LFP and MPS-Li||LFP cells. The mass loading of LFP electrode was 12 mg cm^{-2} and the electrolyte to cathode (E/C) ratio was controlled at around 3 µl mg^{-1}. (b-c) Voltage profiles of Li||LFP and MPS-Li||LFP cells at the 100^{th} and 300^{th} cycles, respectively.

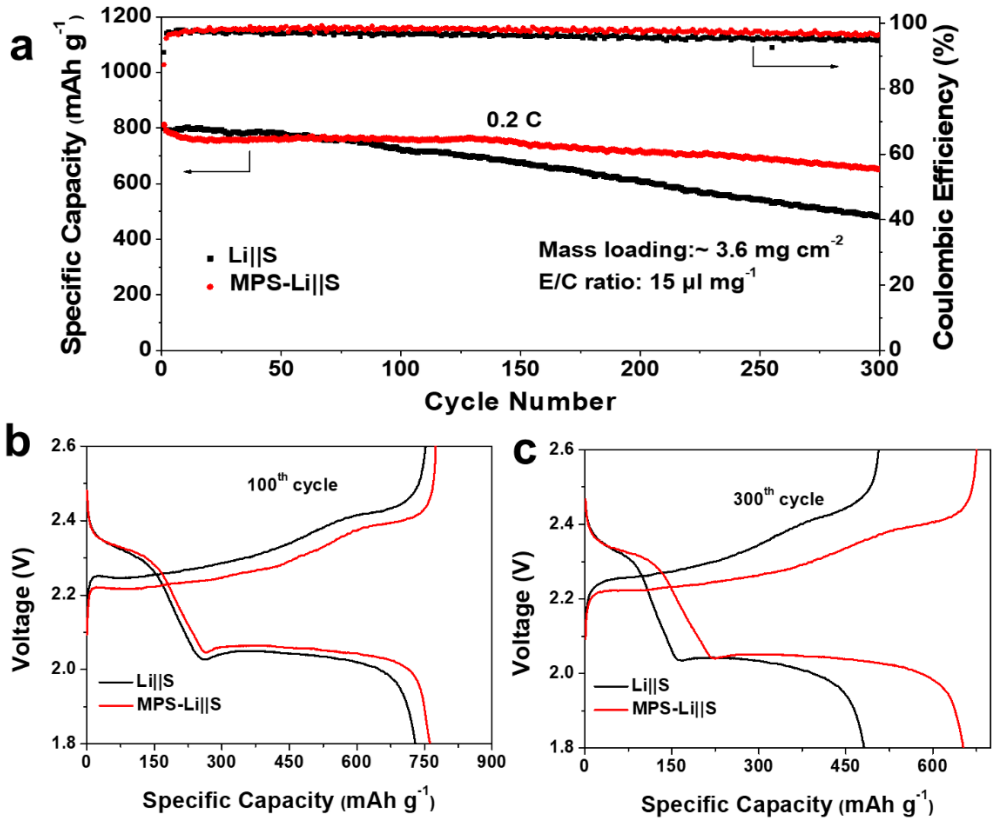

Figure 3.21 (a) Cycling stability of Li||S and MPS-Li||S cells. The mass loading of S electrode was around 3.6 mg cm^{-2}, and the E/C ratio was controlled at around 15 µl mg^{-1}. (b-c) Voltage profiles of Li||S and MPS-Li||S cells at the 100th and 300th cycles, respectively. The electrolyte used in these cells was 1 M LiTFSI in DOL/DME (1:1 by volume) with 2% $LiNO_3$.

Li||S and MPS-Li||S cells were also adopted to verify the effects of the MPS modified layer. The mass loading of S cathode was around 3.6 mg cm^{-2}, and the electrolyte to cathode (E/C) ratio was kept at 15 µl mg^{-1}. When cycled at 0.2 C (1 C = 1670 mA g^{-1}), both the cells deliver a specific capacity of around 800 mAh g^{-1} at first (**Figure 3.21a**). The gap becomes obvious at 100th cycle (**Figure 3.21b**), and the difference is further enlarged at the 300th cycle, where the capacity of MPS-Li||S is 652 mAh g^{-1} and that of Li||S is 482 mAh g^{-1} (**Figure 3.21c**). The Li foil, cycled in the Li||S cell for 20 cycles, has a loose structure with irregular Li particles, while the cycled MPS-Li foil is composed of closely packed grains (**Figure 3.22c-d**).

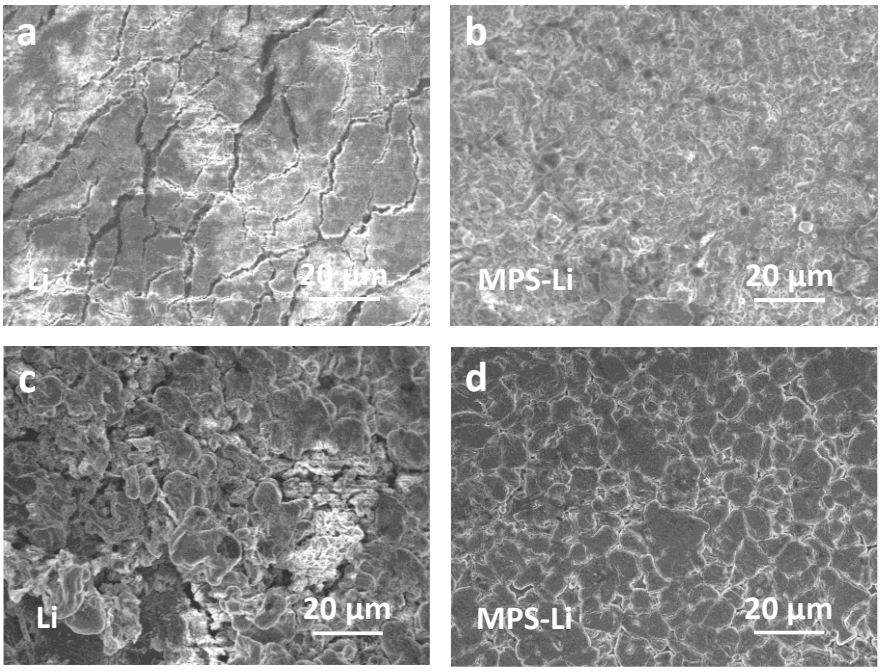

Figure 3.22 SEM images of Li and MPS-Li foils cycled in full cells for 20 cycles. (a) Li foil from Li||LFP cell; (b) MPS-Li foil from MPS-Li||LFP cell; (c) Li foil from Li||S cell; (d) MPS-Li foil from MPS-Li||S cell. The electrolyte used in these cells is 1 M LiTFSI in DOL/DME (1:1 by volume) with 2% $LiNO_3$.

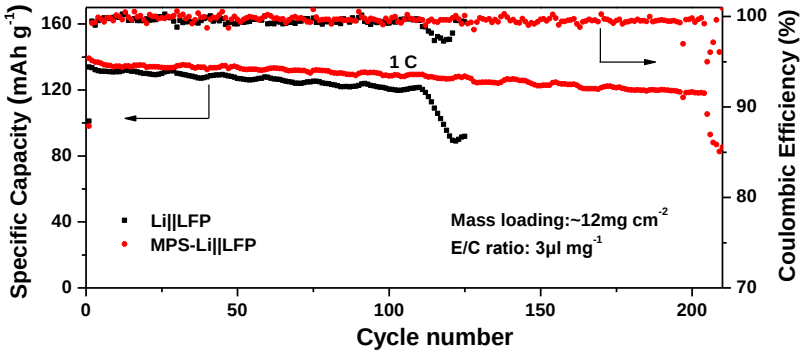

Figure 3.23 Galvanostatic cycling performance of Li||LFP and MPS-Li||LFP cells in carbonate electrolytes. The electrolyte is 1 M $LiPF_6$ dissolved in EC/DEC (1:1 by volume).

To find out if the MPS-Li is compatible in carbonate ester electrolyte, an MPS-Li||LFP cell was assembled with 1 M $LiPF_6$ in EC/DEC (1:1 by volume) as electrolyte. As shown in **Figure 3.23**, the reference Li||LFP cell suffers from a sudden decrease in its specific capacity after 110 cycles due to electrolyte exhaustion, while the MPS-Li||LFP cell exhibits good cycling performance

for 200 cycles. The full cells based on MPS-Li anode show distinct advantages even under practical testing conditions, revealing that the MPS layer is effective in protecting the Li metal anode and mitigating side reactions between Li metal and electrolyte.

3.7 Air stability of MPS-Li

The dense MPS layer also exhibits positive effects towards preventing air penetration when MPS-Li is exposed to air. The optical photograph in **Figure 3.24** displays the corrosion degree of Li and MPS-Li after exposed for different time period to air, where the humidity is ~30%. The Li foil starts to lose its metallic luster and becomes darker after exposure to air for 20 minutes, and it turns to totally black after 1 hour. In contrast, the MPS-Li is still shiny after 2 hours, demonstrating that the MPS modified layer is dense enough to prevent the reaction between active Li metal and air. The foils exposed to air for 1 hour are labeled as Li-1h and MPS-Li-1h, while those exposed for 2 hours are labeled as Li-2h and MPS-Li-2h.

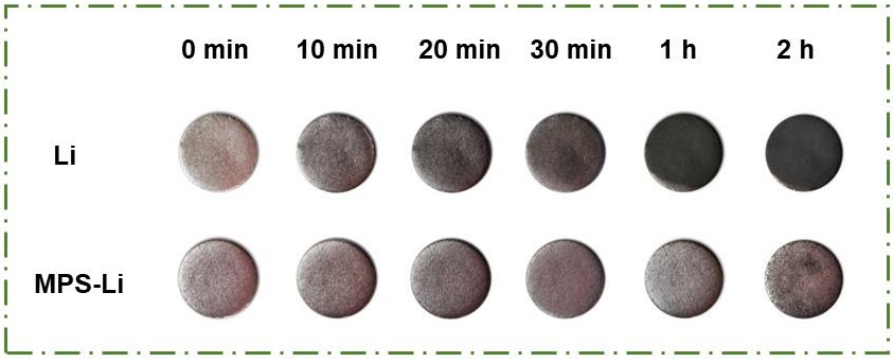

Figure 3.24 Optical photographs of Li and MPS-Li foils after they were exposed to air for different time periods. The air humidity was ~30%.

As shown in **Figure 3.25a**, the capacity retention of air-exposed Li and MPS-Li was tested by galvanostatic stripping from Li or MPS-Li foil and then plating on foamy copper until the overpotential reached 1 V. The Li-1h only delivers a capacity retention of 80.3%, and Li-2h becomes almost electrochemically inactive. In sharp contrast to Li foil, the MPS-Li-1h maintains a capacity that is nearly the same as for fresh Li foil, and MPS-Li-2h still delivers 88.1% of its theoretical capacity. The failure of air-exposed Li foil can be ascribed to heavily covered corrosion products, which block up both the electron and Li^+ transport and thereby damage the capacity of Li foil.

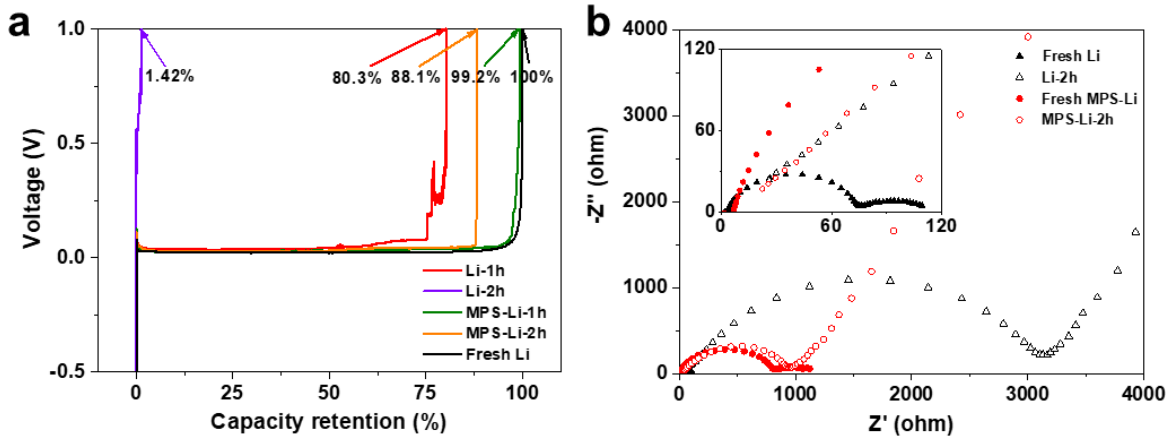

Figure 3.25 (a) The capacity retention of air-exposed Li and MPS-Li foils. (b) EIS curves of symmetric cells based on fresh and air-exposed Li and MPS-Li, with enlargement in the inset.

According to the EIS results on symmetric cells in **Figure 3.25b**, the charge transfer resistance of MPS-Li increases slightly from 812 Ω to 926 Ω after 2 hours of exposure to air, but that of Li is multiplied from 74 Ω to 3167 Ω. Due to the charge transfer barrier on the surface, the Li-2h fails to act as an electrode material in full cells (**Figure 3.26**).

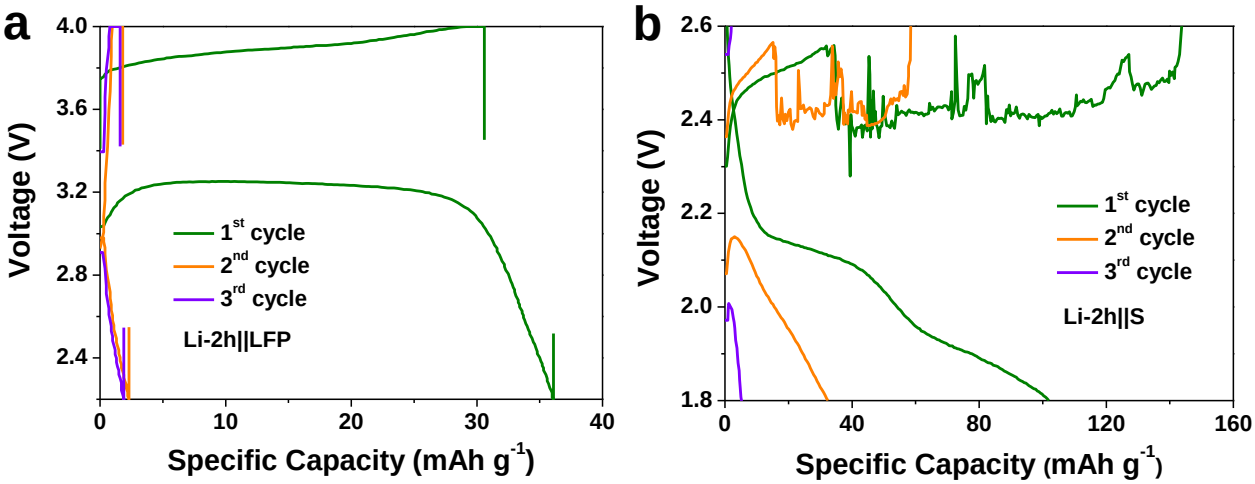

Figure 3.26 The first 3 cycles of (a) the Li-2h||LFP cell and (b) the Li-2h||S cell.

Although the Li-1h still shows electrochemical activity, the capacities of the full cells with Li-1h as anode are greatly degraded. In comparison, the MPS-Li-2h||LFP cell shows a cycling stability that is by no means inferior to that of MPS-Li||LFP (**Figure 3.27a**). The MPS-Li-2h||S cell is still able to deliver a specific capacity of 600 mAh g^{-1} after 300 cycles (**Figure 3.27b**),

which is quite comparable to the performance of MPS-Li||S. The MPS-Li-2h||MPS-Li-2h cell also works well for 600 hours at high working current density and high plating/stripping capacity (Figure S15).

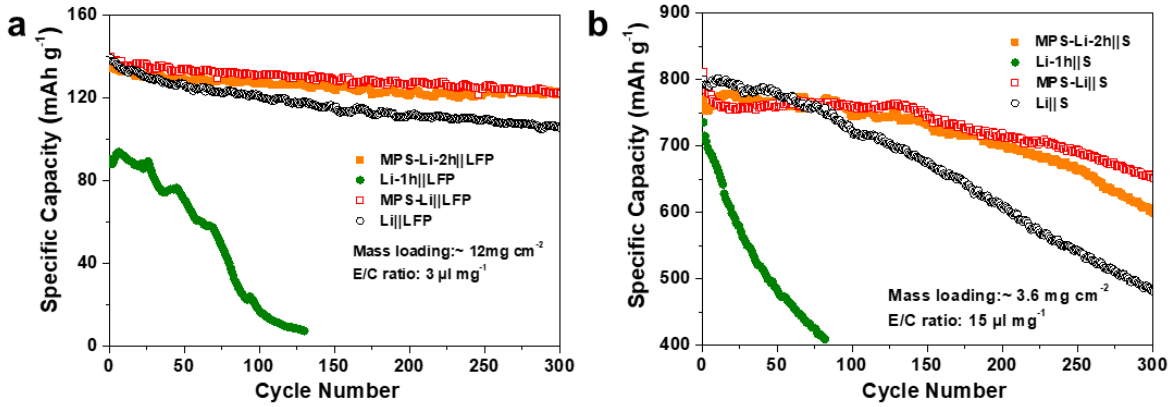

Figure 3.27 Full cell performance comparison of fresh Li/MPS-Li with air-exposed Li/MPS-Li as anode.

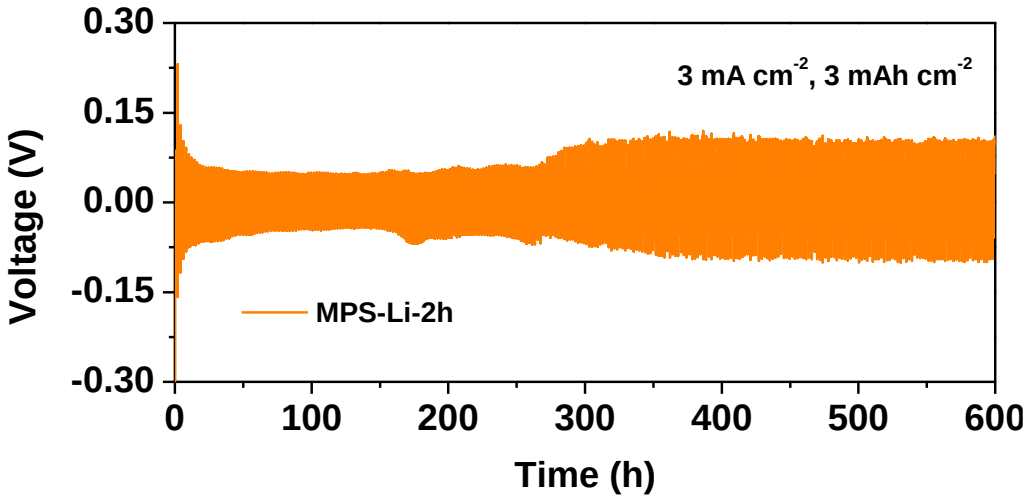

Figure 3.28 Voltage profiles of MPS-Li-2h||MPS-Li-2h cell.

3.8 Discussion

A silane coupling agent, a low-cost adhesion promoter, is adopted to serve as interface link between Li metal anode and SEI layer. The treatment method as presented in this paper is simple and feasible to be integrated into the existing manufacturing technique for Li metal battery. Coincidentally, LiOH, the essential prerequisite for the bonding reaction, is found on

the surface of commercial Li foil, and it would act as a source of reactive sites to guide the assembly of MPS molecules, resulting in the formation of a thin, uniform, and dense MPS layer. CH_3OH, the product of the bonding reaction, will inevitably react with uncovered Li metal and generate CH_3OLi, but this side reaction is slight because the generated CH_3OH is diluted by a large amount of THF and thereby reducing its activity. Moreover, the generated modified layer quickly covers the Li surface, preventing further reaction between CH_3OH with Li metal. The TOF-SIMS results confirm the formation of chemical bonds between the MPS layer and the Li substrate in the form of Li-O-Si. Once MPS molecules are attached to the surface, the treated Li foil inherits the reactivity characteristics of the organic groups. During Li deposition, the electrolyte will decompose and generate a natural SEI layer on MPS-Li. The organic functional groups of the MPS layer will take part in the reactions in this process by opening up its carbon-carbon double bonds and connecting with SEI components. Besides the chemical bonds, physical intertwining effects between the SEI layer and the MPS layer also contribute to the good adhesion. The organic groups of MPS have a high degree of compatibility with organic species, which ensures good interpenetration and diffusion of the organic species of the SEI layer into the MPS layer, thereby enhancing the adhesion of the SEI layer by forming interpenetrating organic networks as illustrated in **Figure 3.29**. In brief, the MPS molecule enhances the adhesion of the natural SEI layer to the Li metal substrate by bridging two materials with both chemical bonds and physical intertwining effects.

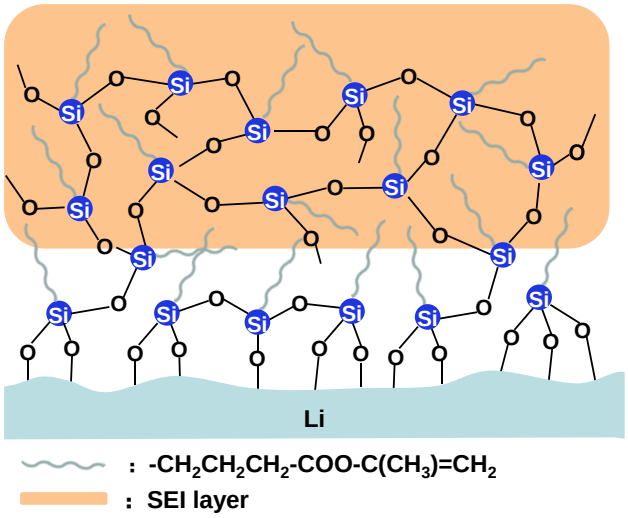

Figure 3.29 Schematic illustration of the structure of MPS layer and the bonding mechanism.

As illustrated in **Figure 3.30**, the reinforced SEI layer shows its advantages under interfacial changes during cycling. The excellent adhesion between the SEI layer and Li metal substrate is able to protect the SEI layer from fracturing and exfoliation, and further decreases the side reactions between the active Li metal and the electrolyte. In the case of commercial Li foil, its SEI layer is prone to crack easily, once the interfacial stress reaches its loading limits, and it even loses adhesion to the Li metal substrate. As a consequence, the plating/stripping process of Li is always accompanied by continual repair of the SEI layer, consuming both Li metal and electrolyte. Worse still, the defects and cracks in the SEI layer would become "hot spots" and attract Li^+ deposition on these areas, which accelerate Li dendrite growth. The symmetric cell tests also demonstrate that Li||Li cells tend to short-circuit during cycling because of dendrite growth, while the MPS-Li||MPS-Li cells show a much longer lifespan. The morphology comparison of cycled Li and MPS-Li electrodes further provides direct evidence that a robust SEI guarantees uniform and dendrite-free plating of Li, while a fragile SEI layer breeds severe dendrite growth. The surface chemical component analysis of the cycled Li electrodes shows that the MPS layer is effective in decreasing side reactions between the Li metal and the electrolyte, confirming that less damage is caused during cycling. With the protection of the MPS layer, both MPS-Li||LFP and MPS-Li||S full cells showed satisfactory cycling performance, even under high mass loading and with limited electrolyte.

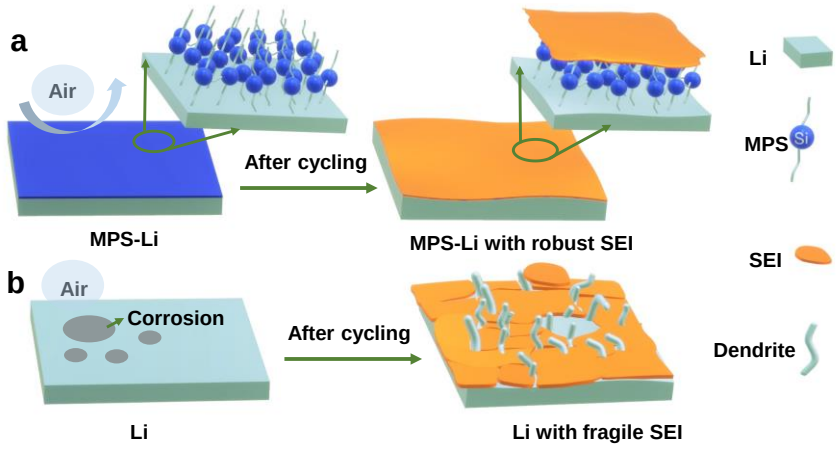

Figure 3.30 Schematic illustration of how the MPS layer protects Li metal in air and in electrochemical plating/stripping processes. (a) The dense MPS layer isolates the Li from air. The MPS layer also enhances the adhesion between Li foil and the SEI layer, and thus reduces cracks in the SEI layer and the growth of dendrites. (b) Pristine Li is severely corroded when exposed to air. The weak SEI layer of pristine Li cracks and exfoliates under volume changes.

The MPS layer is firmly attached to the surface of Li foil via Li-O-Si bonds, which are effective in building a dense barrier to block air diffusion, thus reducing the generation of oxidation products. Unlike the Li-2h, which loses its activity because of sharply increased resistance of charge transfer, MPS-Li-2h is still able to deliver good electrochemical performance both in full cells and in symmetric cell. Compared with previously reported methods for the fabrication of nanoscale protective layers, which make high demands on equipment and have high costs, the silane coupling agent modification is one of the most simple, feasible, and low-cost technique.

3.9 Conclusion

In summary, we introduced a promising method to solve the issue of Li metal electrode via silane coupling agent modification. This modification layer protects the Li metal from air corrosion, which would reduce the high requirement for protection from atmosphere in the manufacture of Li metal based batteries. This layer can also act as promoter to enhance the adhesion between the SEI layer and the Li substrate by forming chemical bonds and physical intertwining effects. As a consequence, both increased air stability of the Li electrode and enhanced electrochemical performance are achieved. MPS is introdued as an example, and apart from it, various silane coupling agents with different organic functional groups are worth investigating to further optimize the bonds between intermediates and the SEI layer.

3.10 Reference

1. Xu W, *et al.* Lithium metal anodes for rechargeable batteries. *Energy & Environmental Science* **7**, 513-537 (2014).
2. Lei D, *et al.* Progress and Perspective of Solid-State Lithium–Sulfur Batteries. *Advanced Functional Materials* **28**, 1707570 (2018).
3. Wang Z, *et al*. Recent Advances in 3D Graphene Architectures and Their Composites for Energy Storage Applications. *Small* **15**, 1803858 (2019).
4. Cheng Y, *et al*. Lithiophobic-lithiophilic composite architecture through co-deposition technology toward high-performance lithium metal batteries. *Nano Energy* **63**, 103854 (2019).
5. Wang Y, *et al.* Spherical Li Deposited inside 3D Cu Skeleton as Anode with Ultrastable Performance. *ACS Applied Materials & Interfaces* **10**, 20244-20249 (2018).
6. Wang Z, *et al.* Building Artificial Solid-Electrolyte Interphase with Uniform Intermolecular Ionic Bonds toward Dendrite-Free Lithium Metal Anodes. *Advanced Functional Materials* **30**, 2002414 (2020).
7. Cheng X-B, *et al*. Toward Safe Lithium Metal Anode in Rechargeable Batteries: A Review. *Chemical Reviews* **117**, 10403-10473 (2017).
8. Hou C, *et al.* Operando Observations of SEI Film Evolution by Mass-Sensitive Scanning Transmission Electron Microscopy. *Advanced Energy Materials* **9**, 1902675 (2019).
9. Zhang H, *et al*. Electrolyte Additives for Lithium Metal Anodes and Rechargeable Lithium Metal Batteries: Progress and Perspectives. *Angewandte Chemie International Edition* **57**, 15002-15027 (2018).
10. Jiang Z, *et al.* Nitrofullerene, a C60-based Bifunctional Additive with Smoothing and Protecting Effects for Stable Lithium Metal Anode. *Nano Letters* **19**, 8780-8786 (2019).
11. von Aspern N, *et al*. Fluorine and Lithium: Ideal Partners for High-Performance Rechargeable Battery Electrolytes. *Angewandte Chemie International Edition* **58**, 15978-16000 (2019).
12. Li Q, *et al*. Progress in electrolytes for rechargeable Li-based batteries and beyond. *Green Energy & Environment* **1**, 18-42 (2016).

13. Qian J, *et al.* High rate and stable cycling of lithium metal anode. *Nature Communications* **6**, 6362 (2015).

14. Song J, *et al*. Ionomer-Liquid Electrolyte Hybrid Ionic Conductor for High Cycling Stability of Lithium Metal Electrodes. *Scientific Reports* **5**, 14458 (2015).

15. Xie J, *et al.* Stitching h-BN by atomic layer deposition of LiF as a stable interface for lithium metal anode. *Science Advances* **3**, eaao3170 (2017).

16. Cheng Q, *et al.* Stabilizing Solid Electrolyte-Anode Interface in Li-Metal Batteries by Boron Nitride-Based Nanocomposite Coating. *Joule* **3**, 1510-1522 (2019).

17. Lin D, *et al.* Conformal Lithium Fluoride Protection Layer on Three-Dimensional Lithium by Nonhazardous Gaseous Reagent Freon. *Nano Letters* **17**, 3731-3737 (2017).

18. Li N-W, *et al*. An Artificial Solid Electrolyte Interphase Layer for Stable Lithium Metal Anodes. *Advanced Materials* **28**, 1853-1858 (2016).

19. Wu J, *et al*. Air-stable means more: designing air-defendable lithium metals for safe and stable batteries. *Materials Horizons* **7**, 2619-2634 (2020).

20. Jiang Z, *et al.* Facile Generation of Polymer–Alloy Hybrid Layers for Dendrite-Free Lithium-Metal Anodes with Improved Moisture Stability. *Angewandte Chemie International Edition* **58**, 11374-11378 (2019).

21. Zhang Y, *et al.* An air-stable and waterproof lithium metal anode enabled by wax composite packaging. *Science Bulletin* **64**, 910-917 (2019).

22. Xiao Y, *et al*. Waterproof lithium metal anode enabled by cross-linking encapsulation. *Science Bulletin* **65**, 909-916 (2020).

23. Ye M, *et al*. Paraffin wax protecting 3D non-dendritic lithium for backside-plated lithium metal anode. *Energy Storage Materials* **24**, 153-159 (2020).

24. Cao Z, *et al.* Ambient-Air Stable Lithiated Anode for Rechargeable Li-Ion Batteries with High Energy Density. *Nano Letters* **16**, 7235-7240 (2016).

25. Liu X, *et al*. Novel Organophosphate-Derived Dual-Layered Interface Enabling Air-Stable and Dendrite-Free Lithium Metal Anode. *Advanced Materials* **32**, 1902724 (2020).

26. Xie M, *et al.* A Li–Al–O Solid-State Electrolyte with High Ionic Conductivity and Good Capability to Protect Li Anode. *Advanced Functional Materials* **30**, 1905949 (2020).

27. Yan K, *et al.* Ultrathin Two-Dimensional Atomic Crystals as Stable Interfacial Layer for Improvement of Lithium Metal Anode. *Nano Letters* **14**, 6016-6022 (2014).

28. Alaboina PK, *et al*. In Situ Dendrite Suppression Study of Nanolayer Encapsulated Li Metal Enabled by Zirconia Atomic Layer Deposition. *ACS Applied Materials & Interfaces* **10**, 32801-32808 (2018).

29. Qu S, *et al.* Air-stable lithium metal anode with sputtered aluminum coating layer for improved performance. *Electrochimica Acta* **317**, 120-127 (2019).

30. Wang J, *et al.* Scalable synthesis of nanoporous silicon microparticles for highly cyclable lithium-ion batteries. *Nano Research* **13**, 1558-1563 (2020).

31. Liu F, *et al.* Fabrication of Hybrid Silicate Coatings by a Simple Vapor Deposition Method for Lithium Metal Anodes. *Advanced Energy Materials* **8**, 1701744 (2018).

32. Xie Y, *et al*. Silane coupling agents used for natural fiber/polymer composites: A review. *Composites Part A: Applied Science and Manufacturing* **41**, 806-819 (2010).

33. Liu Y, *et al.* An Artificial Solid Electrolyte Interphase with High Li-Ion Conductivity, Mechanical Strength, and Flexibility for Stable Lithium Metal Anodes. *Advanced Materials* **29**, 1605531 (2017).

34. Jiang Z, *et al.* Reconfiguring Organosulfur Cathode by Over-Lithiation to Enable Ultrathick Lithium Metal Anode toward Practical Lithium-Sulfur Batteries. *ACS nano* **14**, 13784-13793 (2020).

35. Zhang X-Q, *et al*. Fluoroethylene Carbonate Additives to Render Uniform Li Deposits in Lithium Metal Batteries. *Advanced Functional Materials* **27**, 1605989 (2017).

36. Jiao S, *et al.* Stable cycling of high-voltage lithium metal batteries in ether electrolytes. *Nature Energy* **3**, 739-746 (2018).

37. Zhang X-Q, *et al.* Highly Stable Lithium Metal Batteries Enabled by Regulating the Solvation of Lithium Ions in Nonaqueous Electrolytes. *Angewandte Chemie International Edition* **57**, 5301-5305 (2018).

Chapter 4 Solvent control of water O−H bonds for highly reversible Zn anode

This chapter includes work that has been accepted for publication. Here, we report a hybrid electrolyte (HE) of dimethylacetamide (DMAC), trimethyl phosphate (TMP) and H_2O as solvent. We show that the strong polar DMAC and TMP molecules have a significant impact on H_2O to strengthen the O−H bonds and suppress activity. We evidence that the hybrid electrolyte obviates anode corrosion, extends operation temperature, guides the (002) plane preferred orientation during Zn plating, and is compatible with high-voltage cathode.

Statement of Authorship

Title of Paper	Solvent control of water O–H bonds for highly reversible zinc ion batteries
Publication Status	☐ Published ☑ Accepted for Publication ☐ Submitted for Publication ☐ Unpublished and Unsubmitted w ork w ritten in manuscript style
Publication Details	Yanyan Wang, Zhijie Wang, Wei Kong Pang, Wilford Lie, Jodie A. Yuwono, Gemeng Liang, Sailin Liu, Anita M. D'Angelo, Jiaojiao Deng, Yameng Fan, Kenneth Davey, Baohua Li, and Zaiping Guo.

Principal Author

Name of Principal Author (Candidate)	Yanyan Wang
Contribution to the Paper	Devised the idea, performed experiments, analyzed and interpreted data, wrote and revised the manuscript.
Overall percentage (%)	70%
Certification:	This paper reports on original research I conducted during the period of my Higher Degree by Research candidature and is not subject to any obligations or contractual agreements with a third party that would constrain its inclusion in this thesis. I am the primary author of this paper.
Signature	Date: 10 / Mar. / 2023

Co-Author Contributions

By signing the Statement of Authorship, each author certifies that:

i. the candidate's stated contribution to the publication is accurate (as detailed above);

ii. permission is granted for the candidate in include the publication in the thesis; and

iii. the sum of all co-author contributions is equal to 100% less the candidate's stated contribution.

Name of Co-Author	Zhijie Wang
Contribution to the Paper	Guided to design of the whole experiment, helped with data analysis, and revised the manuscript.
Signature	Date: 10 / Mar. / 2023

Name of Co-Author	Wei Kong Pang
Contribution to the Paper	Assisted in conducting experiment with *in operando* synchrotron-based X-ray powder diffraction (XRPD).
Signature	Date: 15 Mar 2023

Name of Co-Author	Wilford Lie		
Contribution to the Paper	Provided NMR test.		
Signature		Date	14/3-2023

Name of Co-Author	Jodie A. Yuwono		
Contribution to the Paper	Helped with DFT calculation.		
Signature		Date	10/03/2023

Name of Co-Author	Gemeng Liang		
Contribution to the Paper	Assisted to analyze the XRPD data.		
Signature		Date	13/03/2023

Name of Co-Author	Sailin Liu		
Contribution to the Paper	Assisted to conduct in situ FTIR test.		
Signature		Date	10/03/2023

Name of Co-Author	Anita M. D'Angelo		
Contribution to the Paper	Assisted in conducting experiment with *in operando* synchrotron-based XRPD.		
Signature		Date	14/03/2023

Name of Co-Author	Jiaojiao Deng		
Contribution to the Paper	Helped with DFT calculation.		
Signature		Date	14/03/2023

Name of Co-Author	Yameng Fan		
Contribution to the Paper	Assisted in XPS characterization.		
Signature		Date	13/03/2023

Name of Co-Author	Kenneth Davey		
Contribution to the Paper	Help to polish the manuscript.		
Signature		Date	14/03/2023

Name of Co-Author	Baohua Li		
Contribution to the Paper	Supervised development of work, helped in data interpretation and manuscript evaluation.		
Signature		Date	14/03/2023

Name of Co-Author	Zaiping Guo		
Contribution to the Paper	Supervised development of work, discussed the whole design, revised and conceptualized the manuscript.		
Signature		Date	10/03/2023

4.1 Introduction and significance

The emergence of wind, solar and other volatile renewable energy sources calls for suitable energy storage to integrate the generated energy into the electricity grid[1]. Lithium-ion batteries are a successful energy storage system. However, limited Li resource, relatively high cost and some safety risk impede their application to large-scale electrical energy storage[2]. Zinc ion batteries (ZIBs) are seen as a practical alternative because of improved safety, attractive gravimetric energy density, lower cost, the abundance of Zn and environmental 'friendliness'[3]. ZIBs are composed of a metallic Zn anode, a Zn salt-containing electrolyte, together with a Zn^{2+} ion host cathode[4]. Compared with other metal anodes, including Li, Na and K, the low reactivity and acceptable redox potential of − 0.76 V *vs* standard hydrogen electrode (SHE) of metallic Zn assures safety with ZIBs[5]. The electrolyte provides the environment for chemical reactions during battery operation, including Zn plating/stripping and (de)intercalation of Zn^{2+} ions in cathode materials[5]. Electrolyte properties therefore significantly impact anode reversibility and cathode reaction mechanisms[6]. In addition, the electrolyte determines ion migrations between cathode and anode, the electrochemical stability window (ESW) and the temperature adaptability of ZIBs[7]. Aqueous electrolytes, including $ZnSO_4$ and zinc trifluoromethanesulfonate ($Zn(OTf)_2$) solution, are safe, low cost and environmental-friendly, making them attractive for practical application. However, drawbacks include that aqueous ZIBs have a narrow ESW, and exhibit, corrosion of the Zn anode, dendrite growth, poor temperature adaptability and dissolution of cathode materials[8]. The operating voltage of the battery is determined by the potential of cathode and anode materials, and ideally should have an ESW for the electrolyte *ca.* 1.23 V, to prevent hydrogen or oxygen evolution[9]. Gas evolution results also from self-corrosion of Zn anode because some H_3O^+ exists in mild-acid electrolytes that withdraws electrons from metallic Zn. Accompanying hydrogen evolution, accumulated OH^- ions aggregate with Zn^{2+} and anions to form passivation species, including zinc hydroxysulfate [$Zn_4(OH)_6SO_4 \cdot nH_2O$][10]. These passivation species prevent diffusion of Zn^{2+} ions and electron transmission, to produce an 'uneven' Zn deposition and dendrite growth[11]. Because of the freezing and boiling point for water, respectively, 0 and 100 °C, the majority of aqueous ZIBs do not work in sub-zero and 'hot' i.e. > 40 °C environments. Additionally, with aqueous electrolytes there can be dissolution of cathodes that cause active material loss and rapid capacity fading[12].

To address this, a number of approaches have been used including, constructing artificial protection layers, adding functional additives[13] and regulating Zn^{2+} ion deposition behavior[14].

However, practical difficulty remains because these challenges arise from the solvent, water. It is widely acknowledged that self-ionization reaction exists with pure water, in which H_2O ionizes to form OH^- and H_3O^+ ($2H_2O \rightleftharpoons H_3O^+ + OH^-$). Together with the dissolution of zinc salts, including $ZnSO_4$ and $Zn(OTf)_2$, the pH value reduces from near 7 for pure water, to *ca.* 5 for 1 M $ZnSO_4$/$Zn(OTf)_2$ aqueous solution, because Zn^{2+}−water interaction causes water molecules to ionize. The electric field for Zn^{2+} exerts a force on water molecules to induce electron transfer from coordinated H_2O to empty orbitals of Zn^{2+}, which significantly weakens the O−H bonds of H_2O molecules and promotes hydrogen evolution[15, 16]. Theoretically, the self-ionization of water cannot be restrained by limited additives, therefore, practically, significant additive is necessary to ensure intensive interactions with water. Highly concentrated 'water-in-salt' electrolyte is an example in which dissolved salts far outnumber water, confining water molecules in ion solvation shells. Through suppressing Zn^{2+}−H_2O interaction, hydrolysis of zinc salt is eliminated and the pH value for water-in-salt electrolytes approaches pH = 7. Under these circumstances, water exhibits less activity and the ESW for the electrolyte can be expanded to *ca.* 3.0 V[15]. However, this is not cost-effective. Researchers therefore consider organic electrolytes to eliminate H_3O^+. Organic electrolytes are advantageous in ESW, operational temperature range and thermodynamic stability with metallic Zn anode[17, 18]. A drawback however is that most of these electrolytes are flammable and therefore are a safety risk in ZIBs. Additionally, organic electrolytes have high charge-transfer impedance and a high desolvation penalty at the electrode/electrolyte interface, restraining the cathode from exhibiting full capacity[19]. To obviate these drawbacks in using aqueous and organic electrolytes, it was hypothesized that a judiciously designed hybrid electrolytes might be preferable[20].

Various non-aqueous solvents, such as dimethyl sulfoxide (DMSO)[21], dimethyl carbonate (DMC)[22], N-methylpyrrolidone (NMP)[23], triethyl phosphate (TEP) [24], diethyl carbonate (DEC)[25], propylene carbonate (PC)[26] and ethylene glycol (EG)[27], were added into aqueous electrolytes to regulate the solvation structures[28]. The mechanism(s) is to break hydrogen bonds between water molecules, restrict activity of water in solvation sheaths, or exclude water molecules from the electric double layer (EDL), which aims to suppress water decomposition. In this work, we proposed that water reactivity can be suppressed by increasing the electrostatic attraction between O−H via increasing the electron density of the water protons. Dimethylacetamide (DMAC) and trimethyl phosphate (TMP) are selected because they are strong polar molecules with electron-rich regions, C=O and P=O groups, that exert interaction

on both solvated and free water molecules, and therefore impact the O−H bond strength of water. The decomposition of H_2O in the hybrid electrolyte is less thermodynamically favorable compared with that in aqueous electrolyte. By confining the activity of H_2O, H_2O decomposition-related hydrogen evolution, together with undesired side reactions are obviated. The Zn anode in the as-prepared electrolyte exhibits high plating/stripping efficiency of 99.5 % over 2000 cycles at 1 mA cm^{-2}, and boosted anti-corrosion characteristics. DMAC could alter the surface energy of Zn and therefore guide the (002) plane preferred orientation of Zn deposition, which boosts the lifespan of the Zn anode to > 1600 hours despite high applied current density and plating capacity of, respectively, 5 mA cm^{-2} and 5 mAh cm^{-2}.

4.2 Experiments

Materials and Methods

Chemicals: Dimethylacetamide (DMAC, 99.8 %), trimethyl phosphate (TMP, 99 %), zinc trifluoromethanesulfonate ($Zn(OTf)_2$, 98 %), zinc sulfate ($ZnSO_4 \cdot 7H_2O$, 99%), zinc perchlorate hexahydrate ($Zn(ClO_4)_2 \cdot 6H_2O$, 99%) and zinc trifluoromethanesulfonate ($Zn(TSFI)_2$, 98%) were purchased from Sigma-Aldrich.

$Zn_3(Fe(CN)_6)_2$ synthesis: 50 mL of 0.1 M $ZnSO_4 \cdot 7H_2O$ and 50 mL of 0.05 M $K_3Fe(CN)_6$ were mixed with 25 ml deionized water, followed by heating at 60 °C under vigorous stirring for 5 h to complete the reaction. The precipitate was rinsed and centrifuged five times to remove the residues. Then, the product was finally dried at 70 °C for 12 h.

Characterization: A Thermo Scientific Nexsa X-Ray Photoelectron Spectrometer System was used to determine XPS spectra of cycled Zn foils. Fourier-transform infrared (FT-IR) spectra and Raman spectra, were determined, respectively, with a PerkinElmer Frontiers instrument with an attenuated total reflectance (ATR) attachment, and a Raman spectrometer (Horiba LabRam Evolution). *In-situ* optical observation of the Zn deposition process in various electrolytes was conducted with a customized cell (EL-CELL). Linear sweep voltammetry (LSV) was conducted on a VMP3 instrument. Cyclic voltammetry (CV) was conducted with a 3-electrode EL-CELL using well-polished Zn as the reference electrode. NMR testing was carried out with a Bruker Avance Neo 500-MHz NMR spectrometer using a cryoprobe. The ionic conductivity of electrolytes was measured with a Thermo Scientific Orion electrochemistry meter, and the viscosity is measured with capillary viscometers (Huanguang Brand, Zhejiang, China) under certain temperatures. The Mettler Toledo thermogravimetric

analyser (TGA)/differential scanning calorimeter (DSC) 3+ is used for TGA and DSC measurement.

Electrochemical Testing: To prepare the $Zn_3(Fe(CN)_6)_2$ (ZnHCF) electrodes, a slurry composed of active materials, Super P and polyvinylidene difluoride (PVDF) at a mass ratio of 7:1.5:1.5 was cast onto Ti-foil and followed with drying at 80 ℃ for 12 h. Electrochemical data were collected from the Neware battery testers. CR2032-type coin cells were used in all electrochemical tests. Zn foil (99.99%, 100 μm) is used as the anode. For batteries using aqueous electrolyte (AE), a glass-fiber membrane (740 μm) was used as the separator, and for those with hybrid electrolyte (HE) or non-aqueous electrolytes, nylon 66 membrane (130 μm) is used. The glass-fibre membrane was purchased from Filtech Pty Ltd, while the nylon 66 membrane was purchased from Shanghai Xinya Purification Equipment Co., Ltd.

Molecular dynamics (MD) simulation: All of the ion parameters were obtained from the literature, namely GAFF2 force field. Other molecules were optimized *via* gaussian 16 package at a level of B3LYP/def2tzvp firstly and vibration analyses were performed at the same level to ensure that there were no virtual frequencies. The ACPYPE webserver was used to obtain the GAFF2 force-field topology file and Packmol software used for construction of the model. Simulation was as follows: the 5000-step steepest descent and 5000-step conjugate gradient method were used to obviate unreasonable contact with the system; NPT ensemble was used to pre-equilibrate the system, and V-rescale temperature coupling and Parrinello-Rahman pressure coupling were used to control the temperature to 298K; pressure was maintained at 1 atm, non-bonding cutoff radius was 1.2 nm; integration step was 2fs. 30 ns simulations were performed in which bond length and angle were constrained by the LINCS algorithm. The two-way intercept was set to 1.2 nm, van der Waals interaction and the long-distance electrostatic interaction was set *via* the particle-mesh Ewald method. The trajectory file during simulation was saved each 10.0 ps.

Density functional theory (DFT) computation: All DFT computations were performed *via* Vienna *ab initio* simulation package (VASP) developed by Fakultät für Physik. A plane wave energy cut-off of 500 eV was used. The generalized gradient approximation (GGA) and the Perdew−Burke−Ernzerhof (PBE) XC functional combined with the projector augmented wave (PAW) method were used to describe the exchange-correlation functional. The MonkhorstPack scheme was used to generate the k-point sampling grids within the Brillouin zone. Energy differences of 1×10^{-5} eV/atom and energy difference gradients of −0.01 eV/Å were used as convergence criteria.

For deprotonation reaction computation, we picked the Zn^{2+} cluster structures from the MD simulation for further analysis using DFT. The dispersion correction was used by employing the DFT-D3 method. The deprotonation energy for H_2O was computed from the following:

$$E_{deprotonation} = E_{(cluster)} - \frac{1}{2A}(E_{H_2}) - E_{(deprotonated\ cluster)} \qquad (1)$$

where E_{H_2} is the energy of H_2 used for the standard hydrogen electrode scale ($H^+ + e^- \rightleftharpoons ½\ H_2$), $E_{(cluster)}$ and $E_{(deprotonated\ cluster)}$ are the energies of the cluster in the presence and absence of H^+, respectively.

For Zn bulk computations, a 9 × 9 × 9 grid was used for the supercells of Zn (100), Zn (101), Zn (002), and for the solvation model covered structures, the grid was set as 3 × 3 × 1. The solvation models were obtained using the MS FORCITE module, and FORCITE optimizations are performed first, which was a molecular mechanics module for potential energy and geometry optimization calculations of arbitrary molecular and periodic systems using classical mechanics. The surface energy for Zn (100), Zn (101), Zn (002) surfaces (γ_s) was defined by:

$$\gamma_s = \frac{1}{2A}(E_s^{unrelax} - NE_b) + \frac{1}{A}(E_s^{relax} - E_s^{unrelax}) \qquad (2)$$

where *A* is the area of the surface considered, E_s^{relax} and $E_s^{unrelax}$ energies for, respectively, relaxed and unrelaxed surfaces, *N* number of atoms in the slab and E_b bulk energy per atom. For the solvation model the surface energy for Zn (100), Zn (101), Zn (002) surfaces (γ_{sol}) was defined as:

$$\gamma_{sol} = \gamma_s + \frac{BE_{sol}}{A} \qquad (3)$$

where BE_{sol} is given by:

$$BE_{sol} = (E_{slab-sol} - E_{slab} - E_{sol}) \qquad (4)$$

here $E_{slab-sol}$ is energy of the surface covered with the solvation molecules, E_{slab} energy for the Zn (100), Zn (101), or Zn (002) clean surface, and E_{sol} energy for the solvated models.

4.3 Electrolyte and characterization

The hybrid electrolyte formulation was based on the principles of dendrite-free deposition of Zn and non-flammability. It was found that when the volume ratio for DMAC,TMP and H_2O was 5:2:3, the mixture could not be ignited, the preferred orientation of the (002) plane appeared.

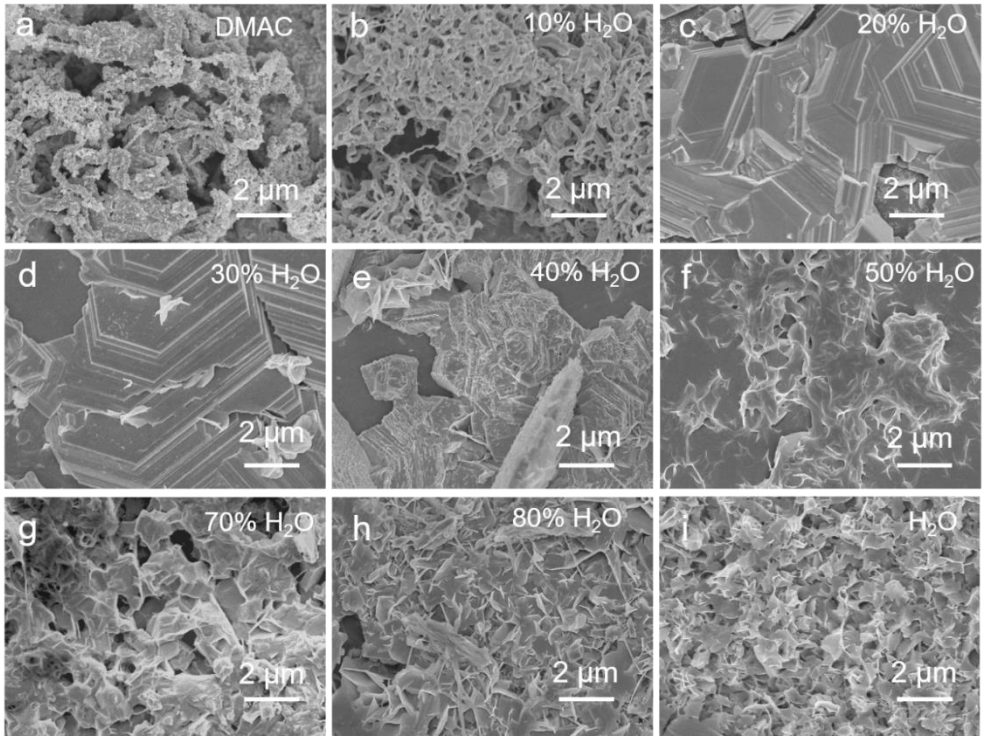

Figure 4.1 Morphology evolution of Zn deposited in 1 M $Zn(OTf)_2$ solutions. The solvent is a DMAC/H_2O mixture with various volume percentages of H_2O.

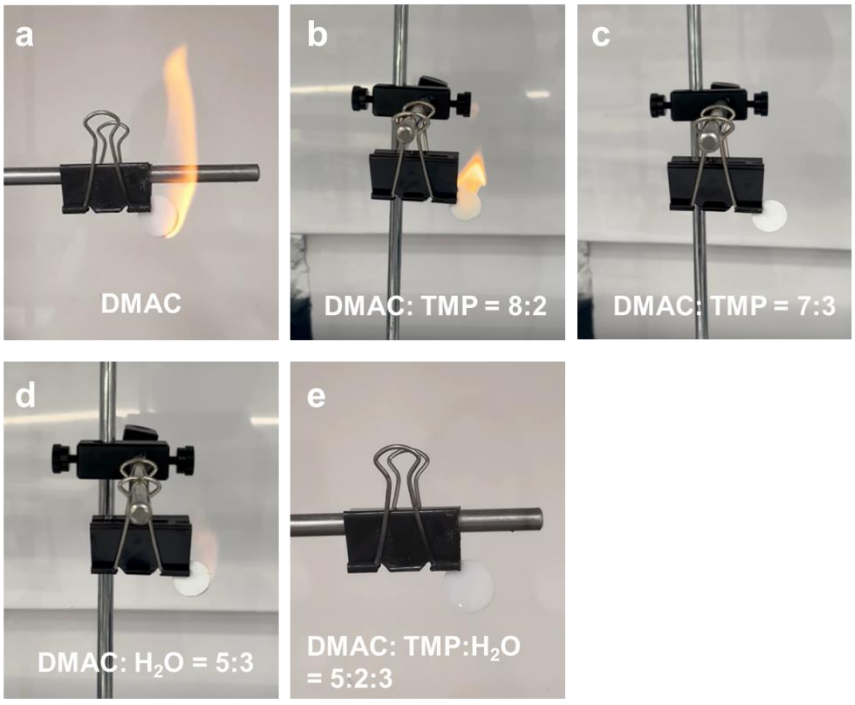

Figure 4.2 Digital images of ignition test for 1 M $Zn(OTf)_2$ solutions. The solvent is (a) DMAC, (b) DMAC/TMP (8:2 by volume); (c) DMAC/TMP (7:3 by volume); (d) DMAC/H_2O (5:3 by volume); (e) DMAC/TMP /H_2O (5:2:3 by volume).

As shown in **Figure 4.1**, the (002) preferred orientation of Zn deposition can be achieved when the ratio of H_2O in the DMAC/H_2O mixture is in the range of 20%-40%. Considering the merits of H_2O as solvent, the percentage of H_2O is maximized to be around 40%. Unfortunately, the DMAC/H_2O mixture is flammable. Fire retardant, TMP, is used to partly replace DMAC to ensure the non-flammability of the electrolyte but the amount needs to be minimized to maintain the low viscosity of the electrolyte. **Figure 4.2** confirms that the minimum usage of TMP is around 30% in the mixture of DMAC/TMP. Therefore, the ratio of DMAC/TMP/H_2O is designed to be 5:2:3. 1 M $Zn(OTf)_2$ dissolved in this mixture is denoted HE whilst 1 M $Zn(OTf)_2$ aqueous solution, AE.

In dilute aqueous electrolytes, including AE, Zn^{2+} coordinates with six water molecules to form $Zn[H_2O]_6^{2+}$ [15]. To determine the solvation structure for HE, molecular dynamics (MD) simulations were carried out. It is found that organic solvents, DMAC and TMP, together with the anion were evidenced to take part in the solvation shells, **Figure 4.3**. Radial distribution functions (RDFs) computed the distribution of the nearest-neighbor molecules around a reference Zn^{2+}, **Figure 4.4**. The coordination number for HE is six, which includes 3.7 H_2O molecules, 1 DMAC molecule, 0.5 TMP molecule and 0.8 OTf^- anion, based on the statistical findings.

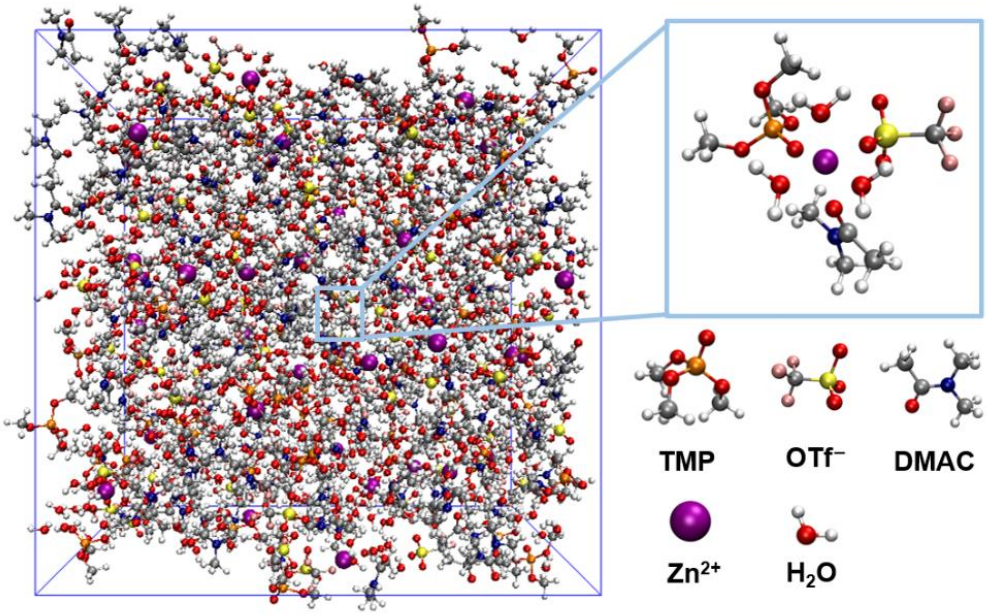

Figure 4.3 Snapshots of MD simulation boxes for new hybrid electrolyte (HE).

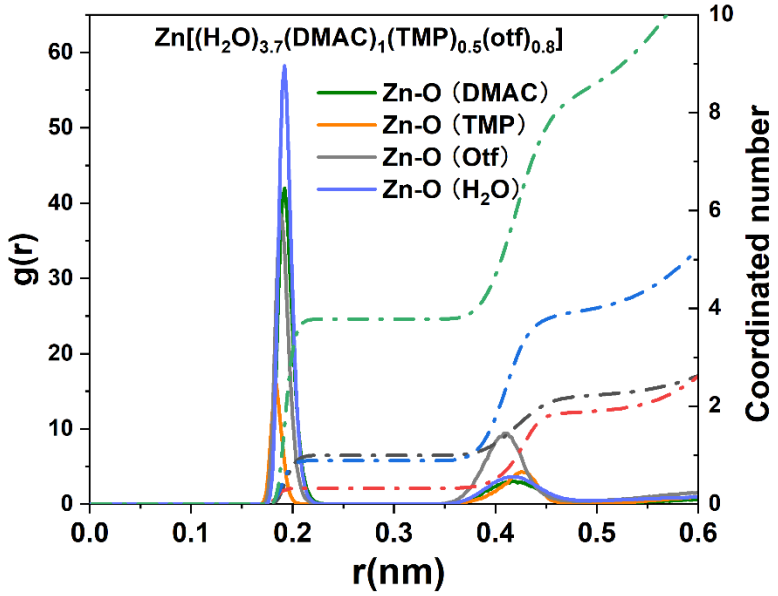

Figure 4.4 RDFs for Zn^{2+}–O pairs in HE.

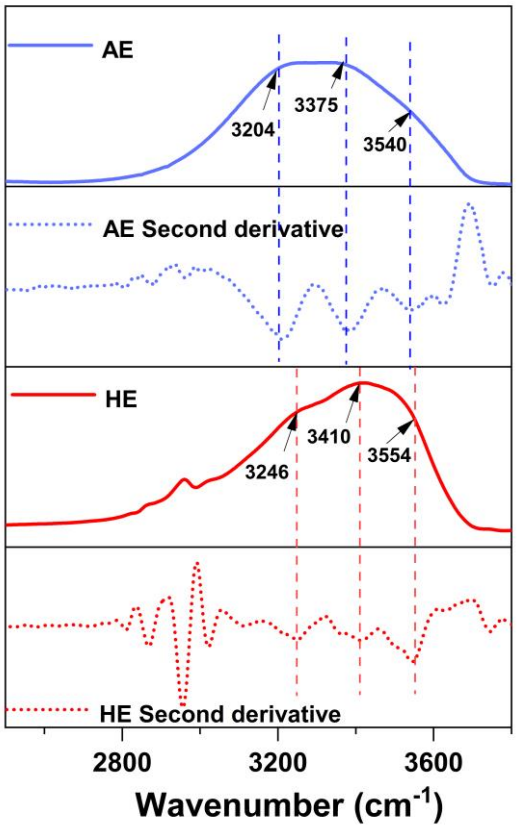

Figure 4.5 FTIR absorption and second derivative spectra for AE and HE.

Fourier transform infrared (FT-IR) spectra that are significantly sensitive to molecular dipole moment change, was applied to determine how polar molecules impact the O−H bonds of water. For AE, the absorbance bands in the region of 2800 to 3800 cm^{-1} are related to O−H stretching vibrations. The second derivative spectra located the three main peaks, 3204, 3375 and 3540 cm^{-1}, corresponding to, respectively, network water, intermediate water and poorly connected water, **Figure 4.5**.[29] It was found that these peaks all undergo apparent blueshift in the spectra for HE, demonstrating that hydrogen bonds are weakened whilst O−H bonds strengthened[26]. This result is different from the previous report, that adding DMAC into the aqueous electrolyte leads to redshift of O−H vibrations because of increasing number of hydrogen bonds. The ratio of DMAC/H_2O is the crucial factor that determines whether the hydrogen bonds are strengthened or weakened[30].

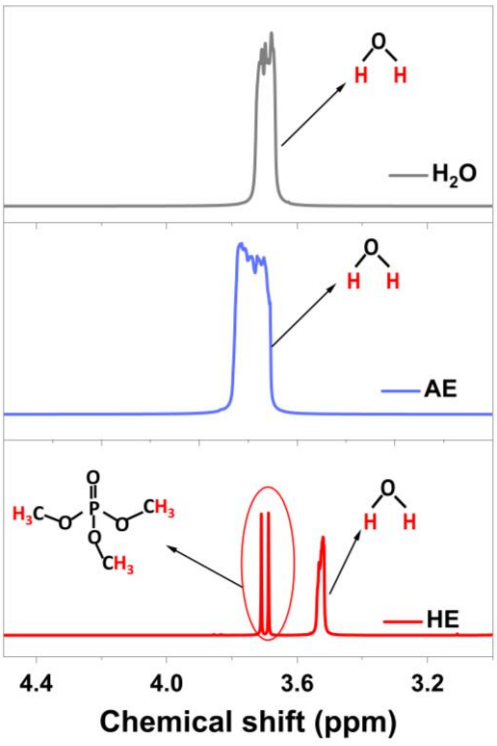

Figure 4.6 ^1H NMR spectra for pure water, AE and HE.

^1H nuclear magnetic resonance (NMR) spectroscopy confirmed that H_2O molecules are under influence from other molecules in HE. As is shown in **Figure 4.6**, water protons resonate at *ca.* 3.7 ppm for pure water. This peak broadens in AE because water molecules are involved in the solvation clusters and induced by Zn^{2+} accompanying a partial transfer of electron from the water proton to the empty orbitals of Zn^{2+}. The reduced electron density on the water proton

deshields the H nucleus, and the proton resonance frequency shifts downfield. The water protons have a significant upfield shift of ~ 3.52 ppm in HE, evidencing that the electron density of water proton for HE increases compared with that for pure water and AE. Electron-rich regions of DMAC and TMP, C=O and P=O groups, increase the electron density of water protons when interacting with water, resulting in shielding of water protons. This significant shift of water proton resonance frequency highlights that the dipole-dipole interactions between DMAC/TMP and water are strong, and that it exists both in the solvation sheaths of Zn^{2+} and amongst the molecules that are out of the solvation structure.

Under the influence of DMAC/TMP, water molecules exhibit boosted O−H bonds and become less likely to decompose. The deprotonation energy for H^+ dissociation from H_2O in the Zn^{2+} inner solvation shell was therefore investigated using DFT, **Figure 4.7**. For AE, the deprotonation energy for $[Zn(H_2O)_6]^{2+}$ was computed to be −4.94 eV. In HE, using the representative solvation structure $[Zn(H_2O)_3(DMAC)_1(TMP)_1(OTf)_1]^+$, the deprotonation energy is −2.43 eV on average, evidencing that H^+ dissociation from H_2O is less favorable in HE than in AE.

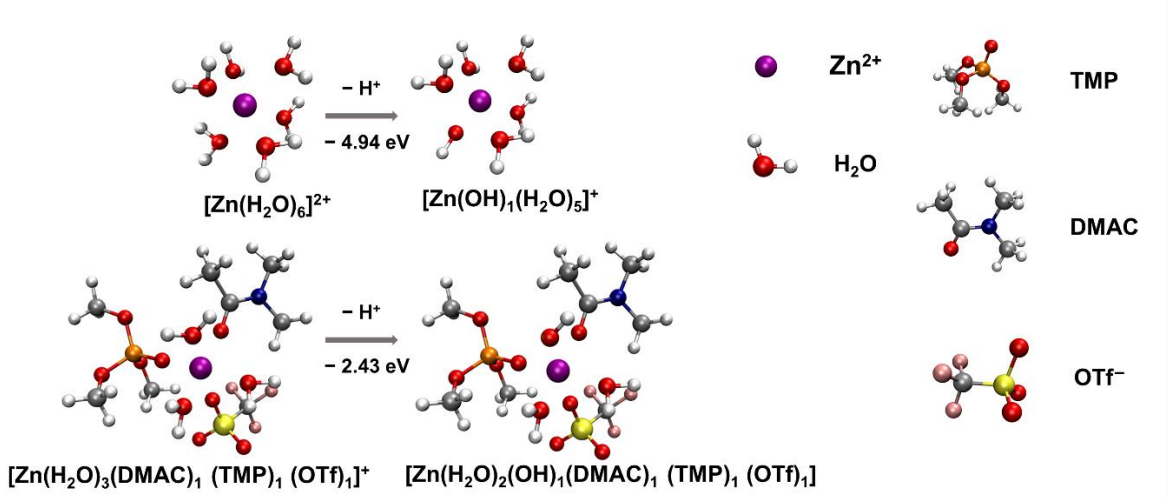

Figure 4.7 Deprotonation (H^+ dissociation of H_2O) energy from Zn^{2+} inner solvation shell of AE and HE.

The ESW of HE is measured by linear sweep voltammetry (LSV), and it is stable up to 2.25 V at a scanning rate of 1 mV S^{-1}, obviously higher than that of AE (1.93 V), confirming the higher stability of water molecules in HE than that in AE (**Figure 4.8**). 3-electrode cyclic voltammetry (CV) is conducted to evaluate the reversibility of Zn in AE and CE, respectively. The

Coulombic efficiency (CE) of Zn plating/stripping is 97.1% for HE, higher than 91.6% of AE, **Figure 4.9**.

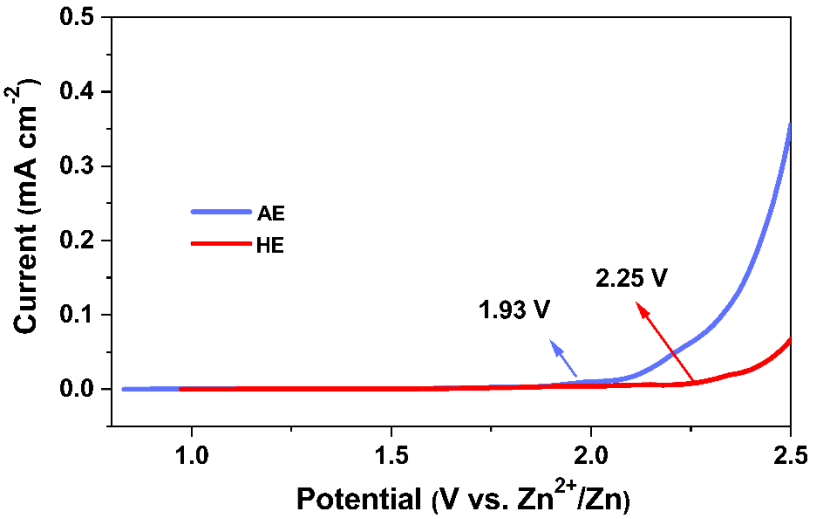

Figure 4.8 ESW for AE and HE measured in Zn||Ti battery at a scan rate 1 mV s^{-1}

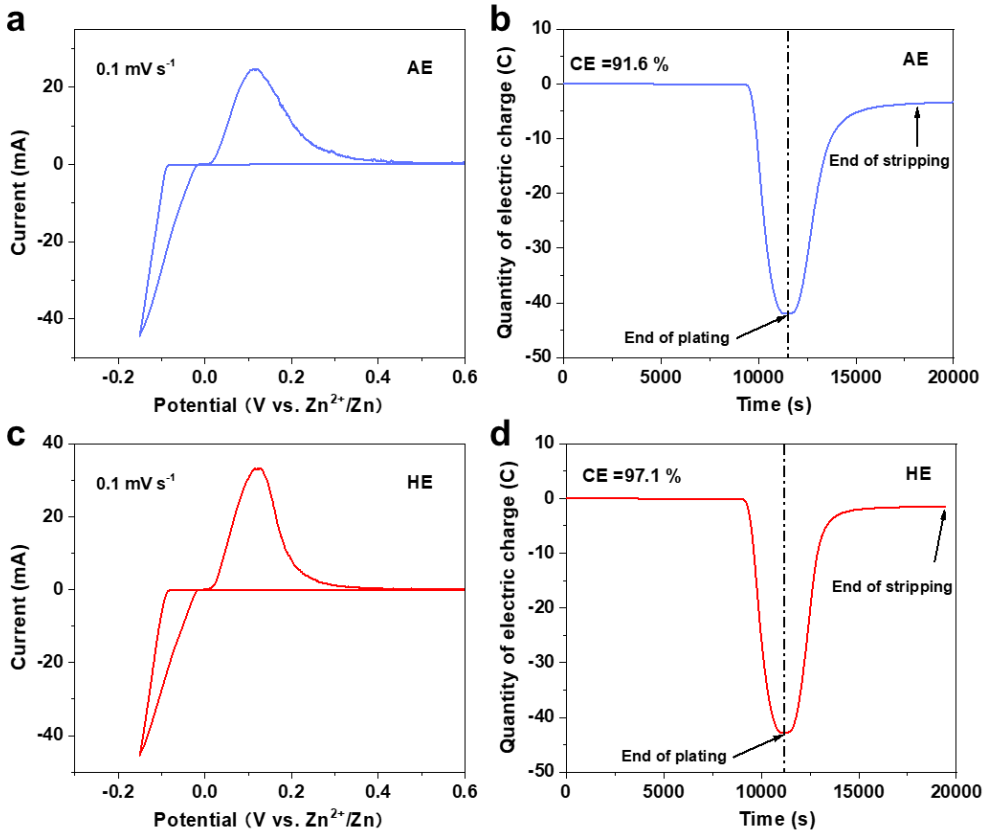

Figure 4.9 3-electrode CV curves and the corresponding CE of Zn plating/stripping in (a-b) AE and (c-d) HE. The working electrode is Cu foil, couter and reference elecyrode is Zn foil.

Figure 4.10 presents the lifespan and CE for Zn||Cu batteries using AE and HE as the electrolyte at, respectively, a current density 1 mA cm^{-2} and plating/stripping capacity of 1 mAh cm^{-2}. It is seen in the figure that HE exhibits a highly significant improvement in stability and reversibility for the Zn anode with a CE as high as 99.5 %.

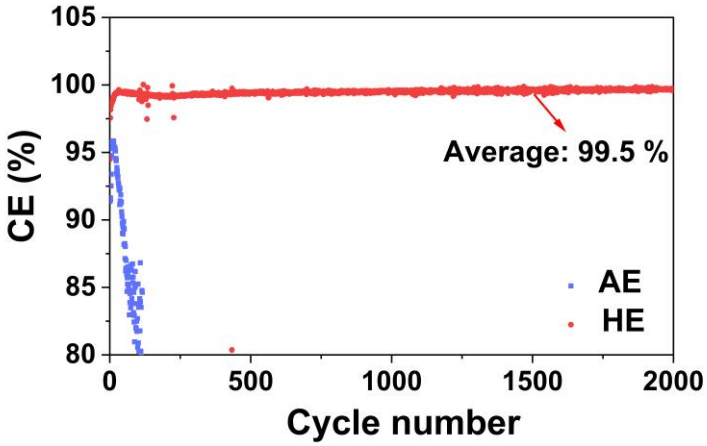

Figure 4.10 CE for Zn||Cu cells using AE and HE as the electrolyte, respectively. The current density is 1 mA cm^{-2} and the plating capacity is 1 mAh cm^{-2}.

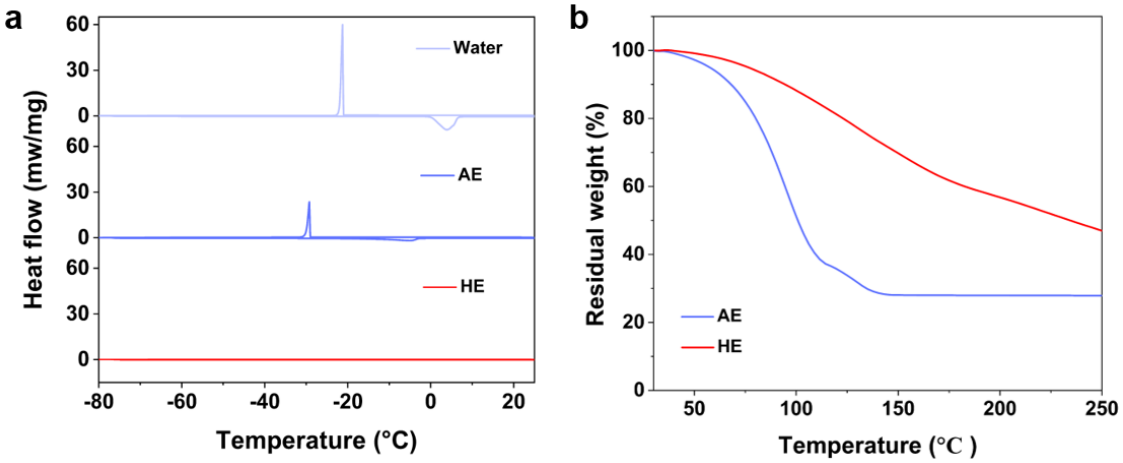

Figure 4.11 (a) DSC curves of water, AE and HE; (b) TGA curves for AE and HE under N_2 atmosphere using a heating rate of 20 °C min^{-1}.

To investigate the operating temperature of AE and HE, differential scanning calorimetry (DSC) and thermogravimetric analysis (TGA) were conducted. For AE, there is an exothermic peak at around −29 °C corresponding to the crystallization of electrolyte and an endothermic peak at −4 °C corresponding to the melting point. In contrast, no exothermic/endothermic peaks are observed for HE even with the temperature cooling down to −80 °C (**Figure 4.11**). The TGA curves show that AE loses weight faster than HE because of fast H_2O volatilization. While in HE, the strong interactions between H_2O and DMAC/TMP effectively reduce volatilization effects, increasing the stability of HE at high temperatures.

Table 4.1 The ionic conductivity and viscosity of AE and HE.

Temperature	AE		HE	
	Ionic conductivity (mS cm^{-1})	Viscosity mPa s^{-1}	Ionic conductivity (mS cm^{-1})	Viscosity mPa s^{-1}
70 ℃	65.8	0.96	22.1	3.73
50 ℃	58.7	1.16	17.1	5.66
25 ℃	49.1	1.77	9.0	11.65
0 ℃	28.4	3.59	5.1	25.62
−20 ℃	—	—	2.1	155.13
−40 ℃	—	—	0.73	1307

The ionic conductivity and viscosity of AE and HE are given in **Table 4.1**. AE has advantages in both conductivity and viscosity at temperatures > 0 ℃. Walden's rule reveals that the product of molar conductivity (Λ) of a liquid solution and its viscosity (η) is a constant at a given temperature, as expressed by the following equation:

$$\Lambda \eta = C = \text{Constant} \quad (1)$$

$$\log \Lambda = \log C + \log \eta^{-1} \quad (2)$$

The data of a dilute aqueous KCl solution, an ideal solution that all ions are dissociated, can be used as the "ideal" Walden line. In Figure 4.30, both the Walden plot of AE and HE are very close to the "ideal" line, indicating that the $Zn(OTf)_2$ salt is well dissociated in these two electrolytes.

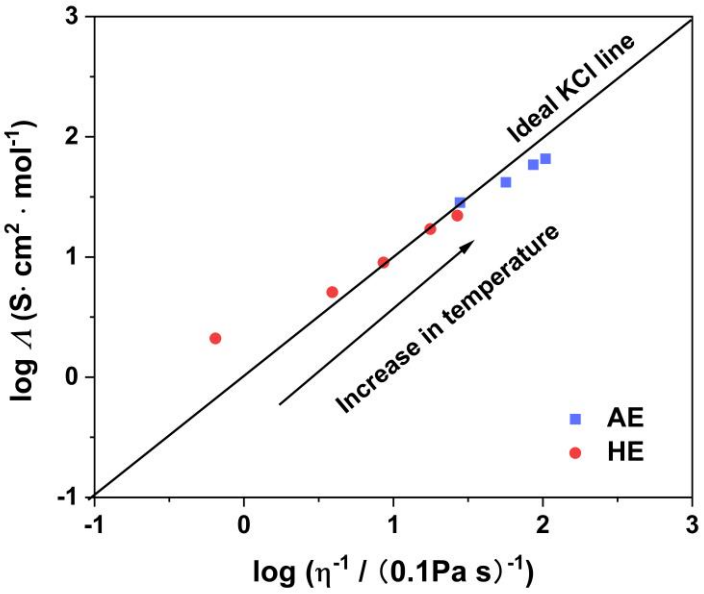

Figure 4.12 Walden plot of temperature-dependent conductivities and viscosities for AE and HE.

4.4 Zn deposition in HE

Solvents significantly impact the morphology evolution of the formation of solid metallic Zn from the liquid electrolyte. When deposited in AE, 'flaky' metallic Zn loosely piles up, resulting in a porous deposition layer on the copper current collector, **Figure 4.13a**. When this flaky Zn loses contact with the conductive substrate, it becomes inactive and irreversible in subsequent plating/stripping. Moreover, the non-planar, porous morphology leads to an inhomogeneous local charge density distribution and therefore induces unwanted dendrite growth that leads to a short circuit. In contrast, the deposited Zn in HE exhibits a close-packed and stepped-surface with a hexagonal-like crystalline structure, **Figure 4.12b,** a typical characteristic of (002) plane preferred crystal orientation[31, 32, 33]. Besides, intensity of the 002 reflection in its XRD pattern increases markedly compared with that in commercial Zn foil and Zn deposited in AE, **Figure 4.14**. The exposed (002) basal plane has a relatively smooth surface and therefore conducive to dendrite-free deposition of Zn^{2+} ions.

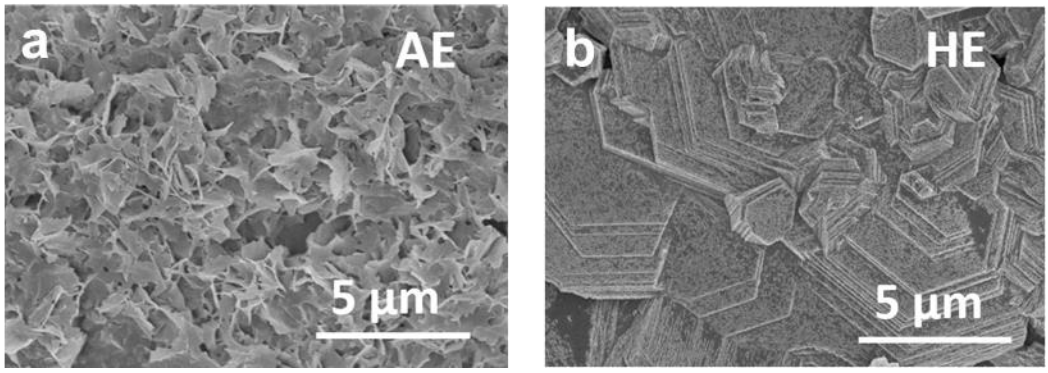

Figure 4.13 Surface morphology for deposited Zn in (a) AE and (b) HE.

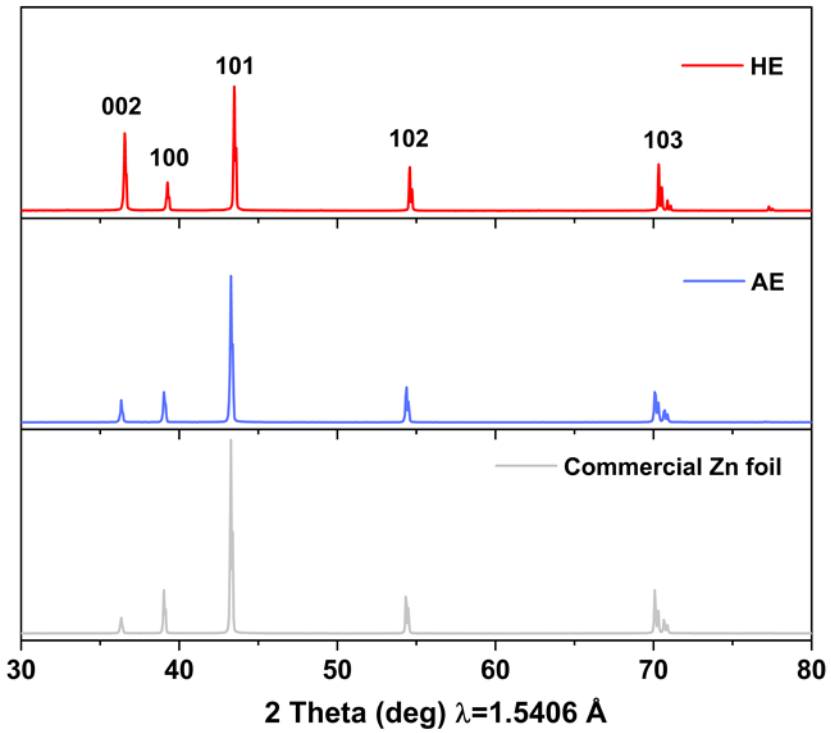

Figure 4.14 The XRD patterns for commercial Zn-foil, Zn deposited in AE and in HE.

To more directly observe Zn electrodeposition, real-time images of the Zn/electrolyte interface were captured *via* an optical microscope, **Figure 4.15**. It can be seen in the figures that several 'sharp' protuberances appear in the initial stage when Zn is deposited in AE, and these continually grow because additional Zn^{2+} is attracted and accumulated on the tips. In contrast, Zn deposition in HE is significantly more uniform and compact, and no protuberance is seen during the entire deposition.

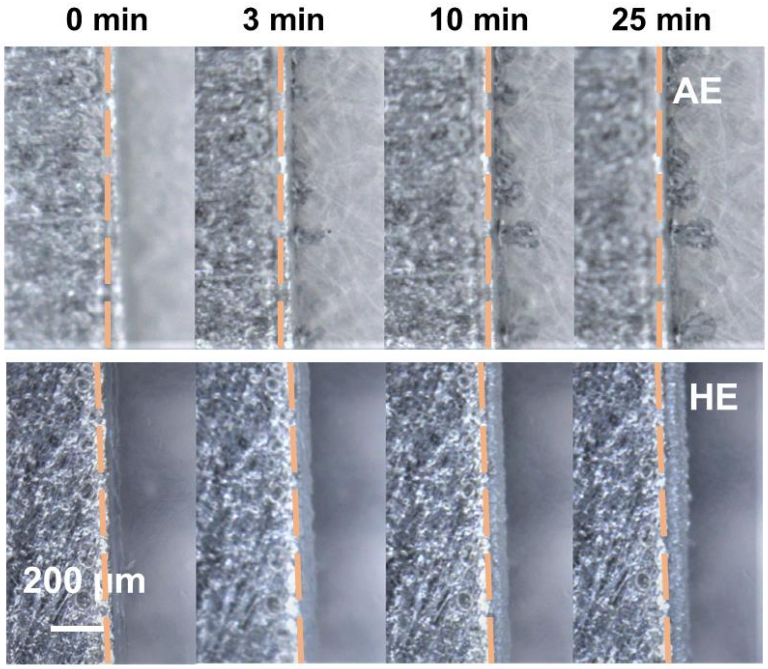

Figure 4.15 Optical microscopy image of Zn/electrolyte interface during Zn deposition in AE and HE.

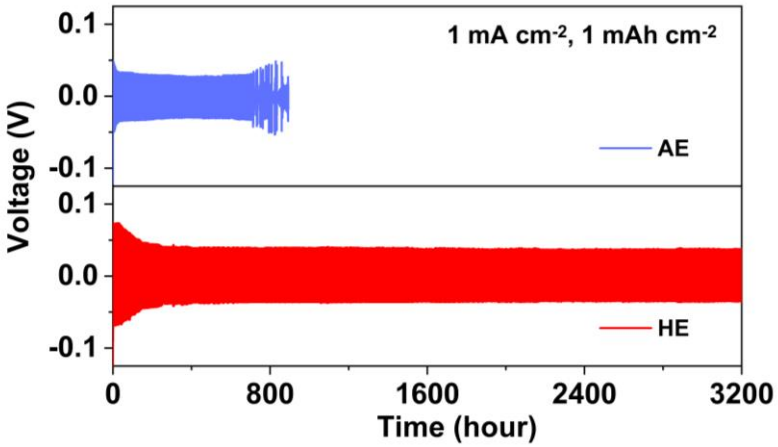

Figure 4.16 Voltage profile for Zn||Zn symmetric cell working in AE and HE, respectively. Applied current density is 1 mA cm^{-2} and plating capacity 1 mAh cm^{-2}.

Because a principal requirement for a Zn anode is to remain robust with extensive cycling, galvanostatic plating/stripping with Zn||Zn batteries is widely used as a test to determine the lifespan in different electrolytes. When a 'regular' current density of 1 mA cm^{-2} and plating

capacity 1 mAh cm^{-2} was applied, the lifespan of the Zn anode in AE was *ca.* 750 h, whilst it was > 3200 h in HE, **Figure 4.16**. When the current density and cycling capacity were increased to, respectively, 5 mA cm^{-2} and 5 mAh cm^{-2} as is presented in **Figure 4.17**, the Zn||Zn battery with AE as electrolyte exhibited a highly significant decrease after 70 h, indicating the anode failed because dendrites penetrated the separator and caused a short-circuit. However in HE the anode worked stably for > 1600 h. This finding is attributed to the preferred orientation of the (002) plane during Zn plating, which has dendrite-free morphology during cycling.

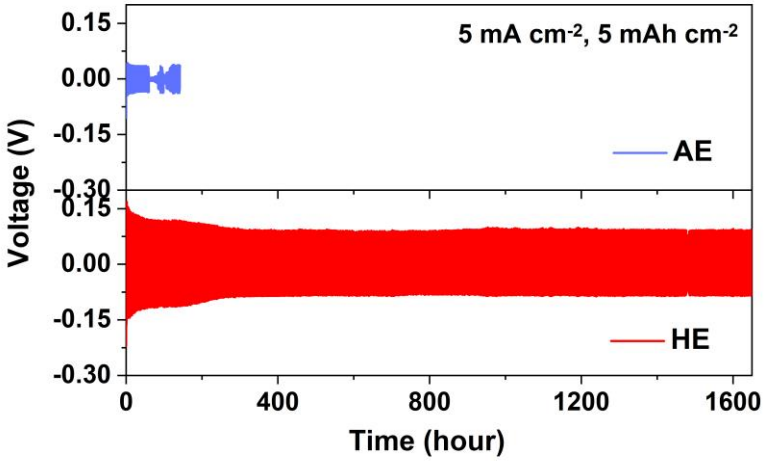

Figure 4.17 Voltage profile for Zn||Zn symmetric cell working in AE and HE, respectively. Applied current density is 5 mA cm^{-2} and plating capacity 5 mAh cm^{-2}.

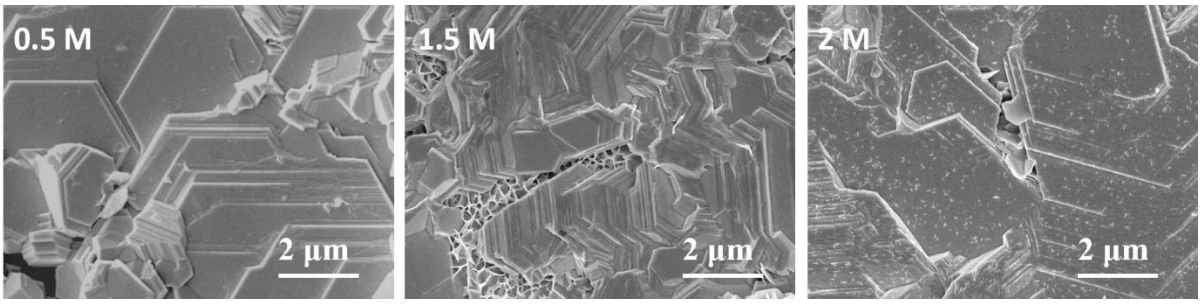

Figure 4.18 Surface morphology for deposited Zn in hybrid electrolyte with differing $Zn(OTf)_2$ concentration. Solvents are DMAC/TMP/H_2O in volume ratio of 5:2:3.

Because the solidification transition for Zn^{2+}/Zn occurs in a solvent medium, we investigated how salt concentration and solvent components of the electrolyte impact morphology of deposited Zn. It was concluded that salt concentration was not the decisive factor because the

special orientation appears also in 0.5, 1.5 and 2 M hybrid solution of $Zn(OTf)_2$ (**Figure 4.18**). With DMAC and TMP as the single solvent and 1 M $Zn(OTf)_2$ as salt, the morphology for Zn deposited in these two electrolytes is porous and irregular without preferred orientation (**Figure 4.19**). It was concluded that DMAC/TMP/H_2O hybrid solvents are crucial in Zn plating.

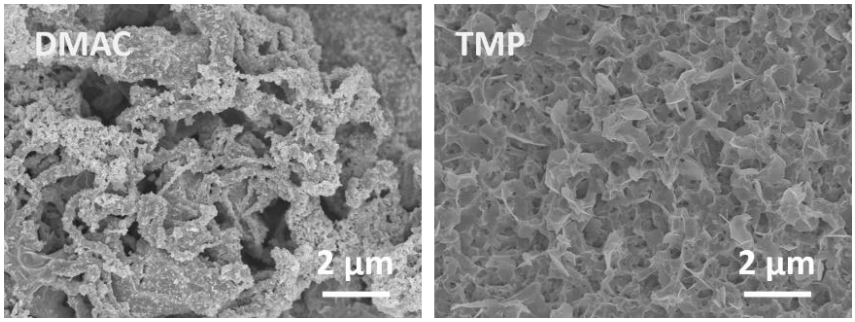

Figure 4.19 Surface morphology for Zn deposited in 1 M $Zn(OTf)_2$ with DMAC and TMP as single solvent.

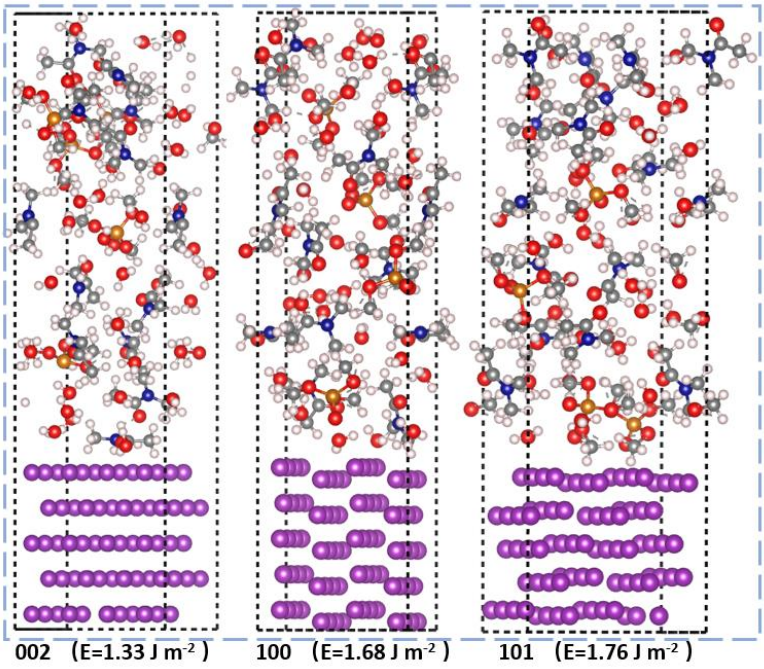

Figure 4.20 Surface energy for (002), (100) and (101) plane of metallic Zn when exposed in mix of DMAC/TMP/H_2O (5:2:3 by volume).

Generally, crystallographic texture is determined by different growth rates amongst crystallites of various orientations, governed by surface energy minimization[34]. Density functional theory (DFT) computations were therefore carried out to determine the surface energy of three main

planes, namely, Zn (002), (100) and (101), in a solvent environment. Surface energy, the excess energy presented at a particular surface, determines the exposed facets and growth orientation of the crystal. It can be modified by solvent molecules *via* interactions[35, 36]. As a result, the surface energy values for Zn (002), (100) and (101) alter when they are exposed to different solvents. **Figure 4.20** shows that Zn (002) exhibits the lowest surface energy of 1.33 J m^{-2}, in the mix of DMAC/TMP/H_2O (5:2:3 by volume) compared with the (100) and (101) planes, which are, respectively, 1.68 and 1.76 J m^{-2}. This thermodynamic difference implies that the metallic Zn maximizes expression of the (002) plane to minimize the total surface energy of the crystal, accounting for the dominant (002) plane in metallic Zn growth. However, when exposed to water, the surface energy of the (002) plane increases to 1.85 J m^{-2}, higher than that of (100) and (101) planes, which are 1.48 and 1.24 J m^{-2}, respectively, **Figure 4.21**.

In DMAC, the surface energy for the (101) plane is less than that for the (002) plane, and therefore (101) has the greatest proportion of exposure and not (002) plane, **Figure 4.22**. It is seen from **Figure 4.23** that DMAC/TMP/H_2O hybrid solvent in a volume tatio of 5:2:3 is the reason of (002) plane prederred orientation during the Zn deposition.

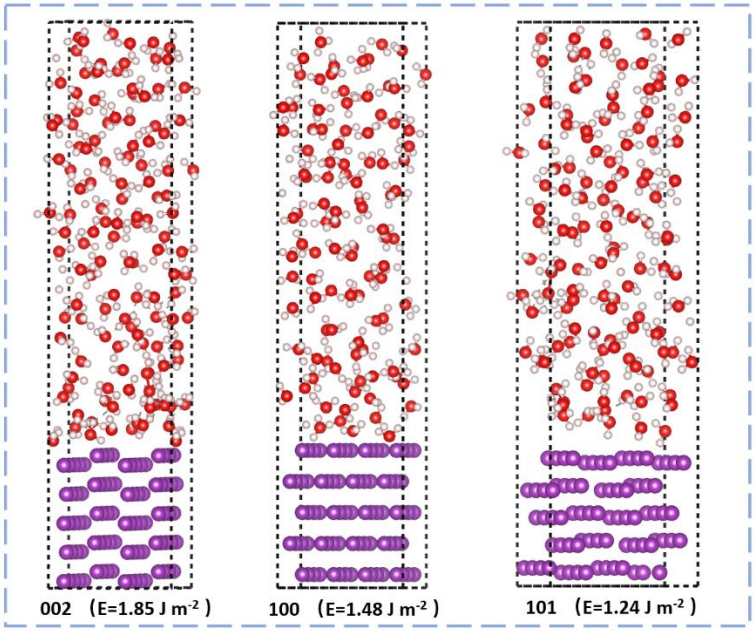

Figure 4.21 Surface energy for (002), (100) and (101) plane of metallic Zn when exposed in pure H_2O.

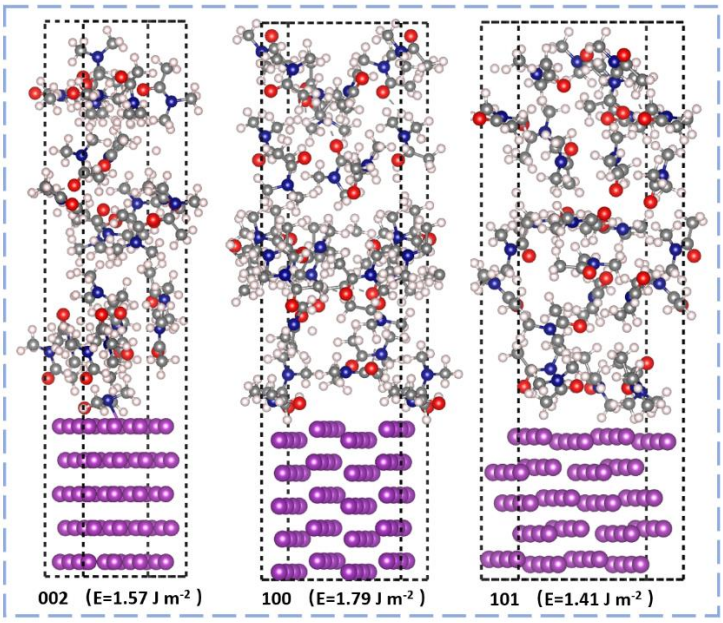

Figure 4.22 Surface energy for (002), (100) and (101) plane of metallic Zn when exposed in DMAC.

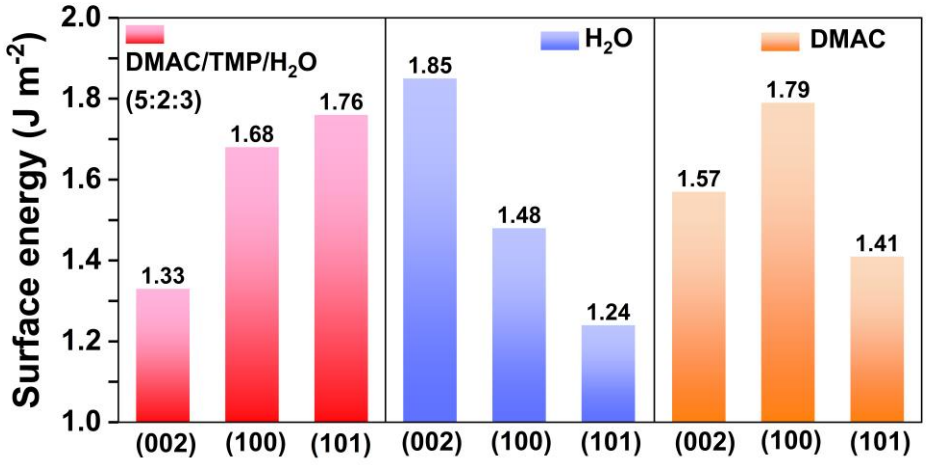

Figure 4.23 Surface energy value for main planes of metallic Zn in the liquid environment of DMAC/TMP/H_2O (5:2:3 by volume), H_2O and DMAC, respectively.

4.5 Stability against Zn metal anode

The OTf^- anion in the electrolyte also interacts with the solvent. To confirm the solvation structure for OTf^- anion, Raman spectroscopy was carried out on $Zn(OTf)_2$ and solutions with various solvents, **Figure 4.24**. The $-CF_3$ symmetric and asymmetric deformation mode for

$Zn(OTf)_2$ powder is seen at 767.9 cm^{-1} and 584.5 cm^{-1}, respectively. It was found that these two (2) peaks shift slightly in AE, evidencing an interaction between H_2O and OTf^- anion. The signals for $-CF_3$ shift when $Zn(OTf)_2$ is dissolved in TMP and DMAC, evidencing strongly that OTf^- anion coordinates with them. However, the signals for $-CF_3$ overlap with that for TMP and DMAC molecules, **Figure 4.25**, making it practically difficult to identify which solvent molecule the OTf^- anion interacts with most within the HE.

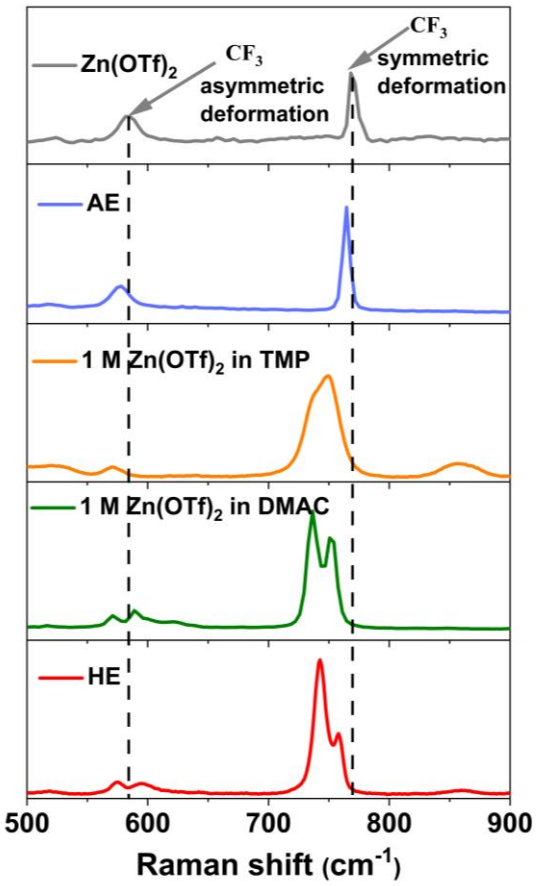

Figure 4.24 Raman spectra for $Zn(OTf)_2$ and selected electrolytes.

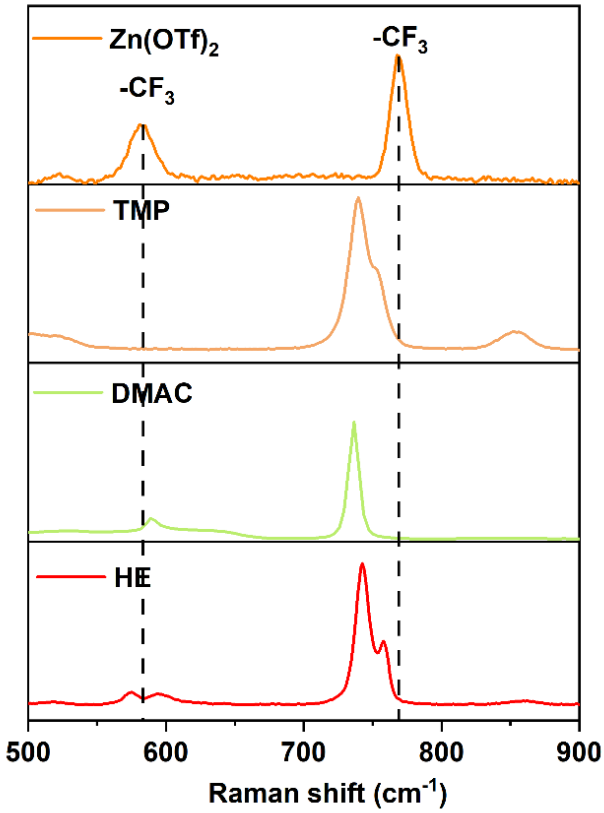

Figure 4.25 Raman spectra for $Zn(OTf)_2$, TMP, DMAC and HE.

Nuclear magnetic resonance (NMR) spectroscopy can be used for complementary data on the chemical environment of the OTf^- anion. **Figure 4.26** shows the ^{19}F resonance frequencies for $Zn(OTf)_2$ solutions with, respectively, H_2O, TMP and DMAC as a single solvent. The ^{19}F signal for these electrolytes appears as a 'sharp', narrow peak at *ca.* −77.8 ppm. Because of different coordination molecules, the chemical shifts are different. The chemical shift for ^{19}F in HE is the same as that in DMAC, evidencing that OTf^- anions have the same chemical environment in DAMC solution and HE. In other words, OTf^- anions are surrounded mainly by DMAC molecules in HE. In a single solvent, DMAC, H_2O and TMP all coordinate with OTf^- anion to some degree, however competition for anions occurs in DMAC/H_2O/TMP mixture. DMAC molecule gains because its electron-rich acyl group exhibits much stronger interaction with $-CF_3$, a strong electron-withdrawing group. Consequently, the OTf^- anion in HE is similar in character with the DMAC solution, with (almost) no anion decomposition.

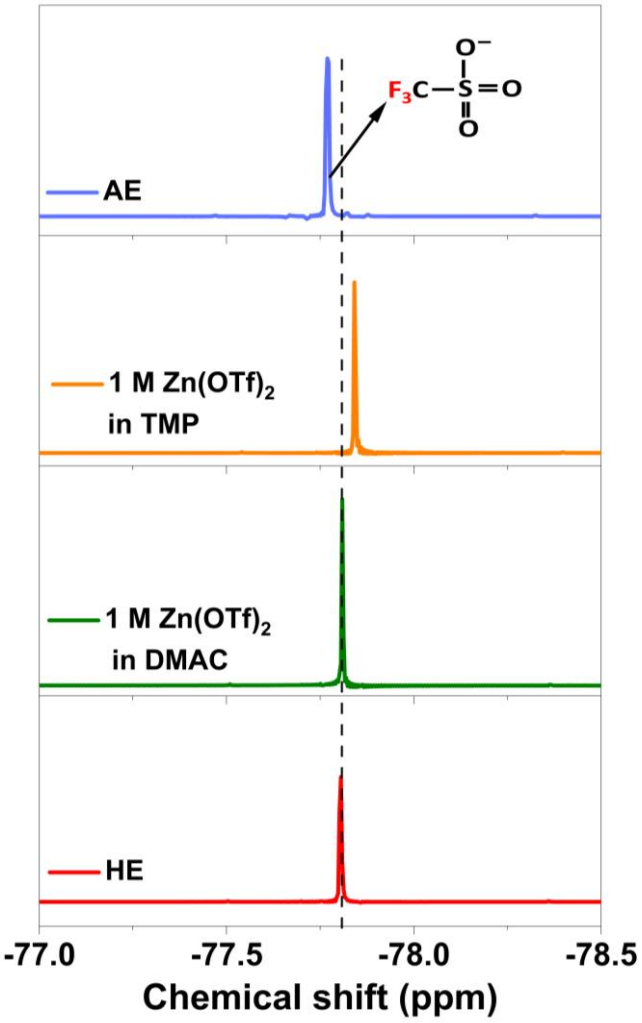

Figure 4.26 ^{19}F NMR spectra for selected electrolytes.

Corrosion of the Zn anode is investigated by immersing the Zn foil in AE and HE for 72 h. Zn foil suffered severe corrosion in AE and was covered with a layer of anion-derived by-products, **Figure 4.27 b and d.** However, Zn-foil immersed in HE exhibits a smooth surface with only 'slight' corrosion spotting, which is also confirmed by the smaller corrosion current (icorr) obtained in the Tafel plots (**Figure 4.27 c and e**). A quantitative analysis of the corrosion rate of metallic Zn in these two electrolytes was conducted by monitoring the potential changes of Zn over time. Initially, a fixed amount of Zn, 0.5 mAh, was deposited onto the Ti foil to form a Zn@Ti electrode, and once all metallic Zn was corroded by the electrolyte, the potential of the Zn@Ti electrode increased significantly. It is calculated that the corrosion rate of Zn in AE is around 0.043 mg h^{-1}, while that in HE is significantly reduced to just 0.003 mg h^{-1}, **Figure 4.28**

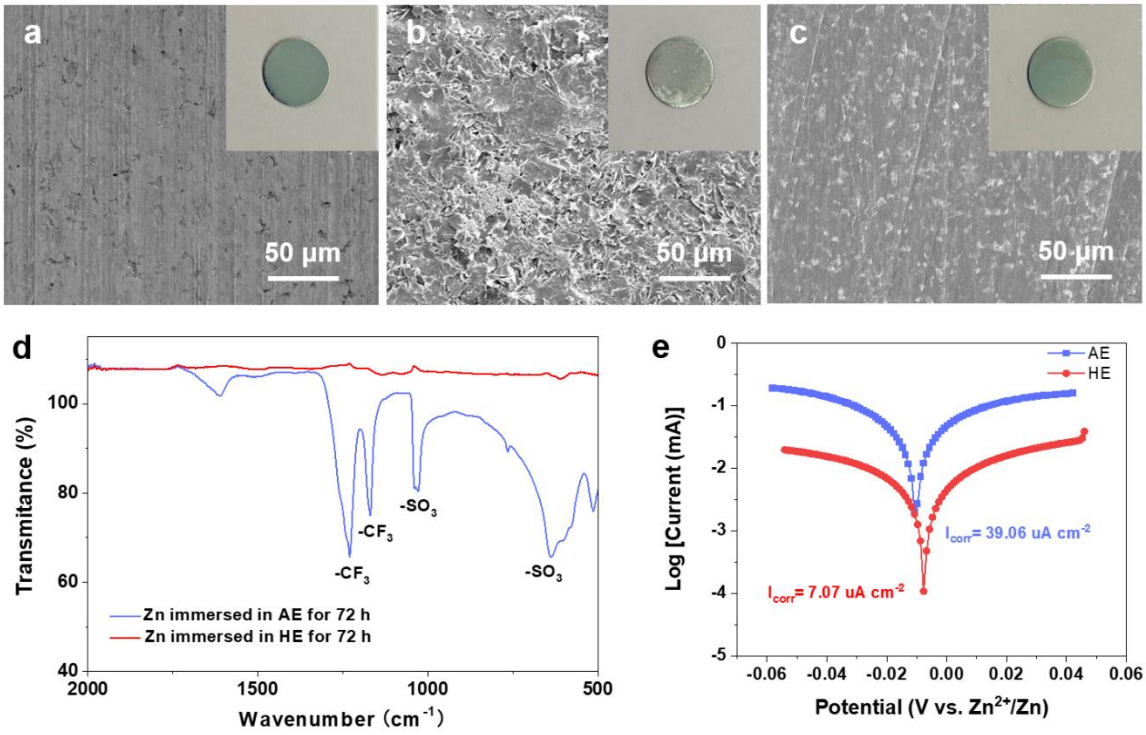

Figure 4.27 SEM images of (a) fresh Zn-foil and these immersed in AE (b) and (c) HE for 72 h. (d) FTIR spectra for Zn-foil immersed in AE and HE. (e) Tafel curves and corresponding corrosion current density for Zn anode in AE and HE. To avoid interference of Zn deposition, Zn^{2+} ion in AE and HE is replaced with Li^{+} ion.

X-ray photoelectron spectroscopy (XPS) was used to analyze the surface chemistry of Zn foil that had been cycled 100 times in AE and HE. For the Zn foil cycled in AE, strong signals appeared in the S 2p and F 1s spectrum, evidencing side reaction products from electrolyte decomposition on Zn-foil, specifically, $ZnSO_4$, ZnS and ZnF_2 [15], **Figure 4.29**. In contrast, no apparent by-products were detected on the Zn-foil cycled in HE, confirming the side reactions between electrolyte and metallic Zn are significantly suppressed. The significantly improved stability of HE is attributed to the strong DMAC/TMP−H_2O and DMAC−OTf^- interaction that restricts activity of water and anion. Moreover, a preferred orientation for the Zn (002) plane is found for the Zn-foil cycled 100 times in HE, confirming that the close-packed growth model with a layer-by-layer structure occurs in the initial plating and is maintained in the following cycling, **Figure 4.30b**. In contrast, the Zn-foil cycled in AE has a 'pulverized' surface which may result in the loss of active metallic Zn, **Figure 4.30a**.

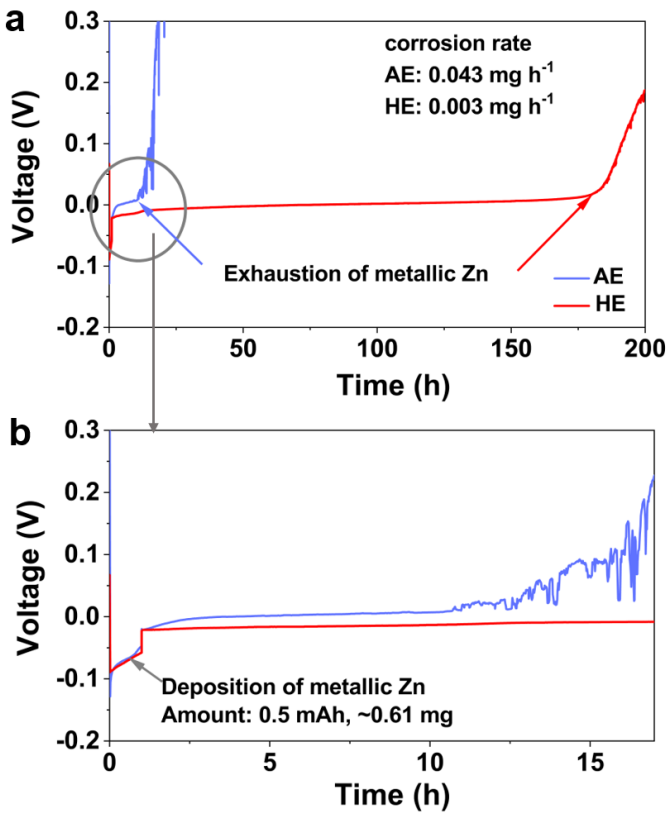

Figure 4.28 Voltage-time curves for Zn@Ti electrodes immersed in AE and HE, respectively. An amount of metallic Zn, 0.5 mAh, was deposited on Ti-foil to form Zn@Ti electrode.

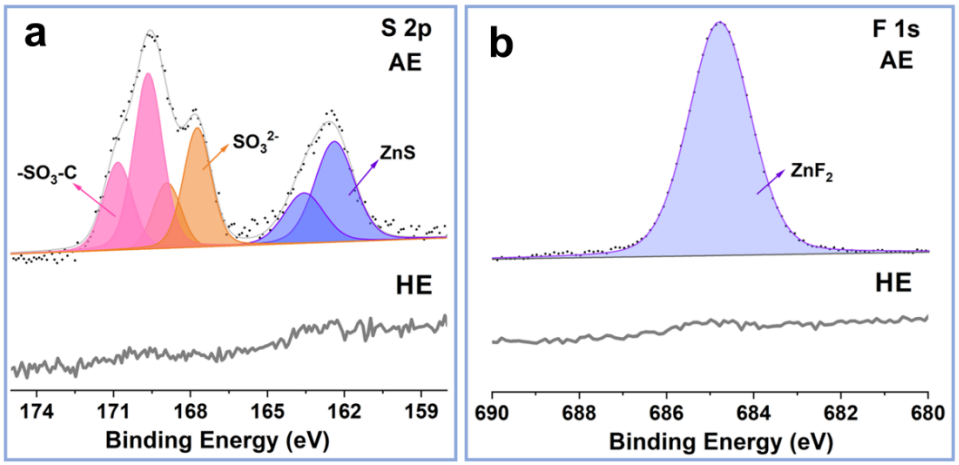

Figure 4.29 High-resolution XPS spectra of S 2p and F 1s for Zn foils following working in AE HE for 100 cycles, respectively.

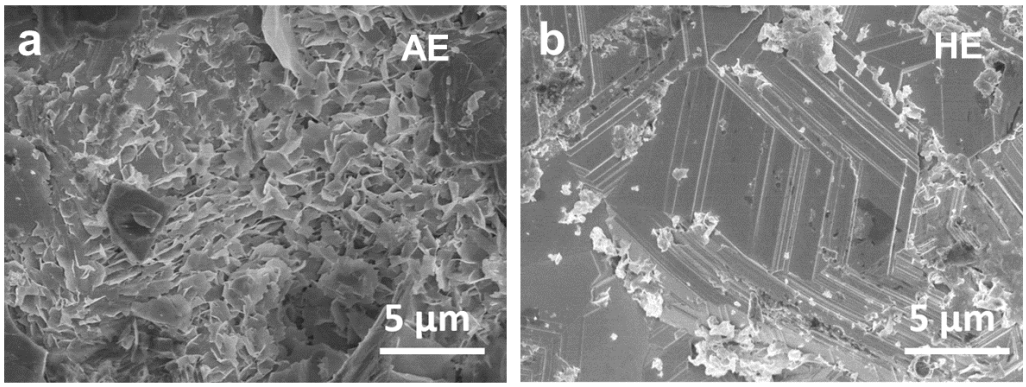

Figure 4.30 Morphology for Zn-foil following working in AE/HE for100 cycles.

The reversibility of Zn foil in AE and HE was further evaluated by applying high depth of discharge of Zn in the symmetric cell test. Initially, 4 mAh cm^{-2} of Zn is deposited on Cu foil to form the Zn@Cu electrode. **Figure 4.31** displays the cycling performance of Zn@Cu||Zn cells with a current density of 1 mA cm^{-2} and a plating/stripping capacity of 3 mAh cm^{-2}, corresponding to 75% depth of discharge. For the cell using AE as the electrolyte, the voltage increases rapidly after 90 hours, revealing that the Zn has been exhausted. By contrast, the rate of Zn consumption in HE is much lower and the Zn@Cu||Zn cell using HE can run up to 280 hours. This is because the side reactions between Zn and electrolyte are effectively suppressed in HE.

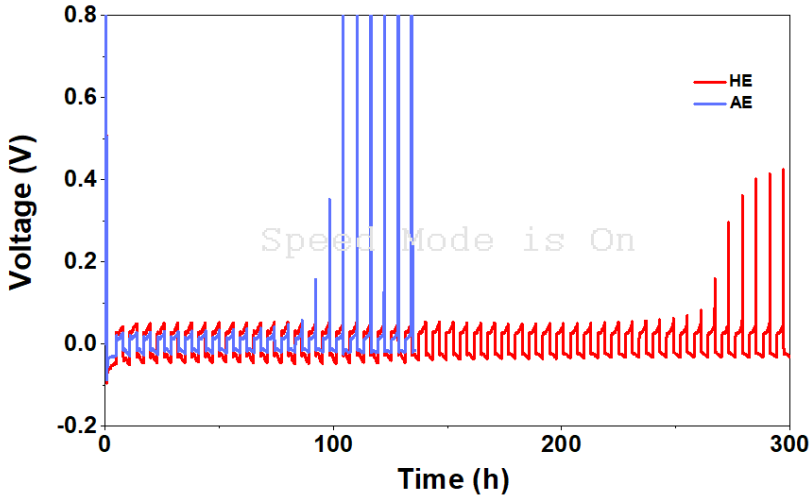

Figure 4.31 The Zn@Cu||Zn symmetric cell tests with AE and HE as the electrolyte, respectively. The capacity of the Zn@Cu electrode is 4 mAh cm^{-2}. The applied current density is 1 mA cm^{-2}, and the plating/stripping capacity is 3 mAh cm^{-2}.

4.6 The performance of Zn|| ZnHCFs cells in AE and HE

Zinc hexacyanoferrates (ZnHCFs) are an analogue of Prussian blue with a 3D open-framework structure. The large cubic interstices, 4.6 Å wide, provide enough space to accommodate bivalent Zn-ion, even in their solvated form. When combined with the Zn anode, the Zn||ZnHCFs battery exhibits an operation voltage of 1.7 V, which is the highest record for ZIBs. The intercalation chemistry of ZnHCF can be concluded as follows:

Cathode: $nZn^{2+} + 2ne^- + Zn_3[Fe(CN)_6]_2 \leftrightarrow Zn_{3+n}[Fe(CN)_6]_2$ (1)

Anode: $nZn \leftrightarrow nZn^{2+} + 2ne^-$ (2)

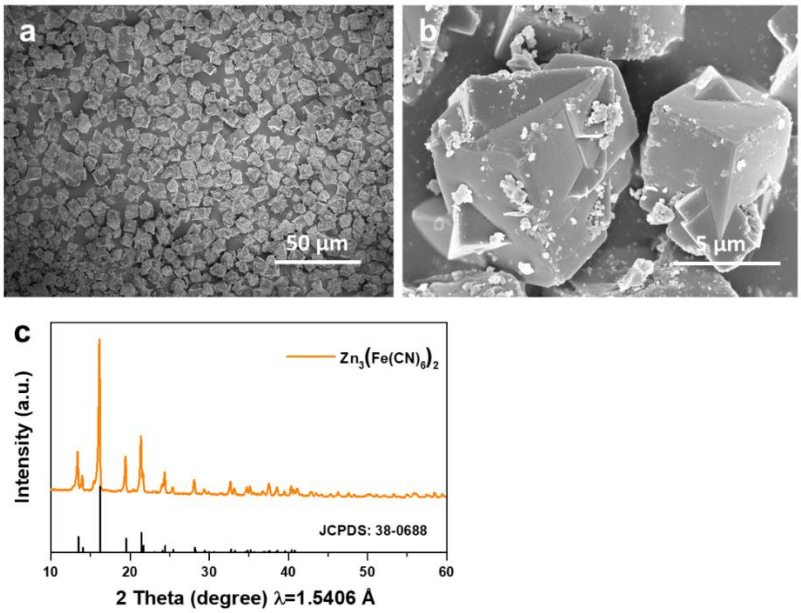

Figure 4.32 (a-b) The SEM images and (c) The XRD pattern of ZnHCFs powders.

The ZnHCFs is synthesized by the high temperature co-precipitation method. As shown in **Figure 4.32a-b**, as-synthesized powders have a uniform morphology with an average size of around 6-10 µm. The XRD pattern is well consistent with ZnHCFs (JCPDS # 38–0688), confirming that as-obtained materials are in high purity.

The initial specific capacity for Zn||ZnHCFs cells is ca. 60 mAh g^{-1} in both electrolytes (**Figure 4.33a**). However, it decreases rapidly in AE accompanied by voltage decay ((**Figure 4.33b-c**). The output voltage for ZnHCFs reduces to 1.6 ~ 1.4 V following 150 cycles in AE (**Figure 4.33d**). This is attributed to material degradation and less stability of H_2O at high voltage during charging, which causes relatively low CE. For AE, the oxidizing potential is measured to be 1.93 V vs. Zn^{2+}/Zn. At a cur-off voltage as high as 2 V, the decomposition of AE is inevitable. In contrast, the oxidizing potential of HE is up to 2.25 V, which is wider than the operation

potential of Zn||ZnHCFs cells. As a consequence, the Zn||ZnHCFs cell exhibits better stability in HE and the high-voltage character is well maintained following 150 cycles, evidencing that HE is compatible with the high-voltage cathode.

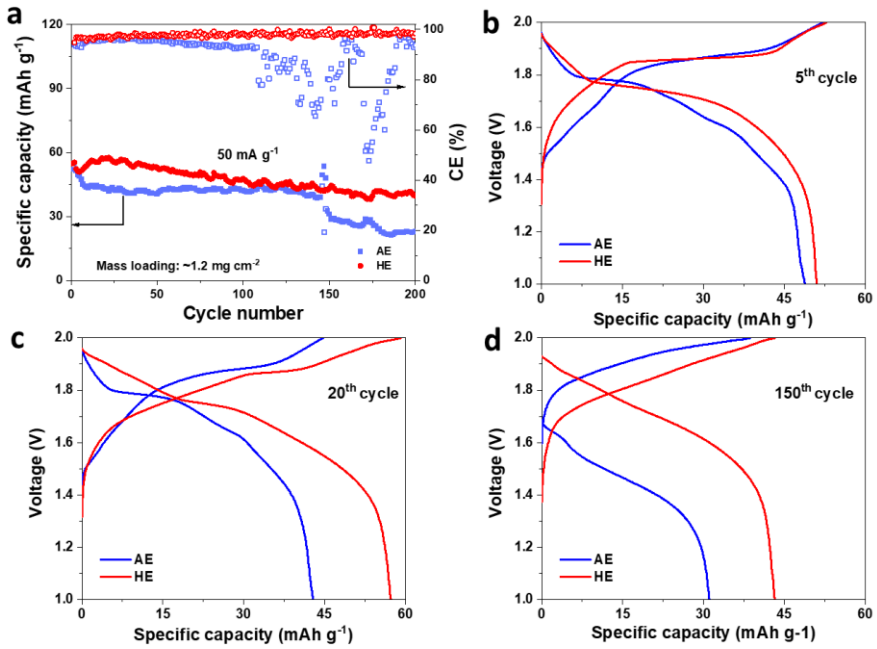

Figure 4.33 (a) Cycling performance of Zn||ZnHCFs cells tested at 50 mA g^{-1} in AE and HE; (b-d) the voltage profiles of the 5th, 20th and 150th cycles, respectively.

4.7 Conclusions

Polar solvents dimethylacetamide (DMAC) and trimethyl phosphate (TMP) in a hybrid electrolyte (HE) exert strong dipole-dipole interaction with H_2O to increase the electron density of water protons making the H_2O dissociation less thermodynamically favorable and therefore strengthening O−H bonds of water. Zn^{2+} plating in HE preferentially orientates the (002) plane because of the lower surface energy of this plane compared with (100) and (101) planes. With confined water activity and favorable orientation, a Zn anode in HE exhibited a high reversibility and ultra-long life in which CE was 99.5 % for 2000 cycles, and Zn||Zn symmetric cells ran for 1600 h at a current density 5 mA cm^{-2} and areal capacity 5 mAh cm^{-2}. Moreover, the extended ESW makes it possible for HE to cope with the high voltage cathode, ZnHCFs, which exhibits a specific capacity of ca.60 mAh g^{-1} for 200 cycles.

4.8 Reference

1. Zhang T, et al. Fundamentals and perspectives in developing zinc-ion battery electrolytes: a comprehensive review. Energy & Environmental Science **13**, 4625-4665 (2020).
2. Wang Z, et al. Building Artificial Solid-Electrolyte Interphase with Uniform Intermolecular Ionic Bonds toward Dendrite-Free Lithium Metal Anodes. Advanced Functional Materials **30**, 2002414 (2020).
3. Wang Y, et al. Electrolyte Engineering Enables High Performance Zinc-Ion Batteries. Small **n/a**, 2107033 (2022).
4. Xu C, et al. Energetic Zinc Ion Chemistry: The Rechargeable Zinc Ion Battery. Angewandte Chemie International Edition **51**, 933-935 (2012).
5. Liu C, et al. Electrolyte Strategies toward Better Zinc-Ion Batteries. ACS Energy Letters **6**, 1015-1033 (2021).
6. Guo S, et al. Fundamentals and perspectives of electrolyte additives for aqueous zinc-ion batteries. Energy Storage Materials **34**, 545-562 (2021).
7. Liu S, et al. From room temperature to harsh temperature applications: Fundamentals and perspectives on electrolytes in zinc metal batteries. Science Advances **8**, eabn5097.
8. Lv Y, et al. Recent Advances in Electrolytes for "Beyond Aqueous" Zinc-Ion Batteries. Advanced Materials **34**, 2106409 (2022).
9. Yang F, et al. Understanding H_2 Evolution Electrochemistry to Minimize Solvated Water Impact on Zinc-Anode Performance. Advanced Materials **34**, 2206754 (2022).
10. Na M, et al. Effects of Zn^{2+} and H^+ Association with Naphthalene Diimide Electrodes for Aqueous Zn-Ion Batteries. Chemistry of Materials **32**, 6990-6997 (2020).
11. Zuo Y, et al. Zinc dendrite growth and inhibition strategies. Materials Today Energy **20**, 100692 (2021).
12. Wang X, et al. Advances and Perspectives of Cathode Storage Chemistry in Aqueous Zinc-Ion Batteries. ACS Nano **15**, 9244-9272 (2021).
13. Li C, et al. Tuning the Solvation Structure in Aqueous Zinc Batteries to Maximize Zn-Ion Intercalation and Optimize Dendrite-Free Zinc Plating. ACS Energy Letters **7**, 533-540 (2022).

14. Liu S, et al. Monolithic Phosphate Interphase for Highly Reversible and Stable Zn Metal Anode. Angewandte Chemie International Edition **n/a**, e202215600 (2022).

15. Wang F, et al. Highly reversible zinc metal anode for aqueous batteries. Nature Materials **17**, 543-549 (2018).

16. Zhang Q, et al. Designing Anion-Type Water-Free Zn^{2+} Solvation Structure for Robust Zn Metal Anode. Angewandte Chemie International Edition **60**, 23357-23364 (2021).

17. Wang N, et al. Zinc–Organic Battery with a Wide Operation-Temperature Window from −70 to 150 °C. Angewandte Chemie International Edition **59**, 14577-14583 (2020).

18. Han S-D, et al. Origin of Electrochemical, Structural, and Transport Properties in Nonaqueous Zinc Electrolytes. ACS Applied Materials & Interfaces **8**, 3021-3031 (2016).

19. Kundu D, et al. Aqueous vs. nonaqueous Zn-ion batteries: consequences of the desolvation penalty at the interface. Energy & Environmental Science **11**, 881-892 (2018).

20. Liu S, et al. Tuning the Electrolyte Solvation Structure to Suppress Cathode Dissolution, Water Reactivity, and Zn Dendrite Growth in Zinc-Ion Batteries. Advanced Functional Materials **31**, 2104281 (2021).

21. Cao L, et al. Solvation Structure Design for Aqueous Zn Metal Batteries. Journal of the American Chemical Society **142**, 21404-21409 (2020).

22. Naveed A, et al. A Highly Reversible Zn Anode with Intrinsically Safe Organic Electrolyte for Long-Cycle-Life Batteries. Advanced Materials **31**, 1900668 (2019).

23. Li TC, et al. A Universal Additive Strategy to Reshape Electrolyte Solvation Structure toward Reversible Zn Storage. Advanced Energy Materials **12**, 2103231 (2022).

24. Naveed A, et al. Highly Reversible and Rechargeable Safe Zn Batteries Based on a Triethyl Phosphate Electrolyte. Angewandte Chemie International Edition **58**, 2760-2764 (2019).

25. Miao L, et al. Aqueous Electrolytes with Hydrophobic Organic Cosolvents for Stabilizing Zinc Metal Anodes. ACS Nano **16**, 9667-9678 (2022).

26. Ming F, et al. Co-Solvent Electrolyte Engineering for Stable Anode-Free Zinc Metal Batteries. Journal of the American Chemical Society **144**, 7160-7170 (2022).

27. Chang N, et al. An aqueous hybrid electrolyte for low-temperature zinc-based energy storage devices. Energy & Environmental Science **13**, 3527-3535 (2020).

28. Wang Y, et al. Electrolyte Engineering Enables High Performance Zinc-Ion Batteries. Small **18**, 2107033 (2022).

29. Petit T, et al. Unusual Water Hydrogen Bond Network around Hydrogenated Nanodiamonds. The Journal of Physical Chemistry C **121**, 5185-5194 (2017).

30. Chen S, et al. N,N-Dimethylacetamide-Diluted Nitrate Electrolyte for Aqueous Zn//$LiMn_2O_4$ Hybrid Ion Batteries. ACS Applied Materials & Interfaces **13**, 46634-46643 (2021).

31. Zheng J, et al. Reversible epitaxial electrodeposition of metals in battery anodes. Science **366**, 645-648 (2019).

32. Hao Y, et al. Gel Electrolyte Constructing Zn (002) Deposition Crystal Plane Toward Highly Stable Zn Anode. Advanced Science **9**, 2104832 (2022).

33. Wang S, et al. A highly reversible zinc deposition for flow batteries regulated by critical concentration induced nucleation. Energy & Environmental Science **14**, 4077-4084 (2021).

34. Tao AR, et al. Shape Control of Colloidal Metal Nanocrystals. Small **4**, 310-325 (2008).

35. Xia Y, et al. Shape-Controlled Synthesis of Metal Nanocrystals: Simple Chemistry Meets Complex Physics? Angewandte Chemie International Edition **48**, 60-103 (2009).

36. Potts DS, et al. Influence of solvent structure and hydrogen bonding on catalysis at solid–liquid interfaces. Chemical Society Reviews **50**, 12308-12337 (2021).

Chapter 5 Effect of the solvation structure on the energy storage mechanism of Zn-sodium vanadate batteries

In this chapter, the data is used in the work entitled as “Solvent control of water O−H bonds for highly reversible zinc ion batteries”, which has been accepted for publication. These data are presented together to reveal the different electrochemical performances of sodium vanadate in the hybrid and aqueous electrolytes. It is observed that the structural stability of the $NaV_3O_8 \cdot 1.5H_2O$ (NVO) cathode is significantly improved during continuous charging/discharging if fewer water molecules are involved in the intercalation processes of Zn^{2+} ions. This is the reason accounting for the longer lifespan of Zn||NVO cell obtained in the hybrid electrolyte compared to that in the aqueous electrolyte.

Statement of Authorship

Title of Paper	Solvent control of water O–H bonds for highly reversible zinc ion batteries
Publication Status	☐ Published ☑ Accepted for Publication ☐ Submitted for Publication ☐ Unpublished and Unsubmitted w ork w ritten in manuscript style
Publication Details	Yanyan Wang, Zhijie Wang, Wei Kong Pang, Wilford Lie, Jodie A. Yuwono, Gemeng Liang, Sailin Liu, Anita M. D'Angelo, Jiaojiao Deng, Yameng Fan, Kenneth Davey, Baohua Li, and Zaiping Guo.

Principal Author

Name of Principal Author (Candidate)	Yanyan Wang
Contribution to the Paper	Devised the idea, performed experiments, analyzed and interpreted data, wrote and revised the manuscript.
Overall percentage (%)	70%
Certification:	This paper reports on original research I conducted during the period of my Higher Degree by Research candidature and is not subject to any obligations or contractual agreements with a third party that would constrain its inclusion in this thesis. I am the primary author of this paper.
Signature	Date: 10 / Mar. / 2023

Co-Author Contributions

By signing the Statement of Authorship, each author certifies that:

i. the candidate's stated contribution to the publication is accurate (as detailed above);

ii. permission is granted for the candidate in include the publication in the thesis; and

iii. the sum of all co-author contributions is equal to 100% less the candidate's stated contribution.

Name of Co-Author	Zhijie Wang
Contribution to the Paper	Guided to design of the whole experiment, helped with data analysis, and revised the manuscript.
Signature	Date: 10 / Mar. / 2023

Name of Co-Author	Wei Kong Pang
Contribution to the Paper	Assisted in conducting experiment with *in operando* synchrotron-based X-ray powder diffraction (XRPD).
Signature	Date: 15 Mar 2023

Name of Co-Author	Wilford Lie		
Contribution to the Paper	Provided NMR test.		
Signature		Date	14/3-2023

Name of Co-Author	Jodie A. Yuwono		
Contribution to the Paper	Helped with DFT calculation.		
Signature		Date	10/03/2023

Name of Co-Author	Gemeng Liang		
Contribution to the Paper	Assisted to analyze the XRPD data.		
Signature		Date	13/03/2023

Name of Co-Author	Sailin Liu		
Contribution to the Paper	Assisted to conduct in situ FTIR test.		
Signature		Date	10/03/2023

Name of Co-Author	Anita M. D'Angelo		
Contribution to the Paper	Assisted in conducting experiment with *in operando* synchrotron-based XRPD.		
Signature		Date	14/03/2023

Name of Co-Author	Jiaojiao Deng		
Contribution to the Paper	Helped with DFT calculation.		
Signature		Date	14/03/2023

Name of Co-Author	Yameng Fan		
Contribution to the Paper	Assisted in XPS characterization.		
Signature		Date	13/03/2023

Name of Co-Author	Kenneth Davey		
Contribution to the Paper	Help to polish the manuscript.		
Signature		Date	14/03/2023

Name of Co-Author	Baohua Li		
Contribution to the Paper	Supervised development of work, helped in data interpretation and manuscript evaluation.		
Signature		Date	14/03/2023

Name of Co-Author	Zaiping Guo		
Contribution to the Paper	Supervised development of work, discussed the whole design, revised and conceptualized the manuscript.		
Signature		Date	10/03/2023

5.1 Introduction and significance

Energy sources are transitioning from fossil fuel dependence to renewable fuel dominance[1]. However, renewable energy sources such as solar and wind power are intermittent and therefore require battery technologies to store the excess energy generated during times of peak availability and to output energy when demand exceeds supply[2, 3]. Large-scale energy storage with batteries makes it possible to rely less on fossil fuels for a constant supply of energy. Zn-ion batteries (ZIBs) are a promising candidate for application in this field because of their high safety, low cost, and environment-friendliness[4]. Moreover, zinc is widely available in the Earth's crust, making ZIBs a more sustainable and cost-effective option than Li-ion batteries[4].

One of the challenges for ZIBs is the need for a stable cathode material that can host Zn^{2+} ions during repeated cycling. The divalent nature of Zn^{2+} ions increases the electrostatic interactions with the host materials and inhibits diffusion of Zn^{2+} ions in the cathode[5]. Because of the strong electrostatic interaction between the Zn^{2+} ions and the surrounding solvents, a significant desolvation penalty occurs for Zn^{2+} ions to take off the solvation sheath at the electrode-electrolyte interface[6]. It is worth noting that the desolvation penalty differs significantly from solvents, more specifically, the solvation structure of the Zn^{2+} ion. Therefore, the electrochemical performance of cathode materials in aqueous and non-aqueous electrolytes are dissimilar[7]. It is important to seek suitable electrolytes to boost the cycling stability of the cathode. Moreover, to meet the real application requirements, the cathode should be usable under outdoor temperatures and a wide range of current densities[8]. The intermittent working mode of ZIBs should also be considered, where the cathode is expected to hold the capacity as well as potential during the rest period[4].

Vanadium-based materials have been reported to accommodate Zn^{2+} ions in their lattices and to deliver quite a high specific capacity[9]. NVO is chosen as the research object because it can be synthesized on a large scale via a low-cost liquid-solid stirring strategy under ambient conditions, providing potential for real applications[10]. Moreover, NVO has a large interlayer distance of 0.77 nm, allowing for reversible Zn^{2+} insertion/extraction[11]. In the aqueous electrolyte environment, Zn^{2+} ions insert into the cathode together with protons in the discharging process, accompanied by the formation of $Zn_4SO_4(OH)_6{\cdot}4H_2O$[3]. This precipitate disappears in the fully charged state[10]. Therefore, the formation/vanishing of $Zn_4SO_4(OH)_6{\cdot}4H_2O$ functions as pH buffers in the electrolyte, and its reversibility is essential for the capacity retention of the cathode materials[12]. However, it may detach or delaminate from the electrode-electrolyte interface, especially during the resting periods, causing

irreversible electrochemical behavior[7]. This issue is not that notable when the NVO is charging/discharging uninterruptedly at high rates, but it causes significant capacity loss at low rates, < 0.5 A g^{-1}, or at rest periods[7].

Here we propose that the cycling stability of NVO cathode can be greatly boosted by designing rational solvation structures for Zn^{2+} ions and suppressing the generation of H^+. It is proven that the NVO cathode exhibits obviously reduced lattice distortion during (de)intercalation of Zn^{2+} in the hybrid electrolyte using dimethylacetamide (DMAC)/trimethyl phosphate (TMP)/H_2O as the solvent than that in aqueous electrolyte. The underlying reason is that only 3.7 water molecules are involved in the solvation structure of Zn^{2+} ions in the hybrid electrolyte, while there are 6 water molecules in the solvation structure of Zn^{2+} ion in aqueous electrolyte[13]. The water dissociation is also well suppressed because of the increased O-H bonds strength and therefore the H^+ insertion into NVO is mitigated and almost no $Zn_4SO_4(OH)_6{\cdot}4H_2O$ is found on the cycled NVO electrode in the hybrid electrolyte. The strong interactions between water and DMAC/TMP break the hydrogen-bonded water structure and reduce the dissociation of water at high temperature, enabling a wide operational temperature range of − 40 to 70 ℃ for Zn||NVO battery.

5.2 Experiments

Chemicals: Vanadium pentoxide (V_2O_5, 98 %), Dimethylacetamide (DMAC, 99.8 %), trimethyl phosphate (TMP, 99 %), zinc perchlorate hexahydrate ($Zn(ClO_4)_2{\cdot}6H_2O$, 99%) and zinc trifluoromethanesulfonate ($Zn(TSFI)_2$, 98%) were purchased from Sigma-Aldrich.

NVO synthesis: To 100 mL, 2 M L^{-1} NaCl solution add 3 g commercial V_2O_5 powder followed by magnetic stirring at 400 rpm for 72 h. As obtained orange-color powders are centrifuged and washed with deionized water and ethanol five (5) times and then dried at 80 ℃ for 10 h.

Characterization: X-ray Powder Diffraction (XRD) measurements on NVO powders were determined with a Rigaku MiniFlex600 with Cu Kα radiation. The Morphology of NVO powders were evidenced with a JEOL JSM-7500FA field emission scanning electron microscope. A Thermo Scientific Nexsa X-Ray Photoelectron Spectrometer System was used to determine XPS spectra of NVO electrodes. Cyclic voltammetry (CV) was conducted with a 3-electrode EL-CELL using well-polished Zn as the reference electrode. I*n operando* mechanistic studies on the NVO electrode were conducted with an *in operando* synchrotron-based X-ray diffraction at the Powder Diffraction beamline at the Australian Synchrotron. CR2032 coin cells with 4mm-diameter windows were especially prepared to ensure

synchrotron beam transmission, and Kapton tape was used to seal the holes to avoid electrolyte leaking. The wavelength of the synchrotron X-ray beam was 0.59040(1) Å or 0.68880(1) Å, as determined using $La^{11}B_6$ NIST standard reference material 660b. The customized coin cells were tested at a current density 100 mA g^{-1} between 0.3 and 1.6 V (*vs.* Zn/Zn^{2+}). The diffraction patterns were recorded with an exposure time of 3 minutes by an MYTHEN microstrip detector. Transmission electron microscopy (TEM) images were collected on FEI Titan Themis 80-200. The ionic conductivity of electrolytes was measured with a Thermo Scientific Orion electrochemistry meter, and the viscosity is measured with capillary viscometers (Huanguang Brand, Zhejiang, China) under certain temperatures.

Electrochemical Testing: Electrochemical data were collected from the Neware battery testers. To prepare the NVO electrodes, a slurry composed of active materials, Super P and polyvinylidene difluoride (PVDF) at a mass ratio of 7:1.5:1.5 was cast onto Ti-foil and followed with drying at 80 ℃ for 12 h. The mass loading of the NVO cathode ranges from 0.6-9.3 mg cm^{-2}. CR2032-type coin cells were used in all electrochemical tests. Zn foil (99.99%, 100 μm) is used as the anode. For batteries using aqueous electrolyte (AE), a glass-fiber membrane (740 μm) was used as the separator, and for those with hybrid electrolyte (HE) or non-aqueous electrolytes, nylon 66 membrane (130 μm) is used. The glass-fibre membrane was purchased from Filtech Pty Ltd, while the nylon 66 membrane was purchased from Shanghai Xinya Purification Equipment Co., Ltd.

5.3 Characterization of NVO cathode

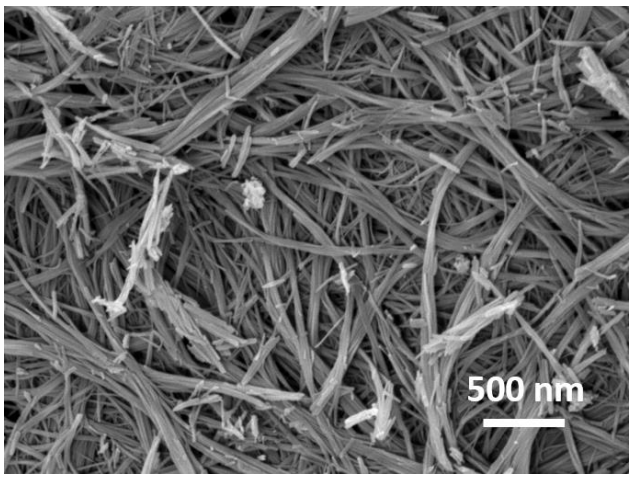

Figure 5.1 SEM image of NVO powders.

The as-synthesized material has a nano-belt morphology (**Figure 5.1**) and the XRD pattern (**Figure 5.2c**) identifies the crystalline phase of the as-synthesized material as NVO (JCPDS: 16–0601). A 0.77 nm interplanar spacing was observed in the high-resolution TEM image, corresponding to the (001) plane for NVO, **Figure 5.2b**. The lattice distance agrees well with the 250 ℃ heated NVO and not the 80 ℃ heated because the interlayer water was extracted in the high-vacuum sample chamber of TEM. The elemental mapping images (**Figure 5.2d**) further confirm the uniform distribution of Na, V and O.

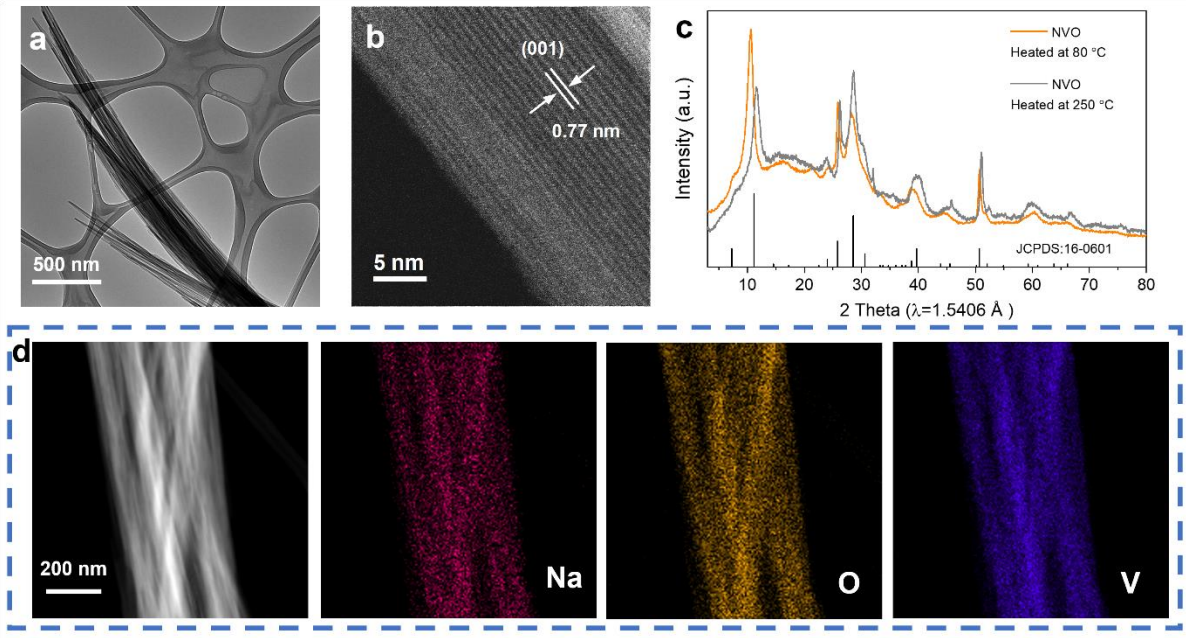

Figure 5.2 (a) The TEM image of NVO nanobelt; (b) The high-resolution TEM image; (c) XRD patterns of 80 ℃ heated and 250 ℃ heated NVO; (d) TEM elemental mapping images of NVO nanobelt.

Zn||NVO battery is assembled using a 3-electrode battery device for CV characterizations to determine the electrochemical properties of the NVO electrode. 1 M $Zn(OTf)_2$ dissolved in water is denoted as AE while 1 M $Zn(OTf)_2$ in DMAC/TMP/H_2O with a volume ratio of 5:2:3 is denoted as HE. As is shown in **Figure 5.3 a** and **c**, there are two oxidation peaks and three reduction peaks on each curve. It is acknowledged that the relationship between the peak current (i) and scan rates (v) is given by:

$$i = av^b \tag{3}$$

$$\log(i) = b\log(v) + \log(a) \tag{4}$$

where b is the slope of $\log(i)$ *vs*. $\log(v)$. Both in AE and HE the fitted plots of $\log(i)$ *vs*. $\log(v)$ (**Figure 5.3 b** and **d**) give the b value for the peaks between 0.5 to 1, evidencing that the

electrochemical reactions for NVO electrode are composited with ionic diffusion and pseudocapacitance control. To quantify, the capacitive contribution is computed from:

$$i = k_1 v + k_2 v^{1/2} \quad (5)$$

$$i/v^{1/2} = k_1 v^{1/2} + k_2 \quad (6)$$

where the current response of capacitive and ionic diffusion contribution is represented by $k_1 v$ and $k_2 v^{1/2}$, respectively.

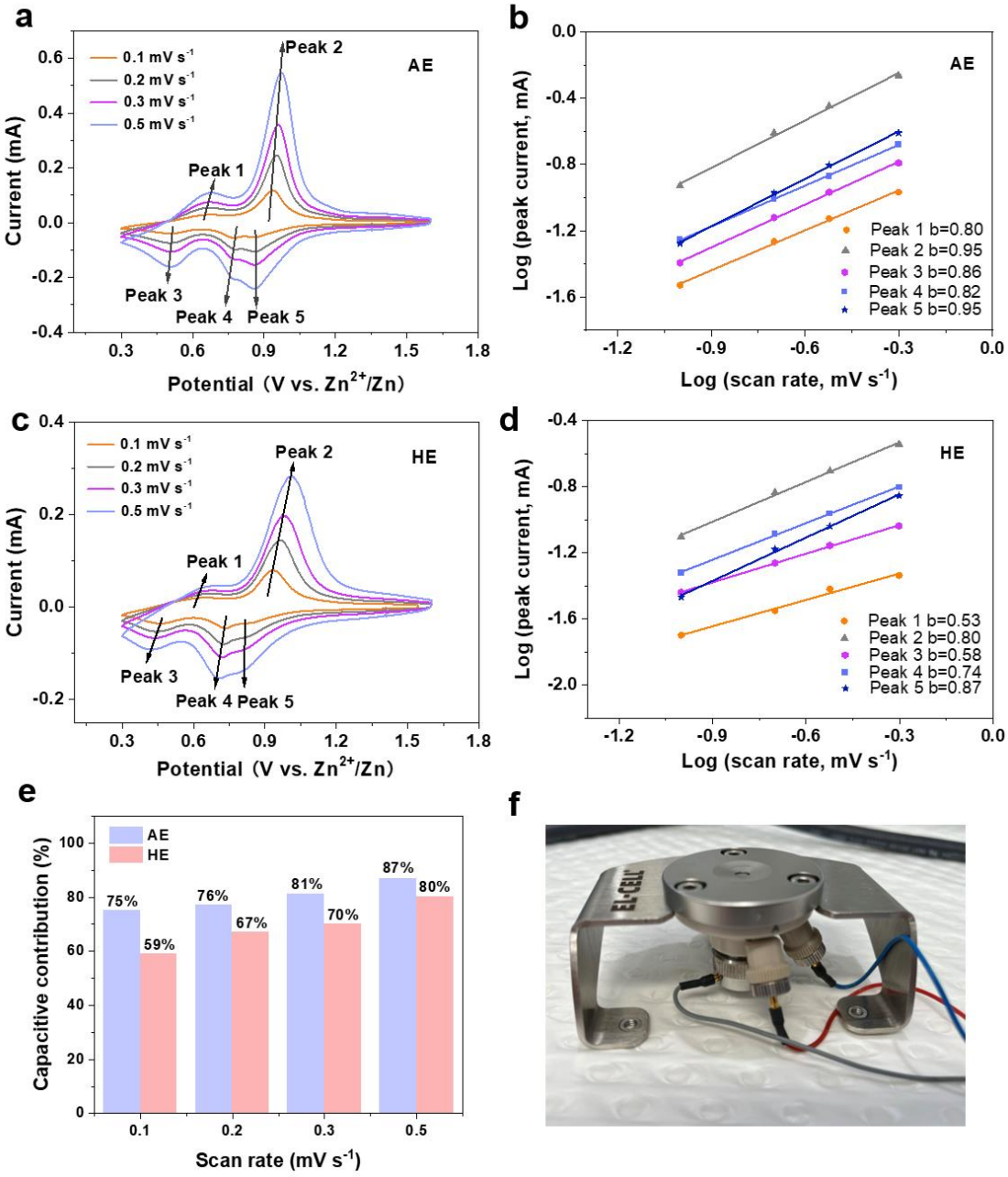

Figure 5.3 CV characterizations. (a-d) CV curves of NVO electrode at various scan rates and corresponding plots of log (peak current) vs. log (scan rate) in AE and HE, respectively; (e)

The comparison of the capacitive contribution at various scan rates in AE and HE, respectively; (f) 3-electrode battery device.

Figure 5.3 e shows that the percent of capacitive contribution increases with increasing scan rate, and the values in AE are overall greater than in HE. Electrochemical reactions of the NVO electrode are composited with ionic diffusion control and pseudo-capacitance control. Since a fraction of the charges is stored by the insertion of guest species into the lattice of NVO, structural expansion and contraction of the cathode occur at each discharging/charging cycle. Repeated volumetric deformations result in internal stresses that may lead to structural disintegration.

The V 2p XPS spectra confirm the valence variation for vanadium during discharge/charge. In the pristine NVO electrode the majority of vanadium is in the 5+ valence and a small portion in the 4+ valence. When discharged at 0.3 V the intensity of the V^{5+} signal decreases, while for V^{4+} it increases. The peak intensity reversed following charging back to 1.6 V, confirming that redox reactions occur during discharging/charging processes and they are electrochemically reversible (**Figure 5.4**).

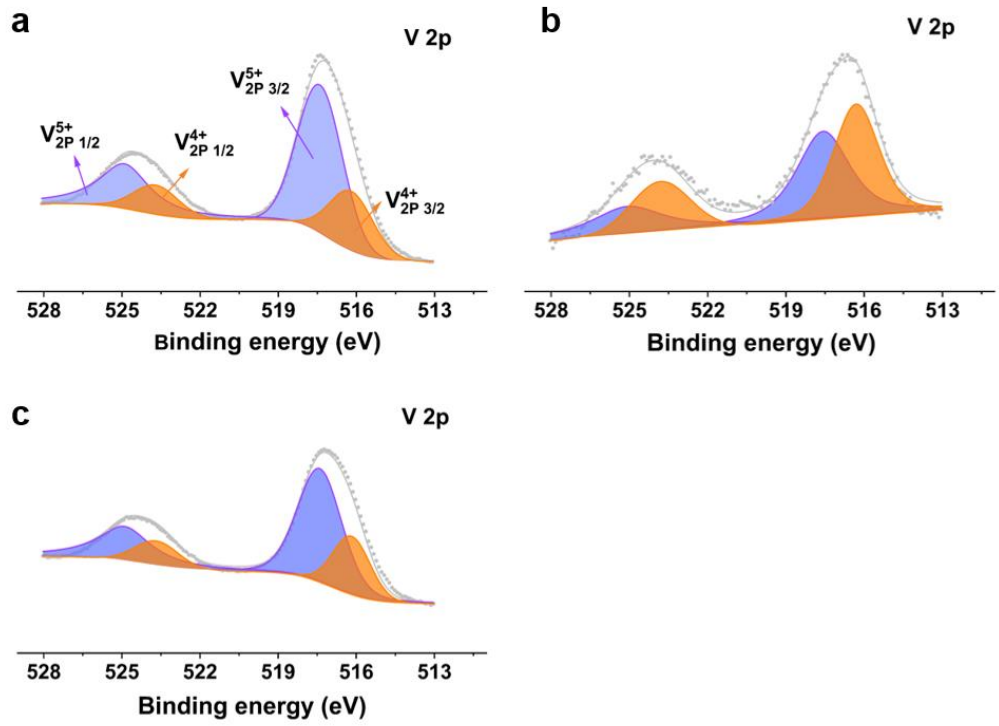

Figure 5.4 V 2p XPS spectra for NVO electrodes in (a) pristine, (b) discharged at 0.3 V, and (c) charged back to 1.6 V, state.

5.4 Electrochemical performance of Zn||NVO batteries in AE and HE

The water content of the electrolytes has a significant impact on the capacity and stability of the NVO cathode. As shown in **Figure 5.5**, the NVO only delivers a specific capacity of ca. 60 mAh g^{-1} in the electrolyte using DMAC as solvent, because of the sluggish interfacial charge transfer process in the nonaqueous electrolyte. With 20% of water, the specific capacity of NVO is increased dramatically to more than 150 mAh g^{-1}. The trend is quite different in the aqueous electrolyte, where a much higher specific capacity is achieved, but the rate of decay is very fast. The comparison reveals that the solvation structure of Zn^{2+} ions affects the desolvation penalty at the electrode-electrolyte interface and the structural stability of the NVO cathode. It has been verified by the DFT simulation in Chapter 4 that the Zn^{2+} ions in HE are solvated by 3.7 water molecules on average, fewer than that in AE, where the average is 6 water molecules[13]. The existence of H_2O in the solvation sheath of Zn^{2+} ions helps to reduce the large energy penalty associated with Zn^{2+} desolvation, facilitating the NVO cathode to deliver a high specific capacity.

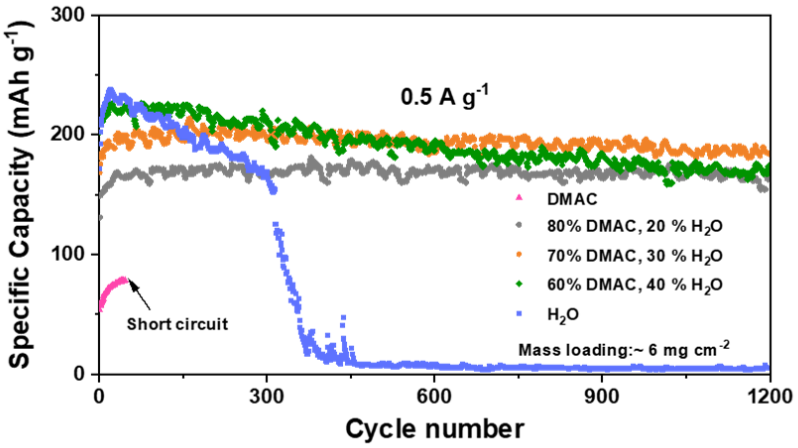

Figure 5.5 The cyclic performance of Zn||NVO cells in 1 M $Zn(OTf)_2$ solutions. The solvent is DMAC/H_2O mixture with various volume percentages of H_2O.

Figure 5.6 shows the electrochemical performance of Zn||NVO batteries using AE and HE as electrolyte, respectively. In AE and HE, Zn||NVO cells deliver an average output voltage at around 0.76 V vs. Zn^{2+}/Zn, and a specific capacity of 370 mAh g^{-1}, at a current density of 0.1 A g^{-1}. There is no marked difference when the applied current density is lower than 1 A g^{-1}, but the specific capacity is lower and the polarization is more severe in HE compared with AE when the current density increases to 2 and 5 A g^{-1}. The Regone plots, **Figure 5.6c**, compare

the energy density and power density of batteries using NVO as the cathode electrode. It can be seen that Zn||NVO batteries with AE and HE exhibit similar energy density at low current density, however, the battery with AE exhibits superiority at high current densities.

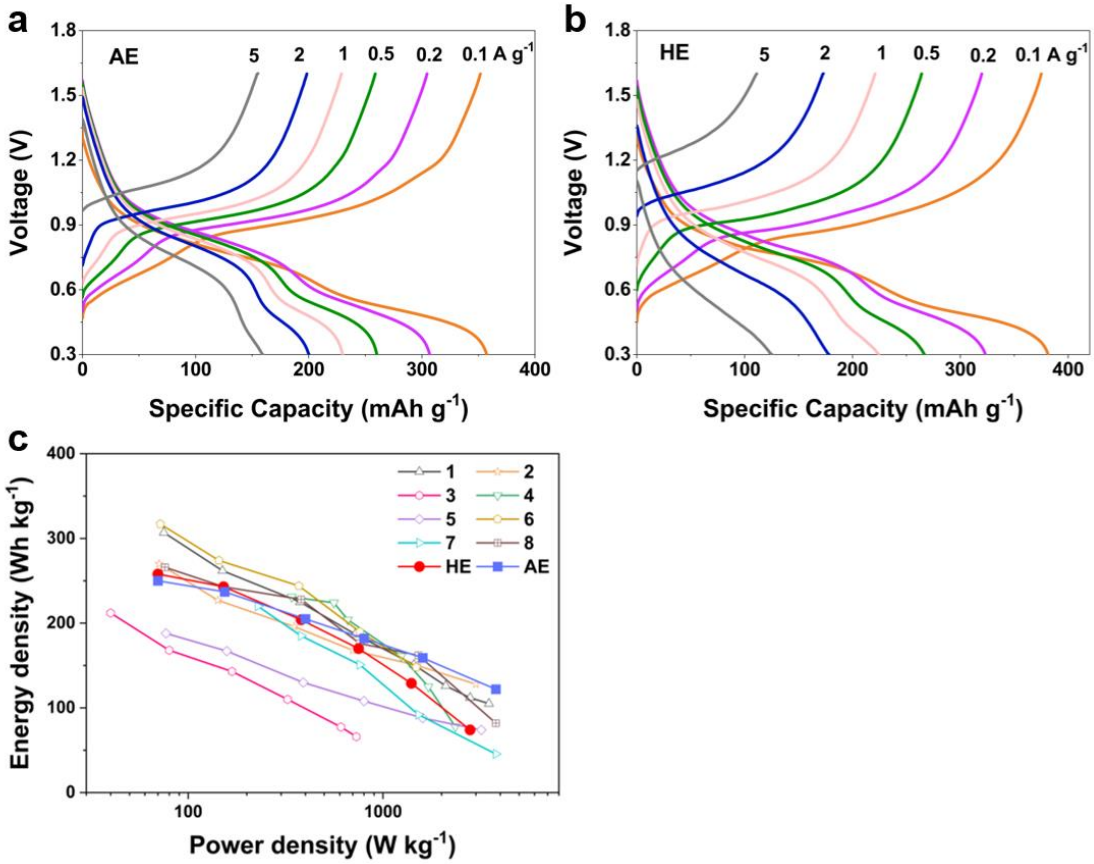

Figure 5.6 Charge-discharge curves for Zn||NVO battery in (a) AE and (b) HE tested at current density, respectively, 0.1, 0.2, 0.5, 1, 2 and 5 A g^{-1}. The mass loading of NVO is 1.8 mg cm^{-2}. (c) Comparison of energy density/power density of this work with reported findings based on the mass of cathode active materials. Detailed data are in **Table 5.1**.

Although HE has no superiority in rate performance, it significantly improves stability of Zn||NVO cells at low and moderate rates. At a low current density of 0.1 A g^{-1} the specific capacity for the aqueous Zn||NVO cell faded significantly within 200 cycles, whilst in HE the Zn||NVO cell maintained a specific capacity of 164 mAh g^{-1} following 700 cycles (**Figure 5.7**). At a current density of 0.5 A g^{-1}, in AE, the NVO cathode exhibits a rapid increase in specific capacity in the first 20 cycles from 170 to 231 mAh g^{-1}, and an apparent decline in subsequent cycling, to fail completely in the following 400 cycles, **Figure 5.8**. The corresponding charge-discharge curves show that the voltage decay remarkably after 300 cycles (**Figure 5.9**). In

contrast, the specific capacity of the NVO cathode in HE remains stable and has a lifespan of 3000 cycles. The advantage of AE in supporting fast ion diffusion and charge transfer can be observed at high current density, 4 A g^{-1}, and the lifespan achieves 6000 cycles (**Figure 5.10**). The lifespan of reported battery systems is poor at low and moderate rates, and the available data for comparison is limited. As can be seen in **Figure 5.11**, HE exhibits significant advantages in supporting the operation of Zn||NVO cells at low and moderate current densities. Niu et al. revealed that the pseudocapacitive Faradaic process accounts for the excellent cycling performance of vanadium-based cathode materials at high rates in aqueous electrolytes[3]. At low rates, the diffusion-controlled Faradaic process contributes more to the capacity than at high rates, and therefore the structural stability of the NVO becomes a crucial factor in the lifespan of Zn||NVO cells.

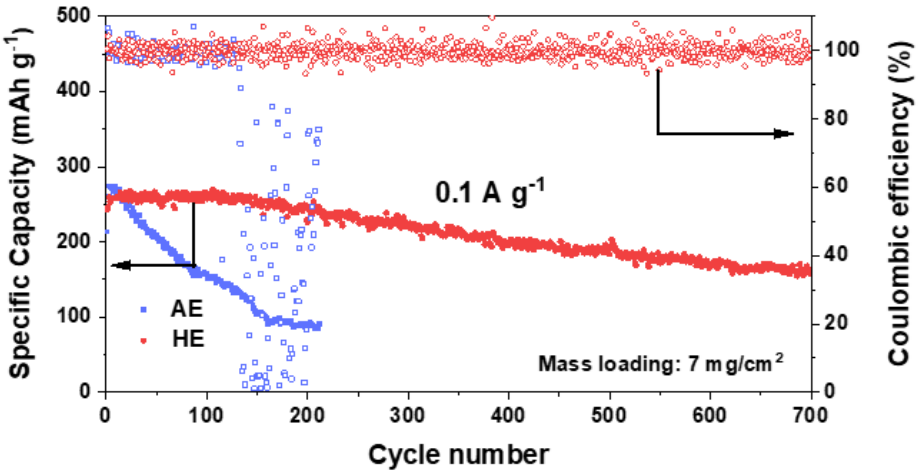

Figure 5.7 Cyclic stability and CE of Zn||NVO cells tested in AE and HE, respectively, at a current density of 0.1 A g^{-1}.

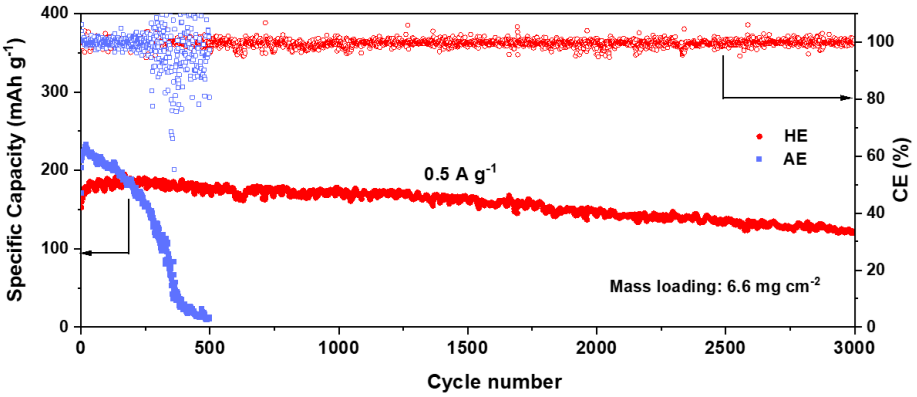

Figure 5.8 Cyclic stability and CE of Zn||NVO cells tested in AE and HE, respectively, at a current density of 0.5 A g^{-1}.

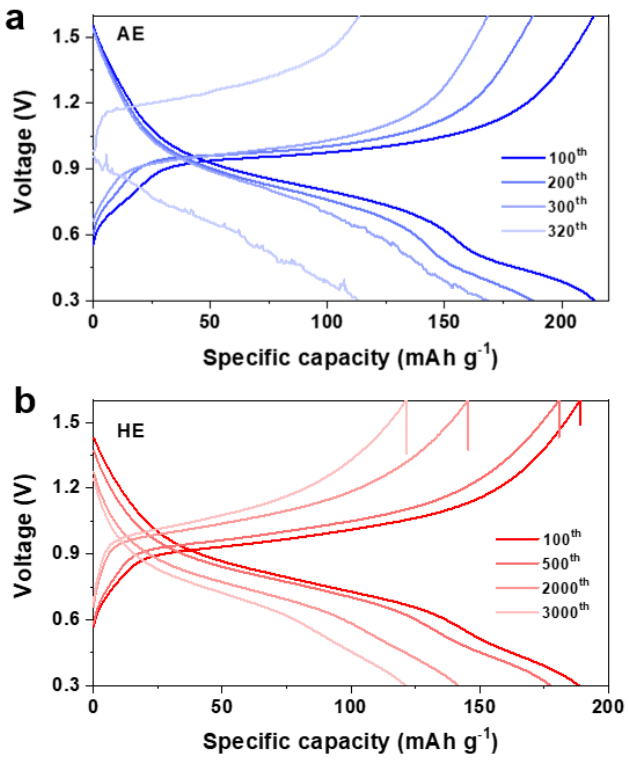

Figure 5.9 The charge-discharge curves of Zn||NVO battery in (a) AE and (

b) HE.

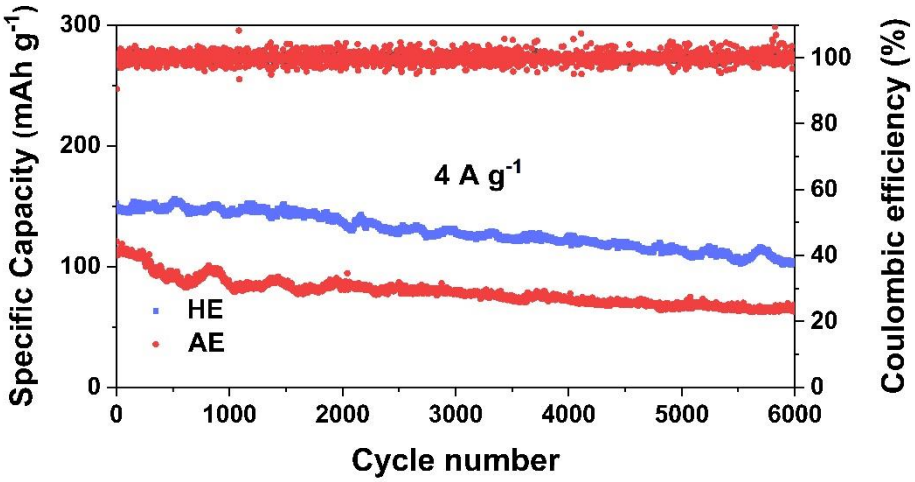

Figure 5.10 Cyclic stability and CE of Zn||NVO cells tested in AE and HE, respectively, at a current density of 4 A g^{-1}.

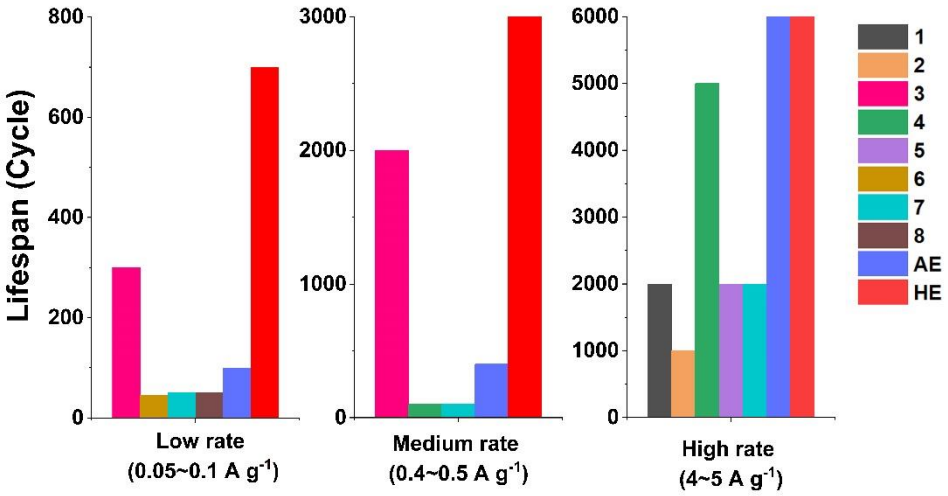

Figure 5.11 Comparison of battery lifespan with reported results based on data of **Table 5.1**.

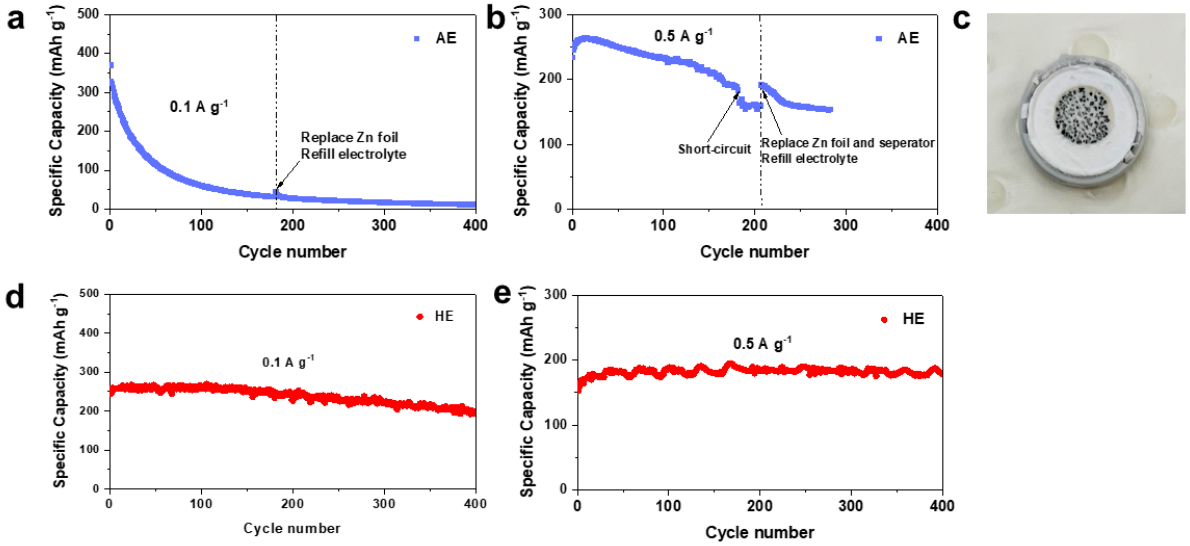

Figure 5.12 Failure analysis of Zn||NVO batteries tested in AE. (a) The battery was tested at 0.1 A g^{-1}, and the Zn anode was replaced and the electrolyte was refilled at the 182nd cycle; (b) The battery was tested at 0.5 A g^{-1}, and the Zn anode was replaced and the electrolyte was refilled at the 207th cycle; (c) The battery disassembled after short-circuit;(d-e) The reference battery tested in HE.

The failure of Zn||NVO cells can be attributed to at least one of the following reasons: short-circuit caused by Zn dendrite growth, exhaustion of Zn anode or electrolyte, poor electrical

contacts due to gas generation induced battery deformation, and cathode degradation. To determine the cause of the failure of the aqueous Zn||NVO battery, NVO electrodes were extracted when the capacity was significantly decreased and reassembled with fresh Zn anode and sufficient electrolyte. For the cells with AE, at a low rate, 0.1 A g^{-1}, the dendrite grows slowly and the Zn anode/electrolyte consumes at a low rate, and therefore, the cathode degradation becomes the primary reason for the failure of Zn||NVO cell. As shown in **Figure 5.12a**, the declined specific capacity of the aqueous full cell cannot be recovered by replacing the Zn anode and refilling the electrolyte. The situation changes when the full cell works at a medium current rate, 0.5 A g^{-1}. The dendrite growth becomes the trigger point that invalidates the Zn||NVO cell. As can be seen from the disassembled battery, **Figure 5.12c,** the dendrites penetrate the separator after cycling for 200 cycles. The cathode electrode was taken out and reassembled with fresh Zn anode, a new separator, and sufficient electrolyte, but its specific capacity failed to recover to its initial value (**Figure 5.13c**). The cathode decay tendency can be still observed even though its decay rate is lower than that at a low current rate, evidencing that cathode degradation significantly affects battery performance in AE.

5.5 The structure evolution of NVO in AE and HE

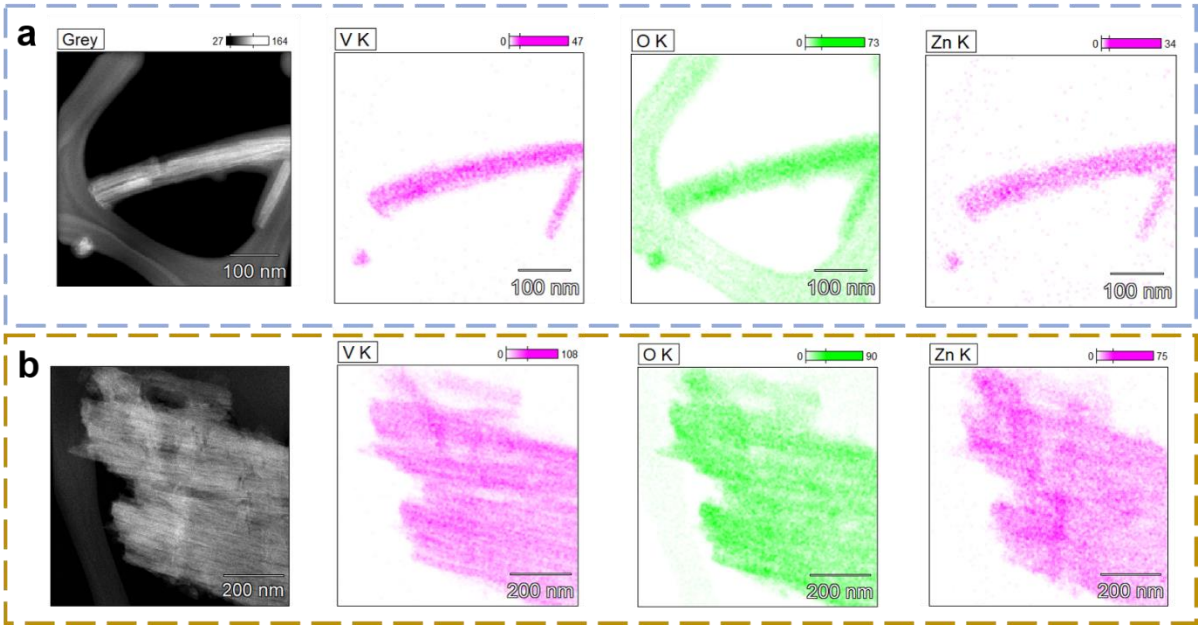

Figure 5.13 The TEM images of NVO fibers after full discharge in (a) AE and (b) HE, and the corresponding EDX mapping of V, O, Zn.

To verify whether the Zn^{2+} insertion contributes to the charge storage in the discharge process, energy-dispersive X-ray (EDX) mapping is conducted to analyze the element composition of the fully discharged NVO fibers. In **Figure 5.13**, a very homogeneous distribution of Zn element is observed in the discharged NVO fibers, confirming the insertion of Zn^{2+} ions into the NVO lattice in both AE and HE.

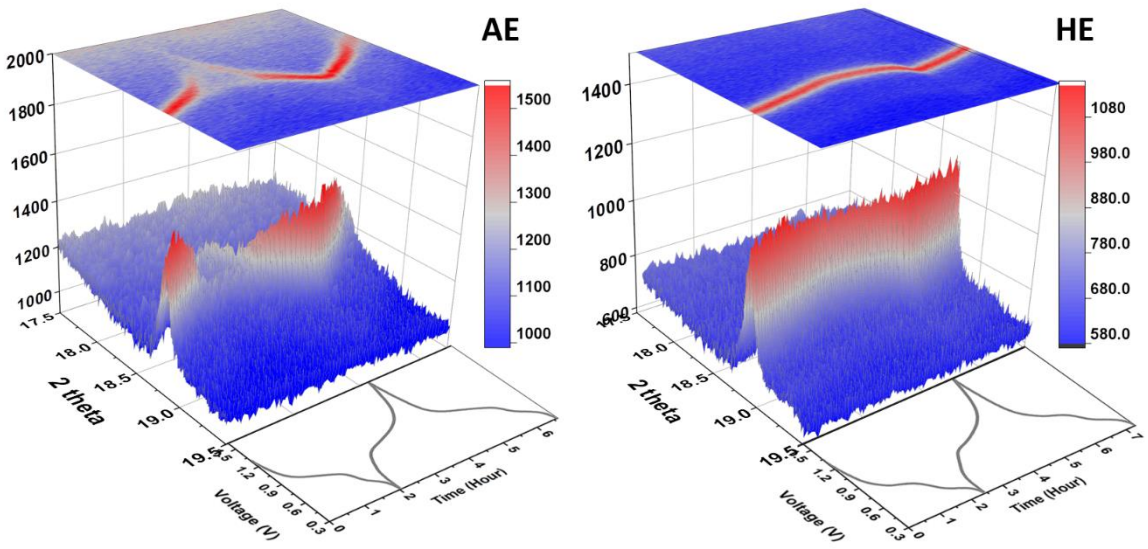

Figure 5.14 Contour plot for NVO (204) reflection, using (a) AE and (b) HE as electrolyte, in which the (204) reflection evolutes along with corresponding charge/discharge curve.

We hypothesized that the difference in reversibility of the NVO cathode in AE and HE is related to structural stability associated with the charge carrier insertion process. To confirm this, *in operando* synchrotron-based X-ray powder diffraction (XRPD) was used to monitor lattice changes in NVO during discharge and charge, respectively, AE and HE. **Figure 5.14** presents the (204) reflection as a contour-plot with color-intensity and corresponding electrochemical curves. The (204) plane was selected for analyses because (204) reflection is the strongest and clearest peak obtained *in operando* conditions (**Figure 5.15**). For the NVO cathode working in AE, its (204) reflection shifts to lower angles when the Zn||NVO battery discharges from open-circuit voltage to 0.3 V. In this, Zn^{2+} ions intercalate into the layer of NVO accompanied by the continuous increase of lattice parameter and cell volume. A reversed behavior is observed during charging. The peak moves right-wards during charging, corresponding to Zn^{2+} ions extraction and a decrease in the d-spacing. The peak shift is continuous and reversible, evidencing solid-solution-like behavior during Zn^{2+}

insertion/extraction. Notably, at deep discharge state, the (204) reflection intensity is greatly reduced, implying the order-disorder transition at high Zn concentrations. A similar trend was found for the NVO cathode using HE as the electrolyte. In HE, the lattice changes are relatively minor and the peak intensity remains nearly unchanged across the charge-discharge processes, confirming that the structural changes in NVO are significantly smaller than with AE and absent of order-disorder transition.

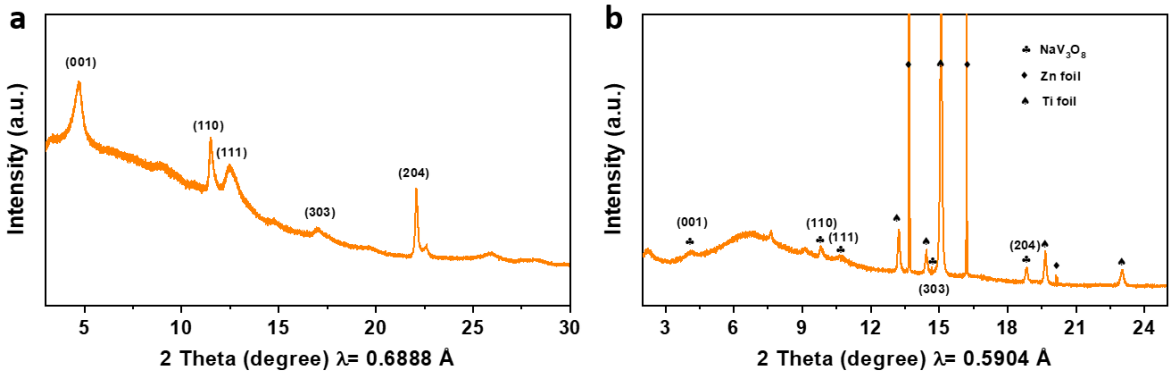

Figure 5.15 (a) XRPD pattern of the NVO electrode; (b) XRPD pattern of the initial state of the *in operando* Zn||NVO cell.

Figure 5.16 shows the single peak fitting of (204) reflection of NVO alongside the discharge/charge processes. In AE, the peak position shifts continuously to lower 2Θ values from 18.82° to 18.39° during discharging, revealing a solid-solution reaction occurs when charge carriers are inserted. In the meantime, the peak height reduces significantly and reaches the lowest point at the end of discharge, accompanied by gradually increased values of the full width at half maximum (FWHM). The decreased peak intensity during discharging reveals the reduced crystallinity of the NVO cathode when H^+/Zn^{2+} ions are inserted. In the subsequent charging process, the peak position returns to its initial value along with the recovered peak height and FWHM. Surprisingly, in HE, the changes of the peak height as well as the FWHM are almost negligible during the insertion and extraction of charge carriers. The variation of peak position in HE is relatively smaller, indicating that the interlayer spacing changes are less severe than that in AE.

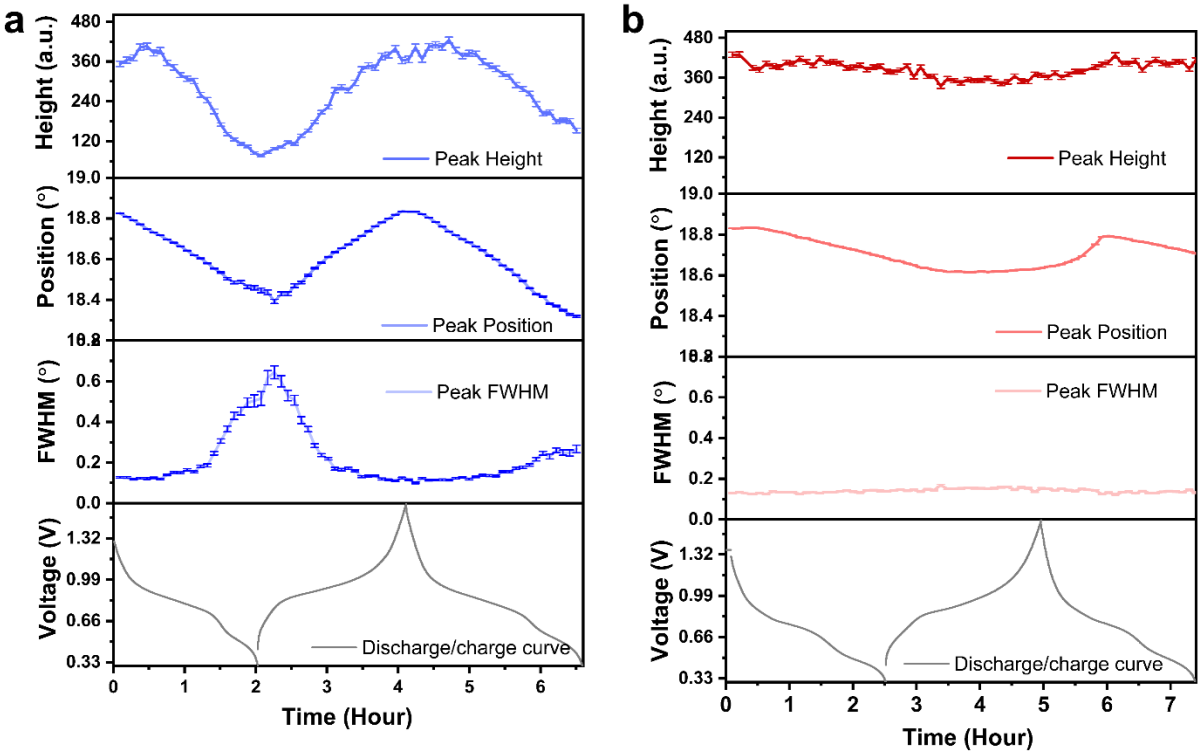

Figure 5.16 The evolution of peak height, position and FWHM along with the discharge/charge curves of Zn||NVO cells in (a) AE and (b) HE, which are extracted from the sequential refinements using in operando XRPD data.

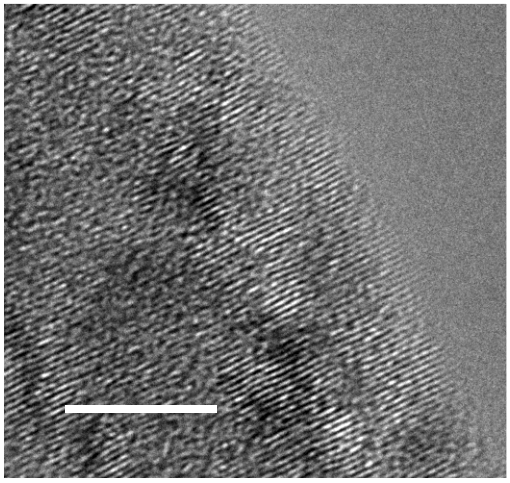

Figure 5.17 The high-resolution TEM image of pristine NVO fiber.

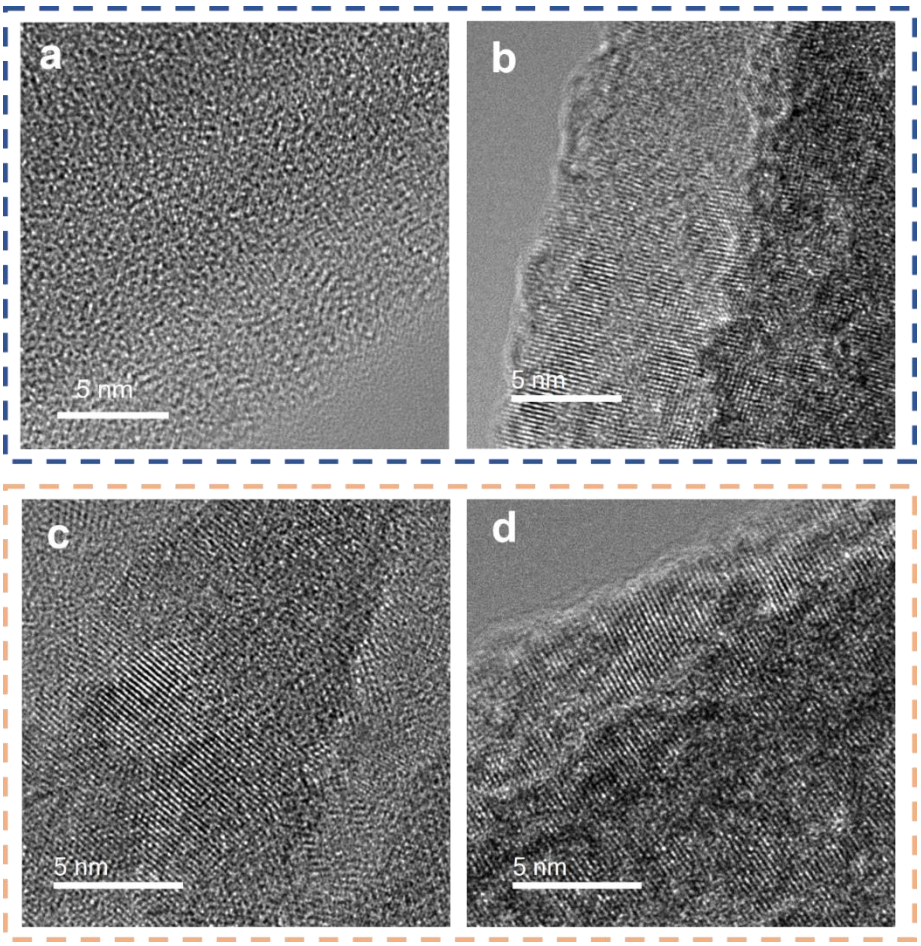

Figure 5.18 The high-resolution TEM images of NVO fibers, which are (a) fully discharged at 0.3 V in AE, (b) fully charged at 1.6 V in AE, (c) fully discharged at 0.3 V in HE, and (d) fully charged at 1.6 V in HE, respectively.

High-resolution TEM images of the fully discharged/charged NVO fibers provide a visible comparison of the differences between NVO in AE and HE. It is observed in **Figure 5.18a** that the NVO fibers become nearly amorphous after full insertion of H^+/Zn^{2+} ions in AE, but the lattice recovers to a relatively ordered structure at the fully charged state, **Figure 5.18b**. However, clear lattice fringes can still be observed on the NVO fiber after discharge to 0.3 V in HE, **Figure 5.18c**, and the lattice structure is almost recovered to its initial state when fully charged to 1.6 V, **Figure 5.18d**. The changes are consistent with the results observed from XRPD.

These differences likely originate from the solvation structure of electrolytes. Water molecules are co-intercalated with the H^+/Zn^{2+} ions into the structure of NVO during discharge, which circumvents the desolvation energy penalty during (de)intercalation and shields the

electrostatic interaction between the Zn^{2+} ion and the host matrix[14, 15]. Water molecules act as 'pillars' to increase the layer spacing and therefore accelerate reaction kinetics and increase the Zn^{2+} store capacity, which accounts for the higher initial specific capacity and the rapid activation of the NVO cathode in AE. However, the large radius of the hydrated Zn^{2+} clusters ($Zn(H_2O)_n^{2+}$), *ca.* 5.5 Å [16], results in significant lattice distortion of the host material and leads to structural collapse when the lattice stress exceeds its limit[17]. This vulnerable structure of NVO results in a rapid decline in specific capacity and a limited lifespan. The outcome is different when the NVO cathode works in HE, because, unlike AE, where the first hydration shell consists of six water molecules, the number of water molecules in the solvation cluster of HE is reduced to 3.7. DMAC and TMP are large molecules compared to H_2O, and therefore they are too large to squeeze into the NVO lattice. Moreover, DMAC and TMP in the solvation cluster exert strong attraction to H_2O, meaning fewer water molecules combine with Zn^{2+} when hydrated Zn^{2+} enters the structure of NVO. As a result, the smaller size of guest species in NVO crystal brings less lattice distortion and ensures better structural stability during long-term cycling.

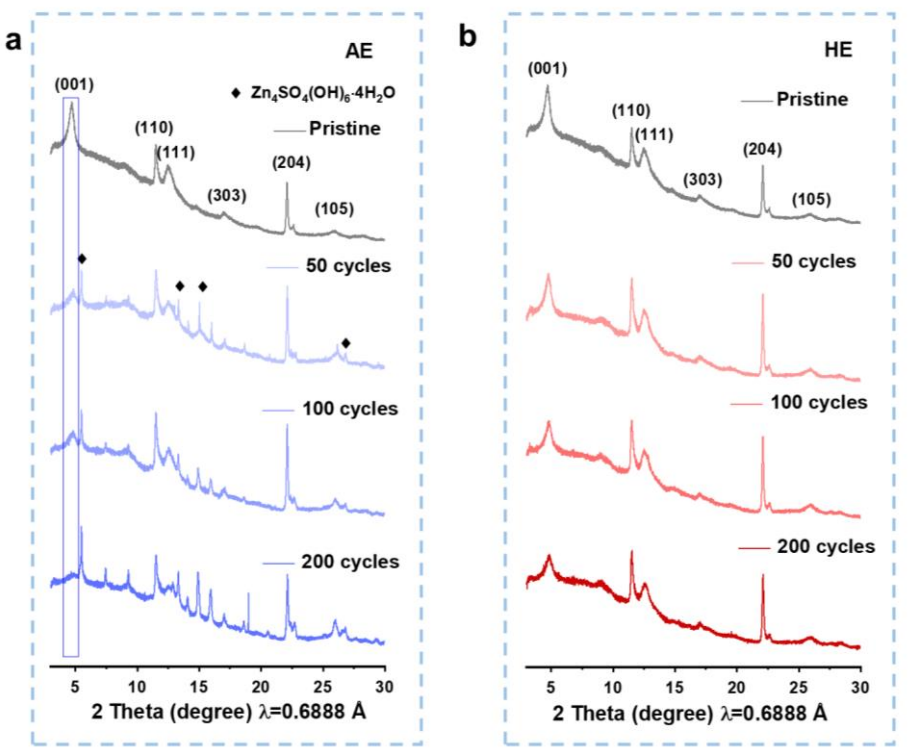

Figure 5.19 Synchrotron-based XRPD patterns for NVO electrodes following cycling in (a) AE and (b) HE.

Figure 5.19b presents the XRPD pattern for NVO electrode following cycling in HE for 50, 100 and 200 cycles, evidencing that the structure of NVO is maintained during cycling and no side product(s) is found. However, in AE, $Zn_4SO_4(OH)_6{\cdot}4H_2O$ formed and the (001) reflection weakened and almost disappeared following 200 cycles, **Figure 5.19a**. The appearance of $Zn_4SO_4(OH)_6{\cdot}4H_2O$ indicates that H^+ intercalation into the NVO lattice occurs in AE, accounting for the higher initial specific capacity. Since $Zn_4SO_4(OH)_6{\cdot}4H_2O$ is detected on the fully charged NVO cathode, it is not completely reversible in AE, which may be one of the reasons for the inferior cycling performance. Besides, the irreversibility of $Zn_4SO_4(OH)_6{\cdot}4H_2O$ also consumes the electrolyte. CV curves of Zn||NVO cell (**Figure 5.20b**) show that the redox reactions are completely reversible in HE, better than that in AE (**Figure 5.20a**).

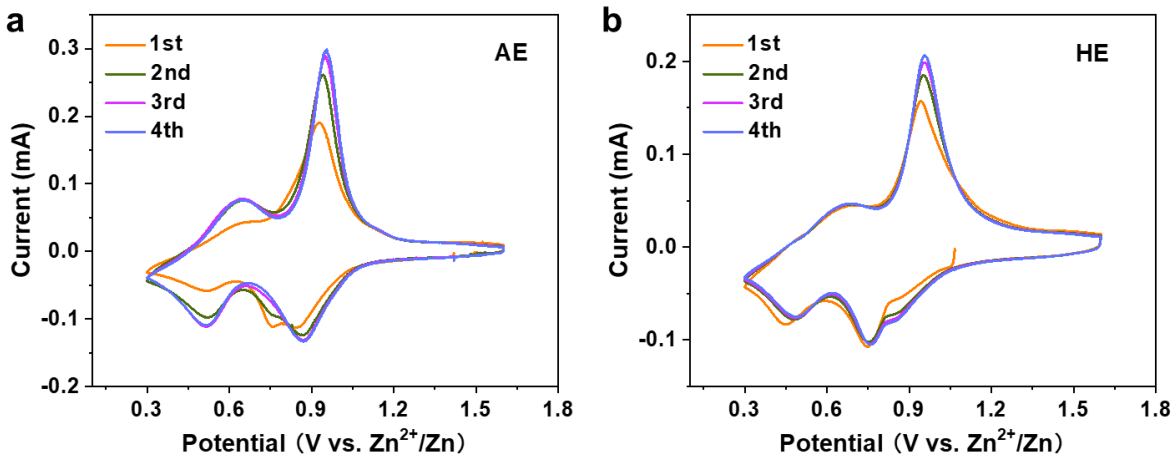

Figure 5.20 3-electrode CV curves for NVO electrode in (a) AE and (b) HE.

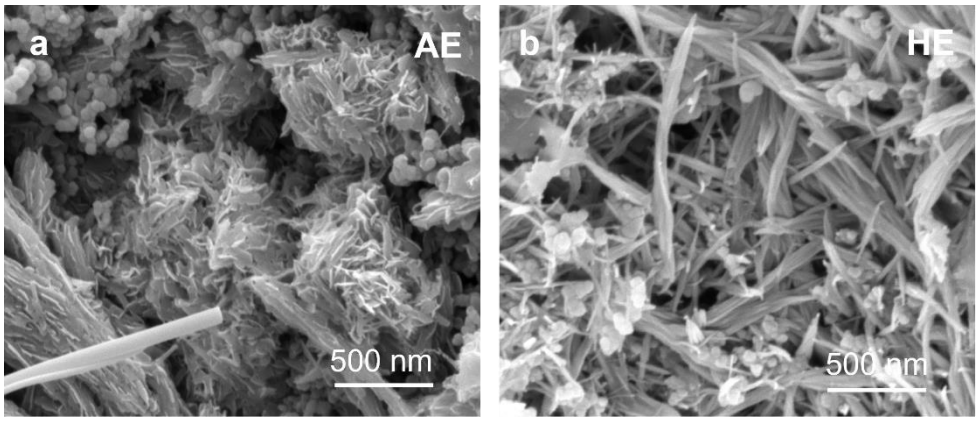

Figure 5.21 The SEM images of NVO cathodes following (a) 500 cycles in AE and (b) 3000 cycles in HE at a current density of 0.5 A g^{-1}.

The NVO cathode is extracted from the Zn||NVO cell when its capacity fades severely after cycling at a current density of 0.5 A g^{-1}. As can be seen in **Figure 5.21**, the cathode undergoes morphological changes following 500 cycles in AE, however, it maintains an intact morphology even after 3000 cycles in HE. This is another evidence that more stable structure of NVO is maintained in HE.

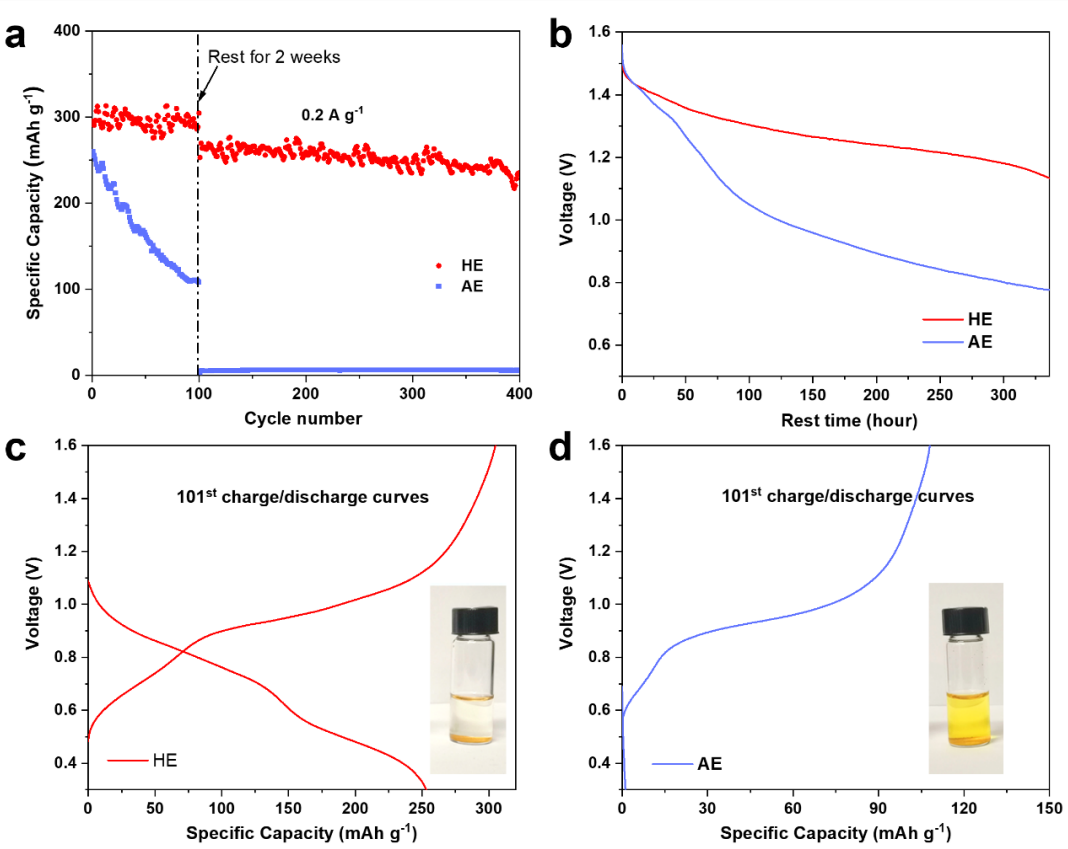

Figure 5.22 (a) The cycling performance of the Zn||NVO cells that are suspended at the 100th cycle and rest for 2 weeks. (b) The OCV variation of Zn||NVO cells during the rest period. (c-d) the 101st discharging curves; the inserted pictures shows the HE and AE solution with immersed NVO powders.

In practice, it is not practical for batteries to be continuously charged/discharged without interruption. To be more realistic, the energy may need to be stored in the batteries for a period of time and extracted when it is required. To investigate the potential performance degradation during rest, the Zn||NVO cells were suspended at the 100th cycle in a fully charged state and rested for 2 weeks. In **Figure 5.22a**, the Zn||NVO cell using AE as electrolyte exhibits inferior cycling performance in the first 100 cycles at a current density of 0.2 A g^{-1}. Worse still, it fails

completely after 2 weeks of rest. Its open-circuit voltage (OCV) falls severely to 0.8 V during the rest period (**Figure 5.22b**) and almost no energy can be extracted for the Zn||NVO cell at the 101st discharge. One of the possible reasons for the failure is the dissolution of vanadium from the NVO cathode in AE, as evidenced by the yellow color of AE when the NVO powders are immersed in the electrolyte for 2 weeks. Surprisingly, the Zn||NVO cell with HE has overwhelming advantages both in capacity and OCV retention. Although a slight decline of capacity is observed after 2 week rest, a specific capacity of 250 mAh g^{-1} can still be achieved at the 101st discharge (**Figure 5.22c**) and keep stable in the following 300 cycles (**Figure 5.22a**). The OCV decline of the Zn||NVO cell with HE is very slow and a value of 1.2 V is measured after two-week rest (**Figure 5.22b**). In **Figure 5.22c**, the colorless HE indicates that the vanadium dissolution from the NVO cathode is well suppressed, accounting for the excellent ability of Zn||NVO cell to maintain the electrochemical performance during rest. The superiority of HE originates from its microcosmic liquid structure.

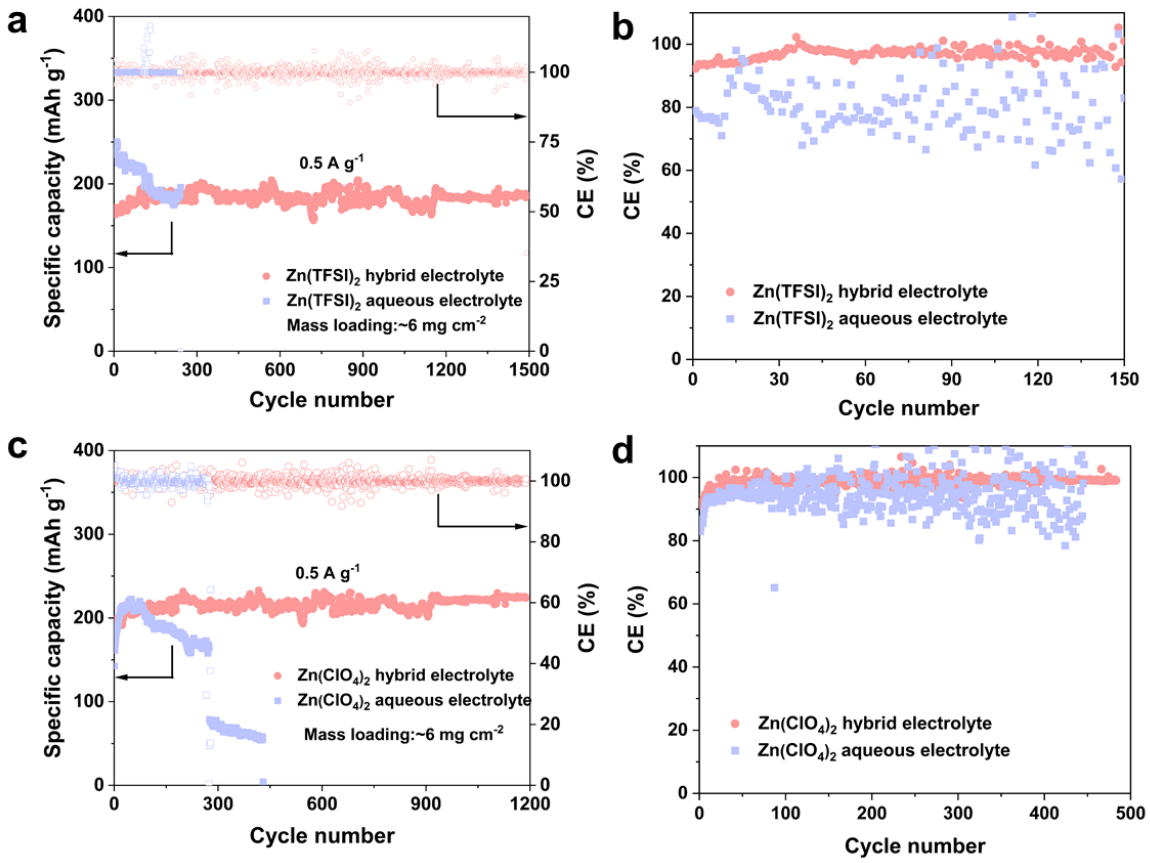

Figure 5.23 The comparison of the cycling performance of Zn||NVO cells and the CE of Zn platting/stripping tested in hybrid electrolyte and aqueous electrolyte. (a) (b) 1 M $Zn(TFSI)_2$ is

used as the salt; (c) (d) 1 M $Zn(ClO_4)_2$ is used as the salt. In the hybrid electrolyte, the solvent is DMAC/TMP/H_2O in a volume ratio of 5:2:3.

DMAC/TMP/H_2O hybrid solvent in a volume ratio of 5:2:3 is compatible with salts including zinc trifluoromethanesulfonate ($Zn(TFSI)_2$) and $Zn(ClO_4)_2$. In hybrid electrolytes using $Zn(TFSI)_2$ or $ZnClO_4$ as salt, the NVO cathode maintains specific capacity without decay for > 1200 cycles, and the CE for Zn plating/stripping is boosted compared with that in corresponding aqueous electrolyte (**Figure 5.23**).

5.6 High-low temperature performance of NVO

To assess the performance of the electrolytes in a high- or low-temperature environment, Zn||NVO batteries using AE and HE as the electrolyte were tested at various temperatures (**Figure 5.24**). The Zn||NVO battery in the presence of AE exhibited a rapid capacity degradation, and significantly increased polarization (**Figure 5.25-26**) at 70 ℃. In contrast, the Zn||NVO battery with HE as electrolyte exhibited an initial specific capacity of 207 mAh g^{-1} and maintained a reversible capacity of 120 mAh g^{-1} following 1400 cycles with a mean CE near 100%. The significantly boosted thermostability of HE is attributed to the participation of DMAC and TMP in the electrolyte, that interacts strongly with H_2O, strengthening the O−H bonds of water and therefore reducing the decomposition of H_2O.

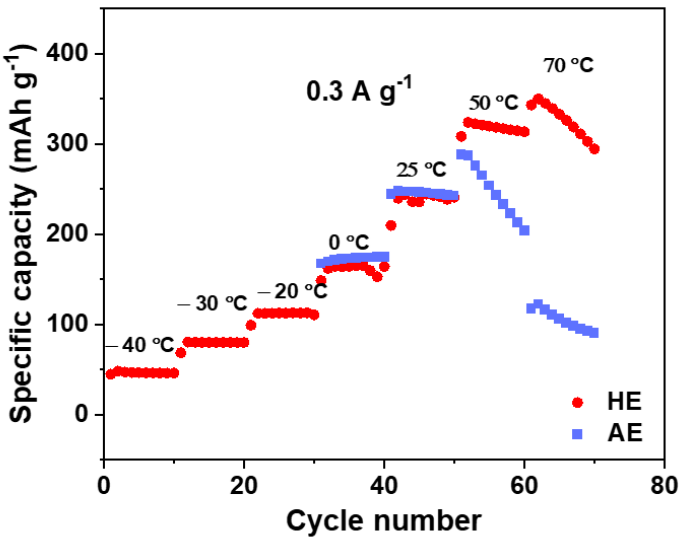

Figure 5.24 The specific capacity of NVO electrode tested at temperatures ranging from −40 ℃ to 70 ℃.

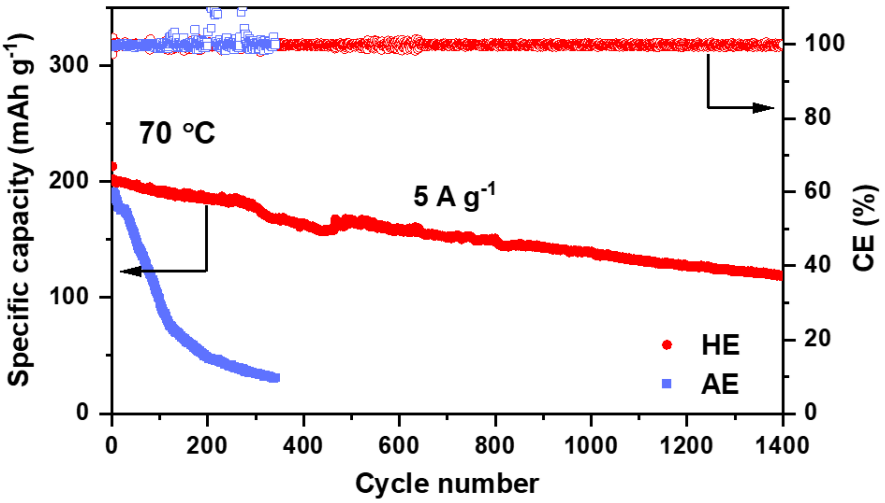

Figure 5.25 Cyclic performance for Zn||NVO cells at 70 ℃ with AE and HE as electrolyte.

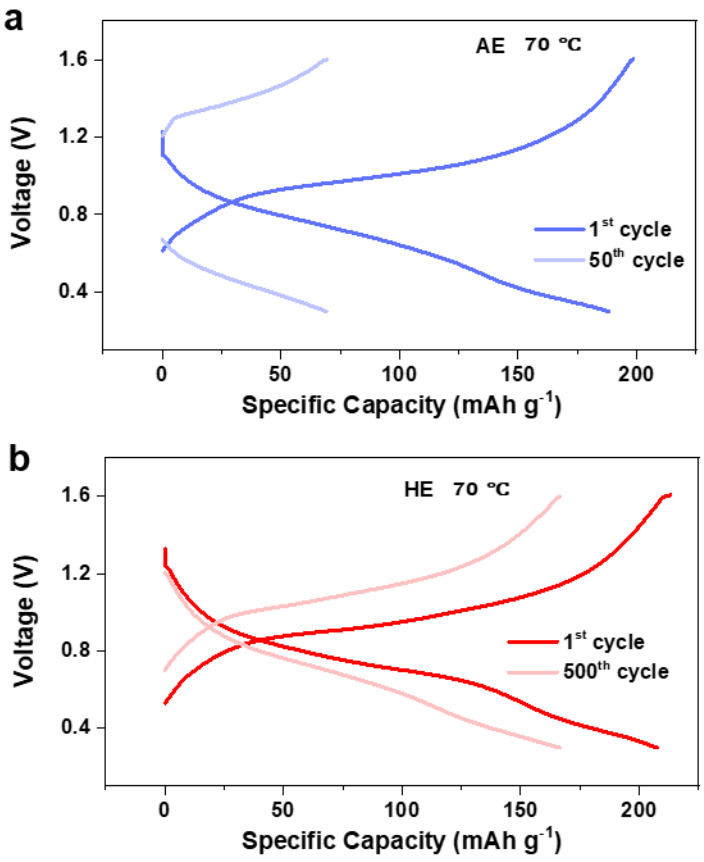

Figure 5.26 Charge/discharge curve for Zn||NVO battery tested at 70 ℃ in AE (a) and in HE (b).

Additionally, HE exhibited a freeze-tolerance at sub-zero temperatures. At − 20 ℃, the Zn||NVO battery exhibited a capacity of *ca.* 140 mAh g^{-1} without apparent capacity fading for 2000 cycles (**Figure 5.27**), confirming that HE contributes to a highly reversible battery. At as low as − 40 ℃, the HE remains in a liquid state and the Zn||NVO battery exhibited a capacity of *ca.* 85 mAh g^{-1}, **Figure 5.28**. AE failed to support the operation of the Zn||NVO battery because it freezes at sub-zero temperatures (**Figure 5.29**). The mechanism of the anti-freezing is attributed to the strong dipole-dipole interaction between DMAC/TMP and water molecules, which breaks the extension of the hydrogen-bonded network of water and reduces the freezing point of the electrolyte.

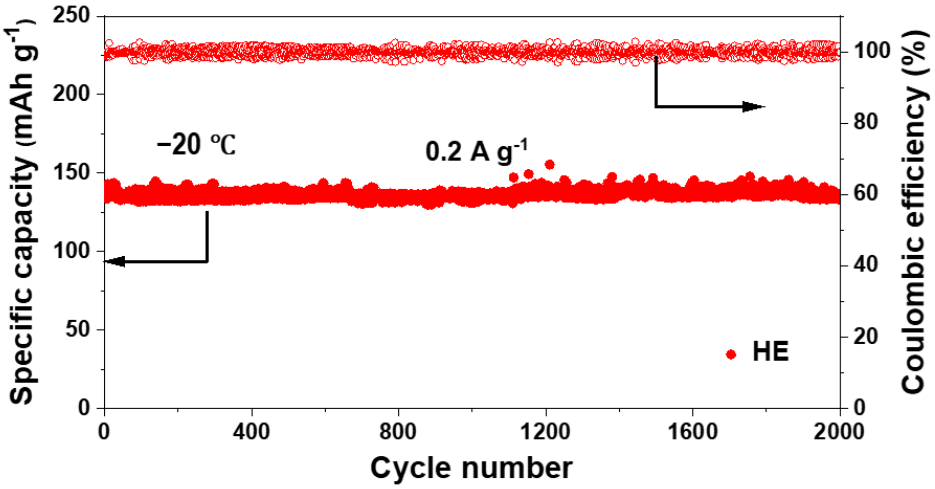

Figure 5.27 Cyclic performance for Zn||NVO cell at − 20 ℃ using HE as electrolyte.

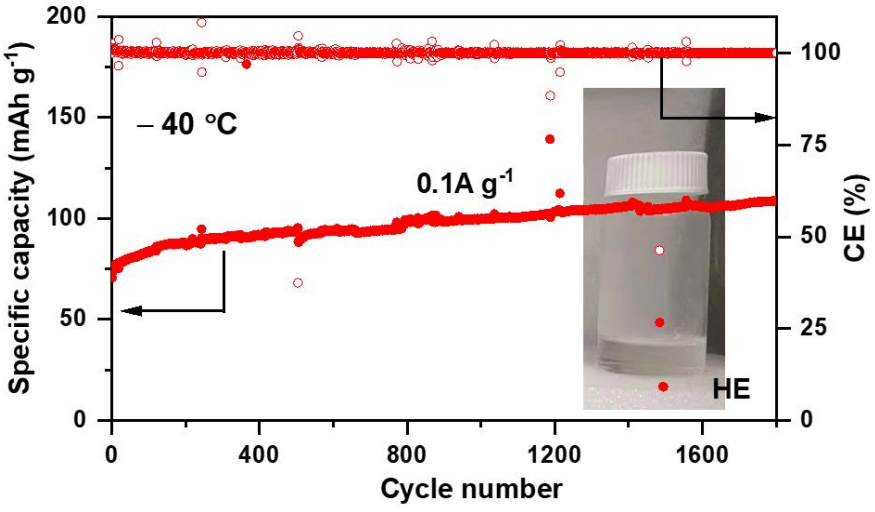

Figure 5.28 Cyclic performance for Zn||NVO cell at − 40 ℃ using HE as electrolyte.

Figure 5.29 Digital image of frozen AE at a temperature − 20 ℃.

5.7 A comparison of HE and state-of-the-art electrolytes

Given the practical usage of ZIBs, the utilization ratio of Zn is vital to ensure the overall energy density of the device. In Zn||NVO cell tests, the capacity ratio of the negative electrode to the positive electrode (n/p ratio) is controlled to be 5. As shown in **Figure 4.30**, in AE, the NVO cathode exhibits an increase in specific capacity in the first serval cycles from 250 to 275 mAh g^{-1}, but it declines rapidly at the 25th cycle and fails completely within a few cycles, indicating that the Zn anode has been exhausted. In contrast, the specific capacity for the NVO cathode in HE remains stable and has a lifespan of more than 200 cycles. This is because the side reactions between Zn and electrolyte are effectively suppressed in HE.

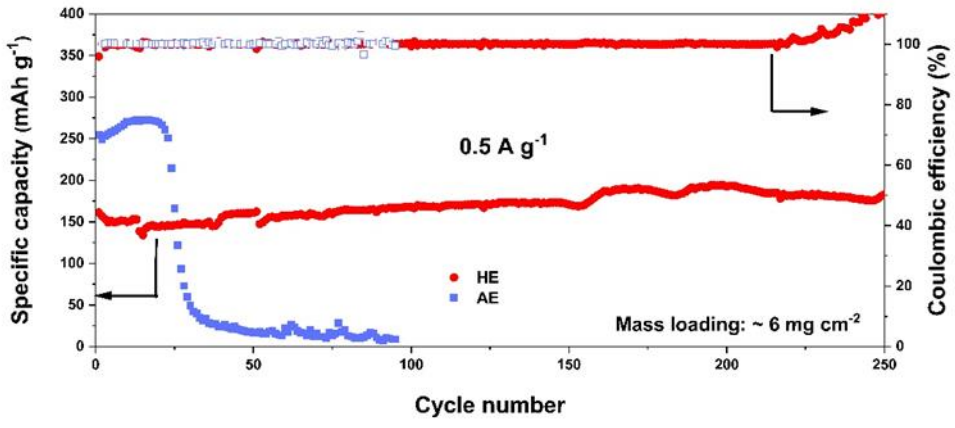

Figure 5.30 The cycling performance of Zn||NVO batteries using AE and HE as the electrolyte, respectively. The mass loading of NVO is around 6 mg cm^{-2} and the n/p ratio is controlled to be 5.

To evaluate the energy density at the electrode scale, Zn||NVO cells are assembled with a thick cathode and a thin Zn foil, in which the cathode mass loading is 9.3 mg cm^{-2} and N/P ratio is 5. Because of high ionic conductivity of AE, the Zn||NVO cell exhibits better rate performance, with ca. 80 mAh g^{-1} at 5A g^{-1}, as is seen in **Figure 5.31a.** The Zn||NVO cell using HE does not exhibit an advantage in specific capacity, especially when the applied current density increases. The energy density and power density of Zn||NVO batteries are given according to the rate performance, calculated with the mass of the cathode and anode (**Figure 5.31b**). The battery in AE exhibits a superior energy density of 86.1 Wh kg^{-1} and a greater power energy density of 1019 W kg^{-1}, while in HE, the energy density is 77 Wh kg^{-1} and the power maximum is 665 W kg^{-1}.

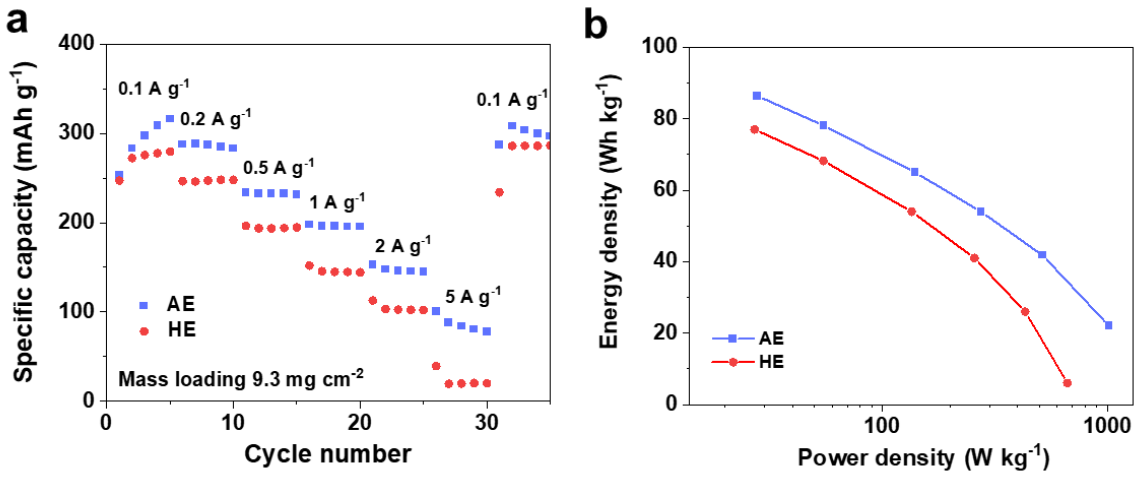

Figure 5.31 Rate performance for Zn||NVO cells; (b) Energy and power density for Zn||NVO cells calculated based on the total mass of cathode and anode electrode.

The energy density of Zn||NVO battery in HE surpasses that of the majority of aqueous Li-ion and Na-ion batteries, and approaches the value of the state-of-the-art Li-ion batteries (**Table 5.2** and **Figure 5.32**). However, Zn||NVO battery is apparently more competitive than aqueous Li-ion batteries when affordability is taken into consideration.

A comparison of state-of-the-art electrolytes is listed in **Table 5.3**. For non-aqueous electrolytes, the choices of compatible cathode materials are quite limited and the electrochemical properties, such as specific capacity and lifespan, of these cathodes are inferior compared with aqueous batteries[18, 19]. As for those aqueous-based electrolytes, in which water accounts for > 50% by volume, the low-rate performance and high-temperature performance of batteries become the shortcomings[20, 21, 22], because the interactions between water and non-

aqueous solvents are not sufficient to suppress the water activity. In our design, we emphasized the impact of water content on the specific capacity and stability of the NVO cathode and further demonstrated that the stability is highly related to the structural evolution of the cathode during battery operation. Upon comparison, the Zn||NVO battery in HE has advantages at low cycling current density (0.1~0.5 A g^{-1}), and has superior temperature adaptability.

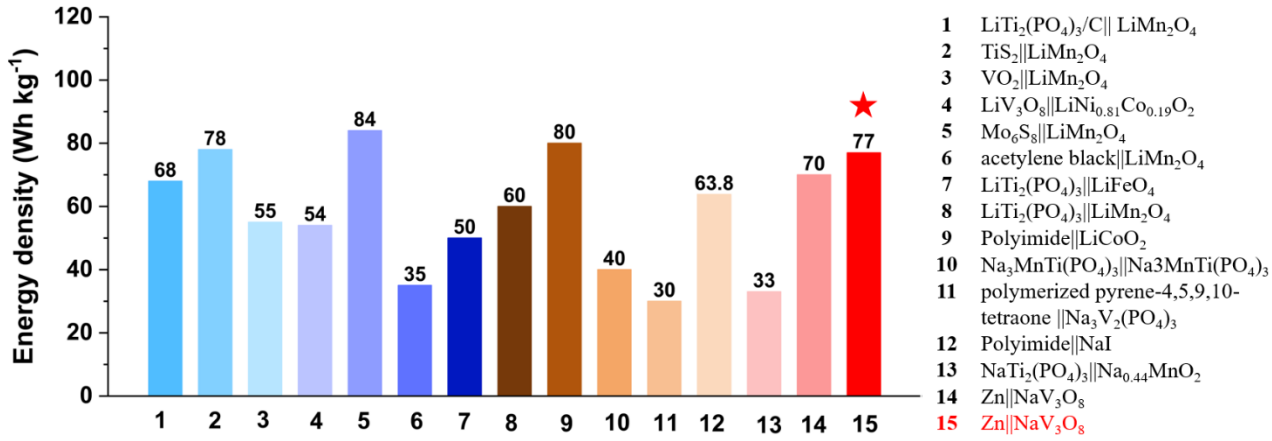

Figure 5.32 Comparison of energy density for Zn||NVO battery in HE with selected aqueous batteries based on mass of cathode and anode active materials. Detailed data are in **Table 5.2**.

5.8 Conclusion

The advantageous of aqueous ZIBs arise from anomalous properties of water, however, drawbacks are also from water. When strong polar molecules, DMAC and TMP, are introduced into the aqueous solution, strong dipole-dipole interaction occurs between DMAC/TMP and water. On the cathode side, DMAC and TMP are large molecules compared with H_2O, and therefore they are too large to squeeze into the NVO lattice, but ensure few water molecules combin with Zn^{2+} to insert into the NVO structure, protecting the host from collapse during long-term cycling. In HE, the structrual deformation of NVO cathode is smaller during the Zn^{2+} insertion, evidenced by the *in operando* XRPD and TEM images of different charge state of NVO. The Zn||NVO cells exhibit excellent cycling stability in HE, especially in low and medium rates. The strong interaction between solvents expanded temperature adaptability of electrolyte with the result that the Zn||NVO cell ran for 1400 cycles at 70 ℃, and for > 1800 cycles at − 40 ℃. Findings will be of immediate benefit in practical design for highly reversible ZIBs and therefore of wide interest to researchers and manufacturers.

Table 5.1 Comparison of energy density and power density for ZIBs based on mass of cathode active materials.

No.	Cathode material	Electrolyte	Mass loading	Energy density (Wh kg^{-1})	Power density (W kg^{-1})	Current density (A g^{-1})	Lifespan (cycle)	Reference
1	NVO	1 M $ZnSO_4$/1 M Na_2SO_4 aqueous solution	1.2 mg cm^{-2}	307	75	5	2000	*Science China Chemistry*, 2019, 62, 609–615
				262	150			
				225	375			
				187	720			
				151	1440			
				126	2100			
				112	2800			
				105	3500			
2	NVO	1 M $ZnSO_4$/1 M Na_2SO_4 aqueous solution	2 mg cm^{-2}	270	71	1	100	*Nat. Commun*., 2018, 9, 1656
				227	142	4	1000	
				196	350			
				168	700			
				150	1500			
				128	3000			
3	NVO	3 M $ZnSO_4$ aqueous solution	2.4 mg cm^{-2}	212	40	0.05	300	*ACS Appl. Mater. Interfaces*
				168	80	0.4	2000	
				143	168			

				110	324			2020, 12, 54627−54636
				77.5	608			
				66	730			
4	$Na_2V_6O_{16}\cdot 3H_2O$	1.0 M $Zn(ClO_4)_2$ in propylene carbonate	N/A	231	340	0.5	100	*Batteries & Supercaps* 2020, 3, 254-260
				224	560	2	5000	
				204	660	5	5000	
				161	1240			
				125	1710			
				78	2350			
5	$Na_2V_6O_{16}\cdot nH_2O$	0.5m $Zn(ClO_4)_2$ with 18m $NaClO_4$ aqueous solution	3~4 mg cm^{-2}	188	77	4	2000	*Energy Environ. Sci.*,2021, 14, 4463
				167	158			
				130	390			
				108	800			
				88	1600			
				74	3200			
6	$Na_5V_{12}O_{32}\cdot 11.9H_2O$	3 M $Zn(CF_3SO_3)_2$ aqueous solution	1.1~3.4 mg cm^{-2}	317	72	0.1	45	*Mater. Today Energy*, 2021, 21, 100757
				274	144	1	3800	
				244	370			
				190	760			
				148	1480			

7	$Na_5V_{12}O_{32}$	3 M $ZnSO_4$ aqueous solution	~2 mg cm^{-2}	220 185 151 92 45.6	228 380 760 1520 3800	0.1 0.5 4	50 100 2000	*Adv. Energy Mater.*, 2018, 8, 1801819
8	Mn-Doped $Na_5V_{12}O_{32}$	2 M $ZnSO_4$/0.5 M Na_2SO_4 aqueous solution	~1.5 mg cm^{-2}	266 243 228 176 162 82	76 152 380 760 1520 3800	0.1 1	50 250	*Energy Fuels*, 2021, 35, 13483–13490
9	NVO	AE	~1.8 mg cm^{-2}	248 235 205 182 159 122	70 154 400 800 1600 3800	0.1 0.5 4	100 400 6000	*This work*
10	NVO	HE	~1.8 mg cm^{-2}	260 244 204 170	70 152 380 750	0.1 0.5 4	700 3000 6000	*This work*

	129	1400
	74	2800

Table 5.2 Comparison of the energy density of this work with reported aqueous Li-ion and Na-ion batteries.

No	Cathode/anode electrodes	Cathode/anode mass ratio	Average voltage	Energy density based on the mass of cathode and anode (Wh kg^{-1})	Reference
1	$LiTi_2(PO_4)_3$/C|| $LiMn_2O_4$	1.5:1	1.55 V	68	*Sci Rep*, 2015, 5, 10733
2	TiS_2||$LiMn_2O_4$	2:1	N/A	78	*Electrochem. Commun.*, 2017, 82**,** 71-74
3	VO_2||$LiMn_2O_4$	N/A	1.5 V	55	*Science*, 1994, 264, 1115-1118
4	LiV_3O_8||$LiNi_{0.81}Co_{0.19}O_2$	N/A	1~1.2 V	54	*Electrochimica Acta*, 2000, 46, 59–65
5	Mo_6S_8||$LiMn_2O_4$	2:1	1.5 V and 2 V	84	*Science*, 2015, 350, 938-943
6	acetylene black||$LiMn_2O_4$	1:2	~1.3 V	35	*J. Electrochem. Soc.*, 2006, 153, A450–A454
7	$LiTi_2(PO_4)_3$||$LiFeO_4$	1:1	0.9 V	50	*Nature Chemistry*, 2010, 2, 760–765
8	$LiTi_2(PO_4)_3$||$LiMn_2O_4$	1:1	1.5 V	60	*Adv. Funct. Mater.*, 2007, 17, 3877–3884
9	Polyimide||$LiCoO_2$	1.2:1	1.12 V	80	*J. Power Sources*, 2014, 249,367–372
10	$Na_3MnTi(PO_4)_3$||Na3$MnTi(PO_4)_3$	1:1	1.4 V	40	*Angew. Chem. Int. Ed.*, 2016, 55, 12768–12772
11	polymerized pyrene-4,5,9,10-tetraone ||$Na_3V_2(PO_4)_3$	N/A	0.65 V	30	*Nat. Mater.*, 2017, 16, 841–848

12	Polyimide||NaI	N/A	0.8 V	63.8	*Sci. Adv.*, 2016, 2, e1501038
13	$NaTi_2(PO_4)_3$||$Na_{0.44}MnO_2$	2.5:1	1.1 V	33	*Adv. Energy Mater.*, 2013, 3,290–294
14	Zn||NVO	N/A	0.75	70	*Nat Commun.*, 2018, 9, 1656
15	Zn||NVO	1:1.8	0.75 V	77	*This work*

Table 5.3 Comparative summary of state-of-art selected electrolytes for ZIBs.

No.	Electrolyte recipe	Flammability (Y/N)	Prefered Zn plating orientation	CE of Zn plating-stripping	Oxidation voltage (vs. Zn^{2+}/Zn)	Cathode	Cycle life	References
1	2 M $Zn(OTf)_2$ + 7 M DEC aqueous electrolyte	N	N	Zn‖Cu cell, 99.24%, 400 cycles, 1 mA cm^{-2}, 1 mAh cm^{-2}	N/A	$V_2O_5 \cdot nH_2O$ (mass loading N/A)	202 mAh g^{-1} (2 A g^{-1}), 5000 cycles (RT)	*ACS Nano*, 2022, 16, 9667−9678.
2	0.5 M $Zn(OTf)_2$ in TMP/DMC	N	N	Zn‖SS cell, 99.15%, 300 cycles, current and capacity N/A	2.25 V	VS_2, 4 mg cm^{-2}	~113 mAh g^{-1} (0.1 A g^{-1}), 500 cycles (RT)	*Adv. Mater*,. 2019, 31, 1900668.
3	3 M $Zn(OTf)_2$ in PC/H_2O (2:8)	N	N	N/A	N/A	$NVO \cdot 1.5H_2O$, 8 mg cm^{-2}	150 mAh g^{-1} (0.2 A g^{-1}) 400 cycles, −40 °C; 229 mAh g^{-1} (5 A g^{-1}) 1000 cycles, 30°C	*Adv. Funct. Mater.*, 2022, 32, 2111714.
4	0.5 M $Zn(OTf)_2$ in TEP/H_2O (7:3)	N	N	Zn‖SS cell, 93.71%, 100 cycles, current and capacity N/A	2.25 V	KCuHCf, 1 mg cm^{-2}	~80 mAh g^{-1}, 1000 cycles, average CE 97.66% (RT)	*Angew. Chem. Int. Ed.*, 2019, 58, 2760–2764.
5.	4 M $Zn(TFSI)_2$ + 4 M $P_{444(2O1)}$-TFSI in H_2O	N/A	N	Zn‖Cu cell, ~99%, 1.17 mA cm^{-2}, 1.17 mAh cm^{-2}, 20% Zn utilization, 16 cycles	2.42 V	$Na_2V_6O_{16} \cdot 1.63H_2O$, 1 mg cm^{-2}	~118 mAh g^{-1}, 1900 cycles (0.3 A g^{-1}) (RT)	*Angew. Chem. Int. Ed.*, 2021, 60, 12438–12445.

6	1 M $Zn(OTf)_2$ in PC/H_2O (5:5)	N	Y	Zn‖Cu cell, 99.93%, 1 mA cm^{-2}, 0.5 mAh cm^{-2}, 500 cycles	~ 2.5 V	PANI, 1.5-2 mg cm^{-2}	~75 mAh g^{-1} (0.2 A g^{-1}) 200 cycles, −20 °C	~100 mAh g^{-1} (0.2 A g^{-1}) 200 cycles, 50 °C	*J. Am. Chem. Soc.*, 2022, 144, 7160−7170.
7	3 M $ZnSO_4$ + 10 mM α-cyclodextrin aqueous electrolyte	N	Y	Zn‖Cu cell, ~99.9%, 1 mA cm^{-2}, 1 mAh cm^{-2}, 600 cycles	~ 2.5 V	V_2O_5, 6.4 mg cm^{-2}	~250 mAh g^{-1}, 200 cycles (1 A g^{-1}) (RT)		*J. Am. Chem. Soc.*, 2022, 144, 11129−11137.
8	2 M $ZnSO_4$ and 0.0085 M La(NO3)3) aqueous electrolyte	N	Y	Zn‖Ti cell, ~99.9%, 2 mA cm^{-2}, 1 mAh cm^{-2}, 2200 cycles	N/A	VS_2, 8 mg cm^{-2} (N/P ratio 4:3)	120 mAh g^{-1} (0.1 A g^{-1}), 100 cycles (RT)		*Nat. Commun.*, 2022, 13, 3252.
9	1 mol/Kg $Zn(TFSI)_2$ + 20 mol/kg LiTFSI aqueous electrolyte	N	N	Zn‖Pt (three electrode cell), 99.7%	N/A	$LiMn_2O_4$, 2.4 mAh cm^{-2}	38 mAh g^{-1} (4 C), 4000 cycles (RT)		*Nat. Mater.*, 2018, 17, 543–549.
10	2 M $ZnSO_4$ in NMP/H_2O (5:5)	N/A	Y	Zn‖Cu cell, ~99.7%, 1 mA cm^{-2}, 0.5 mAh cm^{-2}, 1000 cycles	N/A	VS_2, 5.3 mg cm^{-2}	125 mAh g^{-1} (1 A g^{-1}), 2000 cycles (RT)		*Adv. Energy Mater.*, 2022, 12, 2103231.
11	3 M $ZnSO_4$ + 0.5 M glycine aqueous electrolyte	N	Y	Zn‖Cu cell, 99.68%, 2 mA cm^{-2}, 2 mAh cm^{-2}, 650 cycles	N/A	$NH_4V_4O_{10}$ (mass loading N/A)	350 mAh g^{-1} (5 A g^{-1}), 3000 cycles (RT)		*ACS Nano, 2022,* DOI: 10.1021/acsnano.2c09317
12	1 M $ZnAc_2$ + 4 M NH_4I aqueous electrolyte	N	N	Zn‖Cu cell, 99.8%, 1 mA cm^{-2}, 1 mAh cm^{-2}, 100 cycles	N/A	I_2 (mass loading N/A)	~1.1 mAh cm^{-2}, 200 cycles (RT)		*J. Am. Chem. Soc.*, 2022, 144, 18435−18443

13	1.3 M $ZnCl_2$ in H_2O/DMSO (volume ratio of H_2O/DMSO = 4.3:1)	N/A	N	Zn‖Cu cell, 99.5%, 1 mA cm^{-2}, 0.5 mAh cm^{-2}, 400 cycles	~2.2 V	MnO_2 (mass loading N/A)	150 mAh g^{-1} (8 C), 500 cycles (RT)	*J. Am. Chem. Soc.*, 2020, 142, 21404−21409.
14	BMITFSI:$Zn(TFSI)_2$ (water/ionic liquid mass 20%)	N	N	Zn‖Cu cell, 99.27%, 1 mA cm^{-2}, 0.5 mAh cm^{-2}, 400 cycles	~2.5 V	PANI, 0.8-0.95 mg cm^{-2}	~60 mAh g^{-1} (1 A g^{-1}), 1000 cycles (RT)	*ACS Energy Lett.*, 2023, 8, 608−618.
15	2 M $ZnSO_4$ in water/EG (volume ratio of EG 40%)	N	N	Zn‖Ti cell, ~98%, 2 mA cm^{-2}, 1 mAh cm^{-2}, 120 cycles	~2.8 V	PANI/V_2O_5, 2.5-3.0 mg cm^{-2}	~45 mAh g^{-1} (0.2 A g^{-1}) 6500 cycles, −20 °C	~60 mAh g^{-1} (5 A g^{-1}) 50000 cycles, 20 °C	*Energy Environ. Sci.*, 2020, 13, 3527—3535.
16	1 M ZnTFMS/DMF	Y	N	Zn‖SS cell, ~99.8%, 1 mA cm^{-2}, 1 mAh cm^{-2}, 200 cycles	~2.4 V	PQMCT (mass loading N/A)	~22 mAh g^{-1} (0.2 A g^{-1}), 1 cycle, −70 °C	~180 mAh g^{-1} (2 A g^{-1}) 1 cycle, 150 °C	*Angew. Chem. Int. Ed.*, 2020, 59, 14577 – 14583
17	7.5 mol/Kg $ZnCl_2$-based aqueous electrolyte	N/A	N	Zn‖Cu cell, ~99%, 0.2 mA cm^{-2}, 0.2 mAh cm^{-2}, 50 cycles	~1.9 V	PANI, (mass loading N/A)	~75 mAh g^{-1} (0.2 A g^{-1}) 2000 cycles, −70 °C		*Nat. Commun.*, 2022, 11, 4463.
18	4 M $Zn(BF_4)_2$ aqueous electrolyte	N	N	Zn‖SS cell, ~95%, 0.5 mA cm^{-2}, 0.5 mAh, 1 cycle	~2 V	TCBQ2, 1-2 mg	~105 mAh g^{-1} (1 C) 1000 cycles, −30 °C	~90 mAh g^{-1} (0.1 C) 50 cycles, −30 °C	*J. Mater. Chem. A*, 2021, 9, 7042–7047.

19	2 M $Zn(OTf)_2$ in water/DMC (volume ratio 4:1)	N	N	Zn‖Ti cell, ~99.8%, 1 mA cm^{-2}, 1 mAh cm^{-2}, 200 cycles	N/A	V_2O_5, 2 mg cm^{-2}	~405 mAh g^{-1} (2 A g^{-1}) 1000 cycles (RT)	*Chem. Sci.*, 2021, 12, 5843–5852.
20	2.5 M $Zn(NO_3)_2$ +13 M $LiNO_3$in DMAC/H_2O	N/A	N	N/A	N/A	$LiMn_2O_4$, 3 mg cm^{-2}	95 mAh g^{-1} (1 C), 200 cycles (RT)	*ACS Appl. Mater. Interfaces*, 2021, 13, 39, 46634–46643.
21	*1 M $Zn(OTf)_2$ in DMAC/TMP/H_2O (volume ratio 5:2:3)*	*N*	*Y*	*Zn‖Cu cell, 99.5%, 1 mA cm^{-2}, 1 mAh cm^{-2}, 2000 cycles*	*~2.25 V*	*NVO* *~6 mg cm^{-2} for RT testing; ~0.6 mg cm^{-2} for high-low temperature testing*	*~264 mAh g^{-1} (0.1 A g^{-1})* *700 cycles, (RT);* *~190 mAh g^{-1} (0.5 A g^{-1})* *3000 cycles, (RT);* *~100 mAh g^{-1} (0.1 A g^{-1})* *1800 cycles, −40 °C;* *~200 mAh g^{-1} (5 A g^{-1})* *1400 cycles (retention ~60%), 70 °C;*	*This work*

5.9 Reference

1. Dincer I. Renewable energy and sustainable development: a crucial review. *Renewable and Sustainable Energy Reviews* **4**, 157-175 (2000).
2. Poullikkas A. A comparative overview of large-scale battery systems for electricity storage. *Renewable and Sustainable Energy Reviews* **27**, 778-788 (2013).
3. Wan F, *et al*. Design Strategies for Vanadium-based Aqueous Zinc-Ion Batteries. *Angewandte Chemie International Edition* **58**, 16358-16367 (2019).
4. Wang Y, *et al*. Electrolyte Engineering Enables High Performance Zinc-Ion Batteries. *Small* **18**, 2107033 (2022).
5. Zeng X, *et al*.. Recent progress and perspectives on aqueous Zn-based rechargeable batteries with mild aqueous electrolytes. *Energy Storage Materials* **20**, 410-437 (2019).
6. Kundu D, *et al*. Aqueous vs. nonaqueous Zn-ion batteries: consequences of the desolvation penalty at the interface. *Energy & Environmental Science* **11**, 881-892 (2018).
7. Blanc LE, *et al*. Scientific Challenges for the Implementation of Zn-Ion Batteries. *Joule* **4**, 771-799 (2020).
8. Zhang T, *et al.* Fundamentals and perspectives in developing zinc-ion battery electrolytes: a comprehensive review. *Energy & Environmental Science* **13**, 4625-4665 (2020).
9. Ming J, *et al*. Zinc-ion batteries: Materials, mechanisms, and applications. *Materials Science and Engineering: R: Reports* **135**, 58-84 (2019).
10. Wan F, *et al*. Aqueous rechargeable zinc/sodium vanadate batteries with enhanced performance from simultaneous insertion of dual carriers. *Nature Communications* **9**, 1656 (2018).
11. Soundharrajan V, *et al.* Na2V6O16·3H2O Barnesite Nanorod: An Open Door to Display a Stable and High Energy for Aqueous Rechargeable Zn-Ion Batteries as Cathodes. *Nano Letters* **18**, 2402-2410 (2018).
12. Oberholzer P, *et al*. Oxide versus Nonoxide Cathode Materials for Aqueous Zn Batteries: An Insight into the Charge Storage Mechanism and Consequences Thereof. *ACS Applied Materials & Interfaces* **11**, 674-682 (2019).

13. Wang F, *et al.* Highly reversible zinc metal anode for aqueous batteries. *Nature Materials* **17**, 543-549 (2018).

14. He P, *et al*. Cathode strategies to improve the performance of zinc-ion batteries. *Electrochemical Science Advances* **n/a**, e2100090 (2021).

15. Wang N, *et al.* Reversible (De)Intercalation of Hydrated Zn2+ in Mg2+-Stabilized V2O5 Nanobelts with High Areal Capacity. *Advanced Energy Materials* **10**, 2002293 (2020).

16. Wang X, *et al.* Advances and Perspectives of Cathode Storage Chemistry in Aqueous Zinc-Ion Batteries. *ACS Nano* **15**, 9244-9272 (2021).

17. Mathew V, *et al.* Manganese and Vanadium Oxide Cathodes for Aqueous Rechargeable Zinc-Ion Batteries: A Focused View on Performance, Mechanism, and Developments. *ACS Energy Letters* **5**, 2376-2400 (2020).

18. Wang N, *et al.* Zinc–Organic Battery with a Wide Operation-Temperature Window from −70 to 150 °C. *Angewandte Chemie International Edition* **59**, 14577-14583 (2020).

19. Naveed A, *et al.* A Highly Reversible Zn Anode with Intrinsically Safe Organic Electrolyte for Long-Cycle-Life Batteries. *Advanced Materials* **31**, 1900668 (2019).

20. Ming F, *et al.* Co-Solvent Electrolyte Engineering for Stable Anode-Free Zinc Metal Batteries. *Journal of the American Chemical Society* **144**, 7160-7170 (2022).

21. Liu D-S, *et al.* Regulating the Electrolyte Solvation Structure Enables Ultralong Lifespan Vanadium-Based Cathodes with Excellent Low-Temperature Performance. *Advanced Functional Materials* **32**, 2111714 (2022).

22. Zhao R, *et al.* Lanthanum nitrate as aqueous electrolyte additive for favourable zinc metal electrodeposition. *Nature Communications* **13**, 3252 (2022).

Chapter 6 Conclusion and outlooks

6.1 Conclusion

This Thesis aims to optimize the battery performance of LMBs and ZIBs, especially anode reversibility and cathode stability, via electrode/electrolyte interface modifications and electrolyte design. Two systematic literature reviews related to advanced strategies for the design of artificial protective layers for LMBs and advanced electrolyte designs for ZIBs, respectively, are provided in Chapter 2 to provide a comprehensive understanding of this area. One research work related to the design of a protective layer on the surface of Li metal is included in Chapter 3. Chapters 4 and 5 present the results of the work on optimising the electrochemical properties of Zn anode and sodium vanadate cathode with electrolyte design. Based on the work in this Thesis, the following conclusions are drawn:

1. Modifying the surface of Li metal anode with the silane coupling agent is a promising method to solve the issue of the Li metal electrode. This modification layer protects the Li metal from air corrosion, which would reduce the high requirement for protection from atmosphere in the manufacture of Li metal based batteries. This layer can also act as promoter to enhance the adhesion between the SEI layer and the Li substrate by forming chemical bonds and physical intertwining effects. As a consequence, both increased air stability of the Li electrode and enhanced electrochemical performance are achieved. MPS is introdued as an example, and apart from it, various silane coupling agents with different organic functional groups are worth investigating to further optimize the bonds between intermediates and the SEI layer.
2. Polar solvents dimethylacetamide (DMAC) and trimethyl phosphate (TMP) in a hybrid electrolyte (HE) exert strong dipole-dipole interaction with H_2O to increase the electron density of water protons making the H_2O dissociation less thermodynamically favorable and therefore strengthening O−H bonds of water. Zn^{2+} plating in HE preferentially orientates the (002) plane because of the lower surface energy of this plane compared with (100) and (101) planes. With confined water activity and favorable orientation, a Zn anode in HE exhibited a high reversibility and ultra-long life in which CE was 99.5 % for 2000 cycles, and Zn||Zn symmetric cells ran for 1600 h at a current density 5 mA cm^{-2} and areal capacity 5 mAh cm^{-2}. Moreover, the extended ESW makes it possible for HE to cope with the high voltage cathode, ZnHCFs, which exhibits a specific capacity of ca.60 mAh g^{-1} for 200 cycles.

3. The advantageous of aqueous ZIBs arise from anomalous properties of water, however, drawbacks are also from water. When strong polar molecules, DMAC and TMP, are introduced into the aqueous solution, strong dipole-dipole interaction occurs between DMAC/TMP and water. On the cathode side, DMAC and TMP are large molecules compared with H_2O, and therefore they are too large to squeeze into the NVO lattice, but ensure few water molecules combin with Zn^{2+} to insert into the NVO structure, protecting the host from collapse during long-term cycling. In HE, the structrual deformation of NVO cathode is smaller during the Zn^{2+} insertion, evidenced by the *in operando* XRPD and TEM images of different charge state of NVO. The Zn||NVO cells exhibit excellent cycling stability in HE, especially in low and medium rates. The strong interaction between solvents expanded temperature adaptability of electrolyte with the result that the Zn||NVO cell ran for 1400 cycles at 70 ℃, and for > 1800 cycles at − 40 ℃. Findings will be of immediate benefit in practical design for highly reversible ZIBs and therefore of wide interest to researchers and manufacturers.

6.2 Outlooks

Although marked improvements have been achieved in LIBs and ZIBs, the following critical issues are still worth highlighting:

For LIBs:

I) Improving the adhesion of SEI or ASEI layers on the surface of Li metal. Studies of SEI and ASEI layers have focused on the properties of the modulus, flexibility, composition, and stability, however, little attention has been paid to the adhesion of the protective layer and the Li metal anode. In particular, inorganic species typically lack effective chemical bonds with Li metal and may exfoliate due to interfacial strains. By improving the adhesion between the SEI component and the Li anode, the ASEI layer will be more durable and effective in long-term cycling.

II) Investigating how protective layers affect the stripping process. Researchers usually focus more on the plating behavior and kinetics of Li^+ while overlooking the stripping process. However, the stripping of Li^+ also affects the reversibility, depletion, and lifetime of the Li metal.

III) Understanding the effect of ASEI layers on the formation of the final layer. In general, the presence of the ASEI layer may affect the overpotential of Li deposition, which may

also alter the electrolyte decomposition. With clear understanding of the interaction between ASEI and naturally formed SEI layer, more reasonable ASEI can be designed.

IV) Designing protective layers with self-healing ability. Since the large volume change of Li metal remains a critical unsolved issue, the ability to reform the damaged ASEI layers becomes a crucial factor in determining the durability of ASEI layers. Polymeric ASEI layers are featured with designable functions, making it possible to design protective layers with self-healing capabilities.

V) Increasing air stability of Li anode. Li metal foils are highly sensitive to ambient air, rendering them difficult to handle and transport. If LMBs could be assembled without a protective atmosphere, the cost of their production would be significantly reduced. Chemical stability in the electrolyte should also be taken into account when designing air isolation layers.

For ZIBs:

I) Suppressing gas generation in aqueous electrolytes. Pressure due to gas generation may cause battery package failure. Quantitative analysis of gas generation during operation of ZIBs could serve as an accurate indicator to understand the suppression of side reactions between electrodes and electrolytes.

II) Further improving the CE of Zn anodes. The CE for Zn plating/stripping processes is normally lower than 99% in aqueous electrolytes and 99.5% in organic electrolytes, respectively. It is well known that for practical applications, the CE should be higher than 99.9%. Selecting solvents with higher stability against Zn anodes and wider voltage operating window is a promising strategy. However, we believe it is difficult to achieve a high CE with only a single approach. Combinations of different strategies, including developing aqueous-organic hybrid solvents, employing electrolytes with carefully optimised concentrations, and adding functional additives, could well repay future research.

III) Improving performance at high temperature. The side reactions in ZIBs are more severe at high temperatures, leading to poor battery performance. The current study of high temperature electrolytes is at an early stage. The cycling stability and rate capability of ZIBs at high temperatures have rarely been reported so far. Seeking suitable solvents with better temperature tolerance is a potentially useful approach.

IV) In-depth understanding of the mechanisms of Zn deposition. Zn growth characteristics can be easily affected by electrolytes, but the precise interrelationships between these two elements are not yet clear. A better understanding of growth behaviours would help to design dendrite-free Zn metal anodes. Previous results have proved that Zn^{2+} can be reliably plated in the 'horizontal' direction with the presence of functional additives or specific solvents. It is worth further investigation to achieve consistently dendrite-free Zn anodes. Besides these aspects, developing advanced *in-situ* techniques to characterize Zn grain growth would be of great use.

V) Attention should be payed to the cost of electrolytes. Low-cost is the most striking feature of ZIBs, however, recent researches mainly focus on the mechanism of proposed strategies while hardly mention their cost. The usage of organic salts and increasing salt concentration would result in a huge surge in cost. Developing high performance electrolyte with affordable price would be of great commercial values.

VI) The properties of polymer gel electrolytes need further improvements. The ionic conductivity of reported polymer gel electrolytes cannot be compared with that of liquid electrolytes, which result in unsatisfactory power density. What is worse, the increase of mechanical strength of gel/polymer electrolytes would further confine the mass diffusion and therefore decrease their ionic conductivities. Designing polymer gel electrolytes with high ionic conductivities and good mechanical properties would be the aim of follow-up studies.

VII) Comprehensive consideration is required in the design of electrolytes. Aqueous electrolytes have advantages in ionic conductivities, safety, and low cost, but fail to provide sufficient ESW, temperature operational range and stability against Zn anodes. Non-aqueous electrolytes show complementary advantages. Aqueous-organic hybrid electrolytes are very promising since they make it easier to balance the property requirements of ZIBs *via* optimizing components and the ratio of the solvents. Besides, synergistic effects among multi-strategies are worth in-depth studies. A better understanding of the compatibility between different components and their interactions would help to guide the design of high-performance electrolytes.

VIII) The charge storage mechanisms of manganese-based and vanadium-based cathode materials are still controversial. It is crucial to develop advanced characterization techniques to uncover the true charge storage mechanism of these cathode materials.

Vanadium-based cathode materials exhibit capacity fading during cycling, particularly at low rates (<0.5 A g^{-1}). This phenomenon is attributed to structural degradation caused by dissolution and inactivation of the active phase. The electrochemical reactions typically involve a combination of ionic insertion/extraction and pseudocapacitance processes. Furthermore, during the discharging process, Zn^{2+} ions, along with protons, are inserted into the cathode, making the charge storage mechanism more complicated. For manganese-based materials, the presence of dissolved Mn^{2+} in electrolytes poses a challenge to the intercalation mechanism. Additionally, phase transitions, such as the transition between the tunneled α-MnO_2 and the layered Zn-birnessite during discharging/charging processes, have been observed. The exact details of the intercalation process and discharge products are still a matter of dispute. The current characterization methods, which rely on *ex situ* techniques, have been unable to provide a comprehensive understanding of the continuous structural changes. Consequently, *in situ* experiment design aiming to distinguish these intermediate products would be the future research direction. It is imperative to employ characterization techniques and advanced analysis methods to obtain a more detailed and precise understanding of the reaction mechanisms involved. This deeper understanding will aid in the further optimization of the electrochemical performance of manganese-based and vanadium-based cathode materials.

Appendix: Publications During the PhD candidature

[1] **Wang, Y.**, Wang, Z., Yang, F., Liu, S., Zhang, S., Mao, J., Guo, Z., Electrolyte Engineering Enables High Performance Zinc-Ion Batteries. ***Small***, 2022, 18, 2107033.

[2] **Wang, Y.**, Wang, Z., Zhao, L., Fan, Q., Zeng, X., Liu, S., Pang, W. K., He, Y.-B., Guo, Z., Lithium Metal Electrode with Increased Air Stability and Robust Solid Electrolyte Interphase Realized by Silane Coupling Agent Modification. ***Adv. Mater.,*** 2021, 33, 2008133.

[3] **Wang, Y.**, Wang, Z., Pang, W. K., Lie, W., Yuwono, J. A., Liang, G., Liu, S., D'Angelo, A. M., Deng, J., Fan, Y., Davey, K., Li, B., Guo, Z. Solvent control of water O−H bonds for highly reversible zinc ion batteries. ***Nat. Commun.***, 2023, 14, 2720.

[4] Wang, Z., **Wang, Y.**, Li, B., Bouwer, J. C., Davey, K., Lu, J., & Guo, Z., Non-flammable ester electrolyte with boosted stability against Li for high-performance Li metal batteries. ***Angew. Chem., Int. Ed.***, 2022, 61(41), e202206682.

[5] Wang, Z., **Wang, Y.**, Wu, C., Pang, W. K., Mao, J., Guo, Z., Constructing nitrided interfaces for stabilizing Li metal electrodes in liquid electrolytes. ***Chem. Sci.***, 2021, 12(26), 8945-8966

[6] Wang, Z., **Wang, Y.**, Zhang, Z., Chen, X., Lie, W., He, Y.-B., Zhou, Z., Xia, G., Guo, Z., Building Artificial Solid-Electrolyte Interphase with Uniform Intermolecular Ionic Bonds toward Dendrite-Free Lithium Metal Anodes. ***Adv. Funct. Mater.,*** 2020, 30, 2002414.

[7] Liu, S., Vongsvivut, J., ***Wang, Y.***, Zhang, R., Yang, F., Zhang, S., Davey, K., Mao, J., Guo, Z., Monolithic Phosphate Interphase for Highly Reversible and Stable Zn Metal Anode. ***Angew. Chem., Int. Ed.***, 2023, 135(4), e202215600.